Doctoral Dissertations 1896 - February 2014

1-1-1989

Structure and morphology of electrically conducting poly(p-phenylene vinylene)/

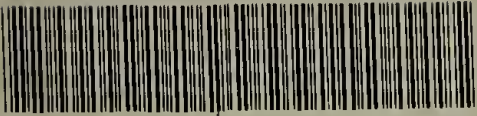Michael A. Masse
University of Massachusetts Amherst

Follow this and additional works at: https://scholarworks.umass.edu/dissertations_1

Recommended Citation

STRUCTURE AND MORPHOLOGY OF ELECTRICALLY CONDUCTING

POLY(*p*-PHENYLENE VINYLENE)

A Dissertation Presented

by

MICHAEL A. MASSE

Submitted to the Graduate School of the

University of Massachusetts in partial fulfillment

of the requirements for the degree of

DOCTOR OF PHILOSOPHY

September 1989

Department of Polymer Science and Engineering
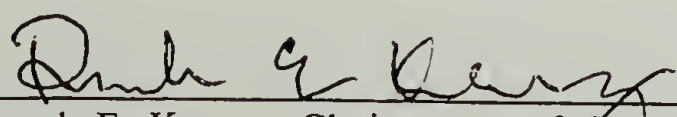
STRUCTURE AND MORPHOLOGY OF ELECTRICALLY CONDUCTING

POLY(*p*-PHENYLENE VINYLENE)

A Dissertation Presented

by

MICHAEL A. MASSE
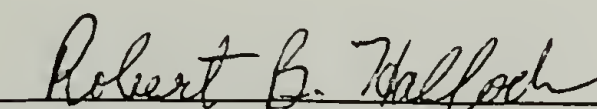
Approved as to style and content by:

_____
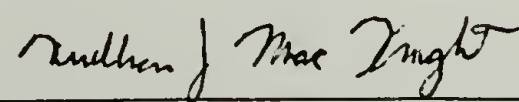
Frank E. Karasz, Chairperson of Committee

_____
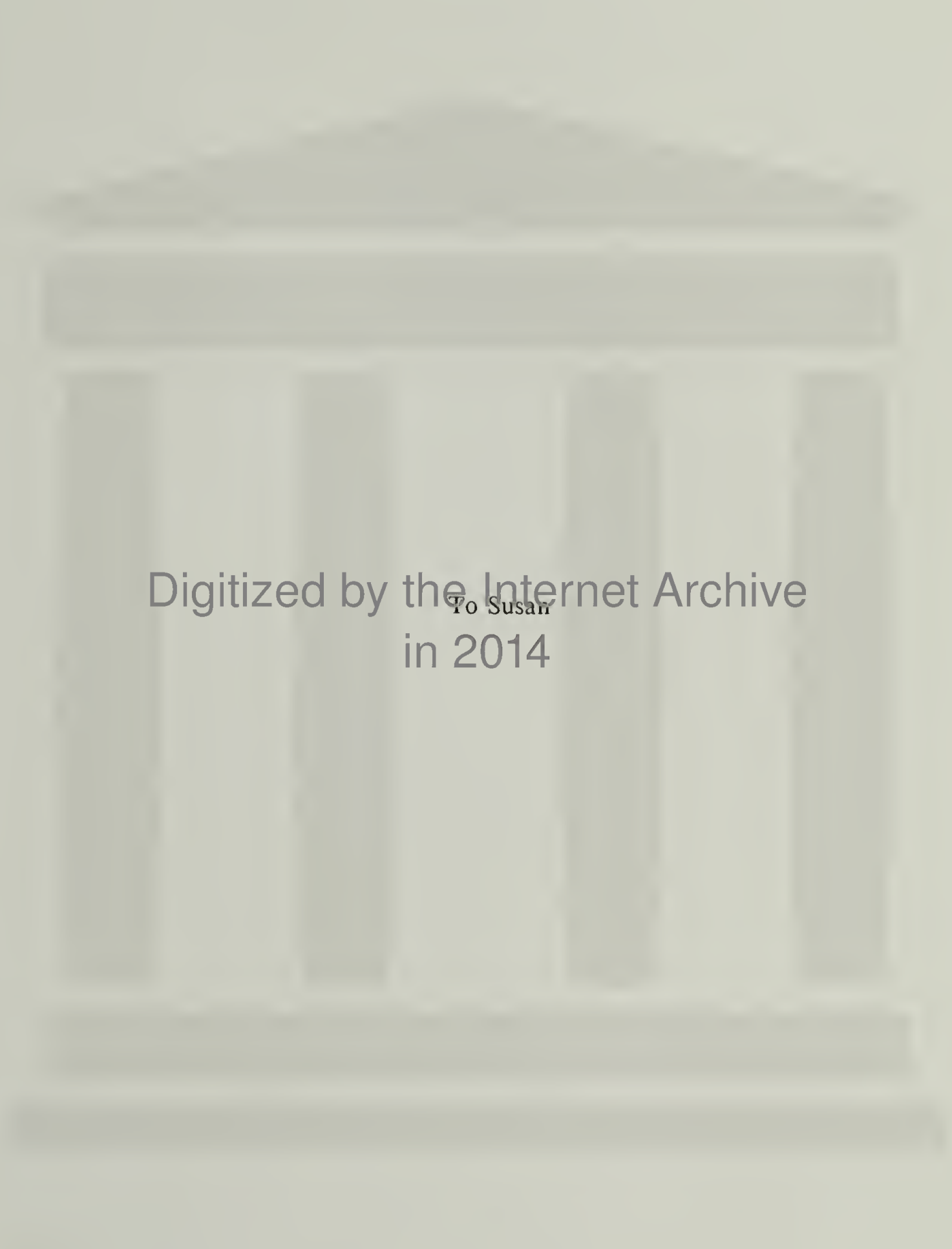
Edwin L. Thomas, Member

_____

Robert B. Hallock, Member

_____

William J. MacKnight, Department Head
Department of Polymer Science and Engineering

To Susan

iv

his assistance with RBS. Many grateful thanks are due to Mr. Jacob A. Hirsch for his assistance with the x-ray photoelectron spectroscopy. His helpful advice concerning the handling of AsF_5 is also acknowledged. Ms. Victoria A. White is thanked for her assistance with the GC-mass spectrometry. Mr. Jeffrey H. Simpson is thanked for his assistance in the laboratory.

Finally, this work could not have been so expeditiously or enjoyably carried out without the continual encouragement and loving support of my wife, Susan. For this I am truly indebted.

ABSTRACT

STRUCTURE AND MORPHOLOGY OF ELECTRICALLY CONDUCTING

POLY(p-PHENYLENE VINYLENE)

SEPTEMBER 1989

MICHAEL A. MASSE, B.S., UNIVERSITY OF MAINE

M.S., UNIVERSITY OF MAINE

Ph.D., UNIVERSITY OF MASSACHUSETTS

Directed by: Professor Frank E. Karasz

Poly(p-phenylene vinylene) (PPV) is a conjugated polymer which becomes
highly electrically conducting when treated with the appropriate doping agents. In
this work the physical and chemical structure of the electrically conducting forms of
PPV have been investigated using a variety of experimental techniques.

The chemistry of AsF_5-doping in PPV was investigated using FTIR, x-ray
photoelectron spectroscopy (XPS) and mass spectrometry. The results confirmed the
formation of AsF_6^- in the doped polymer. Mass spectrometry of heavily AsF_5-doped
PPV showed the thermolysis products to consist only of hydrocarbon chain segments.

A first order crystal-crystal phase transition was observed when PPV was
chemically doped with AsF_5, SbF_5, H_2SO_4 or electrochemically oxidized with ClO_4^- as
the counterion. These structures have been observed using wide angle x-ray
diffraction. Doping with these agents does not disrupt the original orientation of the
PPV crystallites. The crystalline phases obtained with all dopants are similar in
character indicating a closely related family of electrically conducting structures

having orthorhombic symmetry. An electrically conducting phase consisting of layers of stacked, parallel polymer chains separated by a layer of the chemical dopant is proposed.

The crystal morphology of PPV has been investigated using electron microscopy. Dark field imaging revealed small diffracting regions on the order of 7.0 nm in size with an aspect ratio near 1. These diffracting regions were shown by high resolution transmission electron microscopy to be composed of small crystallites 5.0 nm in size. A micellar model of the crystalline morphology in oriented PPV is presented. The model represents PPV as a highly connected network of small crystallites. Crystallites of the electrically conducting phase were observed after doping with H_2SO_4. The general morphological character is preserved in the conversion from insulating to conducting forms.

With the conditions employed dopant penetration was found to be shallow in AsF_5 treated PPV. Based on Rutherford backscattering spectrometry results a model is presented in which shallow conducting skins are formed with dopant profiles characteristic of a chemical fixation process. A thin layer containing arsenic oxides is formed on the doped surfaces.

TABLE OF CONTENTS

LIST OF TABLES

LIST OF FIGURES

CHAPTER 1

INTRODUCTION

1.1 Materials, Structure and Electrical Conductivity

Traditionally polymers have been considered electrical insulators [1]. In fact, common polymers such as polystyrene, polyethylene, and poly(tetrafluoro-ethylene) have electrical conductivities on the order of 10^{-16} to 10^{-18} (Ω cm)$^{-1}$ [1,2]. These values are at least 22 orders of magnitude less than the conductivity of metallic silver and copper. However, in 1977 it was discovered that a synthetic organic polymer, polyacetylene, possessed an electrical conductivity of 220 (Ω cm)$^{-1}$ after doping with AsF$_5$ [3]. This discovery provided the impetus for research into the physics and chemistry of organic conducting polymers. The work presented in this dissertation has been focused on one such electrically conductive polymer, poly(p-phenylene vinylene) (PPV). This polymer consists of alternating phenylene and vinylene groups along a single polymer chain (see Figure 1.1). As such it can be considered as an alternating copolymer of polyacetylene and poly(p-phenylene) both of which are conducting in their doped forms. With regard to electrical conductivity, PPV challenges the best synthetic conductors.

The main point for investigation in this study has been the structural character of the conducting forms of PPV. It is well known that the microscopic structure of materials lies at the basis of their electrical properties [4]. For instance, the nature of the crystalline lattice is one factor responsible for the high electrical conductivity of metals. In metallic lattices the conduction electrons experience a periodic potential arising in part from their Coulombic interactions with the regularly spaced nuclei. This periodic potential provides a background against which the electrons travel with high mobilities. Where the periodic nature of the material

breaks down, as in grain boundaries, the mobility of the electron is to some degree retarded.

The presence of a periodic character is itself not a sufficient condition for the existence of electrical conductivity. Consider for example VO_2. This crystalline metal oxide is an insulator at ambient pressures. As the pressure is increased the lattice parameters are slightly compressed. At a critical distortion the material becomes electrically conductive. This phenomenon is referred to as the metal-insulator transition and is caused by a modification of the periodic potential through a change in the lattice parameters.

In a more recent vein, the structure of the newly discovered copper oxide superconductors [5,6] also plays an important role in the properties of these materials. For instance, $YBa_2Cu_3O_x$ is orthorhombic and superconducting for 6.5<x<7.0 [7]. The crystal is a layered structure [8] as shown in Figure 1.2. This material is antiferromagnetic with neighboring copper atoms having alternating spins [9]. Because of the periodic lattice structure a spin density wave is created which is related to the occurrence of superconductivity. Disruptions of the periodic structure at grain boundaries [10] or intragrain twin boundaries [11] leads to the formation of non-superconducting regions.

Clearly, crystalline structure and morphology play an important role in material properties.

In the field of conducting polymers the understanding of the structure-property relation is less well developed. Because of the anisotropic nature of bonding in π-conjugated polymers theoretical treatments have considered conduction as a one-dimensional process [12-14]. However, significant transverse conductivities have been experimentally measured in oriented conducting polymer films [15-17]. Thus, while stongly anisotropic, the transport of electrons in conducting polymers has at least a two-dimensional character. Admittedly, the many-body problem of conduction in a

three-dimensional array of polymer chains is a difficult one. Further, the one-dimensional approach satisfactorily accounts for many properties of conducting polymers [12]. Nonetheless, consideration of the physical structure in the conducting phases of polymeric materials may lead to important refinements.

1.2 Objectives

The purpose of this dissertation work has been to investigate the structural features of electrically conducting PPV from a materials point of view. It is hoped that the results presented here will serve as a basis for a deeper understanding of electron transport in synthetic polymers. Rather than focus on one particular aspect, this work has investigated the structure of electrically conductive PPV on three different levels. First, wide angle x-ray diffraction studies were undertaken to investigate the crystal structure of PPV oxidized with a variety of dopants. Second, the morphology of the conductive crystalline domains was probed using transmission electron microscopy (TEM). Third, the penetration of dopant into bulk films was studied using Rutherford backscattering spectroscopy (RBS). This approach is schematically represented in Figure 1.3. Hopefully, from this work a clear picture of the structure and morphology of electrically conductive PPV will emerge.

1.3 Organization of the Dissertation

Before presentation of the experimental results a review of conducting polymers and their physical structures will be presented in Chapter 2. The experimental procedures will be discussed in Chapter 3. Next, the electrical properties and the chemistry of doping of PPV will be presented in Chapter 4. In Chapters 5, 6, and 7 respectively the x-ray diffraction crystal structure study, the morphology investigation, and the dopant penetration results will be discussed. The correlations between the results of these three areas of study will be discussed in Chapter 8 along with other general conclusions and suggestions for future study.

3

To improve the readability of this manuscript the text, tables, and figures are not interleaved. Rather, the text, tables, and figures are separate and follow in this order in each chapter.

trans-Poly(*p*-phenylene vinylene), PPV
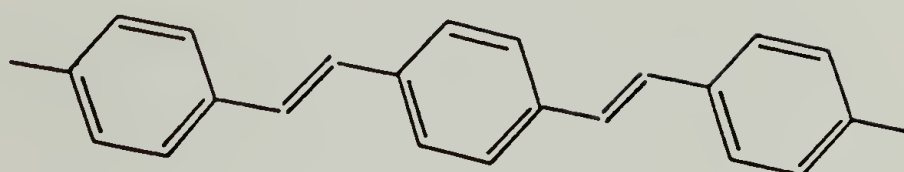
Poly(*p*-phenylene), PPP
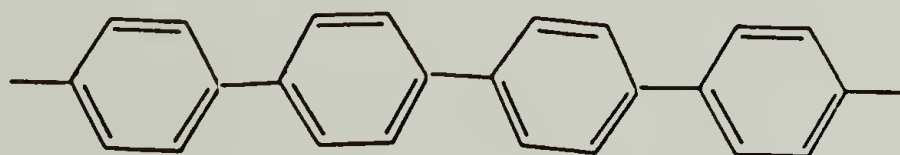
trans-Polyacetylene, PA

Figure 1.1   Chemical structure of poly(*p*-phenylene vinylene) and related compounds.
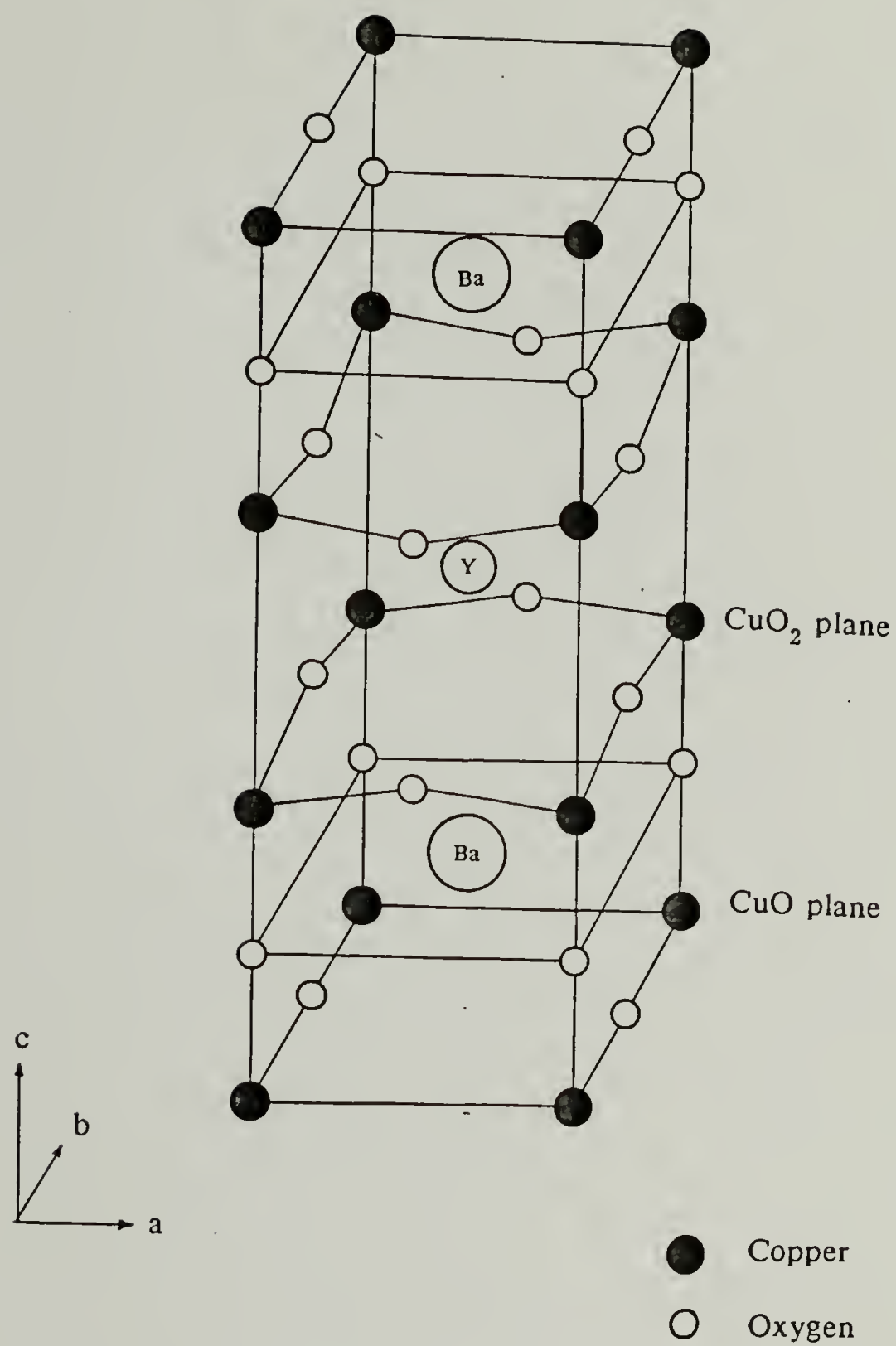
Figure 1.2   Crystal structure of high T_c superconductor $YBa_2Cu_3O_7$
(after ref. 7).

II. MORPHOLOGY OF THIN DOPED LAYERS

film cross-section

III. DOPANT PENETRATION IN BULK FILMS

C_{dopant}

film depth

ELECTRICALLY CONDUCTING POLY(p-PHENYLENE VINYLENE)
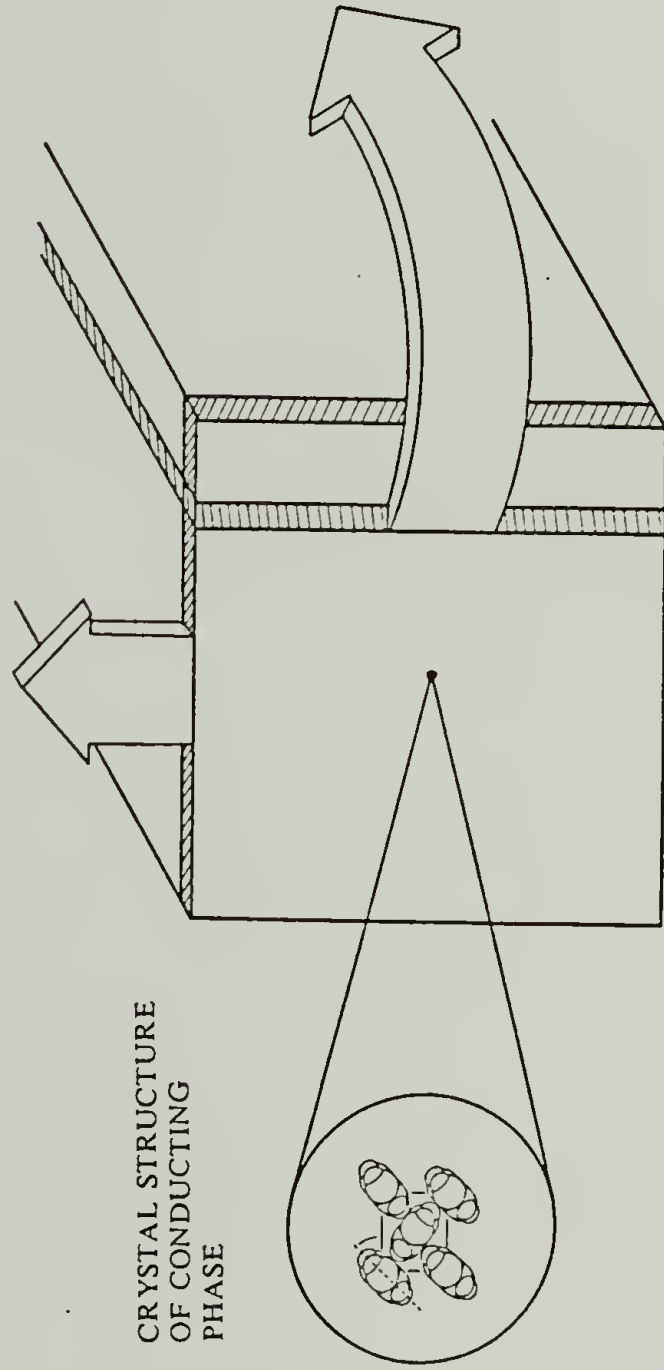
I. CRYSTAL STRUCTURE OF CONDUCTING PHASE
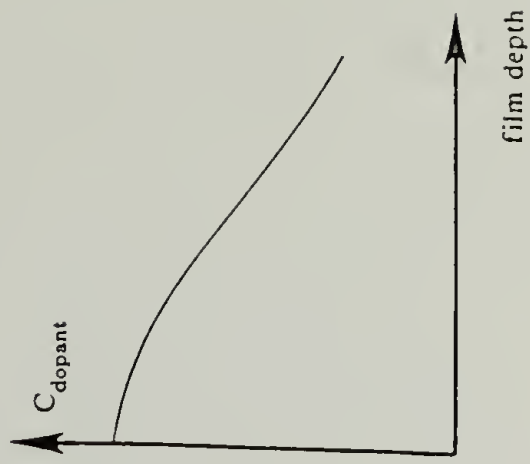
Figure 1.3   Schematic representation of the structural character investigation of conducting PPV.

7

CHAPTER 2

LITERATURE REVIEW

Beginning with the discovery of electrical conduction in polyacetylene [3] the potential of synthetic organic polymers as electrical conductors has been vigorously studied [18]. Much effort has been expended in the synthesis and characterization of new macromolecules with the goal of achieving conductivities equal to or greater than metals. In fact the synthetic nature of organic polymers has allowed the synthesis of dozens of chemically different macromolecules each with differing electrical properties [19,20]. To date the highest electrical conductivities have been achieved with Ziegler-Natta synthesized polyacetylene: Naarmann and coworkers [21] measured room temperature conductivities as high as 1.5×10^5 $(\Omega \text{ cm})^{-1}$. While still lower than copper ($\approx 10^6$ $(\Omega \text{ cm})^{-1}$) this value of electrical conductivity challenges metallic conductivity when normalized by mass density. On the other hand, non-conjugated polymers such as cis-polyisoprene have been found to possess conductivities of $\approx 10^{-1}$ $(\Omega \text{ cm})^{-1}$ when iodine-doped [22]. Thus, by employing a variety of chemical structures a wide range of electrical properties can be achieved with synthetic polymers.

In this chapter a review of pertinent conducting polymer literature is presented. First the developments concerning PPV are discussed. This is followed by a review of morphological and structural studies performed on conducting polymers in general.

2.1 Direct Synthesis of Poly(phenylene vinylene)

The investigation of PPV as an electrical conductor was initiated using low molecular weight fractions obtained by direct synthetic routes. Oligomeric PPV was

8

synthesized by Wittig condensation of p-xylene bis-(triphenylphosphonium chloride) with terephthaldehyde or by dehydrohalogenation of p-xylylidene dihalides [23-25]. Because of the oligomeric character and insolubility of these molecules the PPV thus obtained was in powder form. The highest electrical conductivities measured on pressed pellets of oligomeric PPV powder was on the order of 1 $(\Omega\ cm)^{-1}$. While the conductivity values are low with respect to metals these studies revealed important features concerning the relationship between chemical structure and conductivity. The conductivities of Wittig and dehydrohalogenation PPV were essentially identical even though the former route produces a large fraction of *cis* double bonds and the latter primarily *trans* double bonds [25]. On the other hand, when *meta* linkages are incorporated on the phenyl group rather than *para* linkages the molecule does not react with AsF_5. This was attributed to a change in electronic structure producing an increased band gap. Further, the model compounds stilbene and *trans,trans*-1,4-distyrl-benzene as well as poly(diacetylene phenylene), both the *para* and *meta* forms, did not exhibit conductivity increases after AsF_5-doping. These studies demonstrated that conductivity increases occur when the molecule has a degree of polymerization greater than three and *para* aromatic bonding.

2.2 Precursor Synthetic Route to Poly(p-phenylene vinylene)

As discussed in the preceding section high molecular weight PPV is not obtained from direct synthetic routes. The synthesis of high molecular weight PPV was first performed by Wessling and Zimmerman in 1968 [26]. These investigators synthesized a water soluble sulfonium salt precursor polymer which could be thermally converted to fully conjugated PPV. In this route bis-(sulfonium chloride)-p-xylene is polymerized in water by addition of a strong base (see chapter 3 for a detailed procedure). Recent spectroscopic studies have proposed an anionic polymerization mechanism having an ylid propagating species [27].

This synthetic route has been employed by Karasz and coworkers [28,29] and by Murase et al [30,31] in the study of the electrical properties of PPV. Highly oriented films of PPV can be prepared by simultaneously stretching and heating the precursor films. The electrical conductivity of isotropic films was 10 $(\Omega\ cm)^{-1}$ after AsF_5-doping [28,31]. In the oriented films the conductivity is anisotropic with the largest component parallel to the orientation direction. In fact, films stretched to a draw ratio of 10 had parallel and transverse conductivity values of 60 and 2 giving and anisotropy $(\sigma_\parallel/\sigma_\perp)$ of 30 [32]. (The draw ratio is defined as the ratio of the final length to the original length, L/L_o.) Thus, increased conductivities are measured for high molecular weight PPV synthesized by the precursor route.

Recent developments involving the synthetic route have shown that *incipient* or self-doping might be possible with precursor PPV. Patil et al [33] have synthesized sulfonium salt precursors to PPV which incorporate doping-active counterions. Through an ion-exchange process the usual chloride counterion is replaced by an AsF_6^- anion. Upon mild heat treatments modest conductivities ($\approx 10^{-1}$ $(\Omega\ cm)^{-1}$) were obtained.

The sulfonium salt precursor route has been used to synthesize a variety of chemical derivatives of PPV [34-40]. Table 2.1 lists some of these derivatives and the conductivities achieved upon doping. As can be seen from this table the highest electrical conductivities are achieved with AsF_5 doping. Chemical modification by incorporation of functional groups on the phenylene ring generally decreases the attainable electrical conductivities. However, chemical modification leads to changes in the polymer oxidation potential making possible doping by relatively weak agents such as I_2. This result has been utilized by Han et al [36]. These workers synthesized copolymers of phenylene vinylene and 2,5-dimethoxy-phenylene vinylene. As a result of the lower oxidation potential of the dimethoxy-PPV segments the

copolymers were readily doped with I_2 when only a small amount of dimethoxy repeat units were incorporated into the polymer chains.

The soluble character of the PPV precursor has also allowed the preparation of conducting polymer blends. Blends of precursor PPV with a variety of water soluble non-electroactive polymers have been prepared by casting from common solvents [41-43]. Blends with polyacrylamide were orientable and reached conductivities on the order of 10 $(\Omega \text{ cm})^{-1}$ after doping with AsF_5 [41]. Further, it was found that blending served to accelerate both chemical and electrochemical doping by facilitating ion transport in blends with poly(ethylene oxide), poly(vinyl methylether), and hydroxypropyl cellulose [42]. A detailed study of PPV/ poly(ethylene oxide) blends demonstrated the effect of morphology on electrical properties [43]. At low PPV contents (<10 wt%) spherulitic morphologies characteristic of pure PEO were found. As a result, the PPV did not form a continuous phase and only low electrical conductivities (<10^{-3} $(\Omega \text{ cm})^{-1}$) resulted after doping. At intermediate compositions (25-50 wt%) PPV is segregated in the interlamellar region of the PEO spherulites forming a highly connected network. This PPV morphology facilitates rapid doping to limiting conductivities greater than 200 $(\Omega \text{ cm})^{-1}$. At higher PPV contents (> 60 wt %) the PEO phase is disperse and shows a lessened accelerating effect on doping.

Aside from preparing electroactive PPV, the polysulfonium precursor has also been used to prepare graphite films. Ohnishi et al [44] have pyrolyzed oriented PPV films prepared via the precursor route. They found biaxially oriented PPV, which had been pyrolyzed at 2750°C, to be quite similar in structure and electrical properties to highly oriented pyrolytic graphite (HOPG). They measured a conductivity of 10^4 $(\Omega \text{ cm})^{-1}$ on samples prepared in this fashion. Subsequent intercalation studies have also been performed on PPV derived graphite [45,46].

2.3 Molecular and Crystalline Order in PPV

As previously mentioned high degrees of molecular orientation can be achieved by the simultaneous heating and stretching of precursor films. An excellent study by Bradley et al [47] characterized the molecular orientation in drawn films using infrared dichroism. In this study films having a draw ratio of 5 were found to possess a Hermans orientation function of 0.94. The Hermans orientation function is defined

$$f = (3<\cos^2\phi> - 1)/2 \qquad\qquad (2.1)$$

where ϕ is the angle between the molecular axis and the orientation direction. As can be seen from the above relation f approaches 1.0 as $<\cos^2\phi>$ approaches 1.0. Thus, Bradley's result indicates a nearly perfect orientation of the polymer chain axis with the stretch direction. In fact, the degree of orientation is higher than that predicted by the Kratky model [48]. The Kratky model is based on a pseudo-affine deformation mechanism and represents the upper limit for molecular orientation by deformation in semicrystalline polymers. However, the model is a poor description of PPV deformation since viscous flow and volume change due to the chemical elimination reaction are not taken into account. When the volume change due to reaction is considered it is found that the actual draw ratio is 26% greater than the nominal draw ratio [49]. This correction alone, however, does not bring the observed orientation into agreement with the Kratky model. A deformation mechanism fully descriptive of the high efficiency of molecular orientation in PPV remains to be forwarded.

The molecular orientation of PPV as a function of draw ratio was investigated using both infrared dichroism and x-ray diffraction by Gagnon et al [50]. This study found the molecular orientation to be a strong function of draw ratio at low elongations. At draw ratios of 5 or greater the orientation function reached limiting values near 0.95. For all draw ratios the x-ray derived value was slightly greater than

the infrared value. This was attributed to a higher degree of orientation in the crystalline domains.

The above studies have all focused on fully converted PPV. A recent study by Moon et al [51] has followed the development of crystallinity during the precursor to PPV conversion using x-ray diffraction. The precursor is amorphous. As the films are thermally converted PPV crystallites nucleate and grow, reaching final lateral sizes of 11.0 nm as determined from a Scherrer analysis.

Initial x-ray studies of the chain structure concluded that the solid state order was nematic in character with no long range periodicity [15]. Subsequent x-ray diffraction results by Bradley et al [52] confirmed the crystalline character of PPV. A detailed electron diffraction study by Granier et al [53] determined the crystalline unit cell to be monoclinic (see Figure 2.1). This study also noted that some partial axial translational disorder existed in the [100] direction. A subsequent study by Granier et al [54] refined the setting angle of the PPV chains in the unit cell using packing energy calculations and presented results from a detailed analysis of the scattered intensity distribution along the $c = 1,2,3,4,5,6$ layer lines. This analysis quantified the paracrystalline disorder (second kind) inherent in PPV. Following the developments of Hosemann and Bagchi [55] the components of a fluctuation tensor were determined by fitting of calculated and experimentally observed diffracted intensities. The components of this tensor describe the displacement of a point in a crystalline lattice from its *equilibrium* position. Figure 2.2 schematically represents the atomic position fluctuations in the PPV crystal. Of the nine tensor components eight had values less than or equal to 0.04 nm indicating small contributions to the disorder. The remaining component $\Delta_{33}(1)$ had a value greater than or equal to 0.16 nm. This distance is the magnitude of axial position fluctuation (ie., along the [001] direction) of neighboring chains in the [100] direction. By comparison the corresponding axial fluctuation for neighboring chains in the [010] direction ($\Delta_{33}(2)$)

is less than 0.04 nm. Also, the axial fluctuation component along a single chain makes only a small contribution ($\Delta_{33}(3) < 0.024$ nm). Clearly this last result is expected since the nuclei of a single chain are held in place by covalent bonds. Extending the conclusions of Granier's paracrystallinity study one can imagine the PPV crystal as having some *sheet-like* character where the (100) planes are the well-registered sheets.

2.4 Mechanical and Optical Properties of PPV

Initially the study of mechanical properties of PPV films was hindered by the inability to attain suitable lengths of uniformly drawn polymer. Recently, Machado et al [56] developed a process to controllably stretch-orient precursor PPV films. Uniform strains were imposed in both the stretch (or machine) and transverse directions. The mechanical properties of uniaxially oriented films obtained by this process were measured for "as-stretched" and fully converted films [57]. In the "as-stretched" state the films had low elastic moduli ranging from 2.7 to 15.5 GPa for draw ratios of 1 and 10 respectively. In addition, films with draw ratio less than 5 exhibited classical yielding behavior with the formation and propagation of a neck region. "As-stretched" films of higher draw ratio exhibited elastic behavior. Fully conjugated PPV did not exhibit classical yielding. High moduli ranging from 2.3 GPa for isotropic films to 37 GPa for films of draw ratio 12 were measured. Further, the mechanical properties of oriented films were anisotropic with modulus anisotropies ($E_{\parallel}/E_{\perp}$) as high as 58. The mechanical modulus anisotropy of undoped films was closely correlated to the conductivity anisotropy of doped, conducting films.

Doping by AsF_5 and SbF_5 chiefly served to embrittle the films. Also, the elastic moduli were lowered by a factor of 2-5. From these results it was concluded that the incorporated dopant did not contribute any load bearing capacity to the films but rather merely increased the average cross-sectional area per chain.

14

Optical spectroscopy has been applied to the investigation of the electronic structure of conducting polymers. Absorption spectra of electrochemically oxidized PPV was first reported by Yoshino et al [58]. The investigators observed three doping induced absorptions at 0.7, 2.0 and 2.7 eV. The highest absorption corresponds to the band gap (ie., the energy difference between valence and conduction bands in an electronic band structure). The two lower absorptions were attributed to electronic transitions associated with bipolaron states (see Figure 2.3). (For an excellent introduction to electronic structures in conducting polymers see ref. [13].) Electron spin resonance conducted by these researchers found only a low concentration of spins in the doped sample and this concentration saturated at low doping levels while the conductivity continued to increase. The authors explained this behavior as the initial formation of polaron states (having a spin of 1/2) which would be required as the first step toward formation of a bipolaron.

Similar results were obtained by Bradley et al from absorption studies of doped PPV [59] and from photoinduced absorption studies of undoped PPV [60]. Electrochemically doped PPV exhibited doping induced absorptions at 0.9 and 2.3 eV. PPV doped with AsF_5 had absorptions at 0.9 and 2.1 eV. These excitations were attributed to bipolaron structures and no evidence, in the form of an intragap transition at ≈ 1.4 eV, was observed thereby discounting the possibility of a polaronic structure. Photoinduced absorption of undoped PPV gave transitions at 0.6 and 1.6 eV. While these energies are somewhat lower than in doped PPV they remain consistent with bipolarons.

Detailed molecular orbital calculations have furthered the understanding of the electronic structure in conducting PPV [61]. Comparison of calculated and experimental results has determined the electronic structure to deviate from purely bipolaron character. Rather, the bipolaron-like electron defect experiences a strong Coulombic interaction and is localized within only four repeat units.

15

Thin PPV films have also been investigated with regard to non-linear optical properties. In linear optical materials the polarization is directly proportional to the electric field vector. In non-linear optics second and third order (and higher) dependencies of the polarization on the electric field vector arise [62,63]. In general the polarization of a material is expressed

$$P_i = \chi_{ij}^{(1)}E_i + \chi_{ijk}^{(2)}E_jE_k + \chi_{ijkl}^{(3)}E_jE_kE_l + \ldots \ldots \tag{2.1}$$

where E_i is the ith component of the electric field vector and the $\chi^{(i)}$ are the ith order optical susceptibilities. These non-linear phenomena can be applied to the construction of optical communication and signal processing devices.

A study on isotropic PPV films by Kaino et al [64] found a third order susceptibility of 7.8×10^{-12} esu at a wavelength of 1.85 μm. Oriented PPV films were examined by Singh et al [65]. These investigators measured $\chi^{(3)} \approx 4 \times 10^{-10}$ esu at 602 and 508 nm along the chain direction. Further, the susceptibility possessed an anisotropy $(\chi^{(3)}_{\parallel}/\chi^{(3)}_{\perp})$ of 37. Not unexpectedly, this value is close to the electrical and mechanical anisotropies for highly oriented PPV. Chemical modification of PPV has led to even higher susceptibilities [66].

2.5 Morphology of Undoped and Doped Conducting Polymers

The morphology of directly synthesized polyacetylene (PA) has been shown by Karasz et al [67] and Chien et al [68] to be microfibrillar in nature. These researchers examined PA films synthesized directly on electron microscope sample grids. In this way artifacts due to handling and sample preparation were minimized. Both Ziegler-Natta and Luttinger catalysts were used [69]. TEM images revealed such samples to be composed of microfibrils of 20 nm average diameter. The ultimate morphological entity making up the microfibrils are smaller ones averaging 3 nm in diameter. The effect of doping on the microfibrillar morphology was examined by Epstein et al [70]. Upon doping the general morphological character was unchanged. However, both I_2

16

and AsF_5 doping caused increases in microfibril diameter. Increases of 50-100% were observed for I_2 doping. Doping by AsF_5 increased the microfibril diameter by up to 500% (ie., 100 nm). Further, both iodine and arsenic were observed by energy dispersive analysis of x-rays (EDAX) to have uniform concentrations over the entire sample surface.

By employing an alternate synthetic route continuous, fully dense PA morphologies can be attained. Edwards and Feast [71,72] developed a precursor route to PA in which a triene monomer is synthesized by olefin metathesis (see Figure 2.4). As with precursor PPV, the PA precursor polymer is soluble and can be cast as films. Conversion to the fully conjugated form is conducted thermally. Transmission electron microscopy studies have confirmed the continuous character of both precursor and fully conjugated forms [73]. Further, the conjugated polymer is crystalline and experiences molecular orientation when the thermal conversion is done at conditions of constant length.

Other conducting polymers such as poly(p-phenylene) (PPP) have been studied from a morphological point of view. Using transmission electron microscopy Pradere and Boudet [74] investigated the morphology of PPP synthesized by a variety of techniques [75-77]. The results of the study indicated that of the three routes only the Kovacic route [75] (a Friedel-Crafts polymerization of benzene) yielded a fibrillar morphology. The others [76,77] produced globular mosaic-like morphologies. In a subsequent paper Pradere and Boudet [78] investigated the effect of AsF_5 doping on Kovacic PPP. As with PA, the microfibrils experienced a swelling with the diameter increasing approximately 50%.

2.6 Crystalline Order in Doped Polymers

As with other topics of investigation in conducting polymers, the structural studies have been primarily performed on doped PA. Electron diffraction studies by

17

Shimamura [79-81] focused on iodine-doped *cis*-polyacetylene. The polymer was synthesized using a Ziegler-Natta catalyst according to the Shirakawa technique [17]. The order in the polymer doped to saturation was found to be limited. Two broad equatorial reflections at 0.38 and 0.22 nm and nine broad meridional reflections are apparent in the doped material diffraction patterns. Also, one meridional reflection at 0.123 nm indicated a doping induced *cis*-to-*trans* isomerization. Theoretical calculations of the meridional intensities confirmed an ordering of the polyiodide anions parallel to the chain direction with both I_3^- and I_5^- present.

Subsequent work by Shimamura [82] attempted to clarify the structural issue in I_2-doped PA by using highly oriented polyacetylene epitaxially grown on dibromobenzene single crystals. While this approach yields pristine polymer of a more controlled texture no improvement in doped-complex structure was seen.

X-ray diffraction studies conducted by Baughman et al [83] found the state of order in I_2-doped PA to depend upon doping conditions and post-doping treatments. They observed three equatorial spacings in the ranges 1.43-1.38 nm, 0.82-0.79 nm, and 0.40-0.38 nm along with a meridional reflection at 0.31 nm. On the basis of experimentally determined d-spacings, close-packing energy calculations, and theoretical intensity calculations they proposed a staged doped structure analogous to staging in graphite intercalation compounds [84]. In particular they conclude that a structure with stage 3 character is formed for a composition of $(CHI_x)_n$ when $0.056<x<0.13$ and a stage 1 structure when $x=0.14$.

It is important to note that a strong potential for disorder exists in iodine doping since the dopant anion may exist as any form of I_n^- where n is odd. The structural order in oxidized polymers is expected to increase when doping agents of regular structure such as AsF_5 and SbF_5 are used.

Studies by Wegner et al [85] investigated the crystalline state of electrochemically oxidized polyacetylene with the SbF_6^- counterion. In this study the

pristine polymer was prepared according to the precursor route developed by Edwards and Feast. Films were stretch-aligned to give fiber diffraction patterns. In this case indexation of the reflections is more certain. However, the resulting doped pattern showed only two strong equatorial reflections at 1.0 and 0.45 nm and a broad meridional reflection. From this limited information a model consisting of two incommensurate sublattices, one for the polymer and one for the dopant, was constructed.

Structural studies on AsF_5 and SbF_5 chemically doped PA have been conducted by several groups. Riekel et al [86] used neutron diffraction with deuterated, AsF_5-doped PA. The polymer was synthesized using the Shirakawa catalyst. Both *cis*- and *trans*-polyacetylene yielded the same crystalline doped structure with d-spacings at 0.762, 0.395, 0.317, and 0.293 nm. Further studies by this group [87] proposed an intercalated structure of the doped phase. This conclusion is based on dimensional changes seen during doping. The small angle reflection varied from 0.775 nm when doped at an AsF_5 vapor pressure of 50 mbar to 0.785 nm at 290 mbar. The reflection at 0.40 nm on the other hand was independent of dopant pressure. This result indicates the existence of some crystalline plane in polyacetylene which preferentially experiences expansion.

This type of preferential expansion is common in aromatic charge transfer complexes. One classic example is the tetrathiofulvalinium (TTF)-tetracyanoquinodimethanide (TCNQ) charge transfer complex [88] (see Figure 2.5). In these structures stacks of TTF reside adjacent to TCNQ stacks. The planar molecules stack one upon the other with separation distances of 0.347 and 0.317 nm for TTF and TCNQ stacks respectively. The fused aromatic molecules naphthalene [89] and fluoranthene [90] as well as the linear molecule quaterphenyl [91] also form stacked charge transfer complexes when electrochemically doped with group V hexafluorides. The intermolecular separation distance in all of these complexes range from 0.321 to

0.340 nm. Thus, an intermolecular packing distance of $\approx$ 0.33 nm is characteristic of these aromatic stacked structures.

Similar structural studies have also been conducted with alkali metal doped PA [92,93] and with both donor and acceptor doped poly(p-phenylene) [91,94-97].
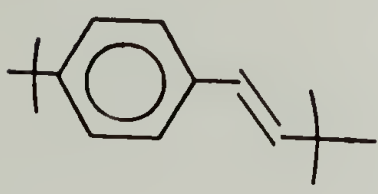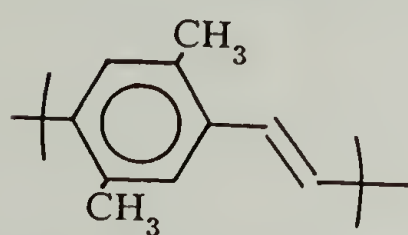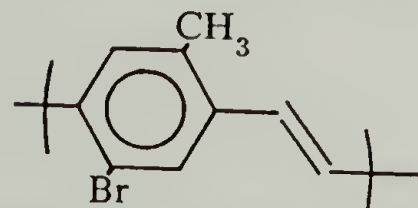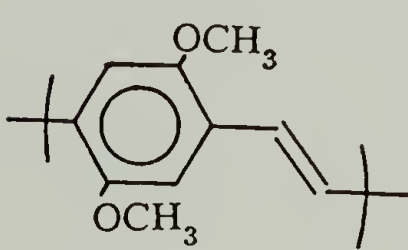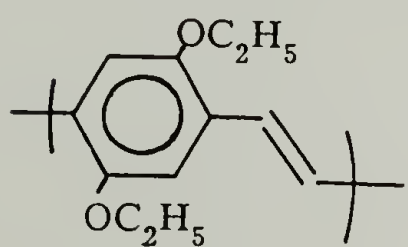
2.7 Dopant Distribution in Bulk Films

A rather limited number of studies have been conducted on the penetration of dopant into bulk films. Direct observation of dopant concentration profiles in doped polyacetylene has been performed using EDAX [98] and Castaing microprobe analysis [99,100]. These studies have shown the penetration to be characteristic of diffusion accompanied by chemical fixation. It is important to note two major drawbacks of these techniques. First, the samples must be extensively handled prior to testing. Typically they are embedded in a rigid matrix such as epoxy and then cross-sectioned. Although necessary, this sample preparation technique probably results in degradation of these reactive, air-sensitive samples. Second, the spatial resolution of these analytical techniques is limited to approximately 5 μm (see for example ref. [101]).

The diffusion of AsF$_5$ in PA film has been studied by weight-uptake measurements [102]. This study found the As weight-uptake curve to be sigmoidal when plotted against (time)$^{1/2}$. Thus, an induction period followed by a Fickian diffusion regime and eventually saturation was inferred. However, as has been noted in connection to small molecule diffusion in glassy polymers direct observation of the concentration profiles are required for accurate determination of the diffusion character [103].
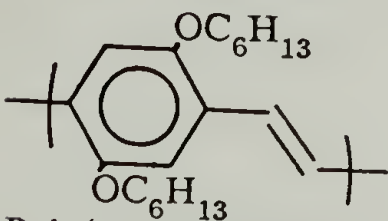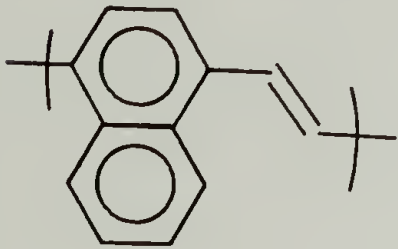
Table 2.1

Poly(p-phenylene vinylene), derivatives, and typical electrical conductivites.

Polymer	Dopant	σ $(\Omega\ cm)^{-1}$	Reference
Poly(p-phenylene vinylene)			

	Dopant	σ	Reference
	AsF_5	2.78×10^3	[30]
	AsF_5	2.50×10^3	[32]
	I_2	$<1.00 \times 10^{-5}$	[36]
	I_2	1.20×10^{-2}	[30]
	H_2SO_4	1.25×10^2	[32]
	H_2SO_4	2.70×10^1	[37]
	SO_3	4.20×10^2	[30]

Poly(2,5-dimethyl-p-phenylene vinylene)

	Dopant	σ	Reference
	AsF_5	3.00×10^{-7}	[34]
	I_2	2.10×10^{-4}	[37]
	I_2	4.00×10^{-7}	[38]
	SO_3	1.00×10^{-4}	[37]

Poly(2-bromo-5-methyl-p-phenylene vinylene)

	Dopant	σ	Reference
	AsF_5	5.00×10^{-6}	[34]

Poly(2,5-dimethoxy-p-phenylene vinylene)

	Dopant	σ	Reference
	AsF_5	6.80×10^1	[37]
	AsF_5	1.80×10^0	[38]
	I_2	5.10×10^1	[36]
	I_2	2.03×10^2	[37]
	I_2	5.00×10^1	[40]
	H_2SO_4	4.11×10^2	[37]
	SO_3	1.59×10^2	[37]

Poly(2,5-diethoxy-p-phenylene vinylene)

	Dopant	σ	Reference
	AsF_5	8.80×10^{-1}	[34]
	AsF_5	1.40×10^1	[37]
	I_2	2.57×10^2	[37]
	SO_3	4.30×10^1	[37]

Table 2.1
(cont.)

Polymer	Dopant	$\sigma\ (\Omega\ cm)^{-1}$	Reference

Poly(2,5-dihexyloxy-*p*-phenylene vinylene)

OC$_6$H$_{13}$

OC$_6$H$_{13}$

| | I_2 | 2.00×10^2 | [39] |

Poly(1,4-Naphthalene vinylene)

| | AsF$_5$ | 3.20×10^{-2} | [34] |
| | I_2 | 1.60×10^{-5} | [35] |

58.5°

b·sinα

a

[001] projection

[100] projection

b

c
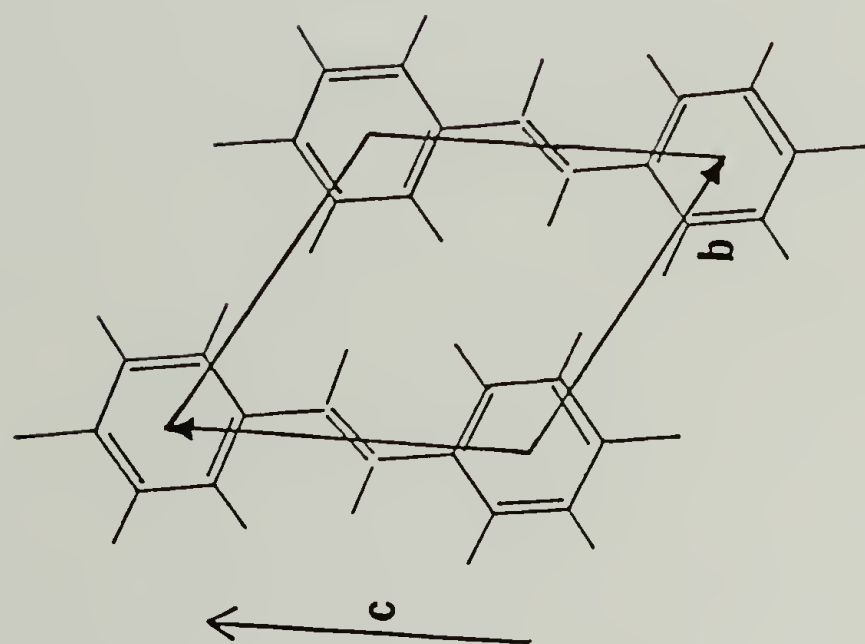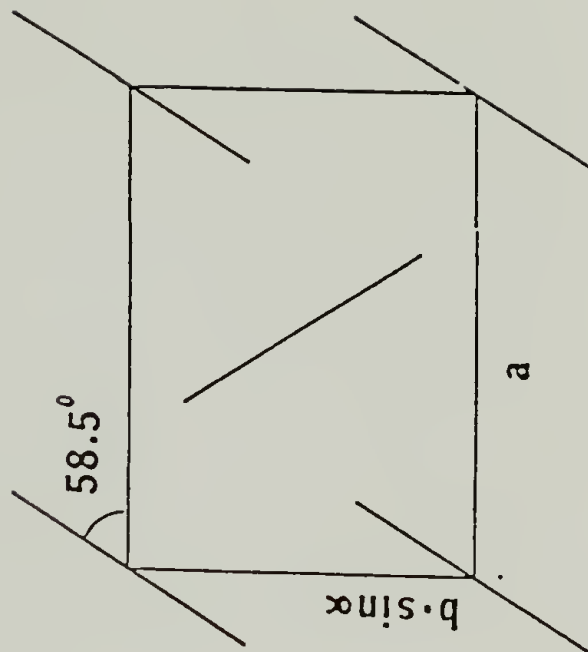
Figure 2.1   Orthorhombic unit cell of crystalline
Poly(*p*-phenylene vinylene).
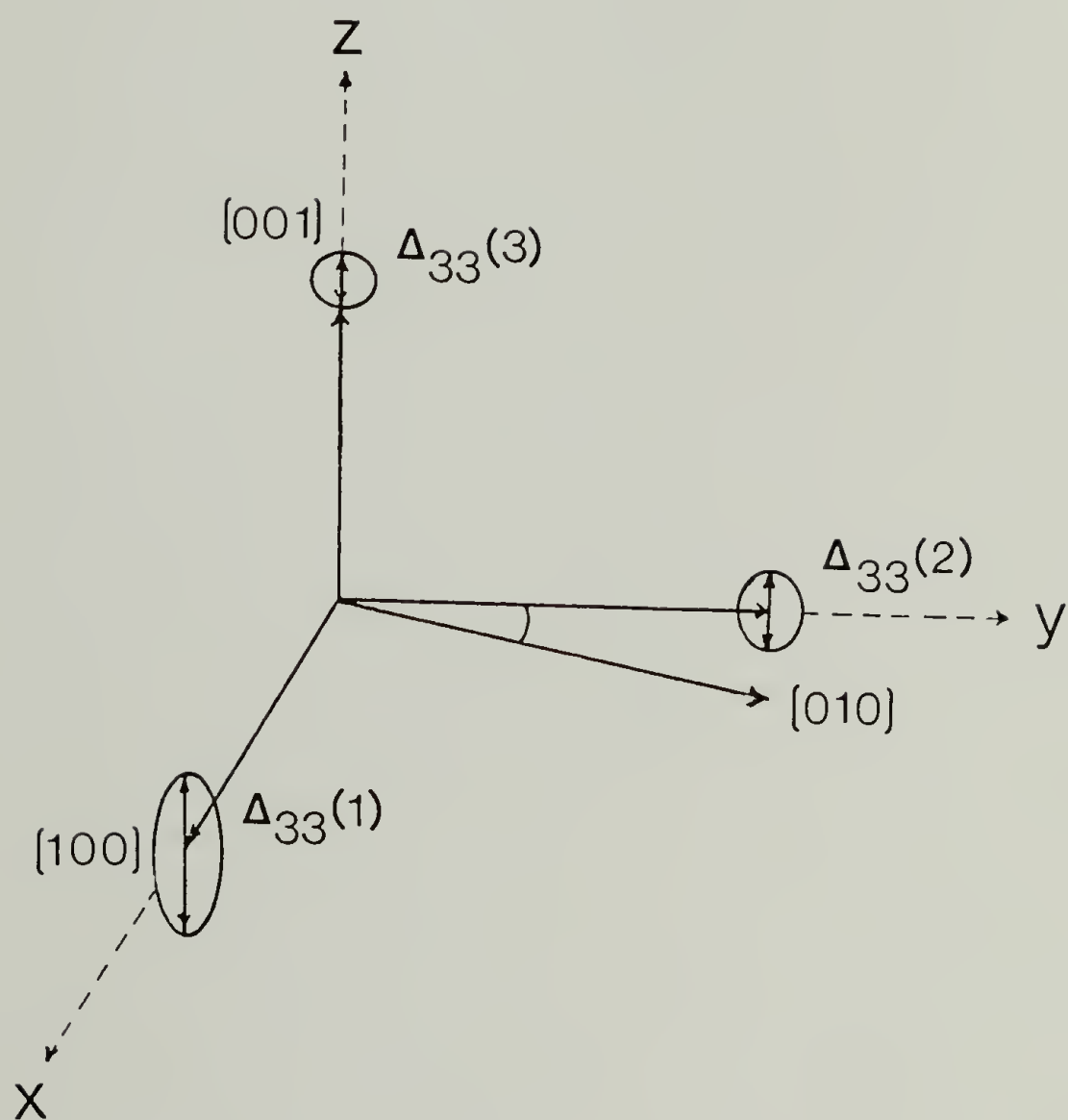
Figure 2.2   Schematic representation of the fluctuation tensor of
paracrystalline PPV. The axial components are shown
($\Delta_{33}(1) > 0.16$ nm, $\Delta_{33}(2) < 0.04$ nm, $\Delta_{33}(3) < 0.024$ nm).
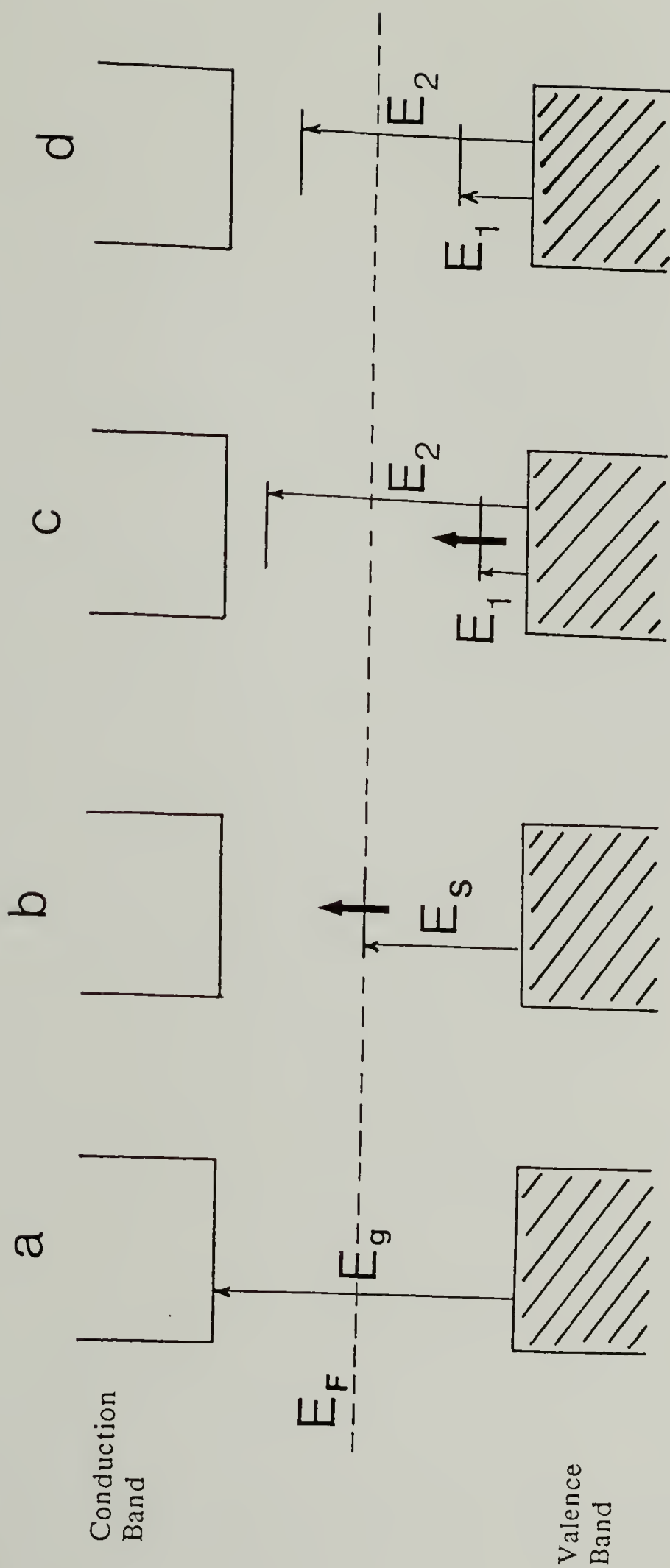
Figure 2.3   Possible electronic states of insulating and conducting polymers: a) large band gap insulator; b) neutral soliton; c) polaron structure; d) spinless bipolaron structure.
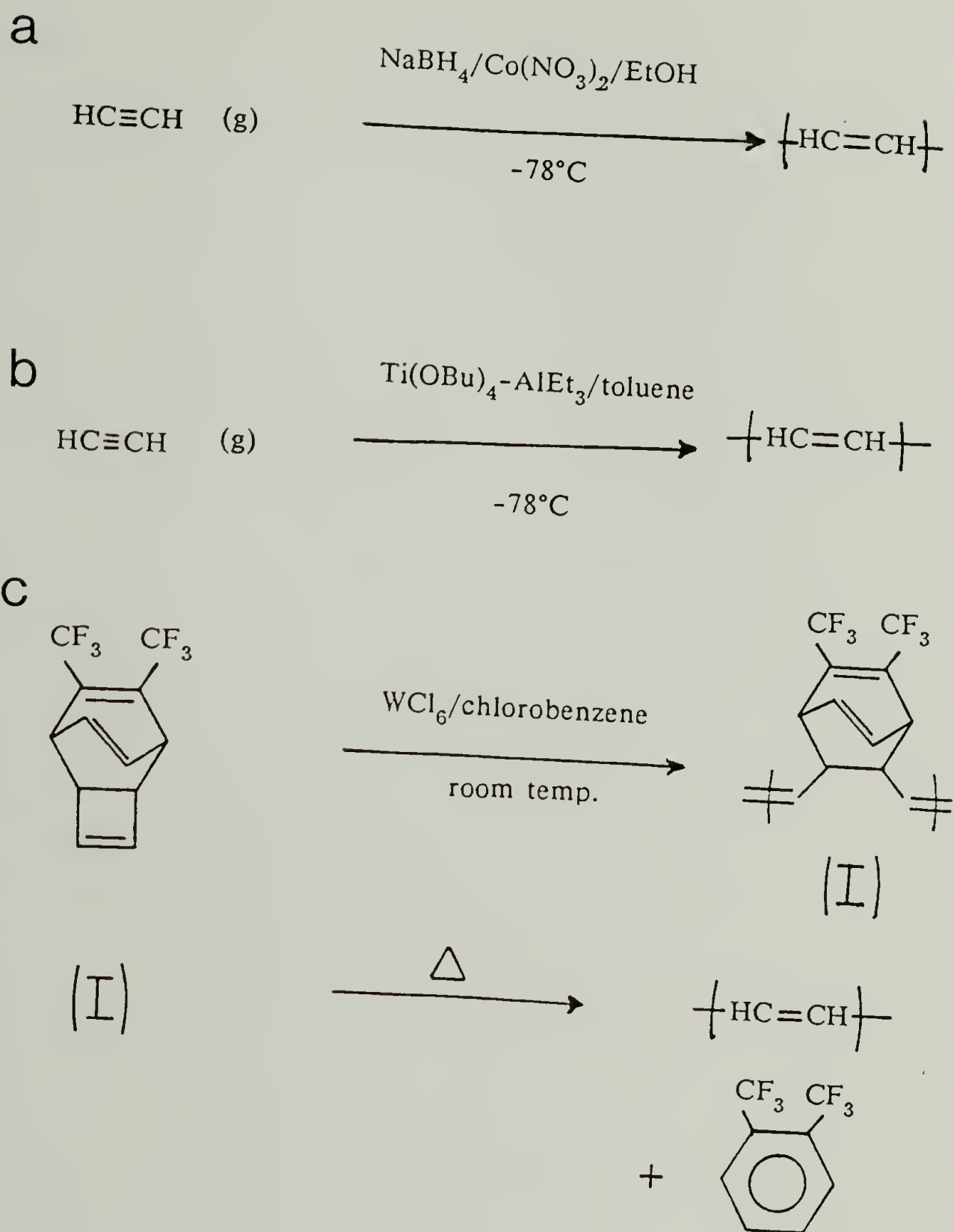
Figure 2.4   Three synthetic routes to polyacetylene: a) Luttingers catalyst; b) Ziegler-Natta; c) olefin metathesis, "Durham route".

Tetrathiofulvalinium (TTF)
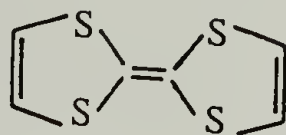
Tetracyanoquinodimethanide (TCNQ)
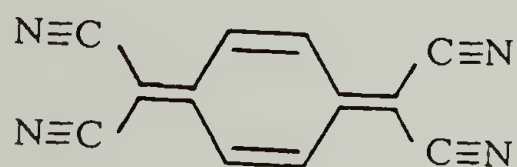
Naphthalene
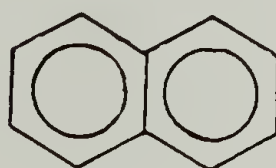
Fluoranthene
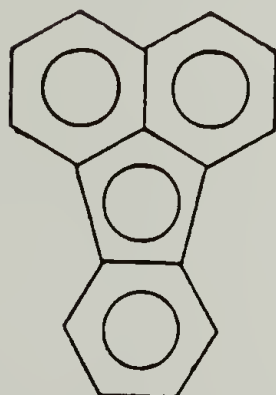
Quaterphenyl
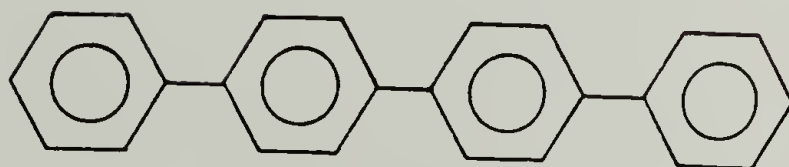
Figure 2.5   Chemical structures of Molecules forming charge transfer complexes.

CHAPTER 3

EXPERIMENTAL PROCEDURES

The use of experimental techniques in this study for the preparation and characterization of electrically conducting PPV has been extensive. The first section of this chapter focuses on the material aspects including PPV synthesis, processing, and doping. The second section describes the characterization techniques employed.

3.1 Preparation of PPV Films

3.1.1 Chemical Synthesis

High molecular weight PPV was first synthesized via a water soluble precursor polymer by Wessling and Zimmerman [26]. This approach was followed by Gagnon [32] and Karasz et al [28] to produce highly oriented PPV films. Subsequently, a scaled-up version of the synthesis and orientation process was developed by Machado [49]. This precursor route has also been employed in this study.

3.1.1.1 Sulfonium Salt Monomer

The synthesis of the monomer for the precursor polymer is shown in Figure 3.1. The starting material α,α'-dichloro-p-xylene (500g) was added to methanol (1L) in a 5L flask. A 40% molar excess of tetrahydrothiophene (600 ml) was then added. The stirred mixture was blanketed with argon, heated to 50°C, and allowed to react overnight. The soluble *bis*-sulfonium salt was then precipitated by addition of the mixed non-solvent diethyl-ether/acetone (3L/1L). The precipitate was washed with cold ether and dried under vacuum at 50°C overnight. This synthesis typically gave yields of 75%.

It should be mentioned that the monomer synthesis initially employed dimethyl-sulfide, a linear molecule. For this study the synthesis was modified to

28

improve the polymerization step by avoiding side reactions. Thus, a cyclic sulfide, tetrahydrothiophene, was used in the synthesis of the monomer as described by Lenz et al [104].

3.1.1.2 Sulfonium Salt Precursor

The details of the polymerization mechanism of the sulfonium salt precursor polymer have been recently published by Lahti et al [6]. The precursor polymer synthesis is shown in Figure 3.2. Dry *bis*-(*p*-xylene tetrahydrothiophenium chloride) (780g) was dissolved in 2.30L of distilled water. The solution was filtered to remove any insoluble impurities. This solution was then diluted with 4.0L of distilled water to make a 0.71N monomer solution in a 22L flask. Argon was bubbled through the solution for 1 hour to remove dissolved oxygen. Once degassing was complete 4.0L of 0.55N NaOH (aq) was added to the stirred monomer solution. In principle equimolar base and monomer solutions are required. However, to avoid deleterious side reactions slightly less base was used. An immediate viscosity increase was apparent. After 5 minutes the reaction was terminated by addition of 4.0L of 0.4N HCl (aq). The solution was then diluted with distilled water to 18L total volume and stored under refrigeration.

The side product of the reaction, NaCl, was removed by either one of two procedures. In the first procedure polymer solution was dialyzed against distilled, deionized water for 24 hours. Spectro-por dialysis tubes with 3500 MW cutoff were used. In the second procedure the precursor polymer was precipitated by introducing the solution to an excess of cold isopropanol. The precipitated polymer was collected and washed with an isopropanol/water (3:1) solution. The salt-free polymer was then washed using anhydrous ethyl-ether and freeze dried (-20°C) overnight. A precursor polymer solution was made by redissolving the dried precursor polymer in distilled water.

The molecular weights of the precursor polymers were measured using GPC according to a protocol developed by Machado et al [105]. The solubility character of the precursor polymer was modified through an ion-exchange process. When the chloride ion of the precursor polymer was exchanged for tetrafluoroborate the precursor became soluble in DMF. The molecular weights of the tetrafluoroborate precursor polymers were measured relative to polystyrene standards. The average results for three separately synthesized samples were: $M_n = 5.51 \times 10^5$; $M_w = 1.14 \times 10^6$; $M_z = 1.90 \times 10^6$. The GPC characterization agrees well with earlier absolute molecular weight determinations by ultracentrifugation–low angle laser light scattering [32] ($M_n = 5.0 \times 10^5$, $M_w = 9.9 \times 10^5$). Thus, the synthetic route reproducibly yielded high molecular weight polymer.

3.1.2 Casting of Precursor Polymer Films

Films of the precursor polymer were cast by either one of two techniques. When isotropic films were desired a simple vacuum casting technique was employed. Prior to casting the glass casting dish (250 ml) was treated to prevent adhesion at the glass–film interface. The dish was first cleaned by immersion in a concentrated base bath (KOH/isopropanol). After rinsing with distilled water and oven drying the glass was rinsed twice with 10–15 ml of dichloro-dimethyl-silane. By this procedure a non-adhesive organic layer was formed on the glass surface. To remove residual silane the glass was then sequentially rinsed with THF, acetone, and distilled water. The casting dish was filled with 100–200 ml of approximately 0.2 wt% precursor polymer solution and placed in a vacuum desiccator. A vacuum was pulled until a free standing film was formed.

A second casting technique was used when the films were to be stretch-oriented. A concentrated precursor polymer solution ($\approx$5wt%) was prepared from precipitated polymer. The solution was spread on a clean poly(methyl methacrylate)

(Plexiglas) surface. Dry nitrogen was blown over the film for approximately 24 hours. After this time a free standing film was obtained. The color of the as-cast films ranged from clear to slightly yellow.

3.1.3 Stretch-Orientation of Precursor Films

The stretch-orientation of precursor films was performed on an apparatus developed by Machado et al [56]. In this procedure strips of the precursor film were drawn while passing over a heated roll. Temperatures between 120-160°C were employed and film draw ratios (L/L_o where L = drawn length and L_o = original length) up to 12 were achieved. The elevated temperature of the heated roll caused a partial chemical conversion of the precursor to PPV. The details of this conversion will be discussed subsequently. It is the simultaneous conversion and stretching which yields high degrees of molecular orientation in PPV films.

3.1.4 Conversion from Precursor Polymer to PPV

The conversion from precursor polymer to PPV was accomplished by heating the films in an inert environment. Figure 3.3 illustrates the chemical conversion occurring upon annealing. Isotropic films were sandwiched between teflon sheets and heated in vaccum to 225-275°C for 4 hours. The stretch-oriented films were annealed in a nitrogen purged oven at 250°C for 2 hours. These oriented films were held at constant length during the annealing process. The degree of conversion was routinely checked by elemental analysis. Samples prepared by this route typically had oxygen levels less than 1.0 wt% and chlorine and sulfur levels less than 0.5 wt% indicating essentially complete conversion. Fully converted films had a yellow color and were transparent if sufficiently thin.

3.1.5 Doping Techniques

The doping of PPV was accomplished by chemical or electrochemical oxidation. In the case of chemical oxidation PPV films were treated with strong Lewis or protonic acids. For electrochemical oxidation the polymer was oxidized at the anode of a standard electrochemical cell in the presence of a suitable electrolyte. Thus, all of these techniques resulted in the abstraction of electrons from the polymer yielding p-type doped polymer. Because each dopant required special handling techniques they will be considered separately.

3.1.5.1 Arsenic Pentafluoride Doping

The AsF_5 doping was performed using a vacuum line equipped with mechanical and Hg diffusion pumps and liquid nitrogen cooled traps. Figure 3.4 schematically shows the vacuum line arrangement. The line itself was constructed from glass and all teflon stopcocks were used. This apparatus could routinely achieve a pressure lower than 10^{-4} mmHg.

The AsF_5 was obtained from the Ozark-Mahoning Co. Table 3.1 lists some physical properties of AsF_5. Because this dopant is a gas above -53°C it was stored in a spherical gas storage bulb equipped with a cold finger. (Extreme caution must be exercised during any procedure which involves AsF_5 as it is highly toxic and reactive.) The AsF_5 was purified by three sequential freeze-pump-thaw cycles. After purification the cold finger of the gas storage bulb was immersed in a methanol bath. The cold bath was maintained at a constant temperature using a Neslab CC-100 cryogenic refrigerator. The vapor pressure of the dopant was controlled by employing vapor-liquid equilibrium. The pressure of the AsF_5 vapor in equilibrium

with the liquid was calculated using a Clapeyron-type equation [106] of the form

$$\log_{10} P = A + B/T \qquad (3.1)$$

where the values of A and B are 7.8449 and 1093.0 respectively. T is the absolute temperature and the units of pressure are mmHg. Equation (3.1) was experimentally confirmed to be accurate within 3 mmHg at -70°C. Similarly, solid-vapor equilibrium was employed below -80°C and vapor pressures predicted from the same type of equation [106].

Samples to be doped were held in glass vessels (see Figure 3.4). These vessels were evacuated to $< 10^{-4}$ mmHg before doping. Doping was then performed by backfilling the vessel with AsF_5 vapor at the appropriate vapor pressure. The doping level was controlled by the AsF_5-PPV contact time. Doping was terminated by cryopumping all dopant vapor from the doping vessel. The sample was then pumped at 10^{-4} mmHg for at least 24 hours to remove residual dopant. The doped samples had a dark golden color and a highly reflective surface.

3.1.5.2 Phosphorus Pentafluoride Doping

Phosphorus pentafluoride was obtained from the Ozark-Mahoning Co. Prior to use it was transferred to a gas storage bulb and purified by three sequential freeze-pump-thaw cycles. Doping with PF_5 was conducted with the dopant at room temperature and completely in the gas phase. The vapor pressure was determined by the amount of gas charged to the storage bulb. The dopant vapor pressure was measured using a Hg manometer. Doping was performed by backfilling evacuated sample vessels. After termination of doping residual dopant was removed by pumping for at least 24 hours.

3.1.5.3 Antimony Pentafluoride Doping

Vacuum line techniques similar to those used in AsF_5 doping were employed in SbF_5 doping. In this case, the dopant is a liquid at room temperature. Antimony

pentafluoride was obtained from the Aldrich Chemical Co. The SbF_5 was degassed prior to use. Figure 3.5 shows the storage and doping arrangement. The SbF_5 liquid was stored in a narrow bore glass side-arm fitted with a teflon stopcock. The side-arm was attached to a glass doping vessel fitted with the appropriate connector prior to doping. As with AsF_5, doping was accomplished by backfilling the evacuated sample vessel. All SbF_5 doping was performed at room temperature. Thus, an SbF_5 vapor pressure of approximately 4 mmHg was used for all dopings [106]. The doping level was controlled using the dopant-polymer contact time. After doping the samples were evacuated for at least 24 hours to remove residual dopant. The fully doped films were nearly black in color.

3.1.5.4 Iodine Doping

Fully converted samples held in evacuated glass vessels were exposed to iodine vapor at room temperature and at temperatures as high as 150°C. In no case was I_2 observed to dope PPV.

3.1.5.5 Protonic Acid Doping

Doping by sulfuric acid was performed by immersing PPV films in 98% aqueous H_2SO_4 for 4 hours. The films was then quickly rinsed in dry acetonitrile to remove excess acid. Subsequently, the films were quickly placed in vessels for evacuation. The films were pumped for 24 hours to remove acetonitrile. The doped samples possessed a dark green-gold color. Other protonic acids such as HCl, $HClO_4$, HNO_3, 70% HF(aq), 70% HF(pyridine), methane sulfonic acid, and toluene sulfonic acid were also tried. None of these, however, yielded conductive films.

3.1.5.6 Electrochemical Doping

The samples used for electrochemical doping were prepared by blending PPV precursor with poly(ethylene oxide). Conversion to PPV was performed by heating in

vacuum to 225°C for 4 hours. The blend was determined by elemental analysis to contain 60 wt% PPV. At this composition small crystallites of PEO are interspersed in a continuous PPV matrix [43]. It has been previously noted that for the blend compositions used here PEO is nearly completely extracted from the films during doping [41]. As such, PEO only serves to expedite the doping process and does not complicate subsequent analyses.

Electrochemical oxidation of PPV films was done in an electrolytic solution of 1M LiClO$_4$ in propylene carbonate. A potential of 4.1V (referenced to Li) was used.

3.2 Characterization Techniques

3.2.1 Electrical Conductivity, Dopant Uptake and Density

During PF$_5$, AsF$_5$, and SbF$_5$ dopings the electrical conductivity of the bulk films was measured using an apparatus previously described in detail [32]. PPV films were attached to platinum wires using a carbon-based conductive adhesive (Electrodag 502, Acheson Chem.) The electrical resistance of the bulk films was monitored as a function of doping time using the standard four-terminal geometry (see Figure 3.6). In this way the effect of contact resistance is minimized. The resistance was measured using a Keithly 197 autoranging multimeter. With the resistance (R) the electrical conductivity was calculated according to

$$\sigma = (1/R)(L/A) \tag{3.2}$$

where L and A are the length between voltage measuring leads and the film cross-sectional area. It is important to note that the above calculation gives only a bulk conductivity of the sample. The true or intrinsic conductivity of the film can only be determined if the entire cross-sectional area is homogeneously doped. This point will be discussed further with regard to the experimental results.

The electrical conductivity of PPV films doped by other methods was measured after doping was completed. The films were transferred into an argon

filled Vacuum Atmospheres dry box. Using the four-terminal geometry previously discussed the resistance of these films was measured. The conductivity was calculated according to eqn(3.2).

The dopant uptake was determined gravimetrically. The sample masses were measured before and after doping on a Cahn 31 microbalance. The balance was located in the dry box so that the samples were exposed only to an inert atmosphere during handling and weighing.

Simultaneous conductivity and weight gain measurements were taken using a doping vessel equipped with a calibrated quartz spring. With this apparatus the mass sensitivity was 0.01 mg. Sample masses were on the order of 1 mg. Thus, the smallest measurable weight gain was approximately 1% of the original mass. To obtain meaningful measurements a dope-and-pump protocol was adopted. In this way any volatile side products were removed prior to each weight measurement.

The density of the pristine film was measured in a density gradient column. An aqueous solution of KBr was used to prepare a gradient column in the range of 1.20 to 1.30 g/cm^3 according to the standard procedure [107]. The column was calibrated using glass bead standards. The column was maintained at a constant temperature of 22°C using a temperature controlled water bath. To measure the film density a film was carefully immersed in the solution at the top of the column. The film was allowed to settle overnight. Its position was noted and its density determined by comparison to the linear calibration curve.

The density of the doped films was determined by flotation. Chloroform (ρ = 1.48 g/cm^3), carbon tetrachloride (ρ = 1.58 g/cm^3), and bromoform (ρ = 2.89 g/cm^3) were used to prepare mixed solvents having densies from 1.4 to over 2.0 g/cm^3. Small pieces of the doped films were immersed in the solvents and it was noted whether the films sank or floated. By employing numerous mixed solvents the density of a doped film could be estimated to within ±0.05 g/cm^3. Using this

experimental approach the film densities could be rapidly determined with minimal exposure to reactive environments.

3.2.2 Wide Angle X-Ray Diffraction

X-ray diffraction was used to characterize the crystal structure of the pristine and doped PPV films. Two experimental systems were used and will be discussed separately. While the fundamentals of x-ray scattering are the same for both instruments the operational details and the information obtained from each differ.

3.2.2.1 Statton Camera

Flat-film diffraction patterns were obtained on an evacuable Statton camera. Collimated, nickel filtered CuK_α radiation ($\lambda = 0.15412$ nm) was used. The samples were in film form and were held flush against the collimator so that the incident beam was perpendicular to the sample surface. The camera length could be varied by placing the film cassette in one of four fixed stages. The sample-to-film distance was calibrated using NaF. Kodak DEF x-ray film was used and the latent images were developed according to the manufacturer's instructions.

Diffraction patterns thus obtained were used to measure the crystallographic d-spacings of the samples. The x and y displacements from the negative center was measured for each reflection. Figure 3.7 shows the experimental geometry. The d-spacing was then calculated from

$$d = \lambda/\sqrt{\zeta^2 + \xi^2} \tag{3.3}$$

where

$$\zeta = y/\sqrt{L^2 + x^2 + y^2} \tag{3.4}$$

$$\xi = \sqrt{2 - \zeta^2 - 2L\sqrt{1 - \zeta^2}/\sqrt{L^2 + x^2}} \tag{3.5}$$

In the above equations ζ and ξ are the coordinates of a reciprocal lattice point on the surface of the Ewald sphere [108]. Equations (3.4) and (3.5) take into account the

distortion occurring when the spherical surface of the Ewald sphere is projected onto a flat photographic film.

3.2.2.2 Nicolet Diffractometer

A Nicolet diffractometer equipped with a two-circle camera and a two-dimensional integrating proportional counter was also used to obtain diffraction patterns from pristine films. X-rays were generated in a sealed tube with a copper target. Monochromatic CuK_α x-rays were obtained by diffraction from a graphite crystal. The correction of detector curvature and the calculation of the scattering angles were performed on the instrument computer. The two-circle camera allowed precise rotations of uniaxially oriented samples. This feature permitted the measurement of diffracted intensity as a function of rotation angle. From this information the degree of preferred planar orientation could be evaluated.

3.2.3 Scanning Electron Microscopy

A JEOL 35 CF scanning electron microscope was used to obtain SEM images of PPV film surfaces and fibrillated PPV. The samples were gold-coated before imaging. The microscope was operated at 20 kV and secondary electron images were collected on Polaroid 55 P/N film.

3.2.4 Transmission Electron Microscopy

Transmission electron microscopy (TEM) is a versatile tool for high magnification investigations of materials. In this study two different contrast mechanisms were employed in the imaging of PPV. First, dark field diffraction contrast TEM was used to investigate the crystal morphology of pristine and doped films. Second, high resolution phase contrast TEM (HREM) was used to directly image the molecular packing in PPV crystallites. Each of the techniques will be discussed in turn.

3.2.4.1 Dark Field TEM

Samples were prepared by mechanically fibrillating PPV films. The thin fibrillated samples of both pristine and electrically conducting PPV were imaged. The samples were doped with AsF_5 and H_2SO_4 doping according to the methods previously discussed. The samples were then sandwiched between two copper grids. In the case of doped samples all handling was performed in an argon filled dry box prior to imaging. The doped samples were exposed to air for less than 5 seconds while being transferred to the microscope.

Dark field TEM images were obtained on a JEOL 100CX operated at 100 kV. The diffracted beam was passed to the image plane through a 20 μm objective aperture limiting the diffracted beam to a full angular breadth of 4 mrad. Unless otherwise noted the objective aperture was centered on the optic axis.

A total end point dose of 0.13 C/cm^2 was measured for $g_{(110/200)}$ of PPV with 100 kV electrons. The imaging beam flux was determined by measuring the area of illumination and the screen current taking into account the screen efficiency (60%). Using the objective aperture to isolate the $g_{(110/200)}$ diffracted beams the screen current was measured as a function of time. Figure 3.8 shows the screen current decay as a function of time for the PPV $g_{(110/200)}$ combined reflection. The total end point dose was determined by the time at which the screen current had decayed to a steady value. The typical imaging dose was less than 0.01 C/cm^2. This ensured that multiple exposures of the same sample region could be taken without significant beam damage.

Images were collected on Kodak SO-163 electron microscope film. To achieve the low doses discussed above low electron fluxes and short exposure times were used. This necessitated latent image development using full strength Kodak D-19 developer with 10 minute immersion times.

Tilting experiments were performed according to the procedure of White and Thomas [109]. Using this technique displaced aperture dark field images were taken before and after tilting of the main beam. The tilt angle was determined from knowledge of the camera length and the relative displacement of the corresponding diffraction patterns. This allowed tilt angles as small as 0.2°.

3.2.4.2 High Resolution TEM

Sufficiently thin (<20.0 nm) PPV samples were obtained using a detachment replication technique. Oriented bulk films ($\approx$ 10 μm in thickness) were placed on the surface of a 10% nitrocellulose/amyl acetate solution (Collodion) and the solution was allowed to dry overnight. When the substrate had dried the PPV films were peeled from the surface. Small microfibrils were left embedded in the surface. Regions of interest were cut away and placed on holey carbon grids. The grids were suspended at the surface of fresh amyl acetate and the nitrocellulose was dissolved leaving behind the thin PPV microfibrils. The grids were then allowed to air dry before imaging.

The high resolution images were obtained on a JEOL 2000FX operated at 200 kV. The approximate Scherzer defocus was used with a magnification of 130,000x. No objective aperture was used. The fundamentals of high resolution imaging have been thoroughly discussed by Spence [110].

High resolution images were collected on Kodak SO-163 electron microscope film. The latent images were processed in regular strength Kodak D-19 developer for 4 minutes. Optical diffraction patterns were taken from the negatives using a He-Ne laser. The spacings in the optical diffraction patterns were calibrated by comparison to a graphite standard.

3.2.5 Rutherford Backscattering Spectrometry

Rutherford backscattering spectrometry (RBS) was used in this study to investigate the penetration of AsF_5 in bulk PPV films. The utility of RBS as an analytical tool derives from its sensitivity to sample nuclei mass and nuclei depth. Furthermore, samples do not require handling and sectioning as do samples for microprobe analysis. A short review of backscattering physics will be presented. This will be followed by a description of the experimental details.

3.2.5.1 Backscattering Physics

In the technique of RBS materials are probed by accelerated α-particle ($^4He^{++}$) beams. These high energy particles collide with sample nuclei and electrons and are scattered at all angles. As is clear from the name backscattering spectrometry measures the energy of particles in the back-reflected direction. Figure 3.9 illustrates the experimental geometry involved in RBS. Provided that the incident particle energy is much greater than the chemical bond energy but not so high that nuclear reactions occur ($10eV << E_o < 3MeV$) the collisions will be elastic. Thus, for an incident α-particle with energy E_o its backscattered energy, E, will be given by

$$E = KE_o \qquad (3.6)$$

where K is the kinematic factor. This factor depends upon the masses of the two particles involved in the collision. With backscattering geometry (ie., $\Theta = 180°$) the kinematic factor is expressed as

$$K = (M - m)^2 / (M + m)^2 \qquad (3.7)$$

where M is the sample nuclear mass and m is the incident particle mass (ie., m = 4 for ^4He). The kinematic factors of carbon, oxygen, fluorine, and arsenic are 0.250, 0.360, 0.425, and 0.808 respectively. Therefore, given an incident energy of 2.14 MeV the backscattered energies from C, O, F, and As nuclei on the sample surface

will be 535, 770, 910, and 1730 keV respectively. These energies will be hereafter referred to as surface energies for these specific elements.

Equation (3.6) will only apply if no energy loss mechanisms are operative (ie., backscattering from the film surface). In the case of α-particles backscattered from below the film surface the particle loses energy due to Coulombic interactions with electrons and small angle scattering by sample nuclei therefore the backscattered energy becomes

$$E = KE_o - [S]x \qquad (3.8)$$

where [S] is the energy loss factor and x is the depth below the film surface of the scattering nucleus. Thus, the energy spectrum will allow elemental depth profiling. The energy loss factor for pristine PPV (C_8H_6) is calculated as 313 eV/nm for particles backscattered from carbon nuclei using a mass density of 1.22 g/cm^3 and tabulated elemental stopping cross-sections of carbon and hydrogen and the surface energy approximation [111]. Because of the relatively high atomic number of the dopant atoms the doped films are expected to have a somewhat higher energy loss factor.

The yield, Y_o, of an RBS signal depends upon both experimental and material factors according to

$$Y_{o,i} = b_i \Omega Q m_i \xi / [\epsilon_o]_i \cos\Theta_1 \qquad (3.9)$$

Here, b_i is the scattering cross-section of nucleus i, m_i is the stoichiometric amount of i in the material layer being probed, and $[\epsilon_o]_i$ is the stopping cross-section factor for nucleus i. The remaining factors are associated with the experimental setup and are Ω, the solid angle of the detector, Q, the number of incident α-particles, ξ, the energy per channel of the multichannel analyzer, and Θ_1, the angle between the sample surface normal and the direction of incidence. Note that eqn(3.9) is written for backscattering from surface nuclei but is illustrative in general of the factors

affecting RBS yield. In this study we report normalized yield values given as

$$Y_i = Y_{o,i}/[\Omega Q \xi (1/\cos\Theta_1)]$$　　　　　(3.10)

which are only material dependent. It is important to note that the scattering cross-section is proportional to the square of the atomic number of the target nuclei [111], $b \propto Z^2$. Thus, the yield increases as Z^2 for multielemental samples. Further, in multielemental samples of finite thickness the yield equation can be written for each channel of the multichannel analyzer. The sum of all such yields for a particular nucleus gives its total amount in the sample. In practice this is accomplished by measuring the peak area for the element of interest.

For a more thorough discussion of backscattering physics the reader is referred to an excellent discussion by Chu et al [111]. Analysis of the RBS spectra in this study was performed using the RUMP simulation program developed by L.R. Doolittle [112].

3.2.5.2 Experimental Details

Rutherford backscattering spectrometry was performed at the Ion Beam Facility of the Materials Science and Engineering Department, Cornell University. An α-particle beam ($^4\text{He}^{++}$) was accelerated to 2.14 MeV using a tandem electrostatic accelerator (General Ionex). The samples were mounted on the holder under a nitrogen atmosphere and were transferred to the instrument using a valved load-lock. Backscattered particles were detected at an angle of 173°. The beam current was approximately 15 nA. Spectra were collected at room temperature for an integrated charge of $5\mu C$ over an approximate spot size of 1 mm^2. Because the spot size is much larger than the PPV crystallite size (ie., 5.0 nm) the results thus obtained represent the average diffusion character over a statistical collection of crystallites and disordered grain boundaries. The multichannel analyzer channel width was

approximately 18 keV. Thus, an estimated spatial resolution of 60 nm exists in samples having energy loss factors of 300 eV/nm .

The occurrence of beam damage in doped films was assessed by sequentially collecting spectra at 0.5 μC intervals from a single spot. Both the carbon and arsenic normalized yields were constant with increasing charge up to 15 μC indicating beam stability of these elements. In lightly doped samples the oxygen and fluorine yields showed signs of beam induced degradation up to 5 μC after which the yields became stable. This partial degradation occurred at both room temperature and at liquid nitrogen temperatures (-196°C). While the O and F species showed beam induced degradation the C/As ratio and As profile shapes will be unchanged. The surface of the films were also inspected for α-particle induced ablation using scanning electron microscopy. While some cracking was apparent no serious ablation was observed. The RBS spectra were found to be reproducible within a single sample. Spectra obtained from several spots along the length of a sample showed only a few percent variation in the yields for all elements.

3.2.6   X-ray Photoelectron Spectroscopy

X-ray photoelectron spectroscopy (XPS) was performed on lightly doped PPV films. This technique is a highly surface selective one due to the shallow escape depths of x-ray stimulated photoelectrons. As such it can be used to monitor the doping process on PPV surfaces.

3.2.6.1   Fundamentals of XPS

The process of photoelectron ejection is illustrated in Figure 3.10. The sample surface is flooded by photons of energy hν. If sufficiently energetic these photons will eject an electron from the sample. A simple energy balance can be performed on

this process as follows [113].

$$h\nu = E_b + KE + \phi \qquad (3.12)$$

Here, E_b is the binding energy of the ejected electron, KE is the kinetic energy of the ejected electron, and ϕ is the spectrometer work function, an instrumental parameter. In practice the kinetic energies of the photoelectrons are detected. With knowledge of the incident photon energy and ϕ the binding energies of the photoelectrons are then determined. These energies are characteristic of the atom in which they were bound. Further, the electron binding energy is sensitive, to some degree, to the chemical bonding experienced by the atom. Thus, the binding energy possesses chemical shift information. In this way XPS can be used as an analytical tool to evaluate the chemistry of surfaces.

The estimated sample depth which XPS probes is dependent upon the incident photon energy and the take-off angle at which photoelectrons are detected. Given the mean free path of the electron this depth can be related to take-off angle through a simple geometric analysis.

$$d = 2\lambda(E)\sin\Theta \qquad (3.13)$$

In eqn(3.13) d is the sampling depth, $\lambda(E)$ is the mean free path of an electron with energy E in the sample material and Θ is the take-off angle. The photon energy employed in this study was 1250 eV (MgK_α x-rays), the spectrometer work function was approximately 4 eV, and the binding energy of C_{1s} electrons is typically 284.6 eV. Thus, the kinetic energy of C_{1s} photoelectrons is on the order of 1000 eV. For this energy Powell [114] gives an electron mean free path of 1.5 nm in carbon samples. An escape depth of 2.7 nm is thus calculated for a take-off angle of 65°.

3.2.6.2 Experimental Details

X-ray photoelectron spectra were taken of the films using a Perkin-Elmer Physical Electronics PHI 5100 ESCA system equipped with a hemispherical analyzer.

MgK$_\alpha$ radiation was used at 300 W. A take-off angle of 65° was used (grazing incidence $\approx$ 0°). Charging in all spectra was corrected by shifting the major C$_{1s}$ photoelectron to a binding energy of 284.6 eV. To avoid contamination and atmospheric degradation the samples were mounted and transferred under an argon atmosphere. Survey spectra were taken using a pass energy of 179 eV. Elemental compositions were determined from multiplex scans using a pass energy of 72 eV and atomic sensitivity factors determined by comparison to standard polymer films.

Software curve-fitting was performed on high resolution spectra obtained using an 18 eV pass energy. The components making up the complex peaks were constrained to have a Gaussian profile and a full width at half maximum of 1.7 ±0.2 eV. The binding energies were essentially unconstrained.

3.2.7 Attenuated Total Reflectance FTIR Spectroscopy

FTIR spectra of film surfaces were obtained on an IBM 32 using attenuated total reflectance (ATR). Germanium and KRS-5 crystals with incident angles of 45° were used. The penetration depth, or distance in which the evanescent wave amplitude falls to 1/e, depends upon the incident wavelength and the refractive index ratio of the crystal and sample and is expressed

$$d_p = (\lambda/n_1)/[2\pi(\sin^2\Theta - (n_2/n_1)^2)^{1/2}] \qquad (3.11)$$

where Θ is the incident angle and n_1 and n_2 are the refractive indices of the crystal and sample respectively [115]. At an incident angle of 45° the effective sample thickness is close to the penetration depth [115]. The refractive index of PPV has been measured to be n_{PPV} = 1.6 [65]. Using eqn(3.11) the penetration depth for both crystals was calculated as a function of wavelength. Figure 3.11 shows the results of this calculation for the wavelength region of interest. As this figure shows, the penetration depth varies considerably with wavelength. Thus, the penetration depth with the Ge crystal (n_{Ge} = 4 [115]) was calculated to be 0.230 μm and 1.100 μm at

46

3000 cm^{-1} and 600 cm^{-1} wavenumbers respectively. Because the KRS-5 crystal (n_{KRS-5} = 2.4 [115]) more nearly matches the refractive index of PPV deeper penetrations were achieved with this crystal. The penetration depths were 0.940 μm and 4.70 μm at 3000 cm^{-1} and 600 cm^{-1} wavenumbers respectively with the KRS-5 crystal. The samples were mounted and spectra collected under a nitrogen atmosphere.

3.2.8 Mass Spectrometry

Gas chromatography-mass spectrometry was performed on a Ruska Laboratories Pyran System thermal chromatograph. A Finnigan mass spectrometer was interfaced with the gas chromatograph. The sample masses were less than 1 mg. The pyrolysis was conducted by heating the sample in helium from room temperature to 600°C at 30°C/min. A helium flow rate of 40 ml/min was used. The degradation products were trapped at the column entrance which was initially held at -35°C. The gas chromatogram and mass spectrum of the degradation products were simultaneously taken as the column was heated from -35°C to 315°C at 10°C/min. Analysis of the mass spectra was assisted by reference to the instrument supplied data base (NBS).

Table 3.1

Melting and boiling points of Lewis acid dopants
and related compounds (see ref. [106]).

Compound	MP (°C)	BP (°C)
HF	-83.4	19.5
PF_5	-93.8	-84.6
PF_3	-151.5	-101.2
AsF_5	-79.8	-53.2
AsF_3	-6.0	57.1[*]
SbF_5	8.3	141.0
SbF_3	292.0	319.0

[*]measured at 742.5 mmHg

ClCH$_2$—⟨benzene⟩—CH$_2$Cl   +   ⟨S ring⟩

α,α'-dichloro-p-xylene   tetrahydrothiophene
                                  (excess)

50°C
overnight
⟶
MeOH

bis-(p-xylene tetrahydrothiophenium chloride)
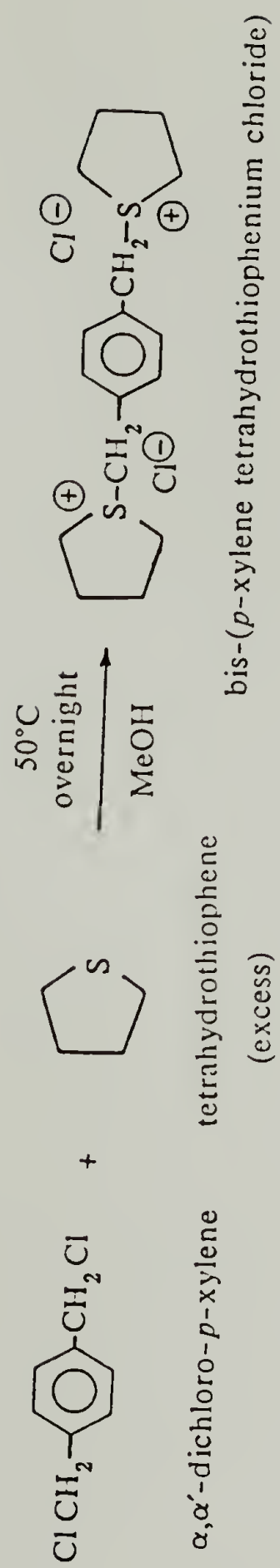
Figure 3.1   Synthesis of sulfonium salt monomer.

Figure 3.2   Synthesis of precursor polymer, poly(p-xylylene tetrahydrodthiophenium chloride).
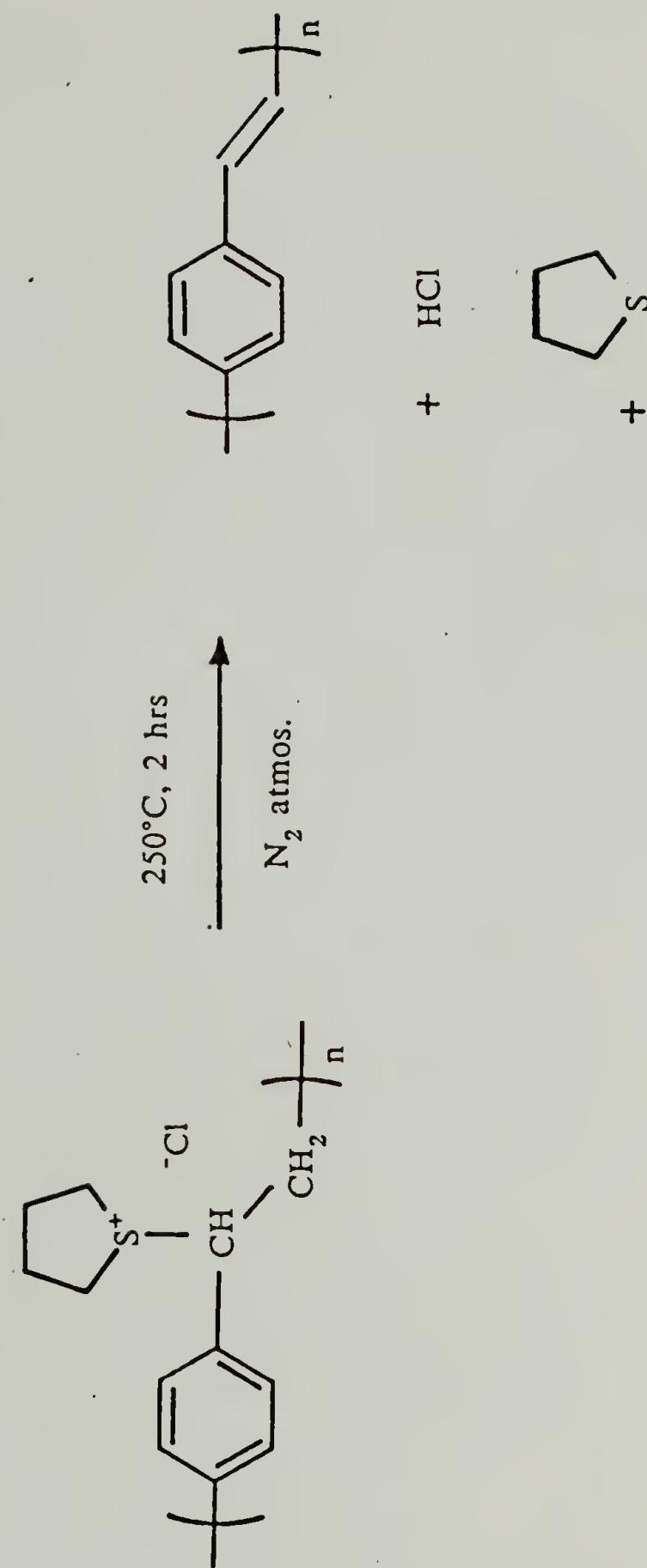
Figure 3.3   Thermal conversion of precursor polymer to poly(*p*-phenylene vinylene)
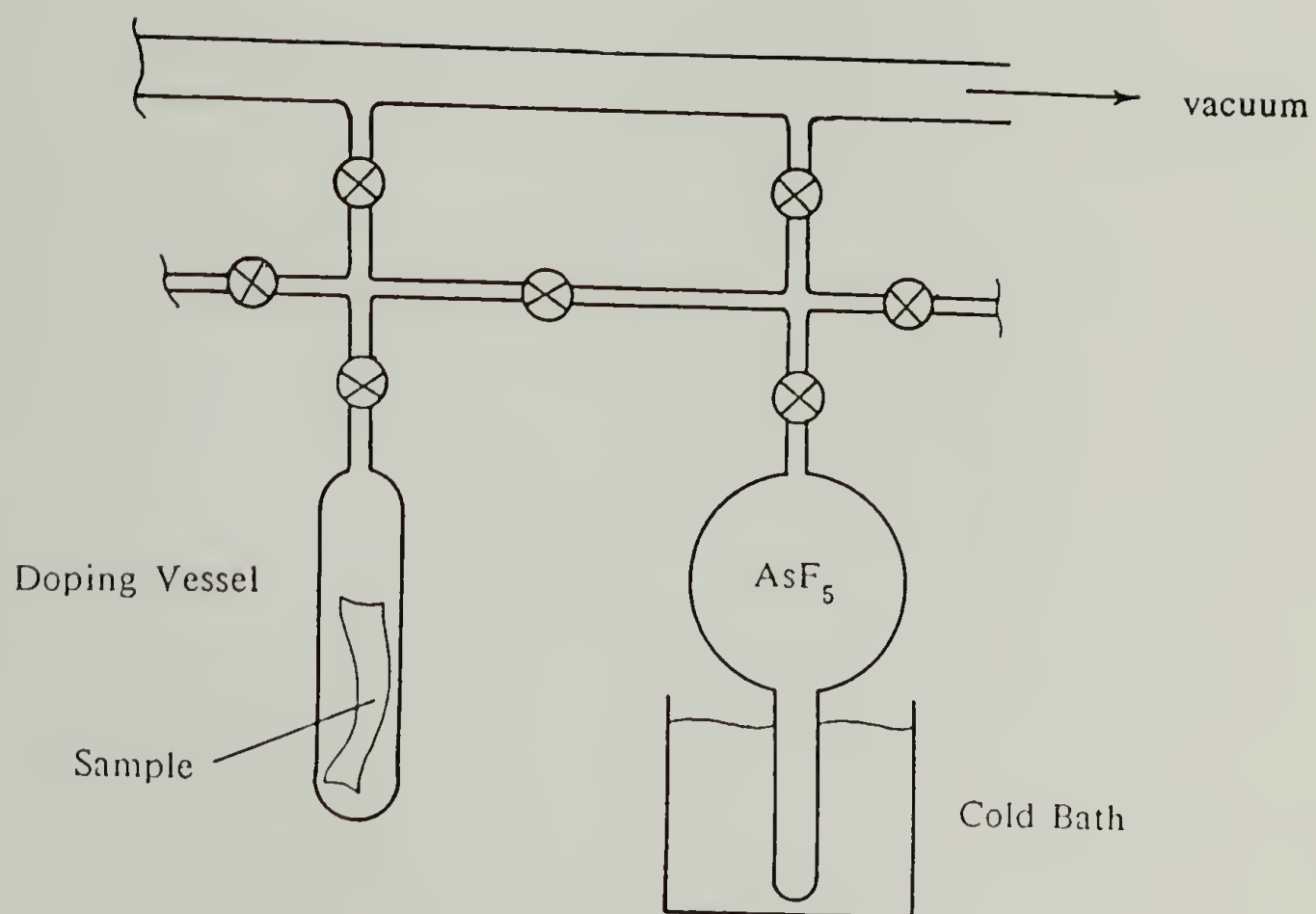
Figure 3.4   Vacuum line and arsenic pentafluoride doping apparatus.

Vacuum

sample vessel

teflon stopcock

sample

glass side-arm

SbF$_5$ liquid
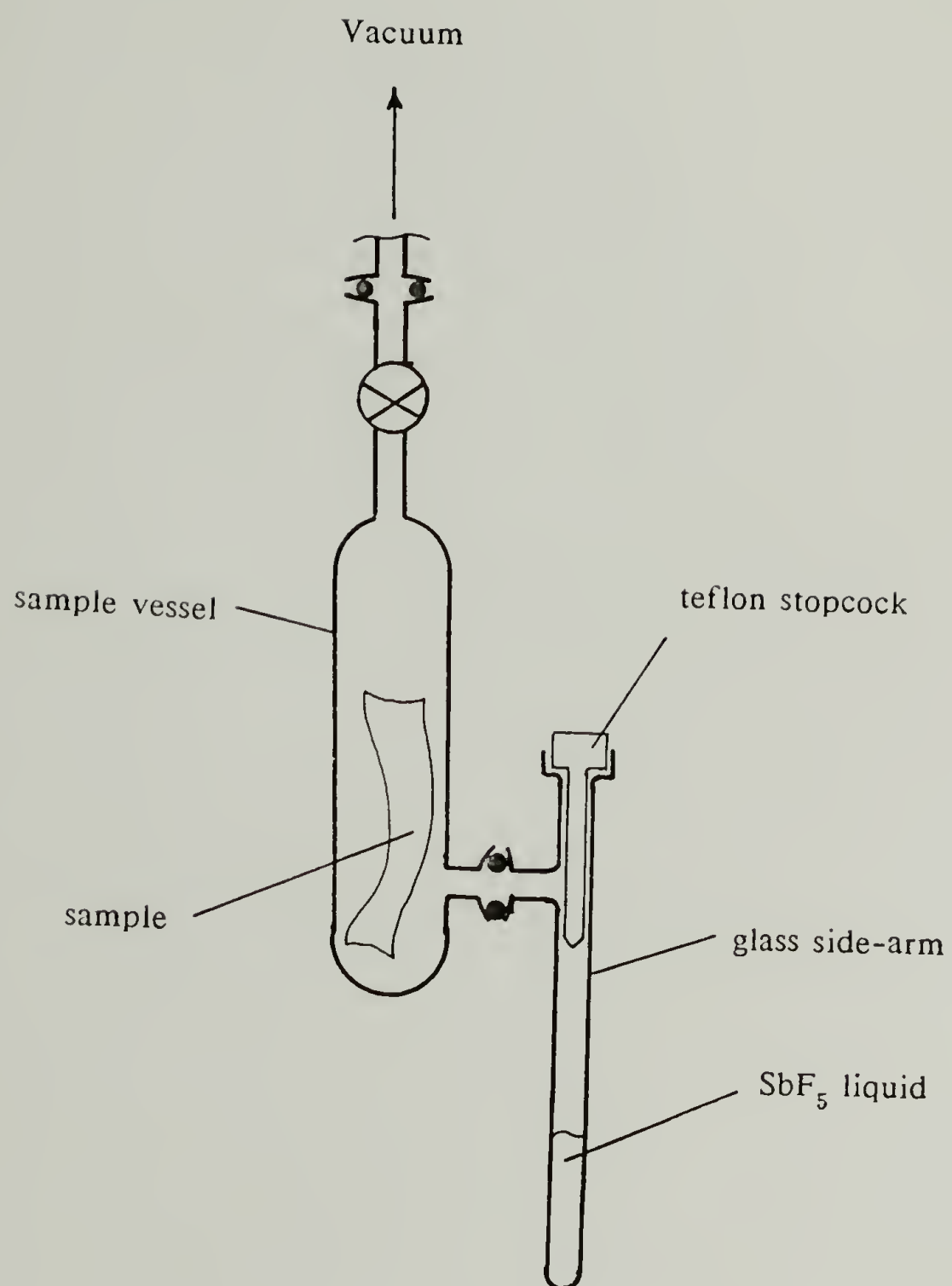
Figure 3.5   Antimony pentafluoride doping apparatus.

constant current

I

V

A

L
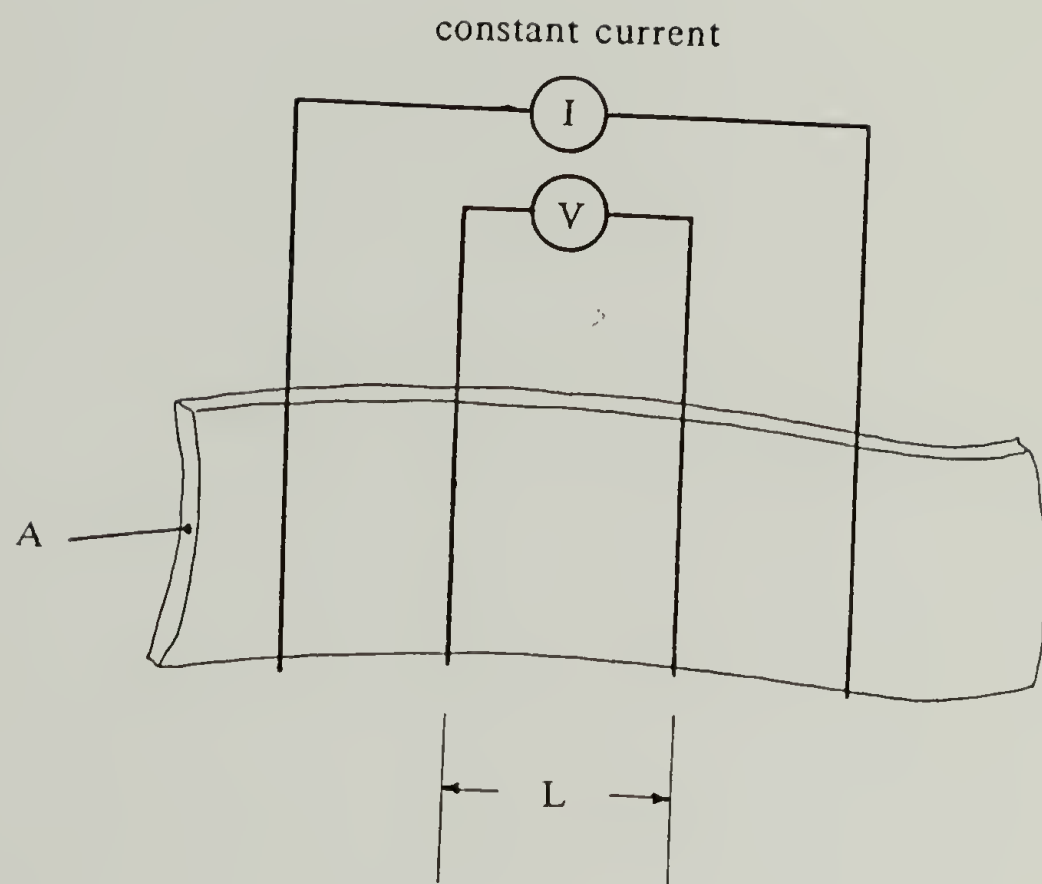
Figure 3.6   Geometry of four-terminal resistance measurement.
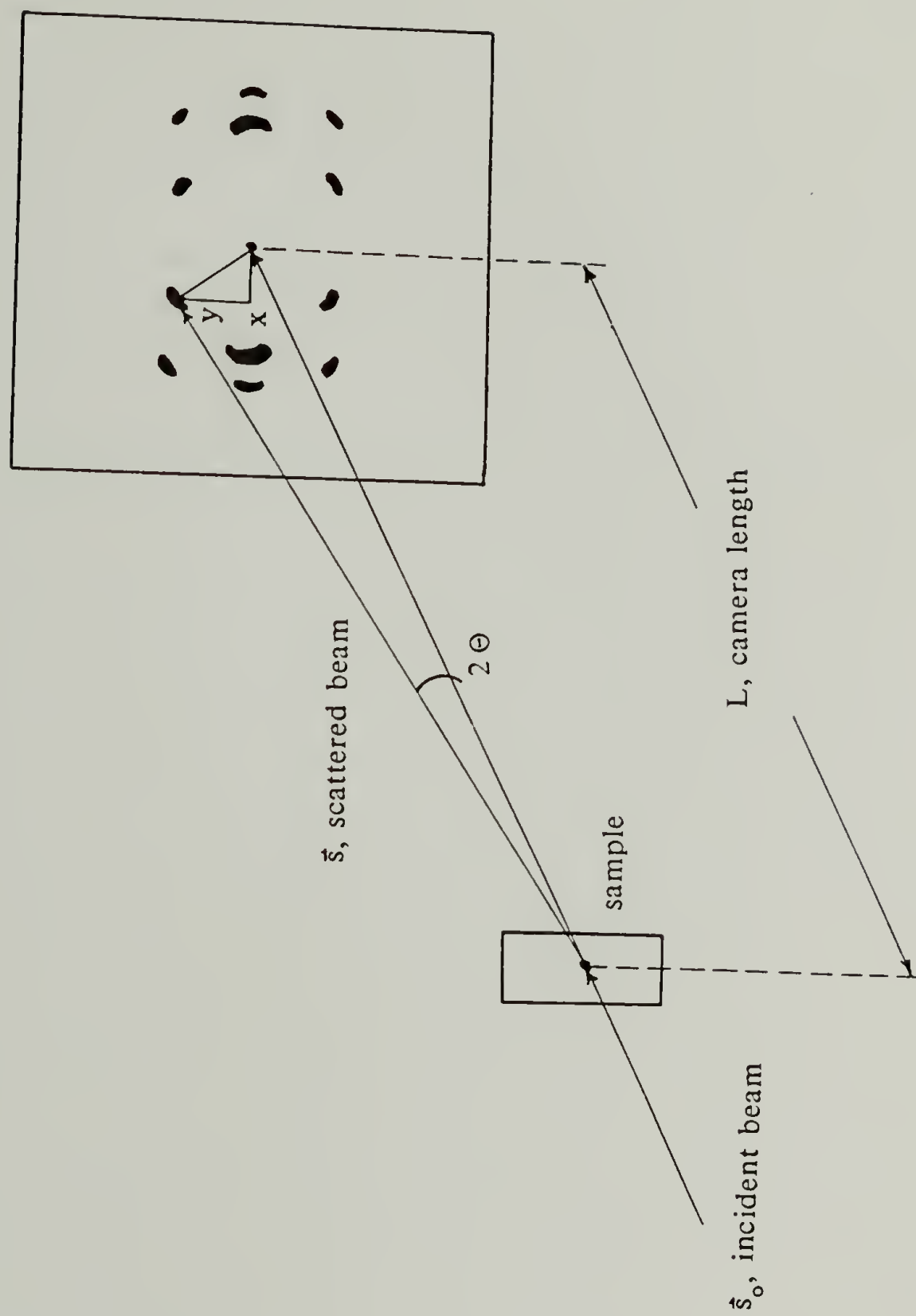
Figure 3.7   Geometry of wide angle x-ray diffraction experiment.
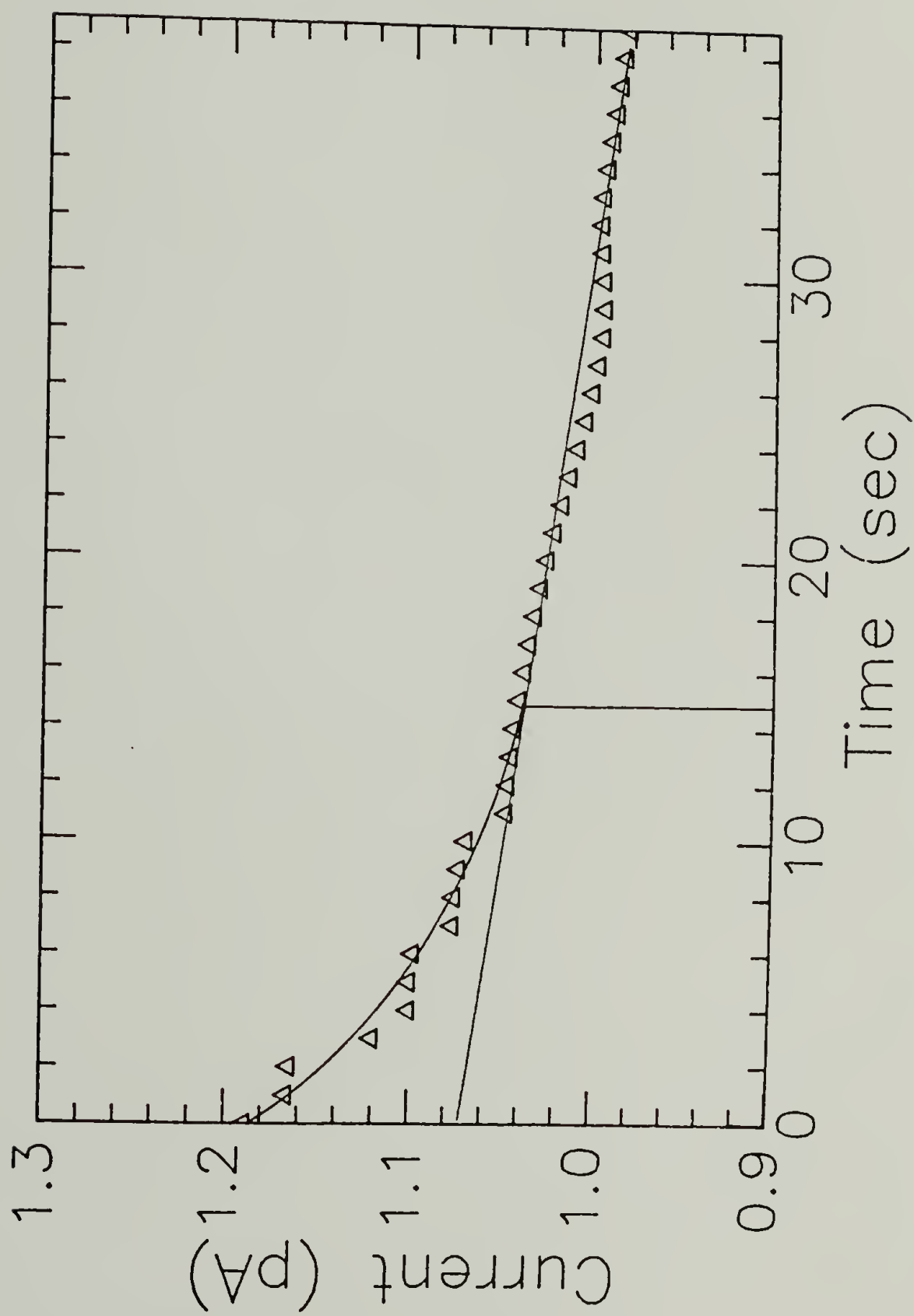
Figure 3.8   Intensity decay of $g_{(110/200)}$ of PPV illuminated
with an electron flux of 5.1 mC/cm^2 sec.

sample surface

accelerated particle beam

^{4}He^{++}

Eo

Θ_1

Θ

E = KEo

E < KEo
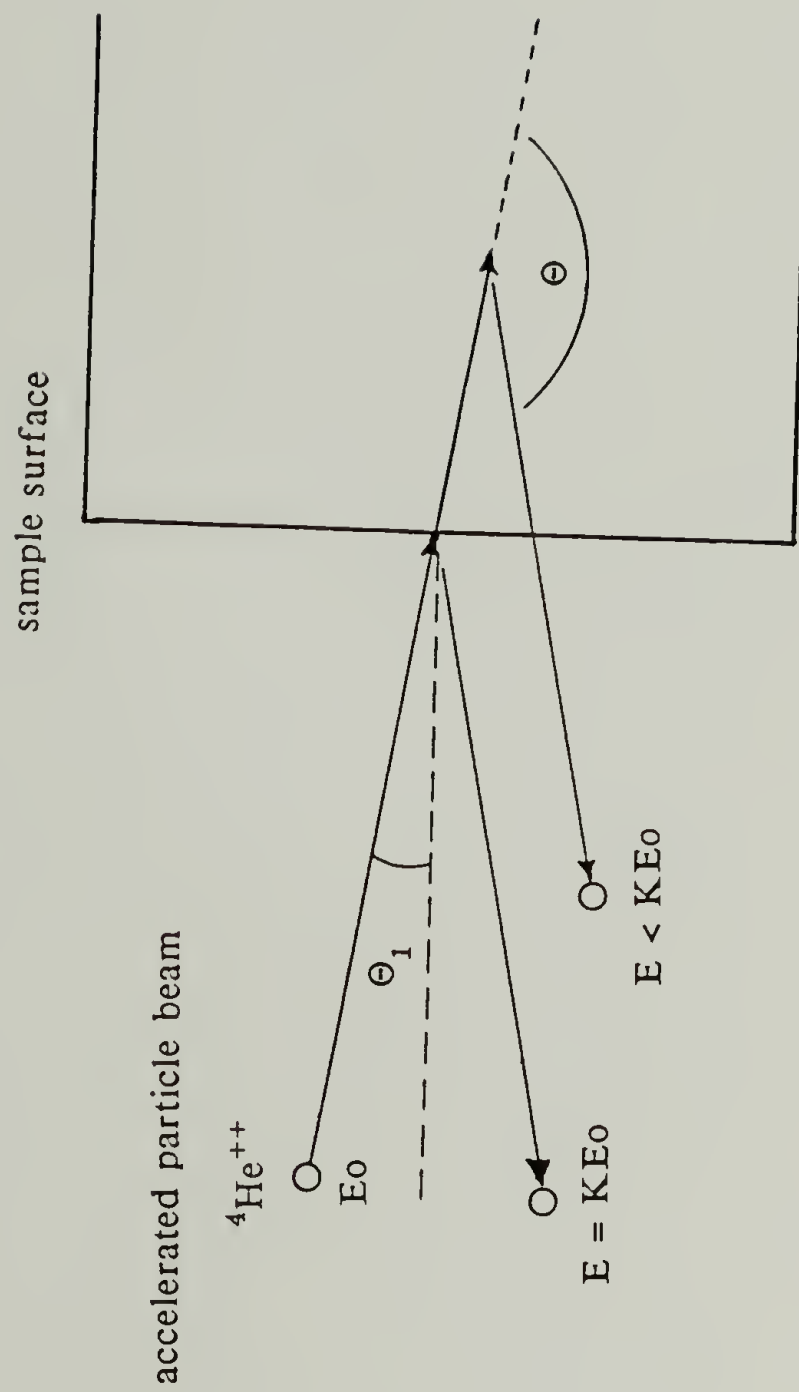
Figure 3.9   Schematic representation of experimental geometry for Rutherford backscattering spectrometry.

incident x-ray, hν

ejected electron

take-off angle, Θ

sample surface
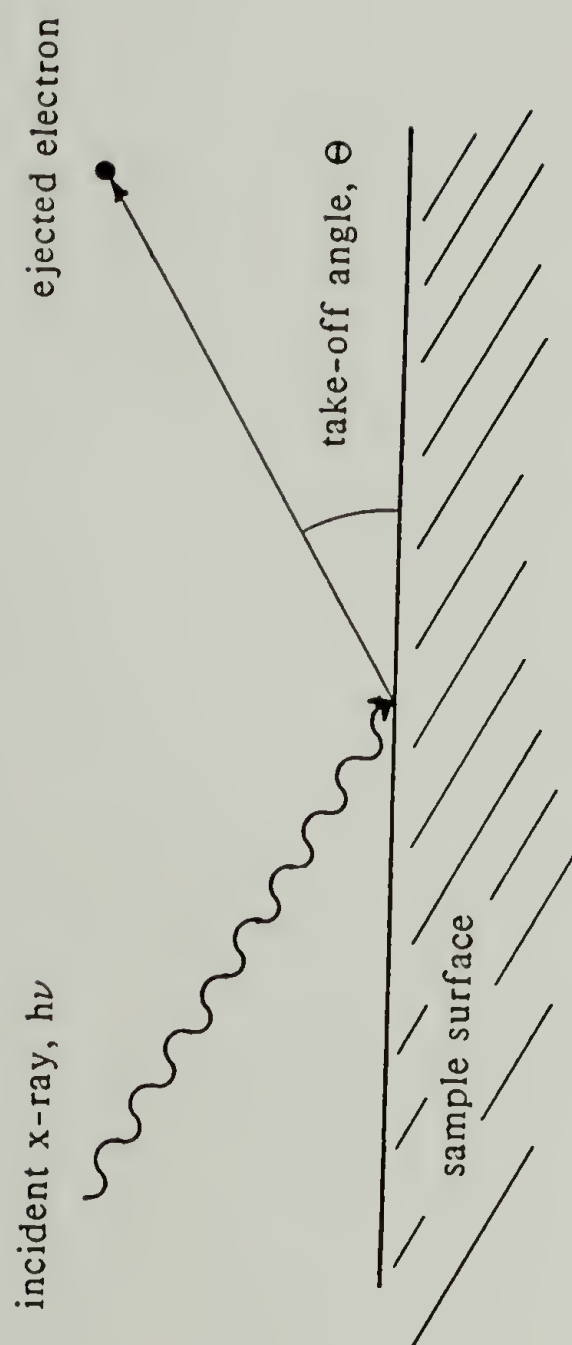
Figure 3.10   Schematic representation of the photoelectron ejection
process.
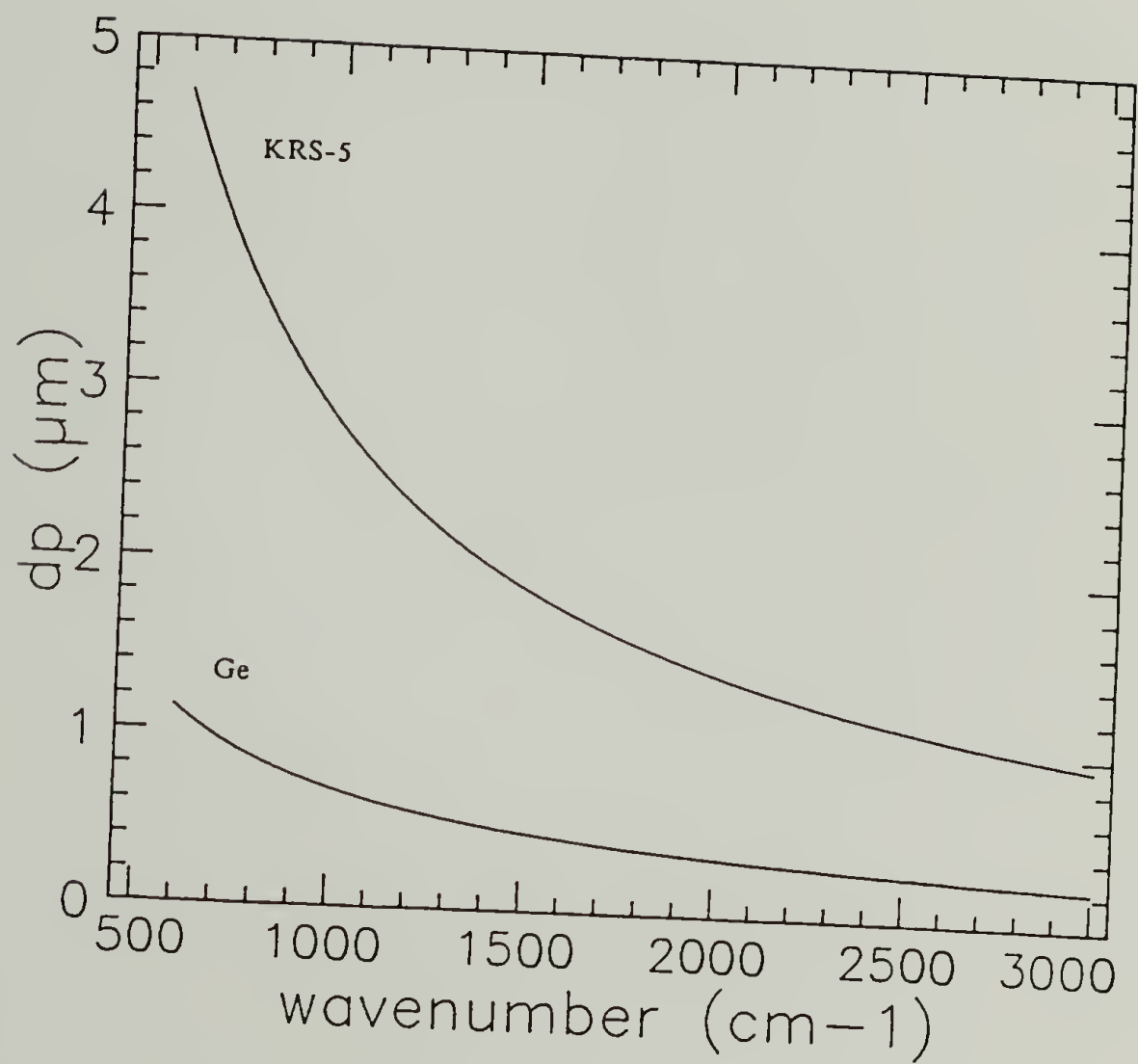
Figure 3.11   Evanescent wave penetration depths calculated for PPV
against germanium and KRS-5 crystals.

CHAPTER 4

ELECTRICAL CONDUCTIVITY AND CHEMISTRY OF DOPED FILMS

Interest in PPV has stemmed from its electrical properties. Also,

understanding of the doping process from a chemical point of view will be essential

in structural considerations. Therefore, before proceding to the discussion of the

structural features, experiments addressing the conductivity behavior and chemistry of

doped PPV films will be presented.

4.1 Electrical Conductivity

In its undoped form PPV is an electrical insulator having a conductivity less

than 10^{-10} $(\Omega \text{ cm})^{-1}$. Figure 4.1 shows the conductivity response to doping time with

group V pentafluorides. Both AsF_5 and SbF_5 cause rapid conductivity increases

during the initial dopant-PPV contact. The conductivity response is fastest and the

limiting value highest with SbF_5 and high pressure AsF_5 (340 mmHg) doping. Both

of these dopants yield limiting conductivities greater than 10^3 $(\Omega \text{ cm})^{-1}$. It is

important to note that the vapor pressure of SbF_5 is only 4 mmHg in this experiment.

In this regard SbF_5 is a most effective dopant. Lower AsF_5 vapor pressures (55

mmHg) show similar rapid initial conductivity increases. However, the limiting

conductivity is a least one order of magnitude less than that for SbF_5 doping. Thus,

the vapor pressure has a significant effect upon the resulting conductivity.

Phosphorus pentafluoride shows a much lessened propensity for PPV doping. The

initial response is slow and very long doping times ($\approx$300 hours) are required to reach

limiting values. At a PF_5 vapor pressure of 710 mmHg the sample reaches a limiting

conductivity of only 1 $(\Omega \text{ cm})^{-1}$. Thus, the trend in dopant activity is

$SbF_5 > AsF_5 >> PF_5$. This is consistent with the oxidizing strengths of these compounds [116].

As a control experiment the hydrogenated analog of PPV, poly(p-xylylene) (PPX) (see Figure 4.2), was doped with AsF_5. The weight-uptake was large (300%) for a 2 day doping confirming the occurence of reaction between AsF_5 and PPX. However, the conductivity of the initially insulating sample experienced only a small increase to 2×10^{-4} (Ω cm)$^{-1}$. This conductivity is attributed to doping created impurities in the sample and as such is not representative of an intrinsic PPX conductivity. The lack of doping induced conductivity in this polymer demonstrates the importance of the π-conjugated backbone in PPV.

These conductivities are electronic. No time dependent effects characteristic of ionic conductivity were observed. Further, AsF_5-doped samples behave Ohmically. Figure 4.3 shows the I-V characteristics of a sample doped to a mass-uptake of 220% and a conductivity of 8820 (Ω cm)$^{-1}$ with AsF_5. Recall from elementary physics that the current passing through an Ohmic conductor is related to the voltage by

$$I = V/R \qquad\qquad (4.1)$$

where R is the sample resistance and is constant. In the log-log plot the slope is nearly unity (ie., 0.994) confirming the linear I-V relation. The last point corresponds to that taken just before sample breakdown. Using this limiting current and the sample dimensions a limiting current density of 1390 A/cm^2 is calculated.

In the fully doped state the sample masses increased by $\approx$200% and $\approx$500–600% for AsF_5 and SbF_5 doping respectively. The high SbF_5 weight-uptakes are attributed to the polymeric character of this dopant [116]. Presumably, the sample is being loaded with non-active SbF_5 molecules along with those active ones responsible for PPV doping. Figure 4.4 shows the dopant uptake plotted against sample conductivity for an AsF_5-doped sample. Here, all the weight gain is attributed to incorporation of AsF_6^- (see section 4.2 for a discussion of doping chemistry).

61

Therefore, the variable x plotted in Figure 4.4 is representative of the hypothetical stoichiometry $(C_8H_6)(AsF_6)_x$. In the early stages of doping the conductivity increases over 10 orders of magnitude for less than a 1% weight gain. Conductivity increases are observed up to $x = 0.3$ corresponding to approximately one dopant anion for every three PPV repeat units. At higher uptakes the conductivity saturates.

The conductivities of H_2SO_4-doped samples reached 2000-4000 $(\Omega \text{ cm})^{-1}$ for 2-4 hour dopings. Table 4.1 lists typical limiting conductivities and the corresponding weight increases measured with the dopants used in this study.

In summary, bulk PPV films can be made highly electrically conductive by doping. This conductivity is electronic in nature and exhibits Ohmic behavior. The immediate increase of conductivity upon doping indicates the formation of a continuous conductive pathway along the entire sample length. These increases occur at very low dopant concentrations (<< 1%). Such rapid increases at low dopant uptake would not be expected if doping were homogeneous or percolative [117]. Rather, significant uptakes ($\approx$ 33%) would be required before conductivity increases occurred. Thus, the results indicate that the doping is heterogeneous with a skin effect suggested.

4.2 Chemistry of AsF_5-Doping

Because of the heterogeneous nature of the doping process, bulk analytical techniques such as elemental analysis are not definitive with regard to doped PPV stoichiometry. Therefore, this study employed surface sensitive techniques such as attenuated total reflectance FTIR spectroscopy and x-ray photoelectron spectroscopy to follow the doping of PPV surfaces. X-ray diffraction and mass spectrometry results for heavily doped bulk films are also presented.

4.2.1 Attenuated Total Reflectance FTIR

Infrared spectra of undoped and AsF_5-doped PPV are shown in Figure 4.5. The spectrum of undoped PPV (curve a) is dominated by two strong absorptions at 965 and 837 cm^{-1}. These bands have been previously assigned [47] and correspond to the C-H trans vinylene and C-H aromatic out-of-plane bends respectively. After a 1 hour AsF_5 doping at 370 mmHg new absorption bands at 695 cm^{-1} and 1142 cm^{-1} appear. The observation of the doping induced bands agrees with previous studies of AsF_5-doped PPV [59] and electrochemically oxidized PPV using AsF_6^- as the counterion [118]. Furthermore, these new features are due to only shallow dopings as can be seen by comparison of curves b and c. Curve b shows the ATR-FTIR spectrum obtained using a KRS-5 crystal. The effective sampling depth with this crystal is estimated as 4.7 μm at 600 cm^{-1} (see Figure 3.11). In the KRS-5 spectrum the doping induced bands are not apparent. On the other hand, the Ge crystal which has a sampling depth of only 1.1 μm at 600 cm^{-1} shows strong bands at both 1142 cm^{-1} and 695 cm^{-1} for the same sample. These results suggest that 1 hour dopings at these conditions achieve reaction depths on the order of 1 μm in PPV films. The KRS-5 spectrum, after a 5 day doping, is dominated by a broad band near 700 cm^{-1} indicating deeper dopant penetrations for long doping times.

The infrared spectra of arsenic fluoride species have been reported in the literature. The characteristic As-F stretching modes of AsF_5 absorb at 808 cm^{-1} and 782 cm^{-1} [119]. In a variety of hexafluoroarsenate salts (ie., $KAsF_6$, $NOAsF_6$, NO_2AsF_6, ONF_2AsF_6, $N_2F_3AsF_6$, OH_3AsF_6) the As-F stretching mode absorbs in the range 692-700 cm^{-1} [120,121] with the cation having little effect on the absorption frequency. Thus, the 695 cm^{-1} band appearing in AsF_5-doped PPV is characteristic of AsF_6^-. Unreacted AsF_5 was not observed in these doped films.

One side reaction possible with this reactive doping system is the fluorination (or hydrofluorination) of the PPV double bonds. However, the 1142 cm^{-1} absorption

is unattributable to carbon-fluorine bonds formed during the doping reaction. As the original electronic structure of the polymer is restored by chemical compensation of AsF$_5$-doped PPV [59] or by discharging the electrochemically oxidized PPV [118] the 1142 cm^{-1} band disappears. Thus, the 1142 cm^{-1} band is attributed to oxidation induced vibrations of the PPV chain rather than chemical bond formation by side reactions of AsF$_5$.

Doping induced absorptions in the range of 1800 to 1600 cm^{-1}, indicative of C–O bond formation, were minimal.

4.2.2 X-Ray Photoelectron Spectroscopy

The survey spectra for pristine PPV is shown in Figure 4.6. As expected, the pristine spectrum is mainly composed of the C_{1s} photoelectron. However, an O_{1s} photoelectron is also apparent. In fact, oxygen makes up 3.6% of the elemental surface composition. This corresponds, on average, to one oxygen atom for every three to four repeat units on the pristine polymer surface. Also, a small amount of fluorine (<1%) is apparent on the undoped surfaces. This arises from contact of the PPV film with a poly(tetrafluoro-ethylene) sheet during processing. Because of the low concentration and the characteristic PTFE binding energy this peak does not complicate the analysis presented here.

Figure 4.7 shows the survey spectrum for PPV doped with AsF$_5$ vapor at 380 mmHg for 1 minute. Fluorine and arsenic photoelectrons are prominent. In addition to the dopant photoelectrons a significantly increased amount of oxygen is observed. Fluorine and oxygen Auger electrons (F_{KLL} and O_{KVV}) are also apparent. Table 4.2 gives the elemental compositions of AsF$_5$-doped PPV surfaces for various doping conditions. These compositions were determined from multiplex spectra of the C_{1s}, F_{1s}, O_{1s}, and As_{3d} regions as discussed in section 3.2.6.2. As the dopant vapor pressure is increased from 120 to 370 mmHg corresponding increases are seen in As,

F, and O for 1 minute dopings. Doping for 5 days at 370 mmHg leads to only small changes in surface concentrations of As and F. Thus, the doping of the surface layer ($\approx$ 3 nm) of PPV is nearly complete after only a 1 minute exposure to AsF_5 vapor at 370 mmHg. At all doping levels the F/As atomic ratio is considerably less than 6/1, the expected ratio for the AsF_6^- anion.

The observed photoelectron binding energies (E_b) are listed in Table 4.3. The As, F, and O binding energies do not significantly vary with doping level. The As_{3d}, F_{1s}, and O_{1s} photoelectrons are observed at 46.8 $\pm$0.3 eV, 686.0 $\pm$0.1 eV, and 532.6 $\pm$0.2eV respectively. The F_{1s} binding energy is close to that measured for the model compound $LiAsF_6$ (686.6 eV). On the other hand, the measured As_{3d} binding energy for the doped polymer more closely matches that of As_2O_5 (46.6 eV). The O_{1s} binding energy is also close to the measured energy of As_2O_5 (532.4 eV). However, O_{1s} binding energies for poly(vinyl alcohol) and polycarbonate have been reported as 533 and 534 eV respectively [122]. Thus, the O_{1s} binding energy does not possess large enough chemical shifts between organically and inorganically bound oxygen to allow assignment.

While the As_{3d} and O_{1s} photoelectrons appeared as single peaks in the doped spectra, both the C_{1s} and F_{1s} showed a complex peak shape attributable to the presence of more than one C and F species. Figure 4.8 shows high resolution C_{1s} spectra for various doping conditions. At all doping conditions the major C_{1s} photoelectron peak occurs near 285 eV. As the films are doped a high E_b shoulder on the C_{1s} peak becomes apparent. At the heaviest doping condition this shoulder is clearly a separate photoelectron peak. Note that in pristine PPV the C_{1s} also has a slight tail at high E_b.

Curve fitting results are shown along with the C_{1s} data in Figure 4.8. Using the constraints mentioned in section 3.2.6.2 three bands were required to fit the carbon profiles in the doped films. The binding energies and relative areas are listed

in Table 4.4 for the various doping conditions. As can be seen the peak positions of the three bands are nearly constant for the various doping levels. The binding energy variations are ±0.10 eV, ±0.40 eV, and ±0.15 eV for bands 1, 2, and 3 respectively for the different doping conditions. Band 1 at 284.5 eV is the major component at all doping levels. Its relative intensity decreases from 80% in the pristine film to approximately 70% at the highest doping levels. With the exception of the heaviest doping level, band 2 at 285.6 eV has a constant intensity near 20%. Band 2 is not expected to be related to the doped form of PPV since it is present in the pristine film and its position and area are invariant to doping level for the 1 minute dopings. On the other hand, band 3, at 287.0 eV, is quite sensitive to doping level. As the dopant vapor pressure is increased from 120 to 370 mmHg the band 3 area increases from 5 to 10%. A five day exposure to AsF_5 vapor at 370 mmHg increases the amount of this band to only 17%. It is important to note that the curve fitting results for AsF_5-doped PPV very closely match those of a previous investigation of electrochemically oxidized PPV [123]. In this study three bands at essentially identical binding energies to the bands of the present study were observed. Thus, the modification of the hydrocarbon polymer backbone appears similar for both chemical and electrochemical doping methods.

The high resolution F_{1s} spectra are shown in Figure 4.9 along with the bands resulting from a curve fitting analysis. At all doping levels the major F_{1s} photoelectron peak is at 686 eV. As the doping level is increased a high E_b shoulder appears and becomes prominent at the highest doping levels. Table 4.5 lists the curve fitting results for the F_{1s} photoelectron region. As with C_{1s} three bands were required to fit the F_{1s} peak profiles except in the case of the 5 day doping. Here, a more extensive high E_b tail exists. The peak positions of the three bands in the 1 minute doping profiles were nearly constant. Band 1, the major F_{1s} photoelectron peak, occurred at 686.0 ±0.1 eV, band 2 at 687.7 ±0.3 eV, and band 3 at 689.3 ±0.1

eV. As the doping vapor pressure was increased from 120 to 370 mmHg the relative area of band 1 decreased from 74% to 58% for the 1 minute dopings. The area of band 2 was insensitive to doping vapor pressures for 1 minute dopings and had a value of approximately 14%. The area of band 3 increased from 11% to 20% as the vapor pressure was increased from 120 to 370 mmHg.

Because the C_{1s} and F_{1s} band positions resulting from the curve fitting analyses were invariant to doping level it is unlikely that they can be attributed to artifacts such as differential charging of the film surface. Rather, they offer chemical shift information regarding the carbon and fluorine species involved in the AsF_5 doping of PPV. Bands 1 and 3 in both the C_{1s} and F_{1s} profiles are certainly significant as can be clearly seen from the spectra. However, care should be exercised in interpreting the intermediate bands of both the C_{1s} and F_{1s} profiles since relaxation of the constraint that the band shapes be purely Gaussian (with no Lorentzian character) may eliminate the need for these bands in the curve fit.

As with the major photoelectron peaks, assignments can be suggested for these bands. The major C_{1s} and F_{1s} photoelectron peaks at 284.5 eV and 686.0 eV are attributed to electrically neutral carbon atoms of the polymer backbone and the hexafluoroarsenate anion respectively. One possibility consistent with the simultaneous appearance of the high binding energy C_{1s} and F_{1s} photoelectrons is the formation of C-F bonds as a doping side-reaction. Inspection of Tables 3.4 and 3.5 show that the relative amounts of the high binding energy components of the C_{1s} and F_{1s} profiles are nearly constant for 1 minute dopings. The F/C ratio is near 2. Thus, difluorinated carbon atoms are indicated (ie., $-CF_2-$). However, this is not consistent with the 287.0 eV binding energy of the C_{1s} band 3. Difluorinated carbon atoms in poly(vinylidene fluoride), poly(trifluoro-ethylene), and poly(tetrafluoro-ethylene) have C_{1s} binding energies 290.4, 291.2, and 291.8 eV respectively [124]. It is more likely that the C_{1s} band 3 at 287.0 eV in AsF_5-doped PPV is attributable to

electron deficient sites along the conducting polymer backbone. Based on molecular orbital calculations the same assignment was made for a 286.5 eV band in electrochemically oxidized PPV [123]. The high binding energy F_{1s} photoelectron cannot alternately be attributed to AsF_5, AsF_3, or HF since their binding energies are significantly higher at 693.6 [125], 693.5 [125], and 694.0 eV [126] respectively. Thus, based on binding energies alone the minor fluorine containing species cannot be assigned to the obvious possibilities.

An important point to address is the stoichiometry of the doped complex. From Table 4.2 the fluorine concentration for the 5 day doped surface is 2.8 F / polymer repeat. While the entire C_{1s} peak is attributed to the PPV polymer backbone only 58% of the F_{1s} peak is attributed to the dopant anion. Thus, the dopant contribution gives 1.6 F / polymer repeat. Since there are 6 fluorine atoms per dopant anion the resulting dopant anion to polymer repeat ratio is 0.27. Thus, the suggested complex stoichiometry is $(C_8H_6^{\delta+})_x(AsF_6^-)$ where x = 3 or 4. This is in agreement with electrochemical oxidation results of PPV using AsF_6^- as the counterion where a PPV repeat to anion ratio of 4:1 was found [61].

4.2.3 Mass Spectrometry

The gas chromatograms of the thermolysis products of pristine and AsF_5-doped PPV are shown in Figure 4.10. As can be seen from comparison of the chromatograms doping does not cause significant changes. Only one new peak at a retention time of 16 min is observed in the doped chromatogram. The molecular weight and compound assignment for each peak is listed in Table 4.6. With the exception of the aromatic aldehyde and tetrahydrothiophene all of the pristine polymer degradation products are hydrocarbons. In fact, the products result from simple cleavage of the polymer chain. In this regard it is different from polyacetylene [69] which rearranges during thermolysis through an electron-proton

exchange mechanism to form a variety of aromatic compounds. Methyl-benzene and dimethyl-benzene are the major low molecular weight thermolysis products of PPV. Higher molecular weight products are simply larger fragments of the PPV chain. Both conjugated and hydrogenated forms of the fragments are observed. The tetrahydrothiophene is residual from the precursor polymer [104]. The benzaldehyde is derived from oxidized PPV repeat units. Both of these peaks are small indicating low concentrations.

The doped chromatogram shows essentially the same features. Tetrahydrothiophene is not observed. The aromatic aldehyde is also not observed but the dialdehyde (peak 10') is observed. Because of the experimental conditions highly volatile AsF_5, AsF_3 and HF will not be observed. No fluorinated organic species were observed, suggesting the absence of fluorinating side reactions of the AsF_5 dopant. This is similar to AsF_5-doped polyacetylene in which the dopant tends to catalyze the formation of hydrogenated thermolysis products but does not fluorinate the conjugated polymer chain [69]. Also, an increase in the amount of the aldehyde thermolysis product is not observed. Thus, the increase in the amount of oxygen in the doped films, as noted with XPS, cannot be attributed to a doping induced incorporation of *organic* oxygen.

4.2.4 X-Ray Diffraction

X-ray fiber diffraction patterns of AsF_5-doped PPV show a superposition of the oriented polymer fiber diffraction and powder diffraction from some randomly oriented compound which is formed during doping. These patterns will be discussed in detail with regard to the doped polymer structure in the following chapter. Table 4.7 compares the crystallographic d-spacings measured for the powder formed in AsF_5-doped PPV and a variety of arsenic compounds. Clearly, the powder formed during doping is not OH_3AsF_6, As_2O_3 or As_2O_4. The two strongest reflections of

69

As$_2$O$_5$ at 0.606 and 0.367 nm have matching reflections in the PPV pattern. The matching reflection at 0.600 nm is of medium strength while the corresponding As$_2$O$_5$ reflection is very strong. Also, many of the medium and weak As$_2$O$_5$ reflections have no apparent match in the PPV pattern. A close match is formed between the hydrated form of As$_2$O$_5$ and PPV. The 0.488, 0.342, 0.305, 0.271, 0.237, 0.218, 0.202, and 0.197 nm reflections of 3As$_2$O$_5$.5H$_2$O have matching reflections in the PPV powder diffraction pattern. The presence of this compound is thus suggested. A small amount of unhydrated As$_2$O$_5$ might also be present accounting for the 0.600 nm reflection. In addition to these compounds at least one other may also be formed since the strong 0.445 nm PPV reflection has no correspondence to either As$_2$O$_5$ or 3As$_2$O$_5$.5H$_2$O. The formation of these oxides in AsF$_5$-doped PPV provides a mechanism for incorporation of inorganic oxygen. Also, the lower than expected F/As ratio measured by XPS can be rationalized by considering arsenic oxides to be present on the film surfaces.

4.2.5 Chemical Model of AsF$_5$-Doping

Both FTIR and XPS confirm the presence of the AsF$_6^-$ anion in AsF$_5$-doped PPV. This species has been proposed as the dopant anion in AsF$_5$-treated PA [129,130]. These previous studies have proposed an electron-transfer fluorine-disproportionation reaction to account for the formation of this species. The results presented in this section support the analogous reaction in AsF$_5$-doped PPV. Thus, the conductive phase is formed through the chemical reaction

$$2\text{PPV (s)} + 3\text{AsF}_5 \text{ (g)} \text{ ------>} 2[(\text{PPV}^+)(\text{AsF}_6^-)] \text{ (s)} + \text{AsF}_3 \text{ (l)} \qquad (4.2)$$
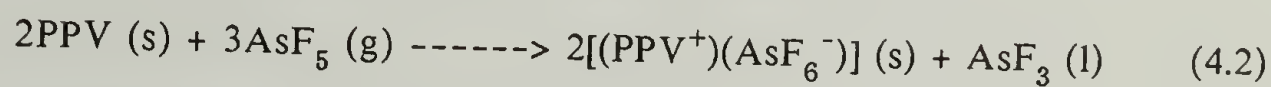
This can be generalized for group V pentafluorides as

$$2\text{PPV (s)} + 3\text{MF}_5 \text{ (g)} \text{ ------>} 2[(\text{PPV}^+)(\text{MF}_6^-)] \text{ (s)} + \text{MF}_3 \qquad (4.3)$$
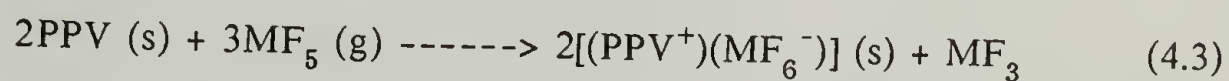
where M = P, As, or Sb. Further, the XPS results suggest a doped complex stoichiometry $(\text{C}_8\text{H}_6)_x(\text{AsF}_6^-)$ where x = 3 - 4 on doped PPV surfaces. This is also

consistent with the electrical conductivity results. As mentioned in section 4.1 no significant conductivity increases were observed for stoichiometries $(C_8H_6)(AsF_6^-)_x$ where $x > 0.30$.

Attenuated total reflectance FTIR has shown only shallow reaction depths. This confirms the skin effect predicted from the electrical behavior. Also, in addition to the primary doping reaction a side reaction occurs which forms arsenic oxides. This reaction occurs even though doping is conducted at low pressures ($< 10^{-4}$ mmHg).

Table 4.1
Typical properties of doped PPV films.

Dopant	$\sigma^{Limiting}$ $(\Omega\ cm)^{-1}$	Mass increase (%)
PF_5 (710 mmHg)	1	3
AsF_5 (340 mmHg)	1600	39
SbF_5 (4 mmHg)	2400	580
H_2SO_4 (98% aq)	3000	130

Table 4.2. Elemental surface composition of AsF_5-doped PPV. Number of atoms relative to one PPV repeat unit (ie., C_8H_6).

Doping Conditions	C	O	F	As	F/As
Pristine	8	0.3	-	-	-
1 minute, 120 mmHg	8	1.9	0.5	0.6	0.8
1 minute, 240 mmHg	8	2.9	0.9	0.9	1.0
1 minute, 370 mmHg	8	2.8	2.5	0.9	2.8
5 days, 370 mmHg	8	3.7	2.8	1.2	2.3

Table 4.3. Binding energies of major photoelectrons, multiplex spectra.
(eV)

Sample	$\underline{C}_{1s}$	$\underline{F}_{1s}$	$\underline{As}_{3d}$	$\underline{O}_{1s}$	$\Delta \underline{E}_b{}^1$
PPV, pristine	284.6	-	-	532.8	-
PPV/AsF$_5$ 1 min 120 mmHg	284.6	685.9	46.5	532.4	639.4
PPV/AsF$_5$ 1 min 240 mmHg	284.6	686.1	46.9	532.7	639.2
PPV/AsF$_5$ 1 min 370 mmHg	284.6	686.0	47.0	532.7	639.0
PPV/AsF$_5$ 5 days 370 mmHg	284.6	685.9	46.9	532.7	639.0
LiAsF$_6$	(284.6)[2]	686.6	48.3	-	638.3
As$_2$O$_5$	(284.6)[2]	-	46.6	532.4	-

[1] ΔE_b is the binding energy difference between F_{1s} and As_{3d} photoelectrons.

[2] The carbon in the inorganic spectrum is due to the tape substrate and is used as an energy calibration.

Table 4.4. X-ray Photoelectron Spectroscopy curve fitting results for AsF_5-doped PPV. Carbon 1s region.

Sample	Band 1 E_b (eV)	%	Band 2 E_b (eV)	%	Band 3 E_b (eV)	%
Pristine PPV	284.4	80	285.2	20	-	-
120 mmHg AsF_5 1 minute	284.5	79	285.7	16	287.0	5
240 mmHg AsF_5 1 minute	284.5	75	285.3	17	286.8	7
370 mmHg AsF_5 1 minute	284.5	67	285.7	22	287.1	10
370 mmHg AsF_5 5 days	284.6	76	286.0	8	286.9	17

All bands have Gaussian line shapes.
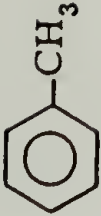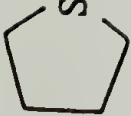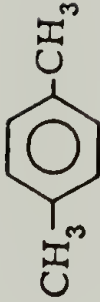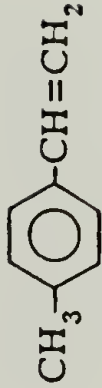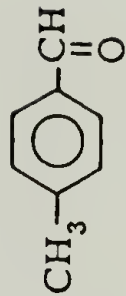
Table 4.5. X-ray Photoelectron Spectroscopy curve fitting results for AsF$_5$-doped PPV. Fluorine 1s region.

Sample	Band 1 E_b (eV)	%	Band 2 E_b (eV)	%	Band 3 E_b (eV)	%
120 mmHg AsF$_5$ 1 minute	685.9	74	687.4	15	689.2	11
240 mmHg AsF$_5$ 1 minute	685.9	77	687.4	11	689.4	12
370 mmHg AsF$_5$ 1 minute	686.1	66	687.9	14	689.4	20
370 mmHg AsF$_5$ 5 days*	685.9	58	687.6	9	689.3	19

*The 5 day doped sample required 2 additional bands (making up 13% of the total) at higher E_b to fit the entire photoelectron peak.
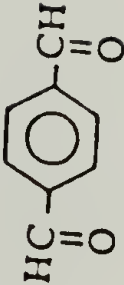
All bands have Gaussian line shapes.

Table 4.6 Pyrolysis products from undoped and AsF$_5$-doped PPV.

Peak	Molecular Weight	Compound
1, 1'	92	(benzene ring)–CH$_3$
2	88	(5-membered ring with S)
3, 3'	106	CH$_3$–(benzene ring)–CH$_3$
4, 4'	120	CH$_3$–(benzene ring)–CH$_2$–CH$_3$
5, 5'	118	CH$_3$–(benzene ring)–CH=CH$_2$
6	120	CH$_3$–(benzene ring)–CH=O

Table 4.6
(cont.)

Peak	Molecular Weight	Compound
7, 7'	196	CH$_3$—⬡—CH$_2$—CH$_2$—⬡
8, 8'	194	CH$_3$—⬡—CH=CH—⬡
9, 9'	208	CH$_3$—⬡—CH=CH—⬡—CH$_3$
10'	134	HC(=O)—⬡—CH=O

Unprimed and primed peaks correspond to pristine and AsF$_5$-doped PPV respectively.

Table 4.7. Powder diffraction d-spacings for AsF$_5$-doped PPV and various arsenic compounds. (nanometers)

PPV/AsF$_5$ [1,2]	3As$_2$O$_5$·5H$_2$O [2]	As$_2$O$_5$ [4]	OH$_3$AsF$_6$ [5]	As$_2$O$_3$ [2]	As$_2$O$_4$ [3]
	0.709(m)				
					0.642(s)
		0.606(vs)			
0.600(m)					
					0.554(m)
	0.553(w)				
0.492(s)					
	0.488(m)				
			0.464(vs)		
	0.459(w)				
0.445(s)					
		0.432(w)			
		0.422(w)			
		0.407(w)			
	0.403(w)				
			0.401(vs)		
					0.381(s)
0.373(s)					
					0.369(s)
		0.367(s)			
					0.364(s)
	0.359(s)				
	0.342(s)				
0.335(m)					
	0.322(m)				
				0.319(s)	
		0.316(m)			
		0.312(m)			
	0.305(m)				
		0.302(m)			0.302(vs)
0.301(m)					
		0.293(m)			
			0.282(s)		0.282(m)

(continued on next page)

Table 4.7
(cont.)

PPV/AsF$_5$[1,2]	3As$_2$O$_5$·5H$_2$O[2]	As$_2$O$_5$[4]	OH$_3$AsF$_6$[5]	As$_2$O$_3$[2]	As$_2$O$_4$[3]
0.274(w)	0.271(m)	–	–	0.278(m)	0.277(w)
–	–	–	–	0.255(m)	0.262(s)
–	–	0.245(w)	0.242(w)	–	–
0.237(w)	0.237(w)	0.236(w)	–	–	0.237(m)
0.232(w)	–	–	0.232(w)	–	–
–	–	–	–	0.226(w)	–
0.218(w)	0.218(m)	–	–	–	–
0.212(w)	–	–	–	0.213(m)	–
0.200(m)	0.202(m)	–	0.200(w)	–	–
0.197(m)	0.197(w)	–	–	0.196(m)	–

Symbols in parentheses represent relative intensities: vs = very strong, s = strong, m = medium, w = weak.

[1]Doping conditions: 4 days at 340 mmHg.
[2]Measured d-spacings.
[3]See ref. [127].
[4]See ref. [128].
[5]See ref. [121].
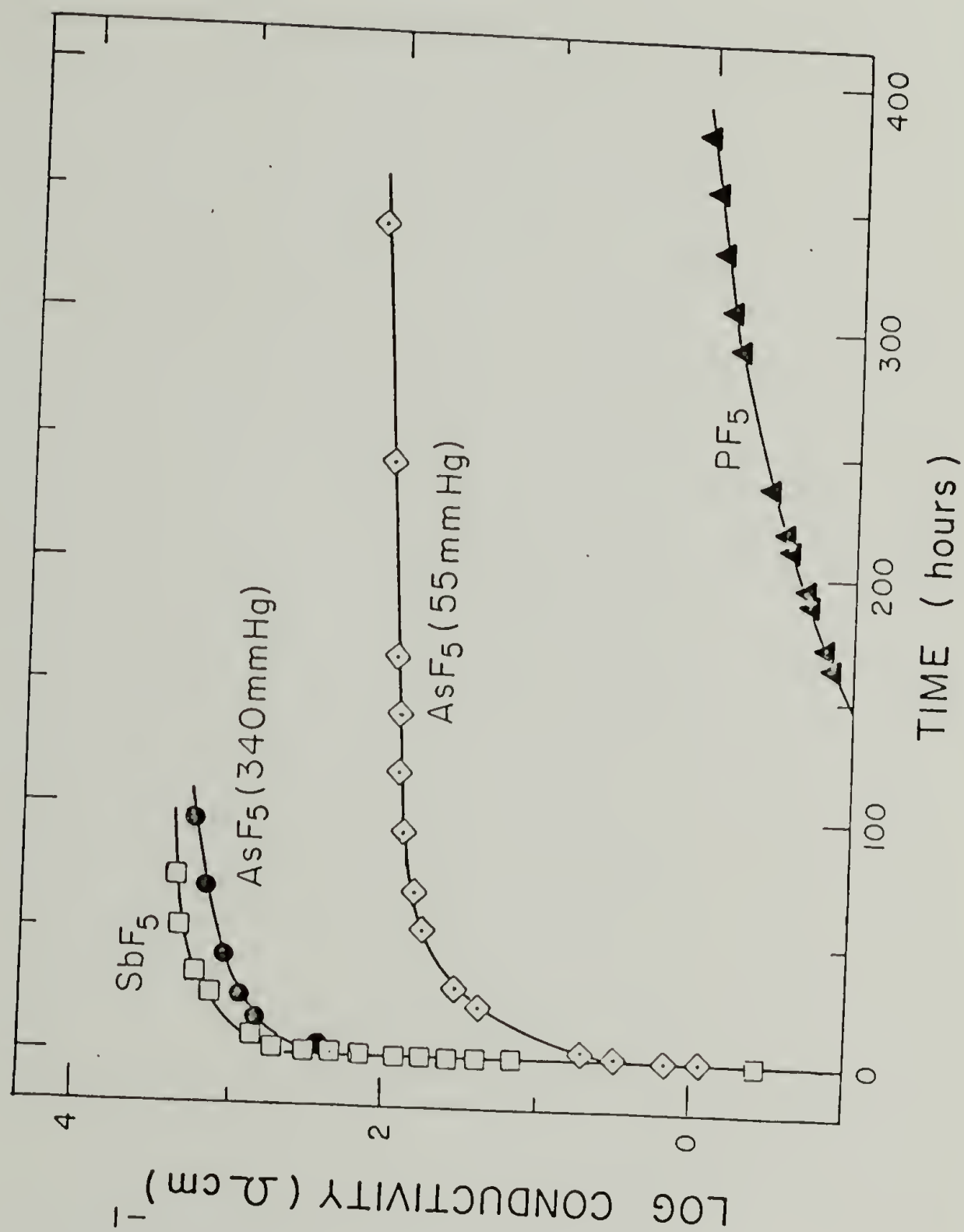
Figure 4.1   Electrical conductivity of PPV films during group V pentafluoride doping.
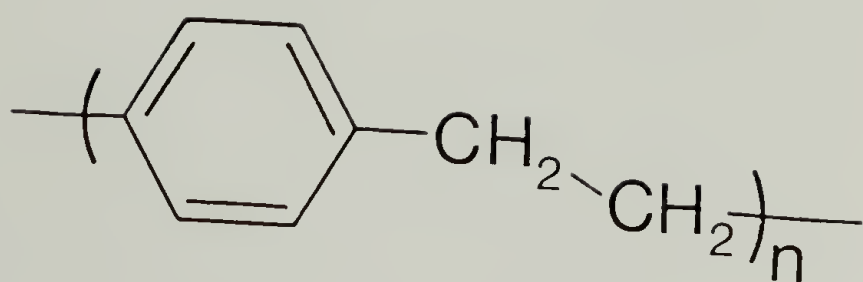
Figure 4.2   Poly(*p*-xylylene), PPX.
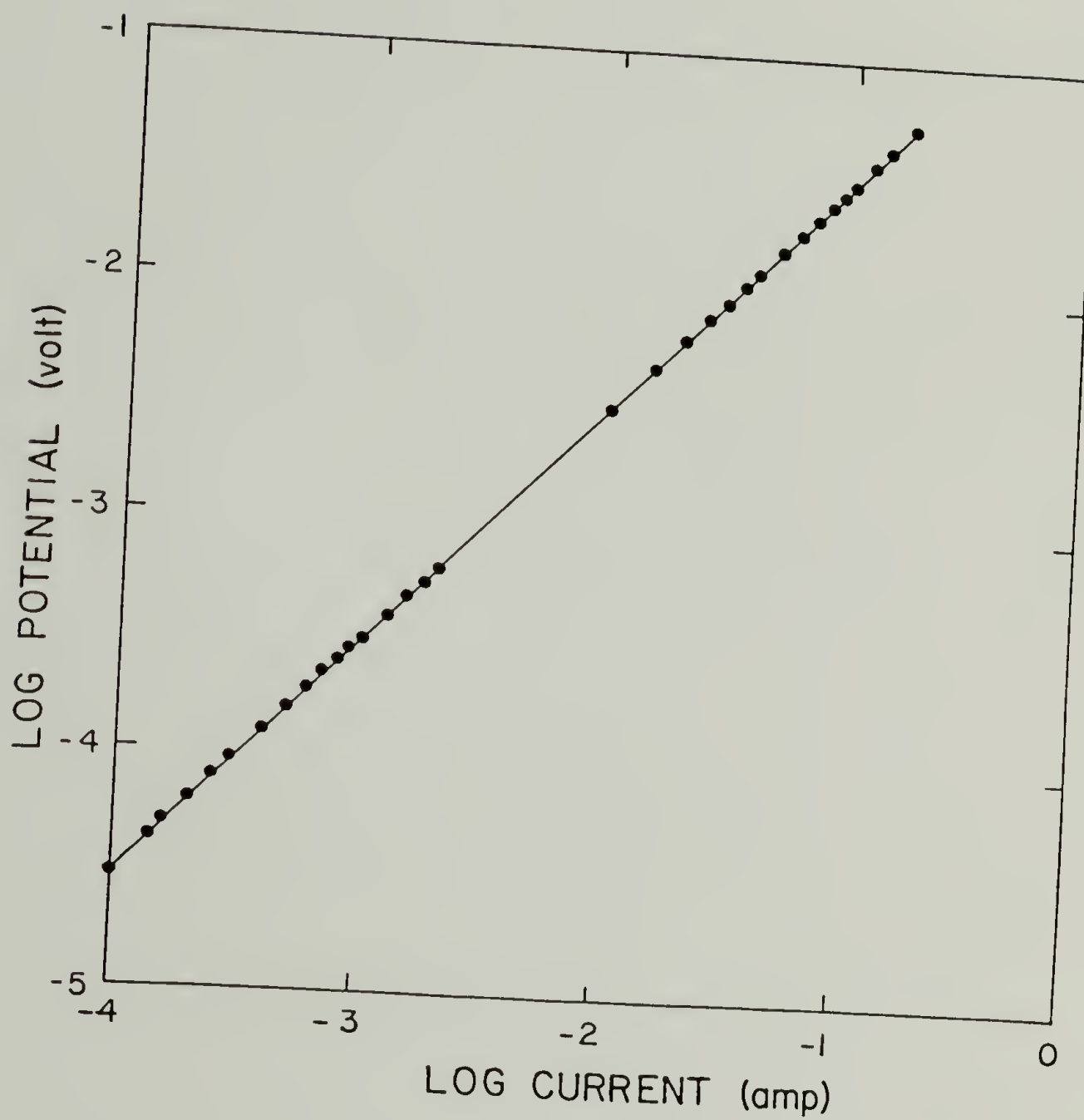
Figure 4.3   I-V plot of heavily AsF$_5$-doped PPV film.
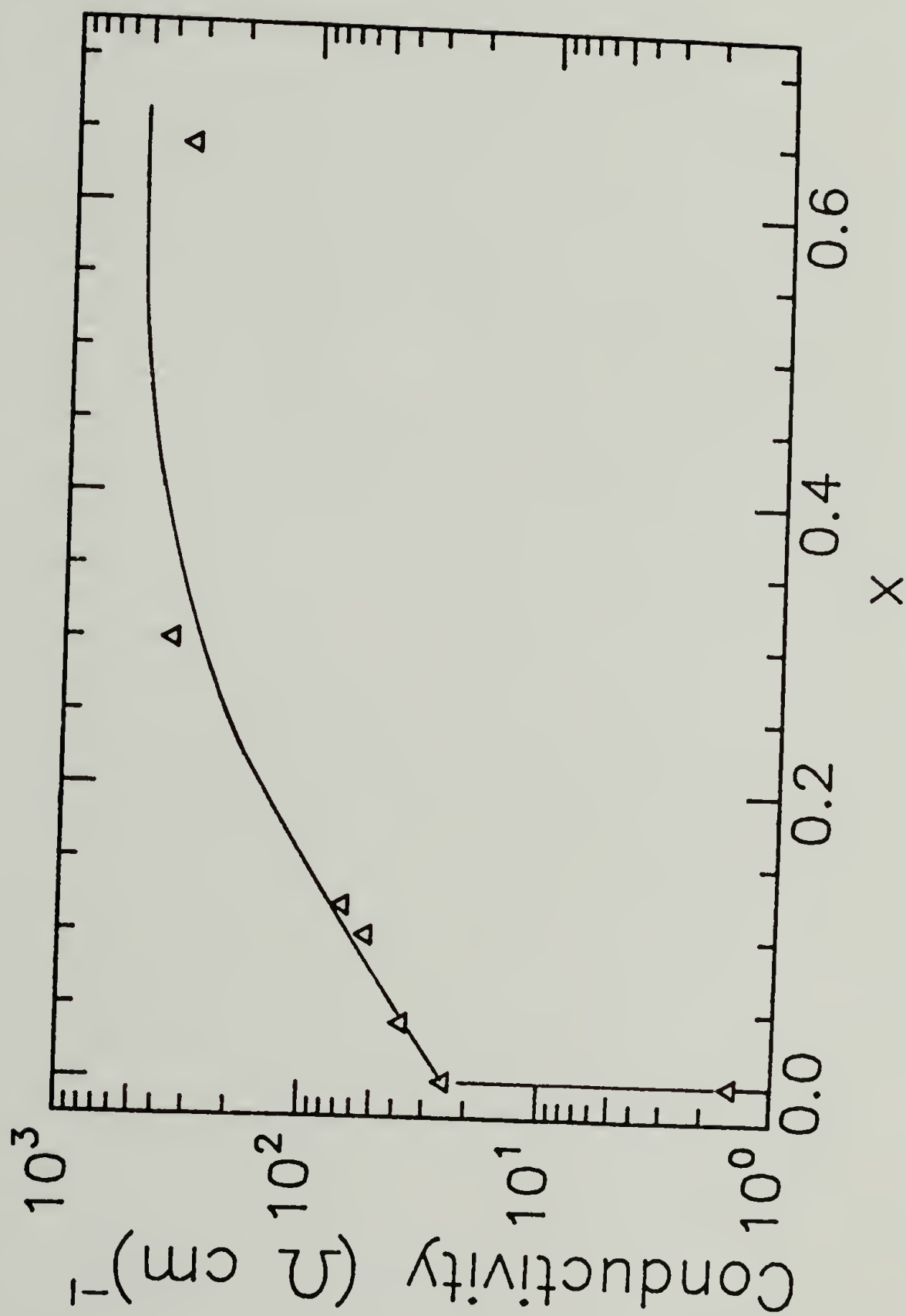
Figure 4.4   Electrical conductivity as a function of weight-uptake for AsF_5-doped PPV. $(C_8H_6)(AsF_6)_x$.
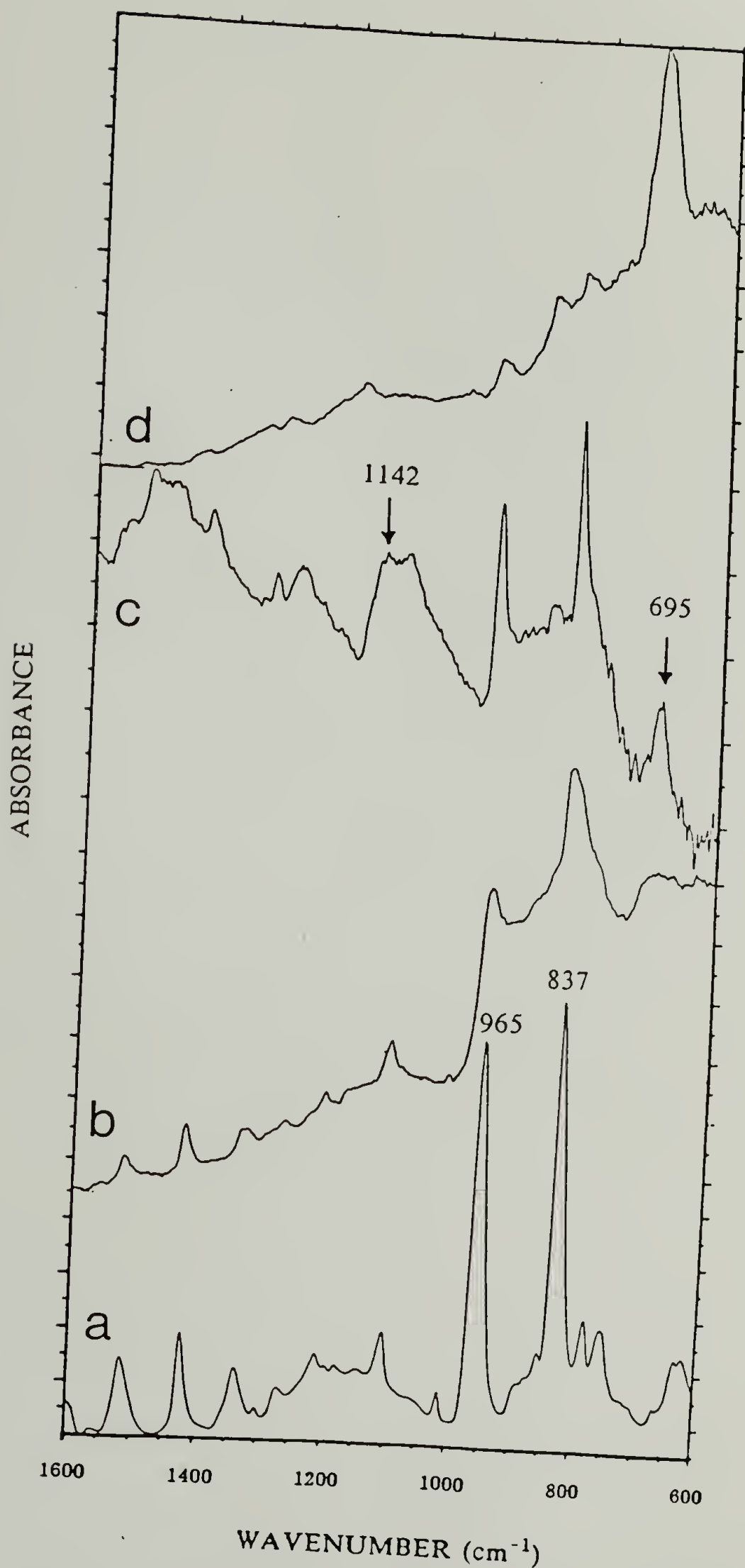
Figure 4.5   Attenuated total reflectance FTIR spectra: a) pristine PPV, KRS-5 crystal; b) AsF$_5$-doped PPV, 370 mmHg, 1 hour, KRS-5 crystal; c) AsF$_5$-doped PPV, 370 mmHg, 1 hour, Ge crystal; d) AsF$_5$-doped PPV, 370 mmHg, 5 days, KRS-5 crystal.
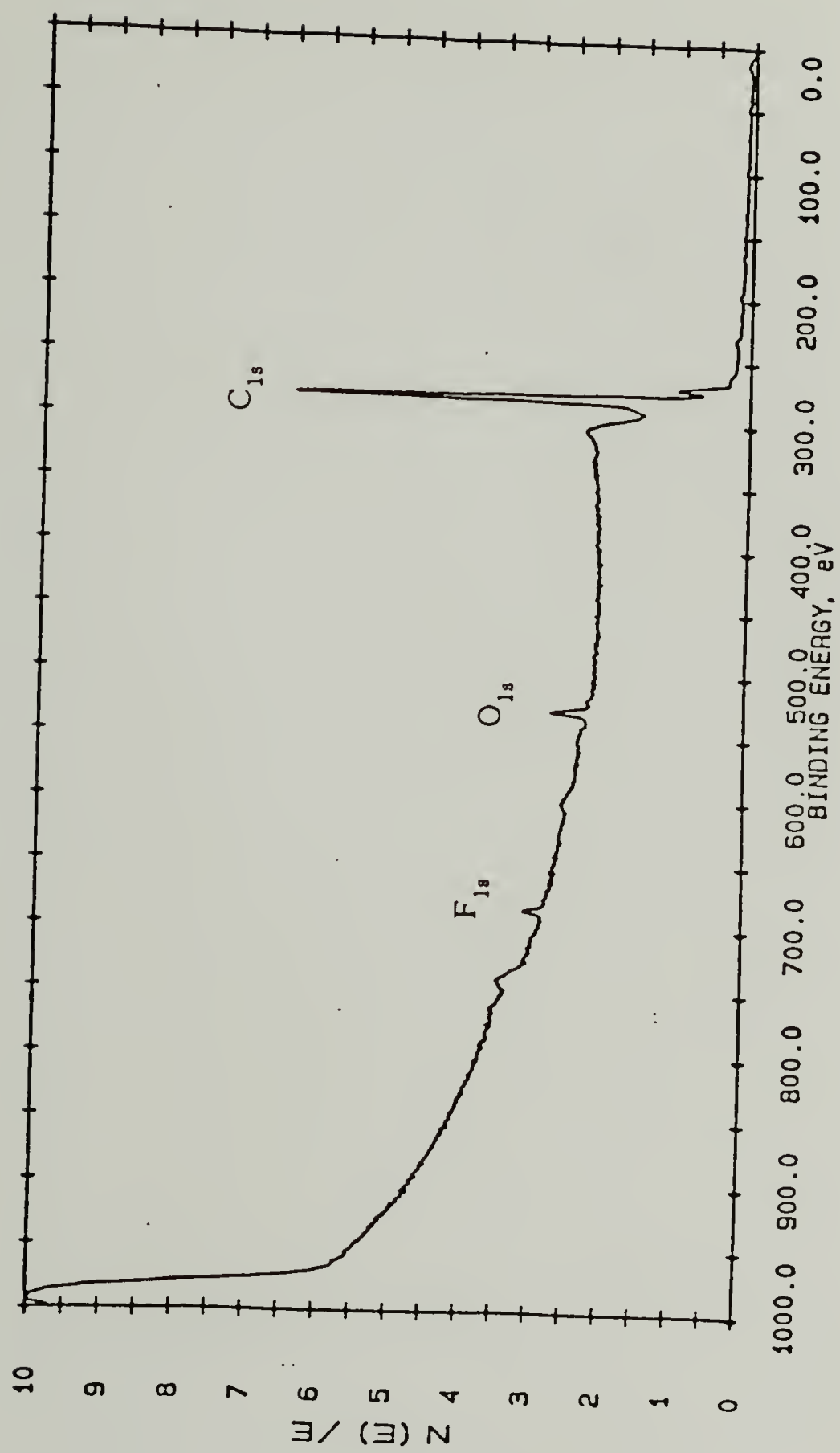
Figure 4.6   X-ray photoelectron survey spectrum of undoped PPV.
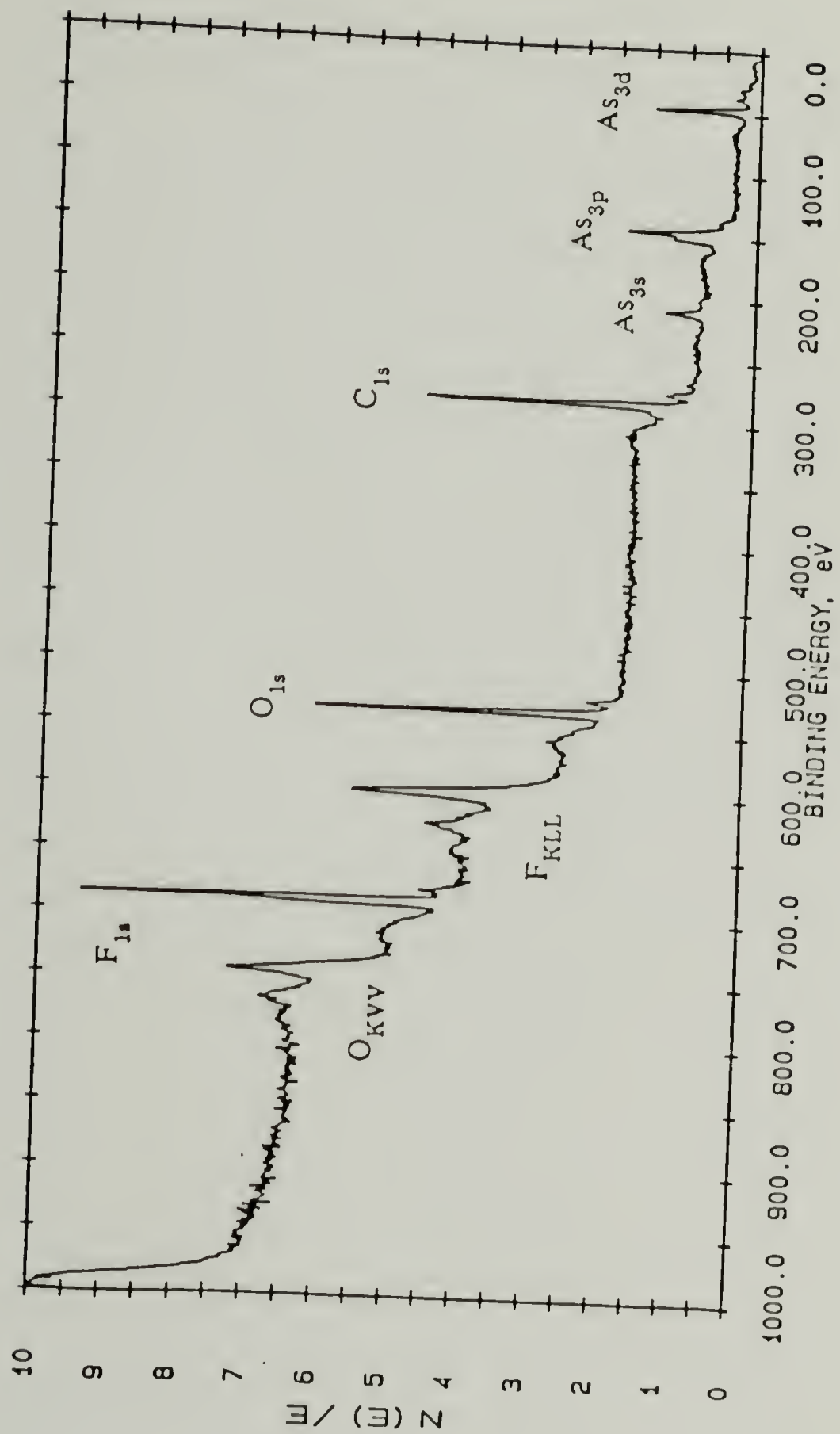
Figure 4.7   X-ray photoelectron survey spectrum of AsF_5-doped PPV, 380 mmHg, 1 minute.
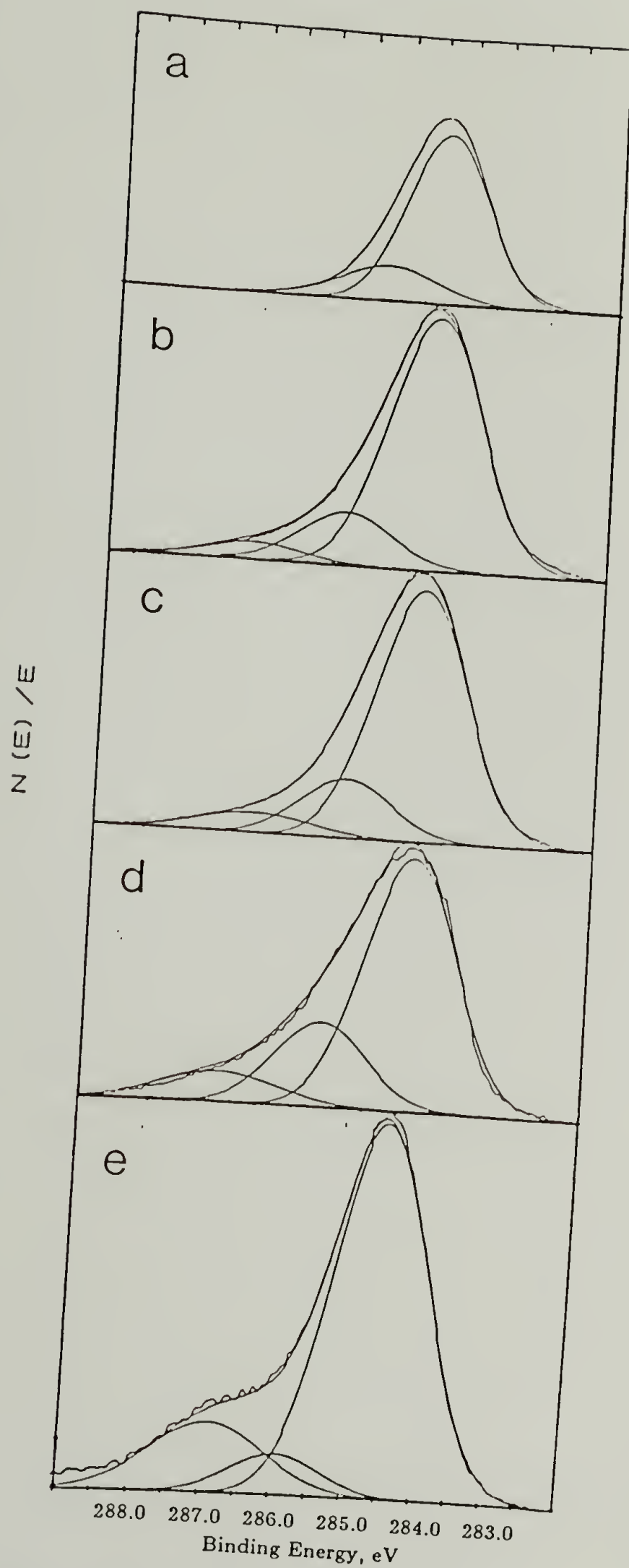
Figure 4.8   High resolution x-ray photoelectron spectra of C_{1s} region:
a) pristine PPV; b) AsF_5-doped PPV, 120 mmHg, 1 minute;
c) AsF_5-doped PPV, 240 mmHg, 1 minute; d) AsF_5-doped PPV,
370 mmHg, 1 minute; e) AsF_5-doped PPV, 370 mmHg, 5 days.
The bands resulting from the curve fitting analysis are included.

88
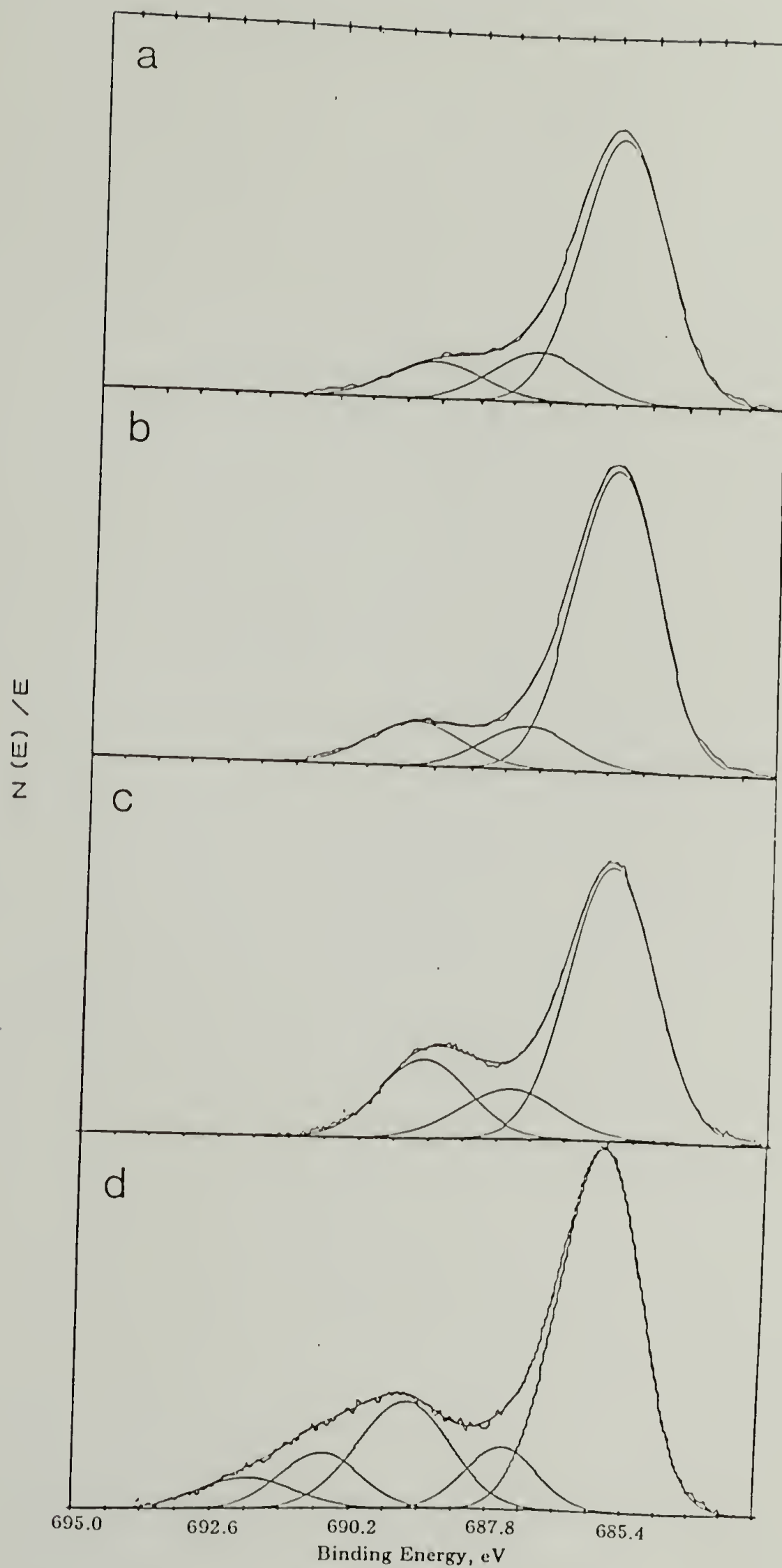
Figure 4.9   High resolution x-ray photoelectron spectra of F_{1s} region
in AsF_5-doped PPV: a) 120 mmHg, 1 minute; b) 240 mmHg, 1 minute;
c) 370 mmHg, 1 minute; d) 370 mmHg, 5 days.
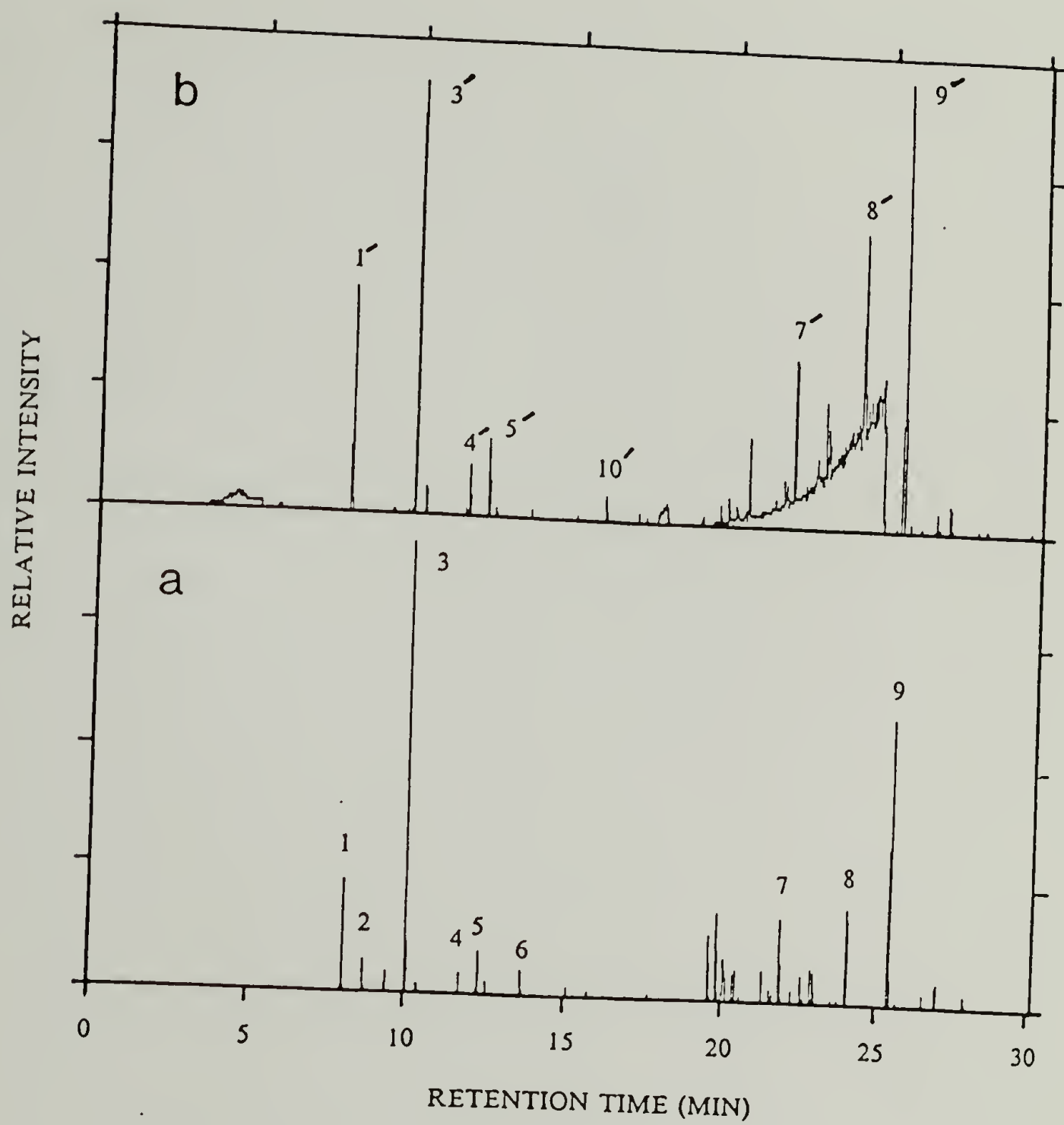
Figure 4.10 Gas chromatograms of pristine PPV (a) and PPV doped with AsF$_5$ for 5 days (b).

CHAPTER 5

CRYSTALLINE STRUCTURES OF THE INSULATING AND CONDUCTING

PHASES

As mentioned in Chapter 2 PPV is a semicrystalline polymer. In this chapter the effect of doping on the crystal structure will be examined. All of the results presented here are derived from the doping of *bulk* PPV films.

5.1 Crystal Structure of Undoped PPV

Figure 5.1 shows x-ray diffraction patterns of isotropic and oriented PPV films. The d-spacings measured for both films are listed in Table 5.1. The d-spacings closely match the calculated values for the $\ell = 1$, 2 and 3 layer lines. These calculated values are derived from the monoclinic structure determined from electron diffraction [53] (see also Figure 2.1). Thus, PPV crystallizes to the monoclinic form in both isotropic and oriented films. Stretching merely serves to orient the c axis of the crystallites with the draw direction.

The reflections along the $\ell = 1$ layer line possess a streaky character. Further, only (0k1) reflections are seen. These observations are consistent with the paracrystalline model of PPV presented by Granier et al [54]. The streakiness of the (0k1) reflections makes their positions less certain. This can be seen in Table 5.1 where the (001) and (0$\bar{2}$1) reflections show the largest deviations from the calculated positions. Also, the streaky (001) reflection is evident as a broad ring in the isotropic sample. This ring was initially attributed to random or amorphous order in unstretched films [32]. While its breadth is typical of disorder, the paracrystalline analysis has shown this broad reflection to arise from a specific axial translational disorder rather than from an amorphous phase.

91

Because several families of hkℓ reflections are simultaneously observable many axial orientations coexist in one particular PPV film [131]. Figure 5.2 shows the diffracted intensity for the $\ell = 0$ layer line of an oriented film. No significant change in relative intensities of the (110), (210) and (310) reflections is seen as the sample is rotated about its orientation axis. Also included in this figure is the calculated equatorial intensities. These diffracted intensities were calculated assuming an axially cylindrically symmetric distribution of crystallites. The details of the calculation and a listing of the computer programs are included in the Appendix. From comparison of the calculated and measured intensities it is clear that a cylindrically symmetric model well describes the axial distribution of crystallites in PPV. These results are consistent with a fiber symmetric morphology in drawn films of PPV.

The lack of amorphous background in the x-ray diffraction patterns suggest a high degree of crystallinity. However, because the backbone of PPV is rigid and PPV does not melt, a purely a amorphous sample cannot be prepared. This prohibits quantitative evaluations of the degree of crystallinity by conventional techniques such as density measurements, calorimetry, or diffraction.

It should be noted that the ability to orient PPV facilitates structural analysis. The resulting diffraction patterns from fiber symmetric PPV are similar to those obtained from a rotation diffraction pattern of a single crystal. All equatorial diffraction spots and many off-axis spots, within the angular limits of the film, are simultaneously observed. Further, the lateral and longitudinal crystallographic spacings are readily identified. This simplifies the study of the conducting phase.

5.2 Structure of Doped PPV

5.2.1 Arsenic Pentafluoride-Doped PPV

Figure 5.3 shows the diffraction patterns of oriented PPV before and after doping with AsF_5. After doping new reflections become apparent. The pattern shown here is from a sample at a relatively low dopant level (ie., 39% weight uptake). Thus, both undoped and doped phases are present. Three new equatorial reflections at 1.032, 0.504, and 0.331 nm are observed. These indicate a new lateral packing in the doped phase. Also, a strong meridional reflection exists on the $\ell = 1$ layer line, indicating a change from the monoclinic symmetry of the undoped phase. This reflection occurs at 0.658 nm which corresponds exactly to the chemical repeat length of the PPV chain. The diffracted intensity along the $\ell = 1$ layer line shows a modulation with discrete reflections discernible (see Figure 5.3c and d). More than one periodicity is also apparent from the spacing of these reflections. Thus, several qualitative assessments can be made concerning the doped phase.

1. Doping induces a new lateral packing of the PPV chains.

2. The symmetry of the doped phase differs from the monoclinic symmetry of undoped PPV. The c^* axis of the doped phase can be assigned as parallel to the draw direction with the strong meridional reflection assigned as the (001) reflection.

3. The discrete reflections present on the $\ell = 1$ layer line and their multiple periodicities indicate a reduced axial translational disorder between neighboring chains.

This last point may be justified on the basis of the different interactions between neighboring chains for the doped and undoped crystal. In the undoped crystal van

der Waals forces act between neighboring chains. In the doped crystal stronger Coulombic interactions will also be operative since the PPV chain possesses a net electrical charge. These stronger forces may serve to strengthen the intermolecular potentials thereby resulting in a higher degree of long range order.

In addition to these points it is also evident that the doped phase retains the orientational order of the undoped PPV; The crystallites do no spatially reorganize during doping.

Also note that within experimental error the chemical repeat length of the polymer is unchanged after doping. Any change in this value would indicate bond length changes associated with electron transfer from the polymer backbone. The magnitude of any length change, however, is expected to be small. Using neutron diffraction Chan et al [132] found the in-plane carbon-carbon bond length to decrease by only 0.2% in first stage graphite intercalation compounds with the electron acceptors H_2SO_4 and $SbCl_5$. Similarly, Murthy et al [133] reported a 0.4% decrease in the chemical repeat unit length of iodine-doped polyacetylene. In the case of such small changes observation of higher order (00ℓ) reflections would be required to make a precise determination of bond length changes.

Figure 5.4 shows the intensity diffracted along the equator for oriented PPV at different doping levels. At a weight uptake of 46% the reflections of the doped phase are apparent but the undoped reflections are still dominant. At a dopant uptake of 158% only the doped phase is apparent. Further, the d-spacings for both undoped and doped phases are independent of doping level. The change from the undoped to the doped structure is a discrete rather than continuous change. Thus, only one new conductive phase is observed. The discrete change in diffraction pattern indicates a "first-order" crystal-crystal transition. If the transition were "second-order" then the doped structure would gradually evolve and the d-spacings would be dependent upon doping level.

The coexistence of undoped and doped reflections demonstrates the heterogeneous nature of doping. Only at high dopant levels does the undoped phase vanish.

5.2.2 Other Group V Pentafluoride Dopants

Figure 5.5 shows the diffraction pattern obtained from PPV doped with SbF_5 to a weight uptake of 51%. The pattern is qualitatively similar to the AsF_5-doped pattern. Three new lateral spacings are observed at 1.039, 0.516, and 0.334 nm. The two largest spacings are slightly larger than those of AsF_5-doped PPV. The 0.334 nm lateral spacing is also seen in AsF_5-doped PPV. Also, a meridional reflection at 0.662 nm is observed corresponding to the chemical repeat distance of 0.658 nm. In addition to the meridional reflection two others are seen on the $\ell = 1$ layer line. As with AsF_5 doping, the doped phase retains the high degree of molecular orientation initially present in the undoped film.

These results indicate that the crystal symmetry of the SbF_5-doped complex is the same as AsF_5-doped PPV. The difference between these two crystals lies in their lateral spacings. This can be understood by considering the dimensions of the dopant anions. Both the hexafluoro-arsenate and -antimonate anions have octahedral symmetry. The As-F and Sb-F bond lengths in these compounds are 0.180 [134] and 0.188 nm [135] respectively (see Figure 5.6). Using the value of 0.147 nm for the van der Waals radius of fluorine, maximum F-M-F distances of 0.654 and 0.670 nm are calculated for the arsenate and antimonate. Thus, as the dopant species becomes incorporated into the polymer lattice the expansion due to the hexafluoro-antimonate anion is expected to be slightly greater than that due to the hexafluoro-arsenate anion.

Another similarity between the AsF_5- and SbF_5-doped patterns is the appearance of a powder diffraction pattern superposed on the polymer fiber

95

diffraction pattern. As with AsF_5 doping, dopant oxides were initially suspected (see Chapter 4). Also, the side-product of this doping reaction is SbF_3. This fluoride is not volatile at the experimental conditions (see Table 3.1) and is expected to remain in the film. Table 5.2 lists the d-spacings for SbF_3, Sb_2O_3, and Sb_2O_5 as well as for the powder formed during SbF_5-doping. These three compounds cannot individually or in any combination account for the powder diffraction pattern in SbF_5-doped PPV. Thus, some compound other than the obvious possibilities is responsible for the powder pattern.

A new phase was not observed in PF_5-doped PPV. Recall from Chapter 4 that only low doping levels (< 5 wt%) were attainable with PF_5 (see Table 4.1). As such, an insufficient amount of the PPV film is converted to the conductive phase for observation using transmission diffraction geometries.

5.2.3 Electrochemical Doping

The electrochemical oxidation of PPV yields conductive films [42]. As PPV is electrochemically oxidized electrons are abstracted from the polymer backbone. The positive charge created is balanced by incorporation of a negatively charged counterion. This counterion diffuses from the electrolytic solution through the polymer matrix to the oxidation site. In this study the perchlorate (ClO_4^-) counterion was used.

Figure 5.7a shows the diffraction pattern after electrochemical oxidation using the ClO_4^- counterion. Here again the diffraction pattern is qualitatively similar to AsF_5-doped PPV. Three new lateral spacings at ≈ 1.0, 0.470, and 0.330 nm are observed. In this pattern the 1.0 nm reflection is weaker than in the AsF_5- or SbF_5-doped films. The d-spacing measurement for this weak reflection is made less certain by the low angle lateral streak. This streak is also apparent in AsF_5- and SbF_5-doped films. However, the strength of the 1.0 nm reflection in AsF_5- and SbF_5-

96

doped films makes its position more certain. The cause of this low angle streak will be discussed in a following section.

This pattern, like the AsF_5- and SbF_5-doped patterns has a 0.33 nm lateral spacing. Also a weak meridional reflection is observed on the $\ell = 1$ layer line. The d-spacing for this reflection is 0.658 nm and corresponds to the polymer repeat distance. The other reflections along the $\ell = 1$ layer line are very streaky. This prohibits accurate measurement of their d-spacings.

With the exception of the 0.330 nm spacing the lateral spacings in this conductive form of PPV are slightly less than those found in AsF_5- or SbF_5-doped PPV. This difference is attributed to the size of the ClO_4^- anion. The perchlorate anion has a tetrahedral geometry and a Cl-O bond length of 0.142 nm [137]. Using this value and a van der Waals radius of 0.135 nm for oxygen a maximum anion size of 0.415 nm is calculated. This is substantially less than either the AsF_6^- or SbF_6^- diameters.

The electrochemical oxidation of PPV is reversible. Once doped the film can be discharged to its neutral form [42]. Figure 5.7b shows the diffraction pattern of the discharged film. The original structure of the undoped PPV is regained. The degree of azimuthal arcing is slightly increased indicating some orientational disorder arising during the charge-discharge cycle. Also, the crystallite size has diminished. Figure 5.8 shows the diffracted intensity along the equator for PPV films before and after electrochemical oxidation and after discharging. The decreased crystallite size after discharging is evident by an increased breadth of the reflections (compare curves a and c). Before oxidation the (210) reflection has an estimated full width at half maximum (FWHM) of 2.0°. After doping and discharging the breadth of

reflection increases to 2.8°. According to the Scherrer equation the crystallite size is calculated as

$$L_{hk\ell} = 0.9\lambda/(\beta_o cos\Theta) \tag{5.1}$$

where λ is the x-ray wavelength, Θ is the diffraction angle, and β_o is the FWHM in radians [131]. It is important to note that instrumental broadening and paracrystalline disorder also contribute to the FWHM. The total FWHM is expressed as

$$\beta_{total} = \sqrt{(\beta^2_{crystallite} + \beta^2_{paracrystal} + \beta^2_{instrument})} \tag{5.2}$$

when the line shape is Gaussian [138]. As such eqn(5.2) calculates a lower limit to the actual crystallite size when the reflection breadth is attributed only to crystallite size. With these limitations in mind the Scherrer analysis can be applied to estimate the effect of the electrochemical cycle on the PPV crystallite size. Thus, eqn(5.1) gives lateral crystallite dimensions of 4.0 and 2.9 nm before and after doping respectively. While the absolute values are only estimates they indicate a relative crystallite size decrease of 25%.

5.2.4 Sulfuric Acid Doping

As with other doping agents H_2SO_4 doping causes a change in PPV crystal structure. Figure 5.9 shows the diffraction pattern from H_2SO_4-doped PPV. This sample had been immersed for 2 hours in 98% H_2SO_4 (aq) and experienced a 130 wt% increase. In the doped polymer lateral spacings of 1.045, 0.522, and 0.330 nm are observed. Here also a 0.33 nm lateral spacing is observed. The position of the $\ell = 1$ layer line is consistent with the 0.658 nm polymer repeat length. However, the $\ell = 1$ meridional reflection is extinguished in this complex. In this regard it is different from the previous patterns.

The chemistry in H_2SO_4 doping is less well understood than in group V pentafluoride or electrochemical doping. Initial studies on H_2SO_4-doped polyacetylene proposed $[H_3O^+HSO_4^-]$ as the doping species [139]. Here the H_3O^+ ion

was presumed to interact in some fashion with the electronic states of the polymer to create charge carriers. A recent study by Han and Elsenbaumer has found the protonic acid doping of poly(2,5-dimethoxy-p-phenylene vinylene) to be accompanied by a strong electron spin resonance (ESR) signal [140]. From this result the formation of a polaron electronic structure was inferred. The mechanism proposed to account for this change involved direct protonation of the polymer accompanied by incorporation of the conjugate base to maintain charge neutrality. According to this mechanism the protonated sulfate anion (HSO_4^-) would be the counterion incorporated into the lattice in H_2SO_4-doped PPV. Using 0.166 nm as the S-O bond length and a 0.135 nm van der Waals radius for oxygen the maximum diameter of a tetrahedral sulfate anion is calculated to be 0.451 nm. Here the proton is neglected. This anion size is less than either AsF_6^- or SbF_6^-. However, the H_2SO_4-PPV complex has the largest lateral spacings. With regard to anion size only it seems likely that the chemical structure of the complex is not simply (H-PPV^+)(HSO_4^-). Rather, the crystal structure may be more consistent with [$H_3O^+HSO_4^-$] as the active dopant anion. In either case further analytical work is required to identify the H_2SO_4-PPV chemisty.

5.2.5 Crystal Model of the Conducting Phase

All four of the conductive complexes discussed in the preceding sections can be indexed to an orthorhombic unit cell. Two periodicities are observed for the lateral spacings. The first two reflections near 1.0 an 0.5 nm scale similarly with the size of the dopant and are thus clearly related. Further, the 0.5 nm d-spacing is essentially half the 1.0 nm spacing in all complexes. As such the 1.0 and 0.5 nm spacings are considered to be first and second order crystallographic spacings respectively. The lateral spacing at 0.33 nm is common to all complexes. Thus, it is independent of the 1.0 and 0.55 nm reflections. In light of these features the 1.0 nm

reflection is assigned as the a lattice parameter and the 0.33 nm reflection as the second order of the b lattice parameter. The 0.5 nm spacing was used to determine the value of a. This was done because of the increased precision generally allowed in the measurement of higher order reflections and also because the 1.0 reflection lies along a low angle streak making measurement of its position somewhat less precise. The c lattice parameter is determined from the meridional reflection on the $\ell = 1$ layer line. The value of this parameter is taken as 0.658 nm for all complexes. The angle between all the lattice vectors is 90°.

Table 5.3 lists the lattice parameters for the four conductive complexes studied. Using these lattice parameters the positions of other reflections can be calculated using

$$(1/d_{hk\ell}) = \sqrt{(h/a)^2 + (k/b)^2 + (\ell/c)^2} \qquad (5.3)$$

It must be borne in mind that eqn(5.3) applies only for cubic, tetragonal, and orthorhombic lattices. Calculations for lattices of lower symmetry must explicitly include the factors $\cos\alpha$, $\cos\beta$, and $\cos\gamma$ [131]. In Table 5.4 the measured and calculated d-spacings are listed along with the assigned crystallographic indices. As already mentioned the (020) reflection has a common d-spacing for all complexes at 0.33 nm. Note also that the measured (011) d-spacing is independent of dopant type at 0.46 nm. This is as expected since only the a lattice parameter is sensitive to dopant type and only the b and c parameters contribute to this spacing. All reflections for which $h \neq 0$ vary with dopant. As can be seen from Table 5.4 orthorhombic symmetry with the lattice parameters of Table 5.3 closely describe the crystalline unit cell of the doped complexes.

Given a unit cell for the conductive phase, the next question to be addressed is that of the spatial arrangement of the PPV chain and dopant anion within the unit cell. Recall that the a lattice parameter varies with dopant type while the b lattice parameter was constant at 0.33 nm for all complexes. Thus the dopant must be

preferentially incorporated along the [100] direction. By similar reasoning the 0.33 nm d-spacing is characteristic of the lateral packing of polymer chains in the [010] direction.

The 0.33 nm lateral spacing is characteristic of the closest approach of two planar aromatic molecules (recall the discussion of charge transfer complexes in Chapter 2). For example, the graphite interlayer spacing is 0.335 nm [84]. In radical-cation salts aromatic molecules typically stack in planar arrays having interlayer spacings of 0.32-0.34 nm [89-91]. Also, quaterphenyl, a model compound for PPP, has been found to form such stacks with a spacing of 0.33 nm [91]. In light of the structural and chemical similarity of doped PPV and the above mentioned compounds it is reasonable to assign the 0.33 nm lateral spacing to an intermolecular distance in stacks of planar PPV chains. In such a stack no free volume would be available for occupation by dopant. Thus, the dopant molecules must occupy an interstack volume. Figure 5.10 shows one structural model of doped PPV based on these observations. It is clear from this model that the [100] direction would experience preferential expansion during doping due to incorporation of the dopant anions. Further, the amount of expansion in this direction should be correlated with dopant size. This effect is experimentally observed with the larger anions yielding the highest values of a. A similar model was proposed by Pradere and Boudet for AsF_5-doped PPP [78].

In addition to being consistent with the observed d-spacings, this structural model also accounts for the significant transverse electrical conductivity of doped PPV. In this arrangement extensive π-orbital overlap exists between neighboring chains. This presents a lateral pathway for electron transport. Further, the physical conversion from the undoped to the doped crystal structure is easily envisioned (see Figure 5.9). The structural change only requires a rotation of chains about the c axis and an expansion in the [100] direction of the undoped crystal. In this conversion the

101

expansion occurs between the (100) planes of undoped PPV. Recall that these planes possess good axial registration between neighboring chains. Axial paracrystalline disorder exists between the (100) planes. The stronger interchain correlation in the (100) plane may explain why this plane remains intact with dopant incorporation occurring between these planes.

One other feature of the diffraction patterns should be mentioned. In all of the doped patterns a low angle streak is apparent. Streaks of this type typically arise when using β-filtered x-rays for diffraction since the filter is not totally effective in eliminating the white radiation (see ref. [131]). In fact, weak streaks can be also seen in the undoped pattern. However, the strength of the lateral streaks in the doped patterns is quite high. Further, no longitudinal streak extending in the direction of the (001) reflection is observed. This suggests that the lateral streak may be due to lateral packing disorder. If this packing disorder existed along **a** then the (200) reflection should also show a streaky character. This is not observed. In this case it is more reasonable to expect any lateral disorder to occur along **b**. Thus, the disorder is likely to be contained within the dopant plane.

While the above model is consistent with the diffraction patterns a classical crystal structure analysis is required to quantitatively confirm the spatial arrangement of polymer and dopant anion within the unit cell. Typically, crystal structure analysis is performed by comparison of calculated and observed diffracted intensities [131]. However, this type of analysis requires many reflections since a large number of atomic positions must be specified. This presents a difficulty in the crystal structure analysis of doped PPV since the number of reflections is small. Nonetheless, calculations were performed to predict the equatorial diffracted intensities. As in the study of undoped PPV the bond lengths and angles have been taken as equal to those in the model compound, stilbene [141] (see Figure 5.11). For the purpose of crystal

structure evaluation only the AsF_5-doped PPV structure will be considered. The geometry of the hexafluoro-arsenate anion is as discussed in section 5.2.1.

The atomic coordinates of the two PPV repeats in the unit cell are given in Table 5.5. Because of the low scattering power (ie., low electron density) of hydrogen only the carbon atoms of the polymer were considered. The atomic coordinates of the dopant anions are given in Table 5.6. It must be noted that at least one anion is required if the unit cell description is to be maintained. Choosing less than one anion would violate the unit cell determined in the previous section since a larger volume of the crystal would be required to describe the elemental repeat structure of the lattice.

Figure 5.12 shows the diffracted intensity calculated when the unit cell contains one dopant anion and also the experimentally observed intensity. The anion lies in the plane of a PPV molecule and is associated with the phenyl ring as shown in Figure 5.13. In both the calculated and observed diffraction the dominant reflections are the (100), (200), and (020). However, the calculation overpredicts the intensity of the (100) reflection. The calculated strength of the (100) reflection arises from the electron density difference between the PPV stack and the dopant plane. Each PPV stack contains 2 repeat units having 51 electrons for a total of 102. The dopant plane contains one anion having 87 electrons. If the dopant plane and PPV stack contained equivalent electron densities then the (100) intensity would be extinguished. The experimental result indicates a fluctuation toward higher electron densities in the dopant plane.

In Figure 5.14 the diffracted intensity from a crystal containing two anions per unit cell is shown. Here 174 electrons reside in the dopant plane. The agreement of this model with the observed diffraction is poor. Strong (010) and (110) reflections are predicted but not experimentally observed.

Similar calculations with fractional inclusion of a dopant ion (ie., a fractional value less than 1.0) were also performed. This only led to increased values of the (100) intensity and poorer agreement with experiment.

The calculated and measured densities can also be compared. The AsF_5-doped unit cell has a volume of 0.439 nm^3. There are 2 PPV chains per unit cell and each has a mass of 102 amu. The AsF_6^- anion has a mass of 189 amu. Thus, the calculated densities for 1 and 2 anions per unit cell are 1.48 and 2.20 g/cm^3 respectively. Table 5.5 lists the measured density for various AsF_5 doping levels. The undoped sample density is 1.22 g/cm^3. This compares well to a previous measurement of 1.24 g/cm^3 and is somewhat less than the theoretical density of 1.28 g/cm^3 calculated from the unit cell parameters [53]. The doped film density increases with increasing dopant uptake. The highest measured density range is 1.78 – 1.88 g/cm^3 for a sample doped to a 185 wt% uptake. This value is intermediate to the calculated densities for 1 and 2 anions per unit cell. However, as shown by the structure factor calculations the unit cell containing 2 anions per unit cell is unreasonable. It should be noted that structure evaluation by density measurements is complicated by the reactivity of the doped polymer. In particular, the results of Chapter 4 have shown that arsenic oxides are formed during doping. These oxide densities are high; As_2O_5 has a density of 4.32 g/cm^3. Thus, these impurities will serve to increase the measured density over the actual density of the PPV/AsF_6^- complex.

In addition to complications presented by chemical side reactions others associated with the heterogeneous nature of doping are also present. The analytical results of Chapter 4 suggest an AsF_6^-/$C_8H_6^{\delta+}$ ratio of 1/3 -1/4. However, the crystalline unit cell must accomodate at least one dopant anion giving a ratio of 1/2 since there are 2 PPV repeats per unit cell. Diffraction results pertain to relatively well formed regions of long range order. Thus, the stoichiometry estimated from

diffraction is of these well formed regions. Lower estimates of the $AsF_6^-/C_8H_6^{\delta+}$ ratio by bulk or surface analytical techniques may be attributable to a lower doping level in the grain boundary regions between crystallites.

In summary, the x-ray diffraction experiments have shown a closely related family of structures possessing orthorhombic symmetry to exist after doping with AsF_5, SbF_5, H_2SO_4, or ClO_4^-. All of these patterns share a 0.33 nm lateral spacing which suggests a stacking of planar PPV chains in the doped complexes. The other lateral spacings increase with increasing dopant size. Thus, a model is proposed in which stacks of PPV chains are separated by a dopant plane. The crystal structure calculations show a unit cell containing two PPV repeats and one dopant anion to be most descriptive of the structural arrangement of the polymer and dopant. Even in this model, though, some discrepancy exists between the measured and calculated (100) intensity.

Table 5.1
Crystallographic d-spacings (nanometers) of isotropic and oriented PPV ($L/L_o = 10$) from x-ray diffraction.

h$k\ell$	calculated[*]	oriented	isotropic
110	0.427	0.428	0.428
200	0.395	0.402	0.401
210	0.312	0.312	0.314
310	0.234	0.238	0.235
220	0.214	0.213	–
001	0.552	0.546	0.568
0$\bar{2}$1	0.301	0.290	–
012	0.329	0.317	–
$\ell = 3$	0.219	0.206	0.213

[*]d-spacings calculated from monoclinic unit cell:

$a = 0.709$ nm $\alpha = 123°$
$b = 0.605$ nm
$c = 0.658$ nm

Table 5.2
d-Spacings of powder diffraction pattern formed upon SbF_5 doping of PPV and various inorganic antimony compounds.

PPV/SbF$_5$	SbF$_3$	Sb$_2$O$_3$	Sb$_2$O$_5$
–	–	0.652 (s)	–
0.513 (s)	–	–	–
0.501 (s)	–	–	–
0.474 (m)	–	0.469 (w)	–
–	–	–	0.447 (m)
0.409 (m)	–	–	–
0.382 (m)	–	–	–
–	0.371 (m)	–	–
–	0.357 (s)	–	–
0.340 (m)	–	0.353 (w)	–
–	–	–	0.347 (s)
0.307 (m)	–	0.324 (vs)	–
–	–	0.316 (m)	0.311 (vs)
0.288 (m)	–	–	0.297 (s)
–	–	0.281 (s)	0.274 (w)
0.253 (m)	0.261 (m)	0.257 (m)	0.267 (s)
–	0.247 (m)	–	0.250 (w)
–	–	–	0.242 (m)
–	0.222 (m)	0.229 (w)	0.225 (w)
–	0.213 (m)	0.216 (w)	–
–	0.209 (m)	–	–
–	0.204 (m)	0.198 (s)	–

Table 5.3.
Unit cell parameters for doped PPV (nanometers).
All unit cells exhibit orthorhombic symmetry.

| | \underline{Dopant} | | | |
	$\underline{AsF_5}$	$\underline{SbF_5}$	$\underline{H_2SO_4}$	$\underline{ClO_4}^{-*}$
a	1.010	1.032	1.045	0.940
b	0.660	0.660	0.660	0.660
c	0.658	0.658	0.658	0.658

*Counterion used in electrochemical oxidation.

Table 5.4.
Measured and calculated d-spacings (nanometers) for
doped phases.

Crystallo-graphic index	AsF_5		SbF_5		H_2SO_4		ClO_4^-	
	d_{meas}	d_{calc}	d_{meas}	d_{calc}	d_{meas}	d_{calc}	d_{meas}	d_{calc}
(100)	1.032	1.010	1.039	1.032	1.045	1.045		
(200)	0.504	0.505	0.516	0.516	0.522	0.522	1.0	0.940
(020)	0.331	0.330	0.334	0.330	0.330	0.330	0.470	0.470
							0.330	0.330
(001)	0.658	0.658	0.662	0.658	N.O.	0.658	0.658	0.658
(101)	0.530	0.551	0.542	0.555	0.557	0.557	S	0.539
(011)	0.454	0.466	0.460	0.466	0.462	0.466	S	0.466
(211)	0.366	0.342	N.O.	0.346	0.348	0.348	S	0.331
(102)	0.309	0.313						
(012)	0.294	0.294						
(212)	0.265	0.254						
(302)	0.239	0.235						

S indicates a reflection whose precise position is indeterminable due to streaking.

N.O. not observed.

Table 5.5
Atomic coordinates of PPV repeats in AsF_5-doped unit cell. The origin is set at the center of the chain I aromatic ring.

Atom	x (nm)	y (nm)	z (nm)
Chain I			
C_1	0.0452	0.0000	-0.2794
C_2	0.0222	0.0000	-0.1372
C_3	-0.1078	0.0000	-0.0878
C_4	0.1300	0.0000	-0.0494
C_5	-0.1300	0.0000	0.0494
C_6	0.1078	0.0000	0.0878
C_7	-0.0222	0.0000	0.1372
C_8	-0.0452	0.0000	0.2794
Chain II			
C_{17}	0.0452	0.3300	-0.2794
C_{18}	0.0222	0.3300	-0.1372
C_{19}	-0.1078	0.3300	-0.0878
C_{20}	0.1300	0.3300	-0.0494
C_{21}	-0.1300	0.3300	0.0494
C_{22}	0.1078	0.3300	0.0878
C_{23}	-0.0222	0.3300	0.1372
C_{24}	-0.0452	0.3300	0.2794

For chain identification see Figure 5.9.

Table 5.6

Atomic coordinates of hexafluoro-arsenate anions in AsF_5-doped PPV. Note that only Anion I is used in the single anion model.

Atom	x (nm)	y (nm)	z (nm)
Anion I			
As_1	0.5050	0.0000	0.0000
F_1	0.6316	0.1266	0.0000
F_2	0.3784	-0.1266	0.0000
F_3	0.3784	0.1266	0.0000
F_4	0.6316	-0.1266	0.0000
F_5	0.5050	0.0000	0.1790
F_6	0.5050	0.0000	-0.1790
Anion II			
As_2	0.5050	0.0000	0.6580
F_7	0.6316	0.1266	0.6580
F_8	0.3784	-0.1266	0.6580
F_9	0.3784	0.1266	0.6580
F_{10}	0.6316	-0.1266	0.6580
F_{11}	0.5050	0.0000	0.8370
F_{12}	0.5050	0.0000	0.4790

Table 5.7

Mass densities of undoped and AsF_5-doped PPV as measured by flotation.

Doping Time (hrs)	Vapor Pressure (mmHg)	Weight Increase (%)	Limiting Conductivity $(\Omega\ cm)^{-1}$	Density Range (g/cm^3)
0	–	–	–	1.22[A]
264	305	74	265	1.49–1.58
91	289	–	6890	1.65–1.68
176	350	167	8000	1.58–1.71
95	289	–	12600	1.74–1.78
>24	305	185	4000	1.78–1.88

[A] measured in density gradient column. All others measured in mixed solvents (see section 3.2.1).
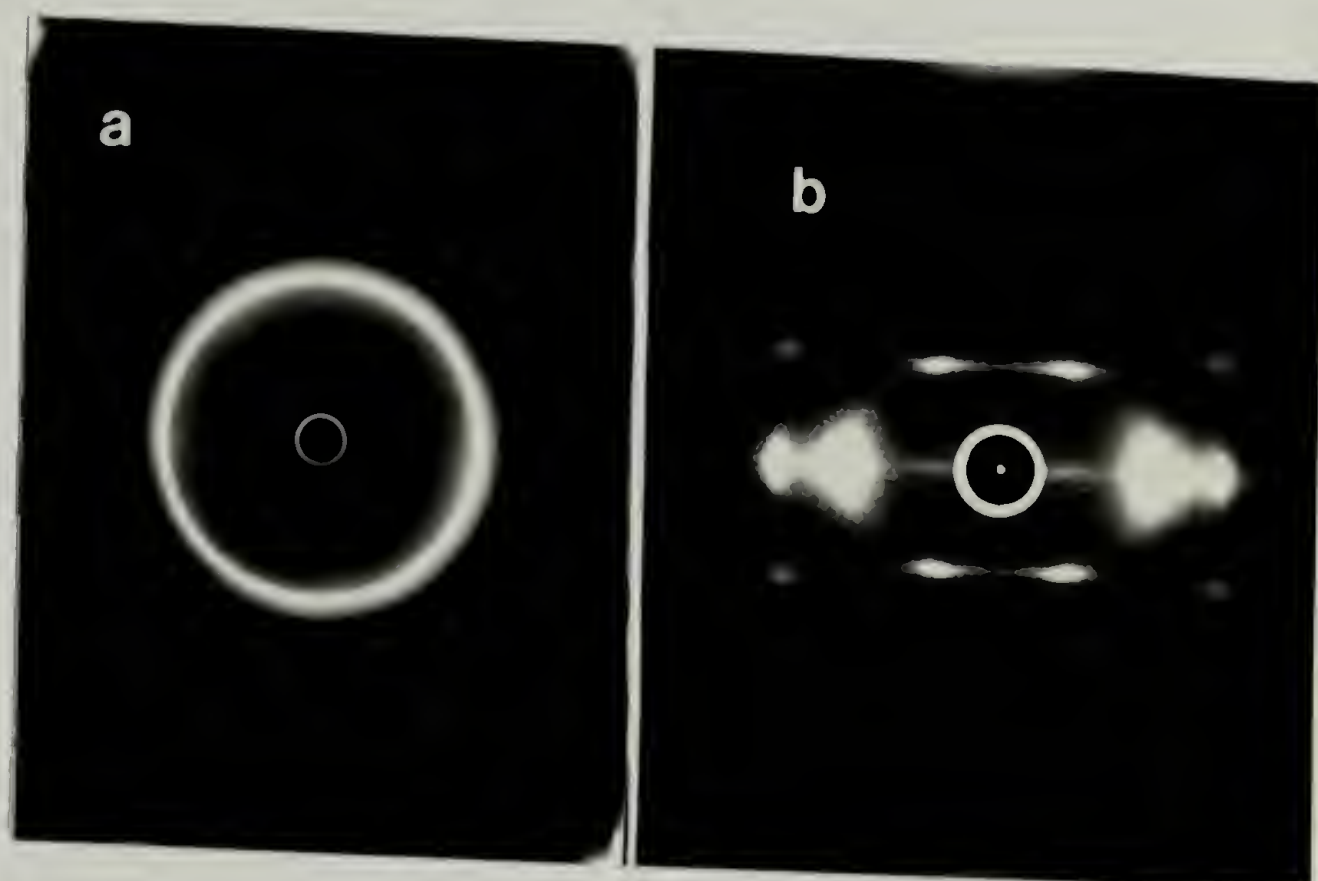
Figure 5.1   X-ray diffraction patterns of undoped PPV: a) isotropic film, b) oriented film ($L/L_o = 8.6$).
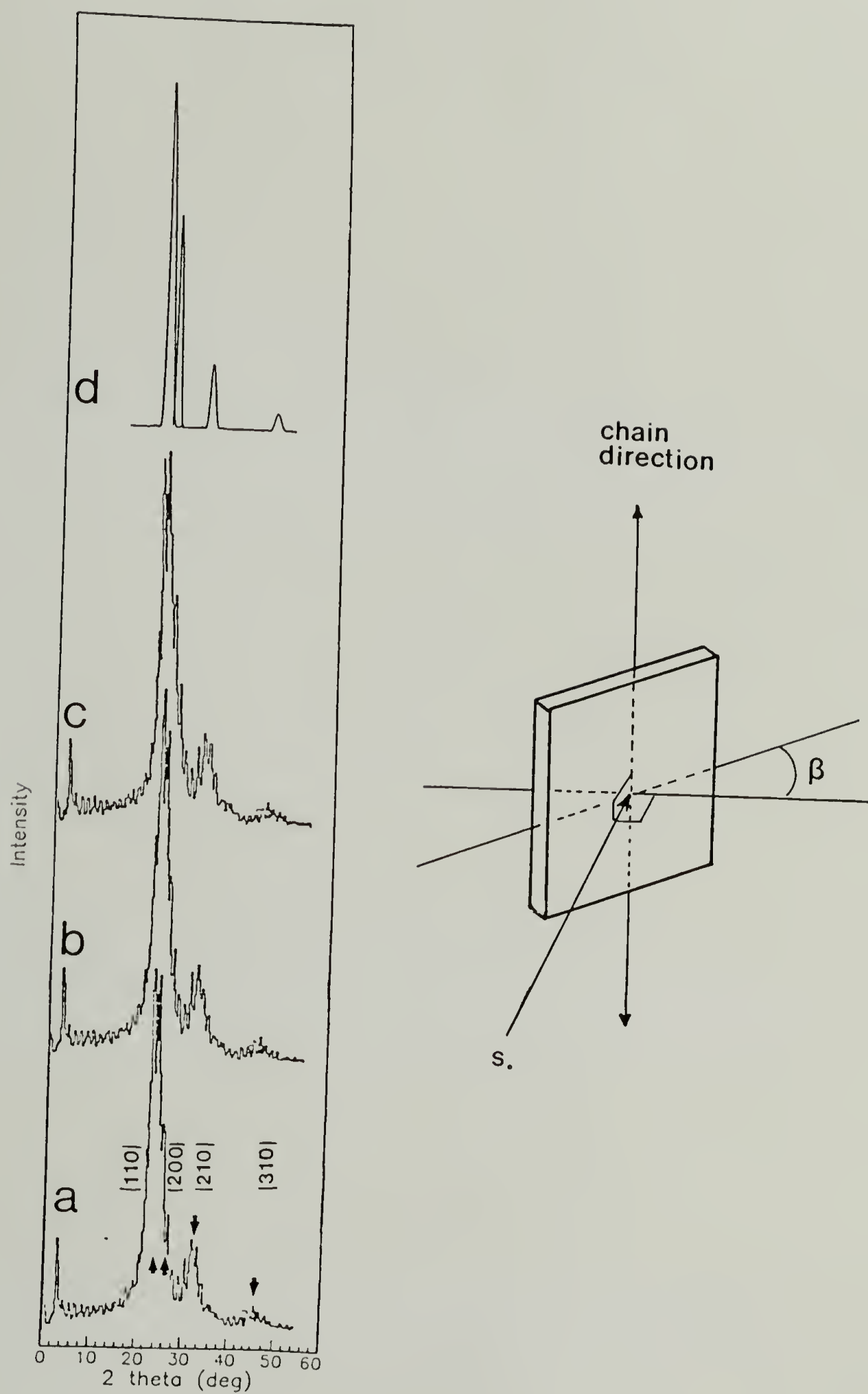
Figure 5.2   Equatorial diffracted intensity from oriented PPV film ($L/L_o = 10$) at different axial rotations: a) $\beta = 0°$, b) 45°, c) 90°, d) calculated intensity for a cylindrically symmetric sample.
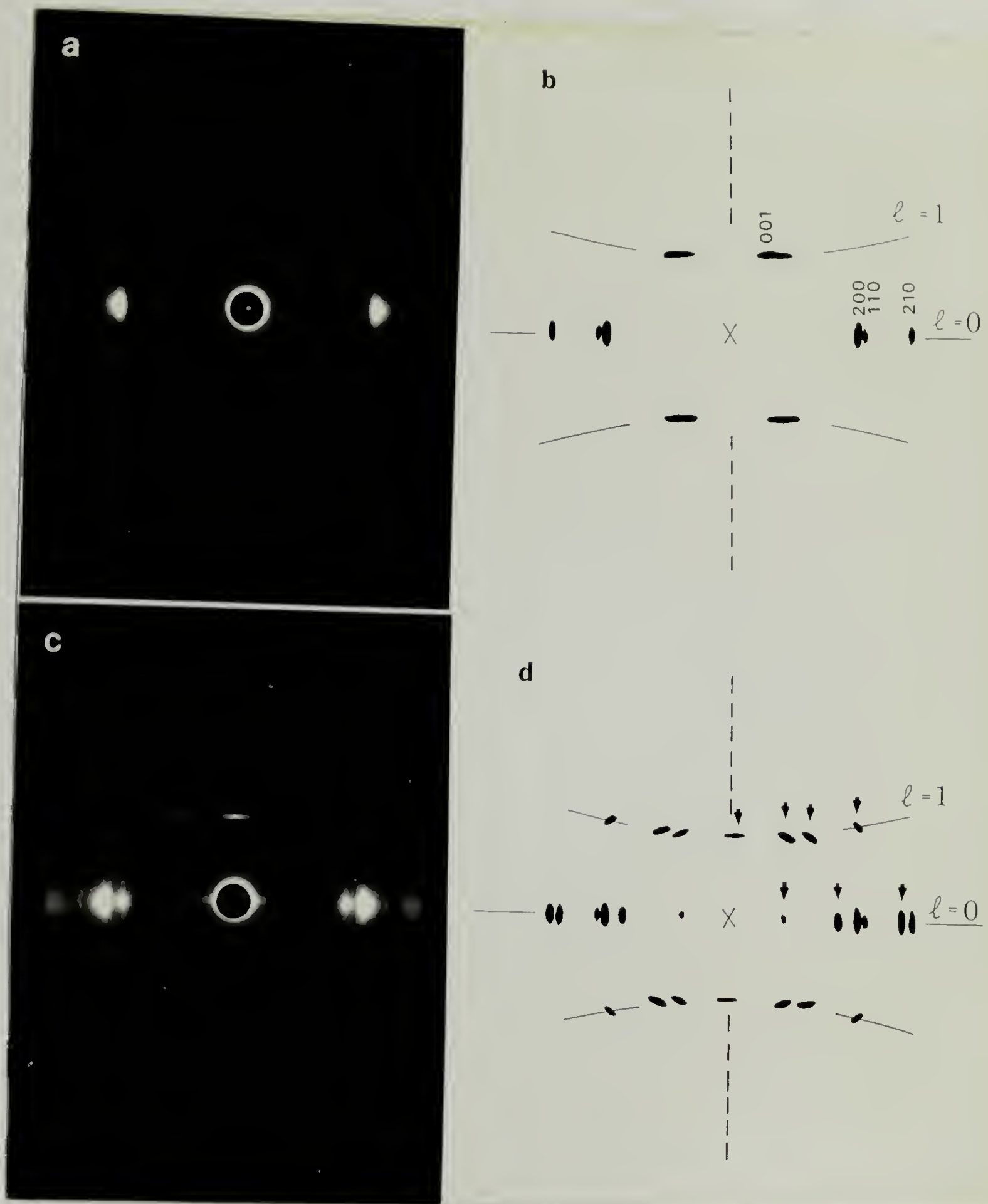
Figure 5.3   X-ray diffraction patterns of neutral and oxidized PPV ($L/L_o = 8.6$):
a) diffraction pattern of undoped PPV, b) Schematic representation of
the undoped pattern, c) diffraction pattern of AsF_5-doped PPV, d)
schematic representation of the doped pattern with the new reflections
indicated by arrows. The fiber axis is vertical.
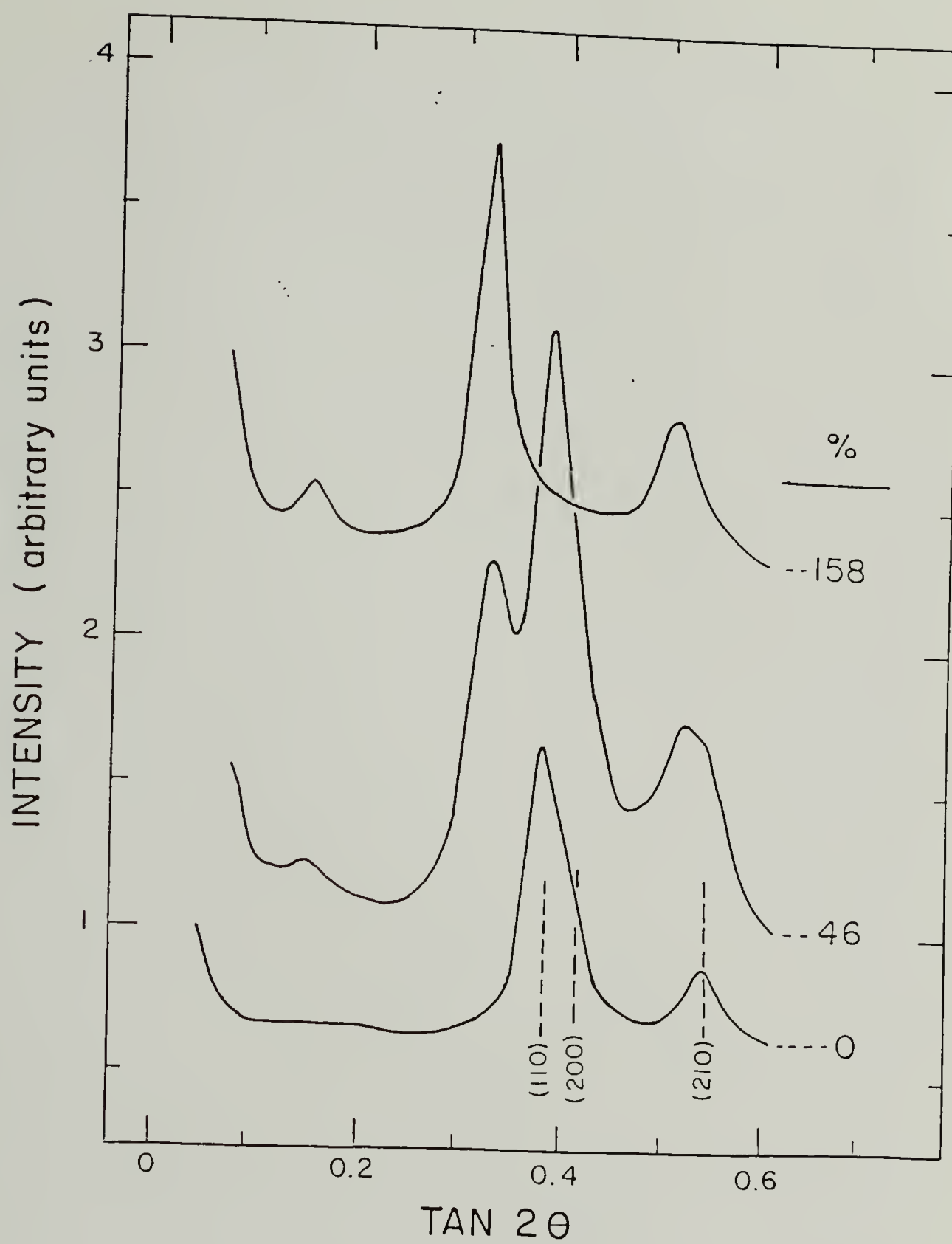
Figure 5.4   Equatorial diffracted intensities for different AsF$_5$-doping levels. The weight uptake is indicated.
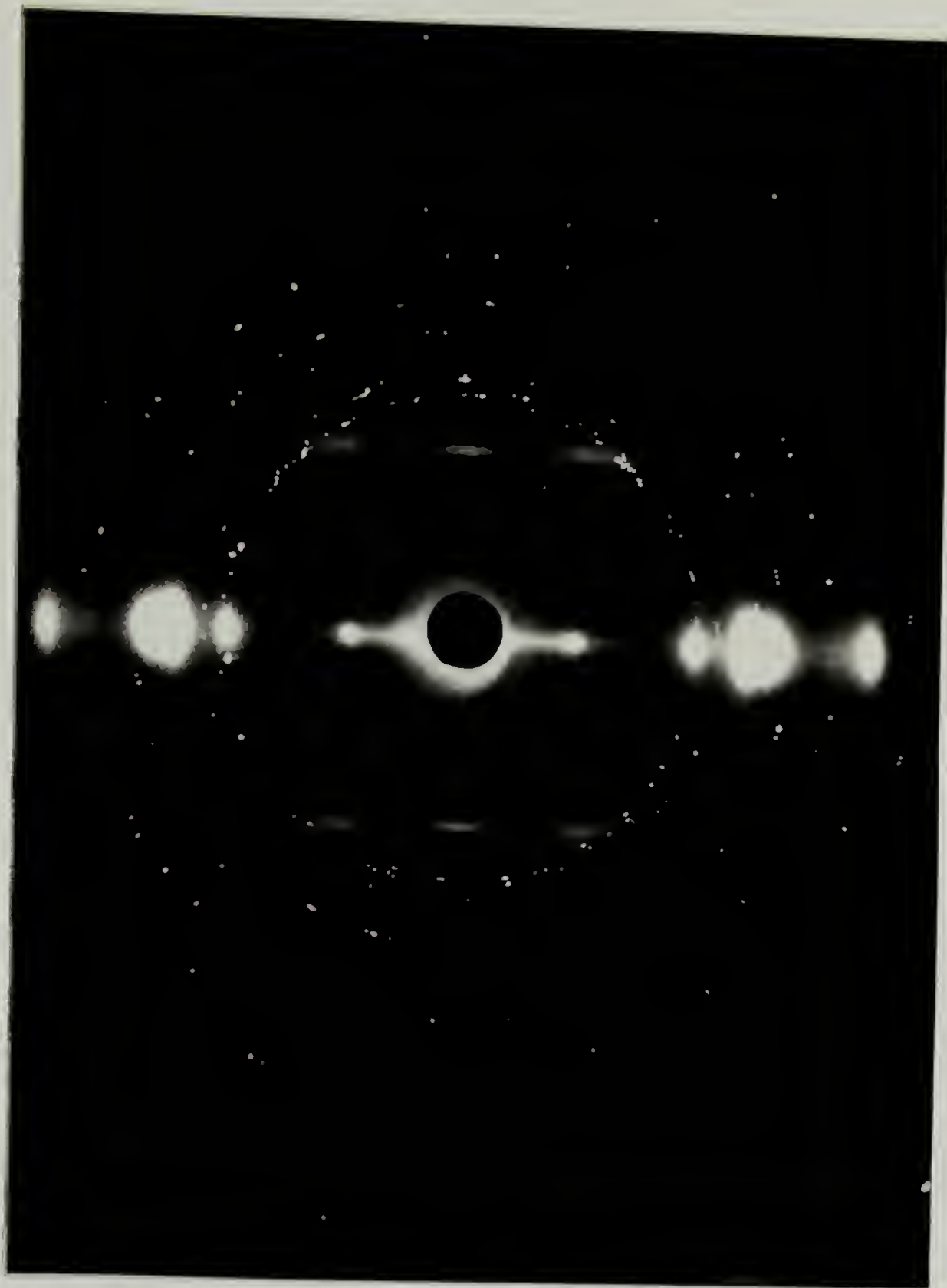
Figure 5.5   X-ray diffraction pattern of SbF_5-doped PPV ($L/L_o = 5$). The fiber axis is vertical.

AsF$_6^-$

SbF$_6^-$

ClO$_4^-$

SO$_4^=$
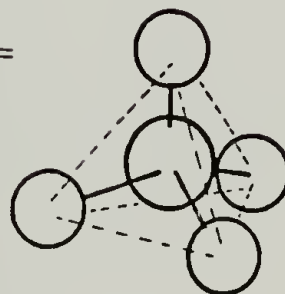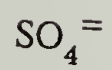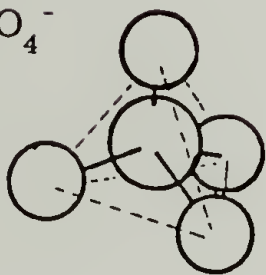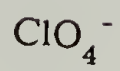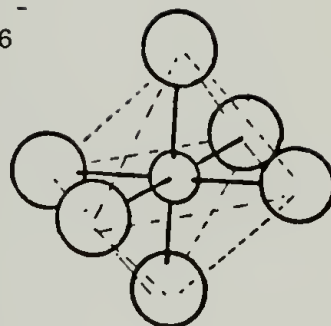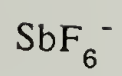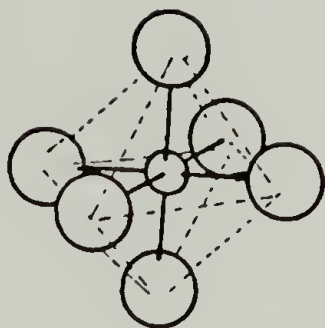
Figure 5.6   Molecular geometry of dopant anions.
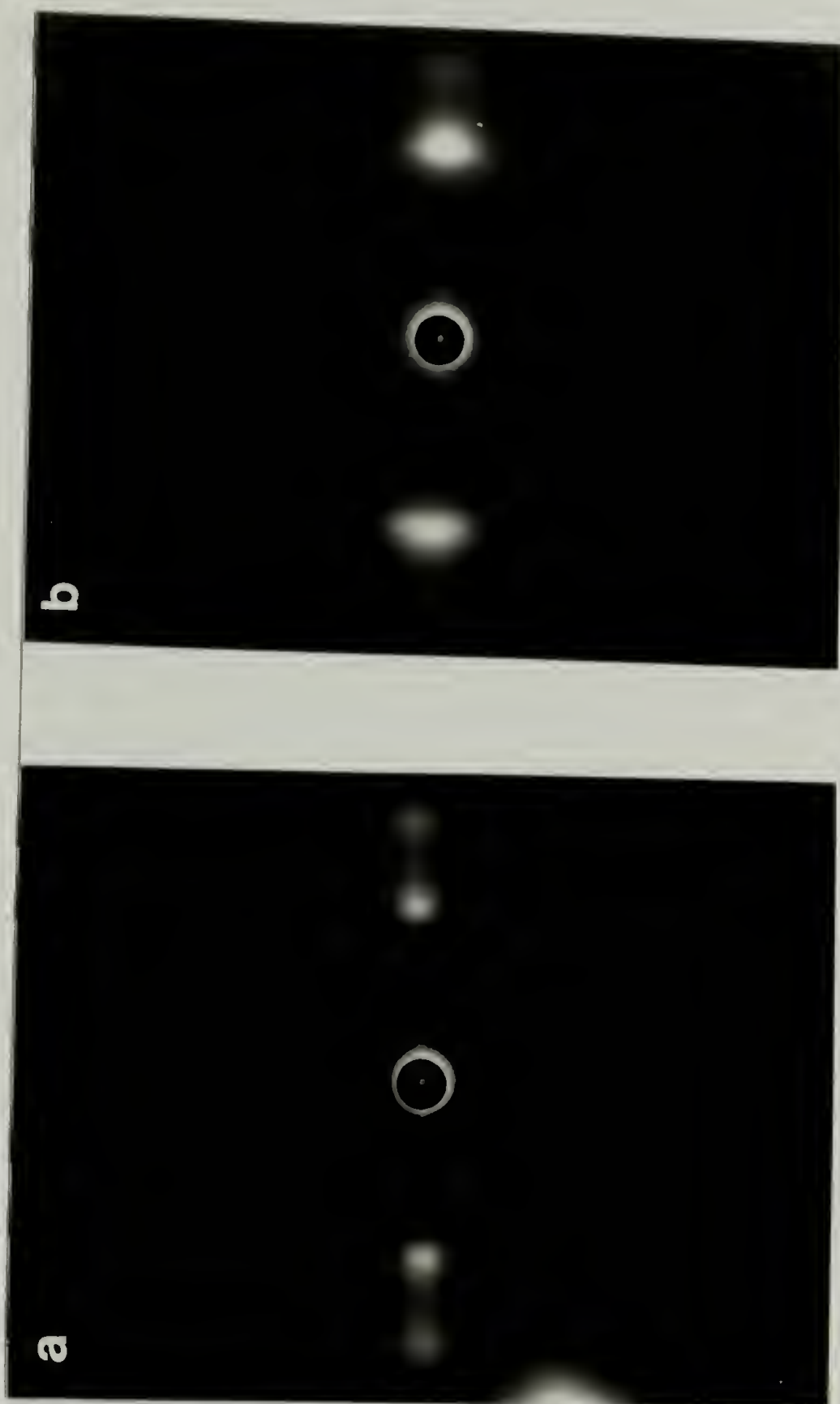
Figure 5.7   X-ray diffraction patterns of electrochemically prepared PPV (L/L_o = 6.5): a) oxidized using ClO_4^- as the counterion, b) neutral PPV after discharging doped film.
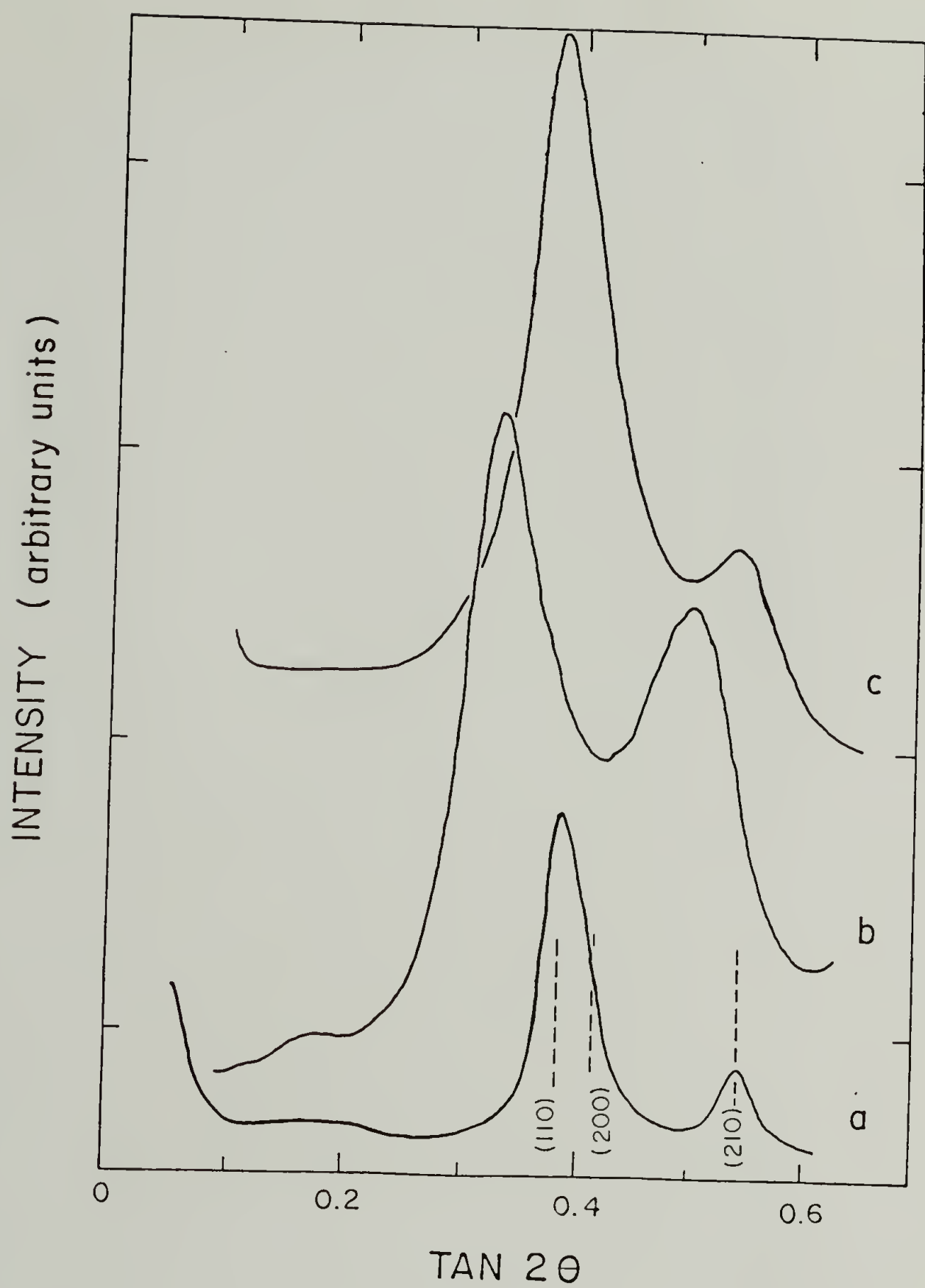
Figure 5.8   Densitometer scans of electrochemically doped PPV: a) neutral PPV before doping, b) electrochemically oxidized using the ClO_4^- counterion, c) neutral PPV after discharging.
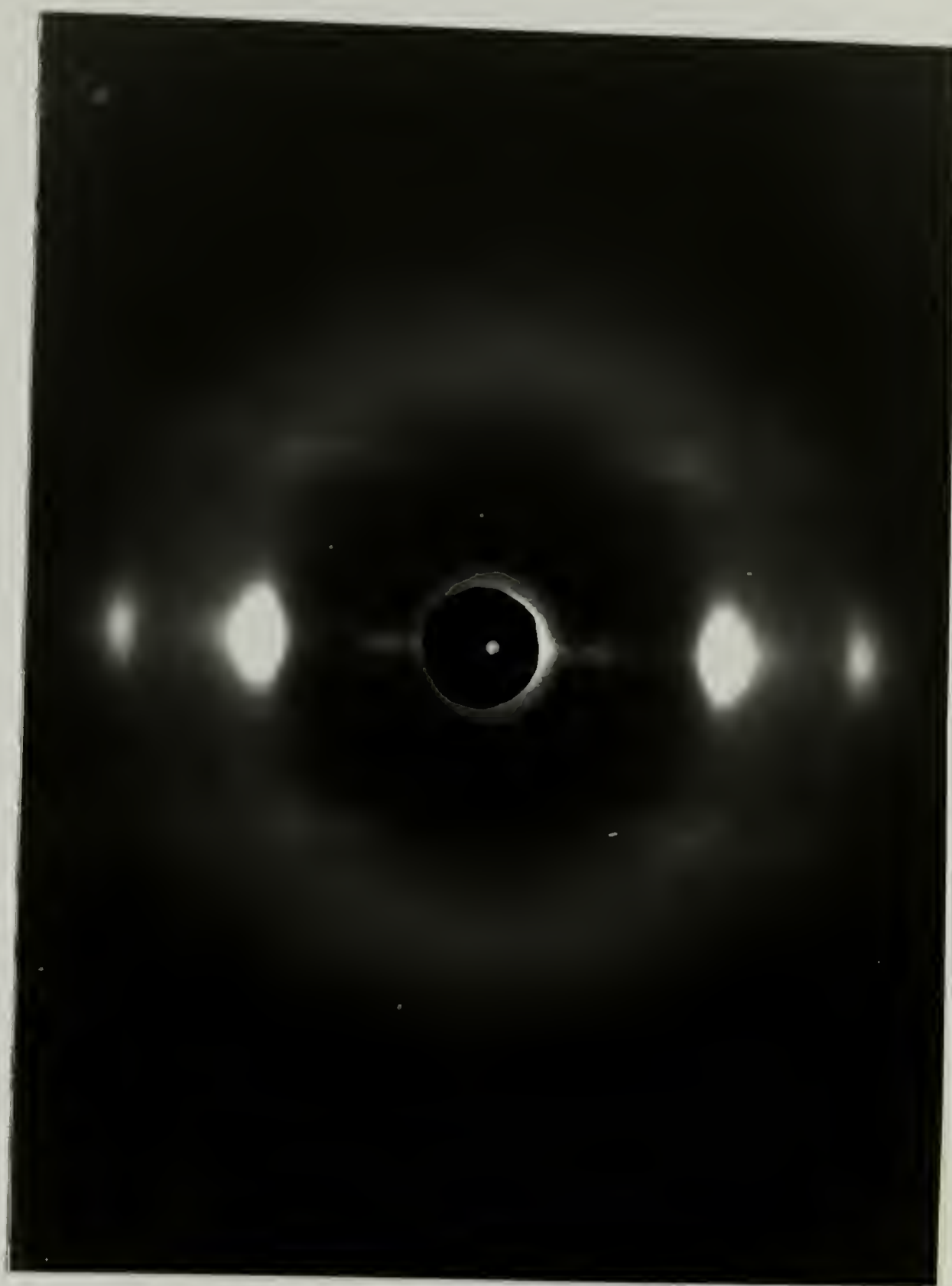
Figure 5.9   X-ray diffraction pattern of H_2SO_4-doped PPV (L/L$_o$ = 10). The
fiber axis is vertical.
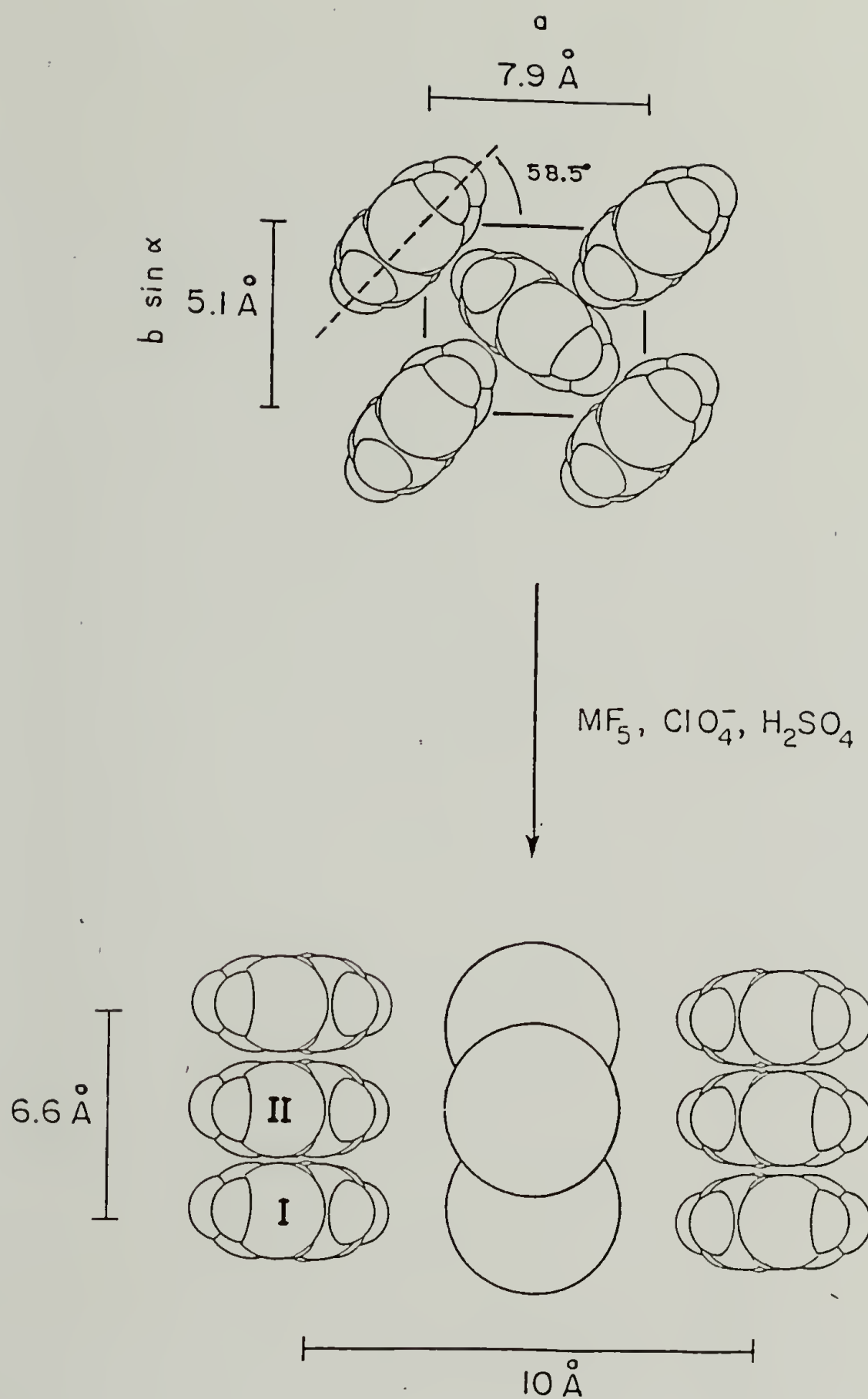
Figure 5.10   Schematic representation of doped PPV structural model. The
structure is projected along the chain axis.

C_1-C_2: 0.144 nm
C_2-C_3: 0.139 nm
C_8-C_9: 0.133 nm
C – H : 0.109 nm
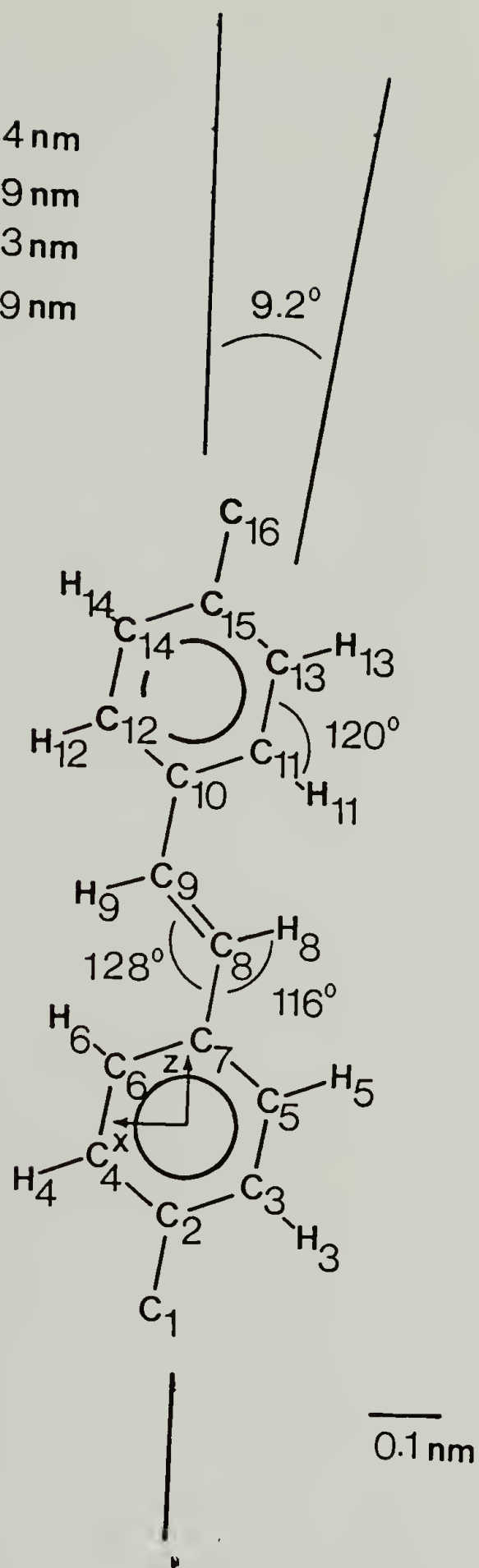
Figure 5.11   Molecular geometry of PPV repeat unit.

123
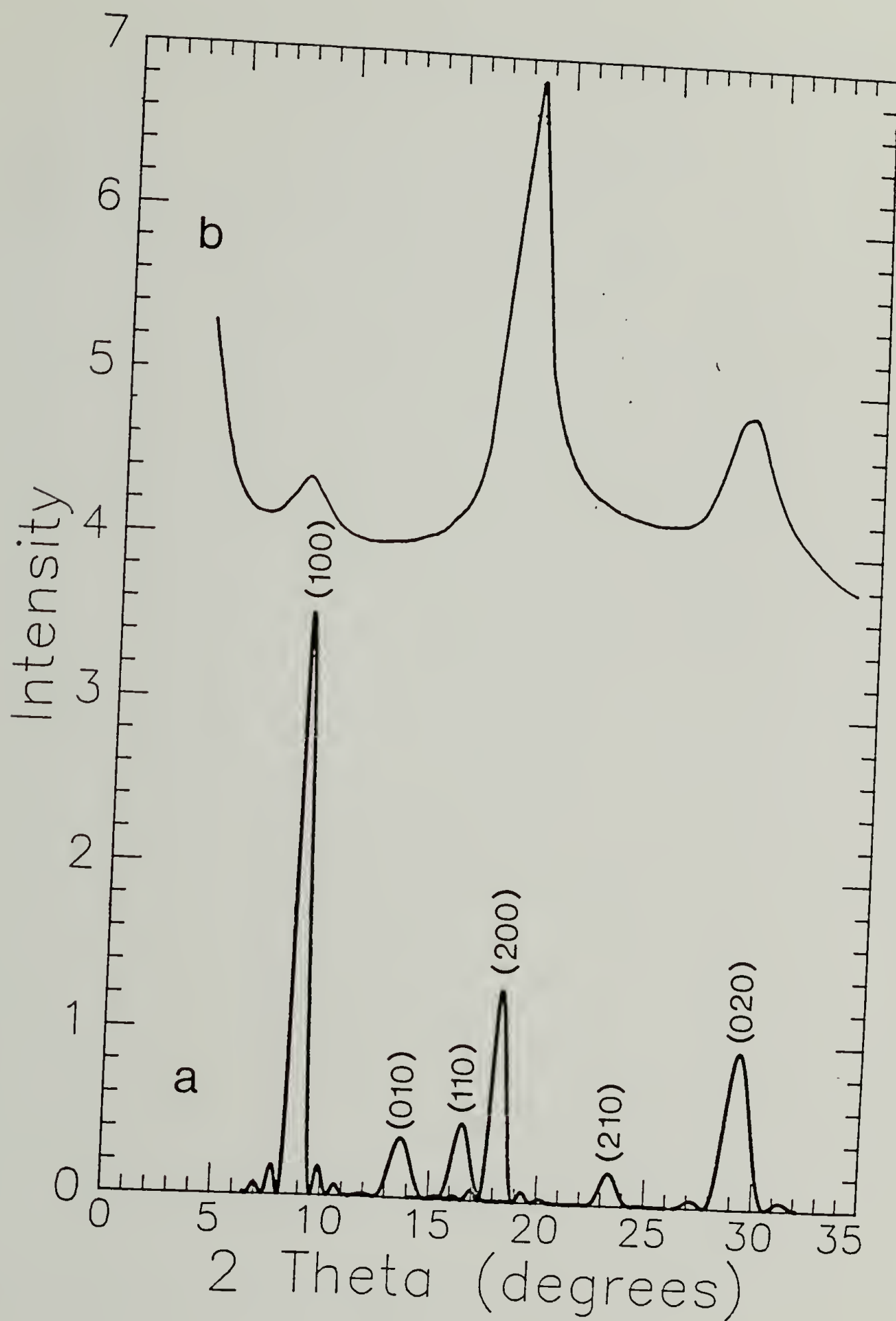
Figure 5.12   Equatorial diffracted intensity of AsF_5-doped PPV: a) intensities calculated based on a unit cell containing one dopant anion, b) experimentally observed diffraction.
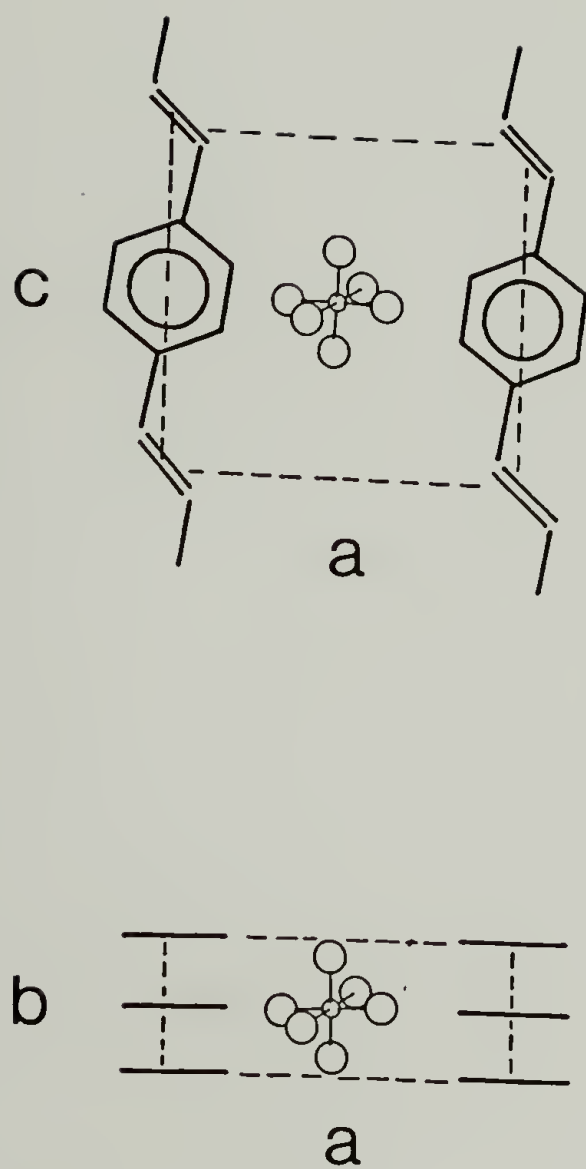
Figure 5.13   Geometry of AsF$_5$-doped PPV containing one anion per unit cell.
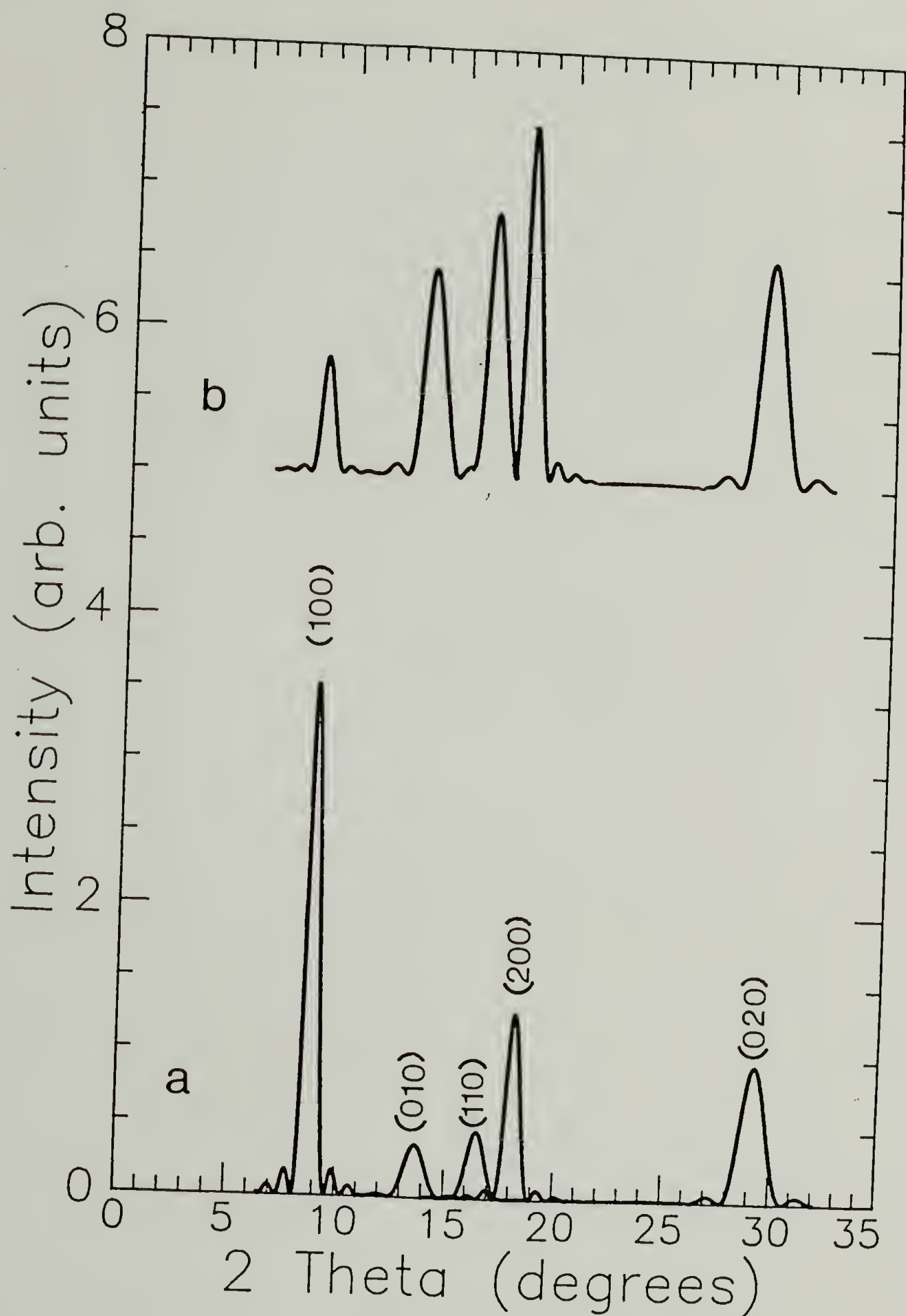
Figure 5.14   Equatorial diffracted intensity of AsF_5-doped PPV: a) intensities calculated based on a unit cell containing one dopant anion, b) intensities calculated base on two dopant anions per unit cell.

CHAPTER 6

CRYSTAL MORPHOLOGY IN UNDOPED AND DOPED PPV FILMS

Having gained some understanding of the crystal structure of the doped phase of PPV the next question one may address is that of crystal morphology. How large are the conductive, crystalline domains and what is their shape? To answer these questions a study employing electron microscopy was undertaken. The experimental results obtained for undoped and doped films are presented in this chapter.

6.1 Bulk Morphology

Oriented films of PPV show anisotropy of both mechanical [57] and electrical [15] properties. The tensile strength of PPV films drawn to $L/L_o = 5$ is 420 MPa in the direction of the molecular chain and 32 MPa in the transverse direction [57]. This mechanical anisotropy leads to an inherent tendency for oriented films to fibrillate parallel to the draw direction. Figures 6.1 and 6.2 show SEM micrographs of a section of fibrillated PPV. The draw direction is along the microfibrillar axis. In this micrograph it is evident that fibrillation along the draw direction and hence along the molecular direction prevails. The surface from which the microfibrils have been detached appears regular with long furrows at least 1 mm in length running along the chain direction. The microfibrils characteristically possess a ribbon–like morphology as can be seen from the twisted sections.

As shown in Chapter 5 the films are fiber symmetric. Thus, the fibrillated morphology does not result from a preferred planar orientation. The tendancy for oriented PPV films to fibrillate and the resulting morphology is attributed to the high degree of uniaxial molecular orientation. In such samples the mechanical strength lies primarily along the direction of the molecular chain backbone. In this arrangement

127

sample rupture is expected to occur along the orientation direction rather than in a transverse direction.

6.2 Crystal Morphology

A $g_{(110/200)}$ dark field TEM micrograph of oriented PPV ($L/L_o = 8$) is shown in Figure 6.3. The average dimension of the crystallites was determined by measuring 40-50 crystallites in a given micrograph. The average size of the diffracting regions shown in Figure 6.3 is 6.9 nm with a standard deviation of 3.1 nm. As observed here the aspect ratio of the crystallites is near 1.0. This image gives the impression that only short crystallites exist. Ordered fibers of other rigid rod polymers such as poly(p-phenylene benzobisthiazole) (PBZT) and poly(p-phenylene benzobisoxazole) (PBZO) also possess short crystallites of the order of 5-10 nm [142,143].

Although the diffracting regions appear equiaxed a single dark field image does not preclude the possibility of a structure involving long needle-like crystals with a tendency to twist about the crystallite axis. If the latter is the case then while a small section of the crystallite is meeting the Bragg condition and diffracting, neighboring segments along the crystallite would be twisted out of the Bragg condition and appear dark. To investigate whether this occurred in PPV, dark field images were taken before and after tilting the incident electron beam. This technique has been previously discussed by White and Thomas [109] and allows precise determination of tilt angles as small as 0.1°. If the crystals were needle-like in morphology then after tilting their diffracting intensity would translate along the draw direction as new segments of the twisted crystal came into the Bragg condition. Figures 6.4 and 6.5 show dark field images of PPV before and after a beam tilt of 0.26° about the chain axis. A relatively small tilt angle was chosen so that the majority of initially diffracting crystals would also be present in the second image.

In this way the crystallite locations are more easily correlated between the two images. While all crystallites are observed to undergo a change in diffracting intensity upon beam tilting only a small fraction of the total population comes into or goes out of the Bragg condition. Those regions labelled A in Figure 6.4 and 6.5 are observed both before and after tilting. However, crystallites labelled B appear after the tilt and those labelled C disappear. This is expected for small beam tilts as is illustrated in Figure 6.6. Here, the $g_{(110)}$ rocking curve is shown. The rocking curve represents the variation in observed scattered intensity as a crystal of thickness T is rotated through the Bragg angle. The curve in the figure was calculated using

$$I_{(110)} = [\sin^2(\pi T\omega d)]/(\pi\omega d)^2 \tag{6.1}$$

where d is the crystallographic spacing and ω is the angular deviation from the Bragg angle. A thickness of 7.5 nm was used for this calculation.

The orientations of crystallites A, B, and C are shown before and after tilting. In no case did the intensity of a single diffracting region translate along the draw direction as the beam was tilted. This result shows that a needle–like crystal morphology can be ruled out. Thus, the rigid character of the polymer chain does not manifest itself by forming extended crystals along the chain axis. Rather, the diffracting regions are equiaxed, with an average length of 7 nm.

A high resolution image of a thin PPV section ($L/L_o = 9.3$) is shown in Figure 6.7. Close inspection of Figure 6.7 shows lattice fringes running parallel to the film edge. From the optical diffraction pattern the spacing of the fringes is measured as 0.43 nm. This corresponds to the (110) crystallographic spacing in the PPV crystal. Hence, this micrograph allows direct observation of the molecular packing in the oriented crystals. The optical diffraction pattern also shows a weaker periodicity corresponding to the (001) reflection. Because of the monoclinic symmetry of the PPV unit cell this reflection appears off the meridian. The (001) fringes (d = 0.552 nm) while present are not obvious in the micrograph itself.

In Figure 6.8 the individual crystallites are outlined. The criterion for identification of an individual crystallite is that the fringes must be continuous both laterally and axially. Further, the fringes within one crystallite must have the same orientation. Thus, relatively large regions displaying fringes can be divided into separate grains. This is clearly seen by comparing crystallites 23 and 24 in Figure 6.8. These neighboring crystallites differ in orientation by 11°. The crystallites and their orientations are shown schematically in Figure 6.9. As can be seen they are highly aligned in a film with a draw ratio of 9.3. In Figure 6.10 a histogram representing the crystallite orientations is shown. Here the crystallite orientations have been measured with respect to the film edge. The average orientation angle is - 1° (clockwise being positive) but the individual orientations range from -9° to +6°. Using the orientation angles, ϕ, shown in Figure 9 for the 27 crystals observed, $<\cos^2\phi>$ can be calculated directly. Using this value the Hermans orientation function is calculated according to

$$f = (3<\cos^2\phi> - 1)/2 \qquad\qquad (6.2)$$

giving a value of 0.94. This is very close to the value of f = 0.95 measured by x-ray diffraction for PPV of L/L_o = 8.3 [32].

It is important to note that the maximum observed crystallite misorientation from the draw direction is only 9°. A recent study by Simpson et al [144] has employed ^2H broadline NMR to evaluate the molecular orientation in drawn PPV films. These investigators observed an orientation distribution which was well modelled by two superposed Gaussian distributions. Each of the two Gaussian profiles have essentially equal contribution to the total and have distribution widths ($\Delta\beta$) of 9.5° and 30°. NMR line shape simulations, though, cannot unequivocally determine whether each component of the simulation corresponds to a separate fraction of the material or simply results from a complex distribution of a single fraction. The direct HREM observations however suggest that the $\Delta\beta = 9.5°$

130

component can be associated with the well oriented crystallites. Also, because NMR probes ordered as well as disordered molecular chains, information regarding the fraction of well oriented crystallites can be inferred. Since in the NMR simulations the narrow distribution component constitutes 50% of the total it is reasonable to expect approximately half of the PPV repeat units to exist in well oriented crystallites. The remaining 50% of the repeat units might be supposed to exist in severely misoriented crystallites. Such crystallites however were not observed by HREM which images all diffracting (110) crystallites regardless of their c axis orientation. As already stated, for the crystallite population observed an angular breadth of misorientation of only 15° was seen. It is thus more likely that the broad distribution component corresponds to PPV chains in the disordered grain boundary regions.

From the lattice image the individual crystallites sizes can be readily measured. On the average the crystallites in Figure 6.7 are 5.6 nm in length and 4.4 nm in width with both the lateral and longitudinal dimensions having standard deviations of 0.9 nm. As can be seen from Figure 6.6 the individual crystallites are not isolated in all cases but may exist closely spaced in clusters. The latter range in size from 5 to 10 nm. In dark field imaging, clusters with crystallites misoriented by up to approximately ±5° would appear as a single diffracting region since an aperture of finite size was used. Indeed, the cluster sizes obtained from lattice images agree well with the size of the diffracting regions in the dark field images. It is important to note that these results indicate that diffracting regions observed in the dark field image are not necessarily individual crystallites but could correspond to clusters of neighboring crystallites having similar but not identical orientations.

The oriented films thus contain equiaxed oriented crystals connected by regions of disordered chains. The well ordered crystallites make up approximately 50% of the sample volume with the remaining material located in grain boundaries.

Because the disordered chains in the grain boundaries cannot be directly observed by dark field TEM their orientational state remains uncertain. However a truly amorphous phase is not expected because of the rigid character of the PPV chain. Rather the molecular chains in the grain boundary are likely to exist in a relatively disordered state with no long range periodicity. A high degree of connectivity between crystallites in the form of tie molecules is also required to be consistent with the good mechanical properties observed in PPV [57]. Further, preliminary neutron scattering results on isotropic polycrystalline films of PPV have indicated that a single chain traverses many crystallites [145]. Thus, oriented PPV can be thought of as a highly connected network of equiaxed crystallites. Figure 6.11 shows a schematic of this micellar morphology.

The morphological results presented up to this point have all been obtained from PPV thermally converted from the precursor at 250°C. Figure 6.12 shows the effect of annealing temperature on the crystallite size. Here, as before, the crystallite sizes have been measured from dark field TEM images. For annealing temperatures of 200°C or 250°C the crystallite size is in the range of 6.0 - 8.0 nm. At annealing temperatures of 300°C and 350°C a slight size increase to 10 - 12 nm is noted. At 400°C the average crystallite size is somewhat less than 10 nm. This may be due to the onset of thermal degradation. Thus, only a slight crystal growth is affected by annealing at relatively high temperatures.

6.3 Kink Band Morphology

Another feature which is apparent in the dark field images is the presence of dark bands within the diffracting film as shown in Figure 6.13. Typically these bands extend from the film edge and are nearly perpendicular to the draw direction. To determine whether these regions were non-crystalline a tilt-rotate series was conducted. Neither tilting of the film about the fiber axis nor tilting about the axis

lying in the plane of the film and perpendicular to the fiber axis changed the appearance of the dark field image. However, a rotation of the sample about a vector normal to the surface or an azimuthal displacement of the objective aperture (see Figure 6.16) caused illumination of these regions. Figures 6.13 through 6.15 show the images resulting from successive displacements of the objective aperture. While Figures 6.14 and 6.15 are displaced aperture dark field images, the displacement is small (Figure 6.16), and the effect of aberrations on image quality is minimal. Figure 6.13 shows a dark field image of a sample having dark bands. This image was formed with the objective aperture centered on the (200/110) combined reflection. At this sample orientation the bands are only slightly darkened. Figure 6.14 shows the dark field image resulting after a $-20°$ azimuthal displacement of the objective aperture. Here, the crystallites of the band are illuminated while the rest of the film is dark. In this position the aperture permits the passage of $g_{(110/200)}$ beams diffracted from crystals misoriented by $-20°$ from the fiber axis. For an azimuthal displacement of $+20°$ the contrast of film and band is reversed, as shown in Figure 6.15.

This series indicates that the bands are crystalline but are characteristic of an orientational defect. Further, the defect can be identified as a rotation of approximately $20°$ about the film normal. This orientational defect is schematically represented in Figure 6.17. As shown in this figure the orientational disorder is represented as purely lateral. This is not meant to exclude the possibility of a component of the displacement normal to the film surface. In fact, there are features apparent from SEM (Figure 6.2) which suggest the presence of stepped regions on the surface of the PPV microfibrils. These regions, like the bands observed in dark field imaging, extend from the film edge perpendicular to the draw direction. Thus while the band deformation appears to have a large lateral component some evidence exists for the presence of a component normal to the film surface.

Kink bands have been observed in other high modulus fibers [146-148] and are characteristic of a microbuckling response to axial compressive forces. The character of the dark bands observed in PPV suggests that these too are kink bands. As such, these bands may not be present in bulk films of PPV but may result from the mechanical action of sample preparation. The effect of the deflection associated with a 20° misorientation should present minimal resistance to charge carrier transport. However, if cleaved or sharply kinked chains existed at these kink band boundaries then disruptions in the conjugated nature of the chain would occur and the carriers could be severely impeded leading to low electrical conductivities. Also, as observed in high modulus fibers [149], the presence of these kink bands suggests a low compressive strength of PPV in the chain direction.

6.4 Doped PPV

Dark field images were taken of doped PPV films to examine the size and spatial distribution of the conductive crystals. Figures 6.18 and 6.19 show dark field images of AsF_5-doped films. The PPV film shown in Figure 6.18 was doped for 75 minutes. The electron diffraction pattern of this film indicated that the crystallites imaged with this history still represent *undoped* PPV. Circular regions of relatively high electron density appear at this low doping level and are seen as dark regions in the micrograph. These electron dense regions grow as the doping level is increased. Figure 6.19 shows a film doped with AsF_5 for 160 minutes. At this point the electron diffraction pattern is very diffuse. This is thought to arise from the increased electron density of the doped film and the resulting increased inelastic scattering. As a result no contrast corresponding to individual crystallites can be observed in the image. Further, the electron dense regions have increased in size with the largest ones appearing spherical. This electron dense overlayer is consistent with the incorporation of arsenic oxides in AsF_5-doped PPV. Because of the

propensity of AsF_5-doped PPV to form an electron dense layer, it was not possible to obtain dark field images of the doped crystallites even on the thinnest sections.

Sulfuric acid doped samples, on the other hand, were amenable to dark field study. Figure 6.20 shows a dark field image of H_2SO_4-doped PPV. The electron diffraction pattern shown in the inset confirms the crystallinity and a high degree of orientation. No indication of undoped regions was apparent from the diffraction patterns. Further, no electron dense overlayer was observed on H_2SO_4 doped films. The 1.04 nm equatorial spacing ($g_{(100)}$) characteristic of this complex is seen close to the main beam. The intense $g_{(200)}$ reflection at 0.52 nm was used to form these dark field images. As in the pristine sample, H_2SO_4-doped PPV shows small crystallites evenly dispersed throughout the film. The contrast is in general lower than seen in the pristine films. On the average the crystallites are 4.4 nm in size with a standard deviation of 1.4 nm. The resulting conductive crystals, while well formed, are slightly smaller in dimension than the undoped crystals. Further, the general morphological character is the same for both pristine and doped films. Thus the micellar model of the pristine films can also describe the doped morphology. However, since the doped crystallites appear significantly smaller than the pristine crystallites the sample volume composed of well ordered doped crystallites may be less than 50%.

It is clear from diffraction that the doped crystallites observed here correspond to those seen in bulk films by x-ray diffraction. Recall from Chapters 4 and 5 that some discrepancy exists between the analytical estimate of the doped complex stoichiometry and that estimated from x-ray diffraction. The x-ray diffraction results indicate a higher $AsF_6^-/C_8H_6^{\delta+}$ ratio of 1/2. Note that TEM indicates a significant volume (ie., > 50%) of disordered grain boundary regions. In light of the microscopy results it is likely that the lower ratio of 1/4 - 1/3 is due to imperfect complex formation in the disordered grain boundary regions.

From the above results conclusions can be drawn concerning the physical transformation of oriented PPV occurring during doping. As the film is converted to its electrically conductive form the pristine crystallites undergo a crystal–crystal transformation. At low doping levels (Figure 6.18) only pristine crystallites are observed in thin films. However, even for doping times on the order of 10 minutes bulk films demonstrate high electrical conductivities. Thus, at low doping levels a continuous conductive pathway must exist along the length of the film. Since the pristine crystals appear largely intact at low doping levels it is reasonable to expect that the grain boundaries are preferentially converted to the conductive phase in the early stages of doping, leaving the bulk of the pristine crystallites unmodified. As doping proceeds the conductive phase would be expected to grow at the expense of the pristine crystallites until only the latter material exists in the fully doped condition (Figure 6.20).

Figure 6.1   SEM micrograph of large PPV section showing ribbon-like morphology.

Figure 6.2   SEM micrograph of section showing regularity of furrows formed during mechanical detachment. Stepped regions on the microfibril surface are indicated by arrows.
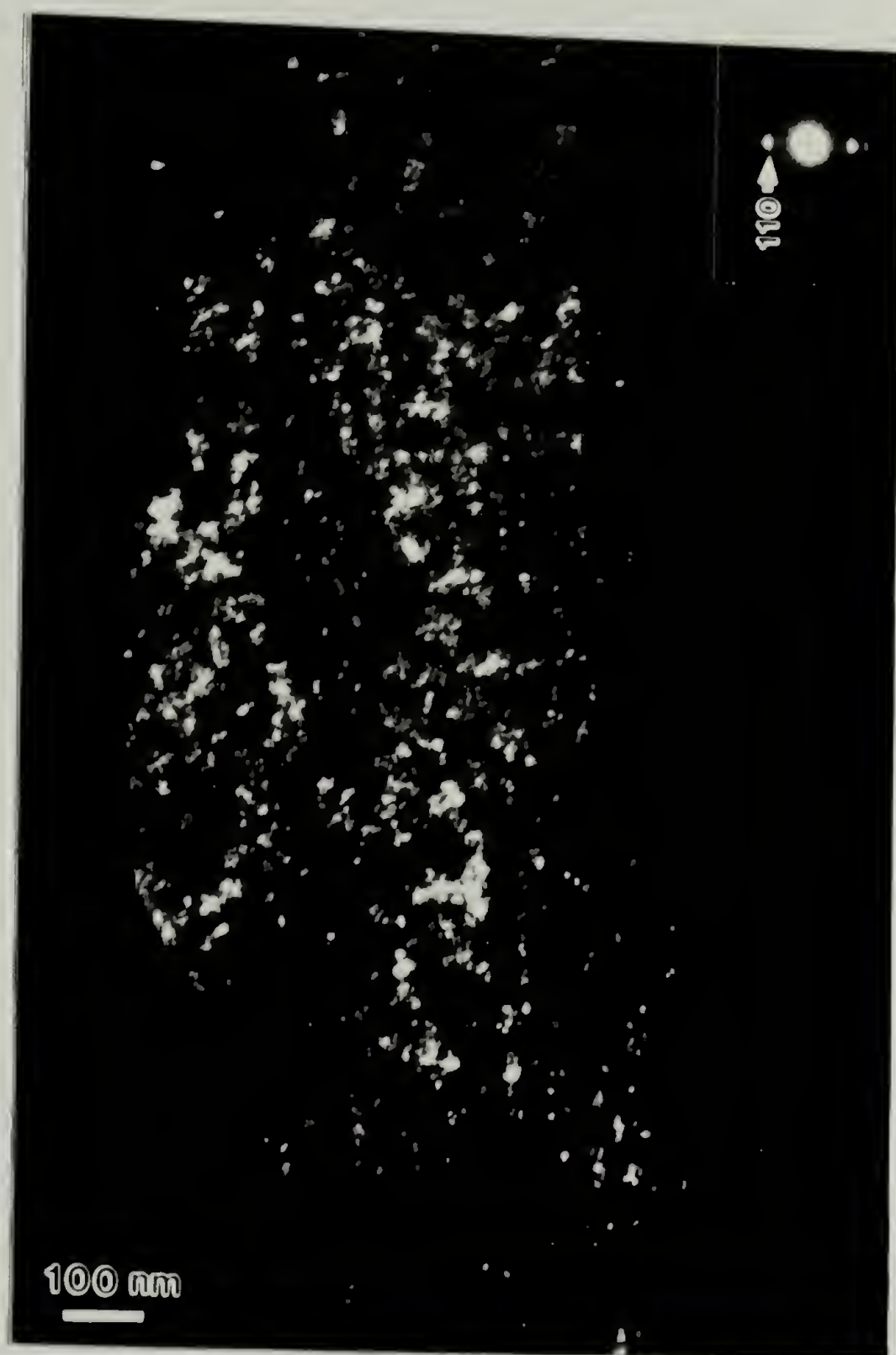
Figure 6.3   Dark field image ($g_{(1\bar{1}0/200)}$) of oriented PPV ($L/L_o = 8$). The molecular axis is vertical.

Figure 6.5
Displaced aperture tilt series of dark field ($g_{(1\bar{1}0/200)}$) images. The draw ratio of the film is 8. The incident beam is tilted from the surface normal by 0.26°.

Figure 6.4
Displaced aperture tilt series of dark field ($g_{(1\bar{1}0/200)}$) images. The draw ratio of the film is 8. The incident beam is normal to the sample surface.

500 nm

139
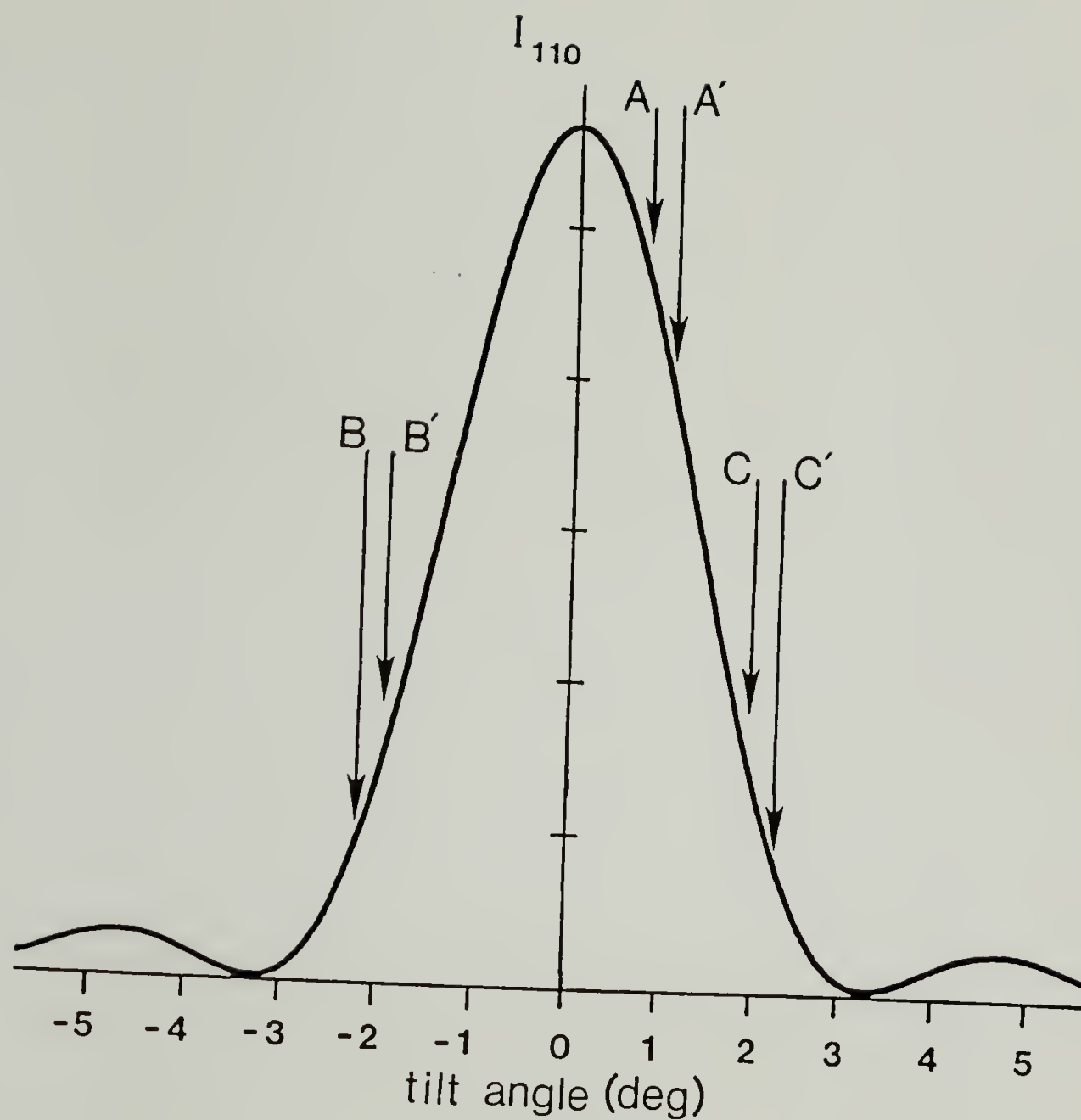
Figure 6.6   Rocking curve for $g_{(110)}$ of PPV. A crystal thickness of 7.5 nm was used in the calculation. The labels A, B, and C correspond to the crystallites indicated in Figures 6.4 and 6.5. The primed labels show the intensity after a beam tilt of 0.26°.
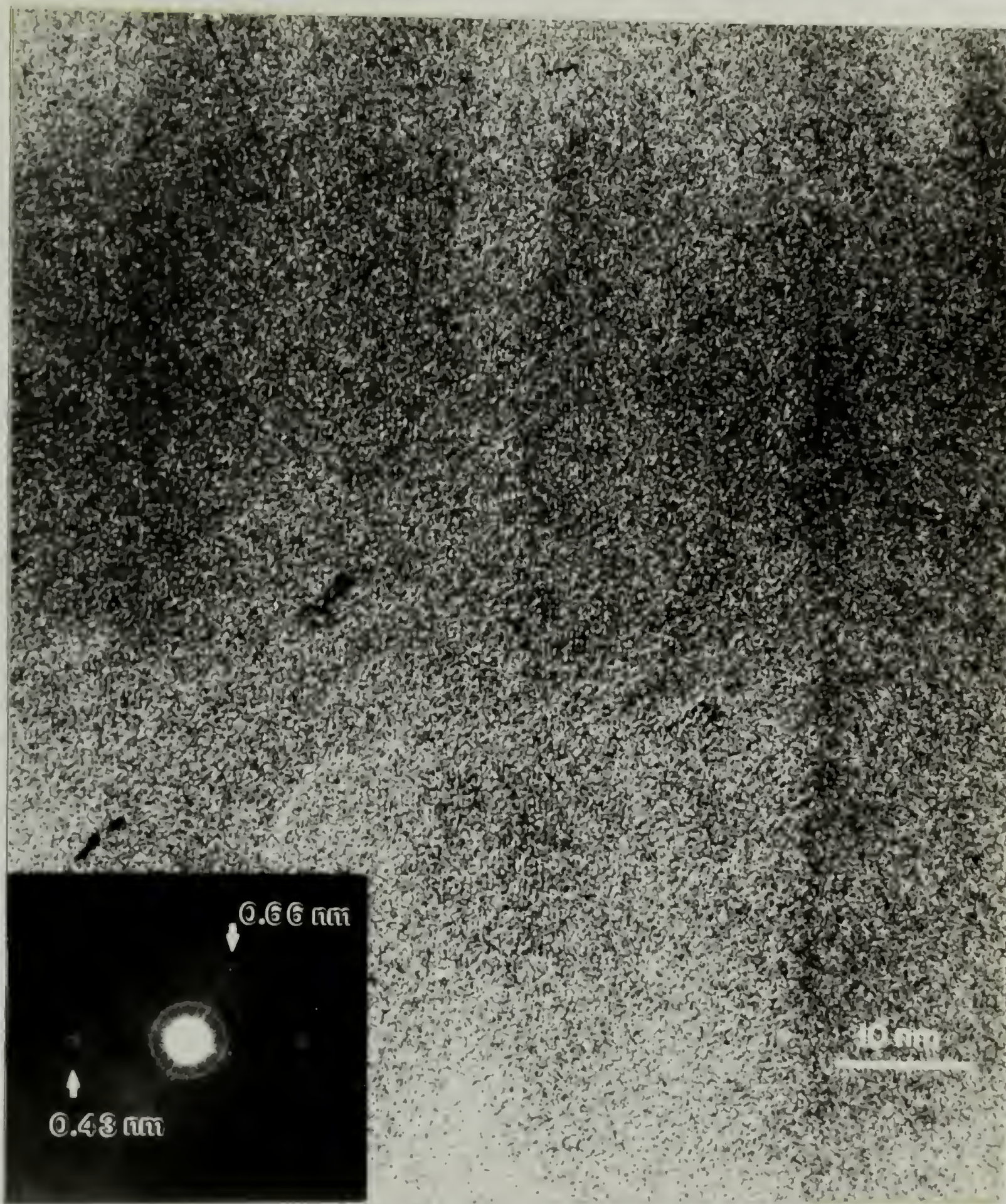
Figure 6.7   High resolution transmission electron micrograph of PPV (draw ratio = 9.3) showing 0.43 nm lattice fringes. The inset shows the optical diffractogram from this image.

141
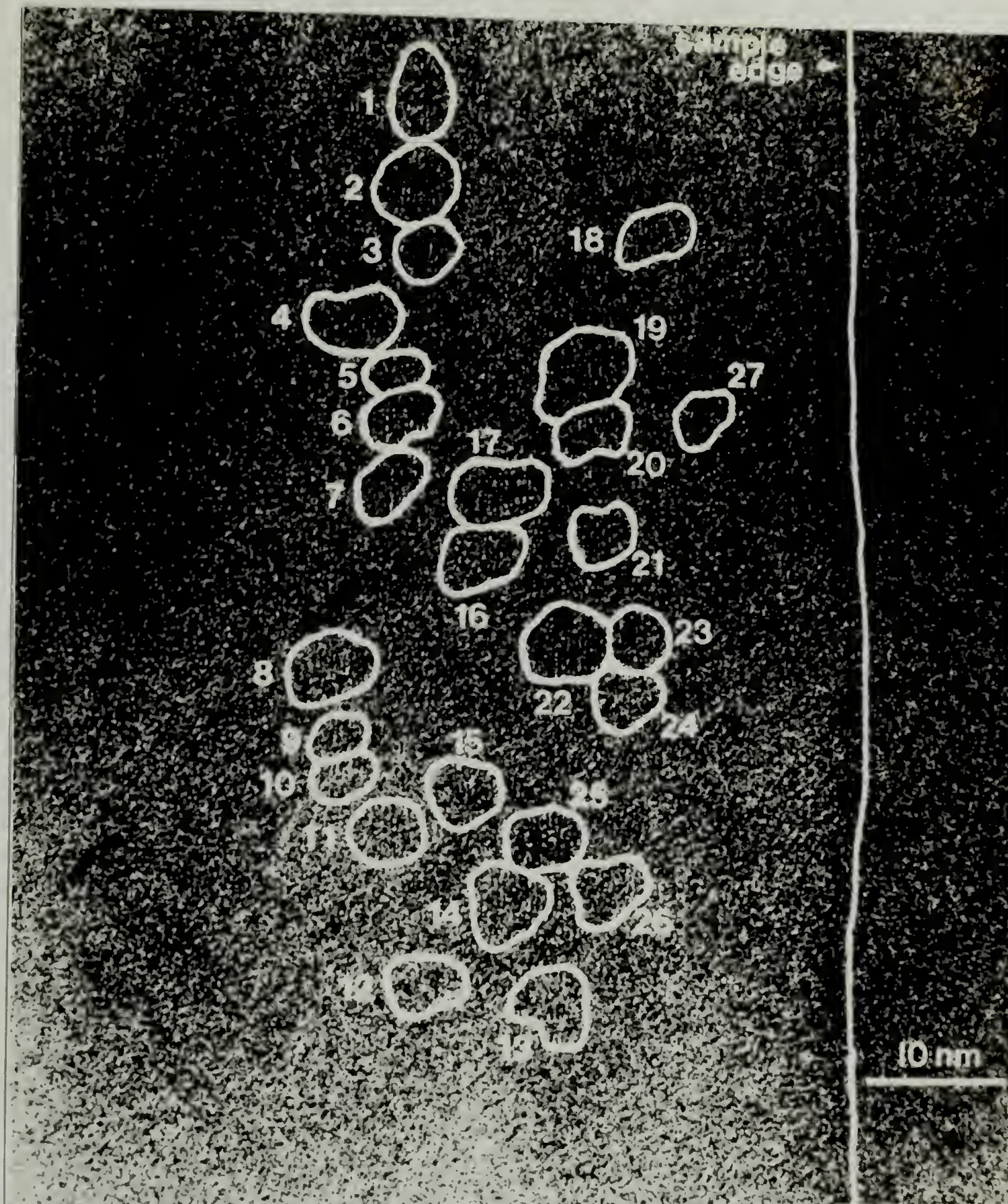
Figure 6.8   High resolution transmission electron micrograph of PPV (draw ratio = 9.3) showing 0.43 nm lattice fringes. The individual crystallites are outlined.

142
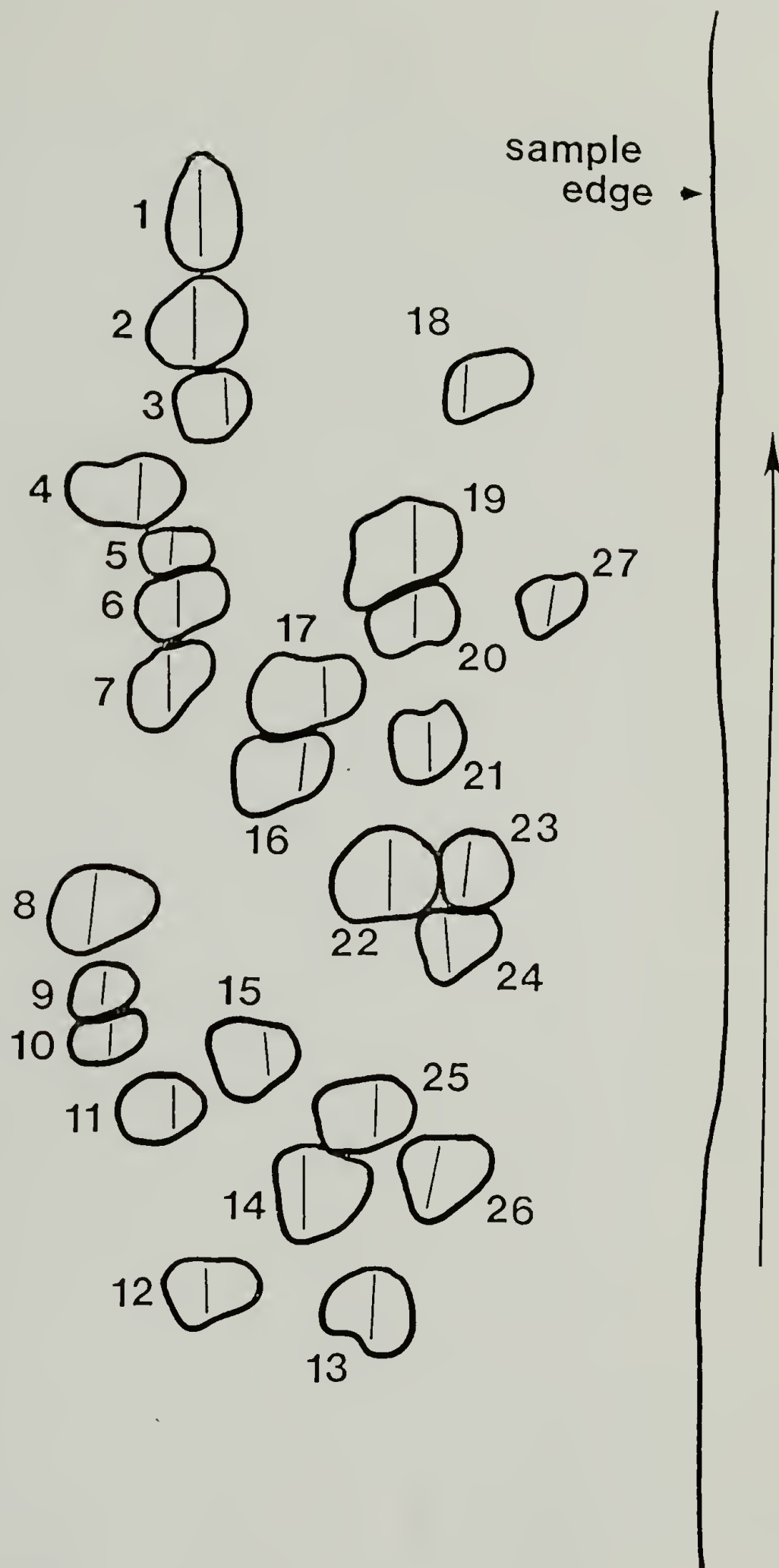
Figure 6.9   Schematic representation of Figure 6.8 showing the crystallite orientations.

143
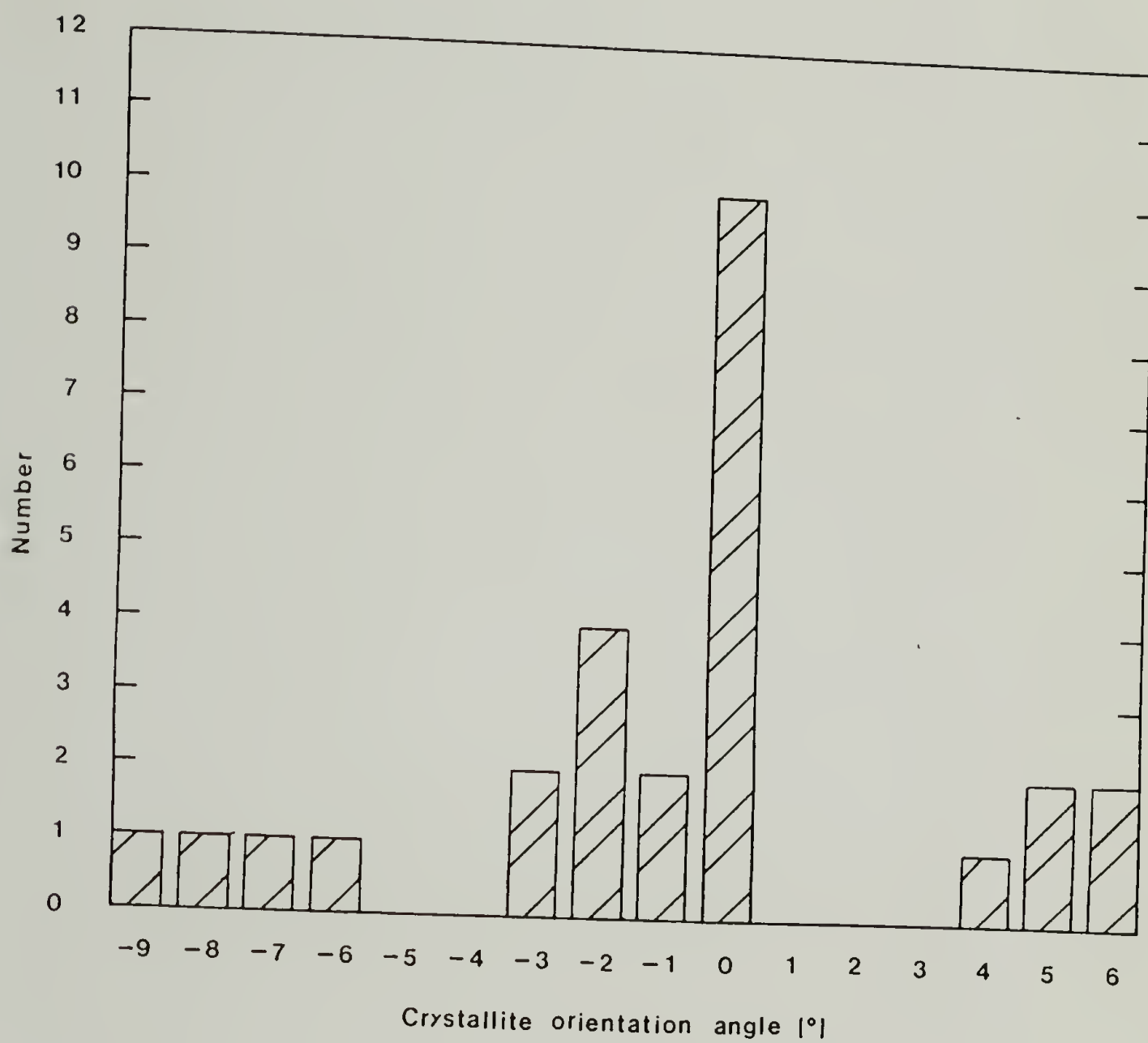
Figure 6.10   Orientation distribution of the crystallites observed in the HREM image (Figure 6.7).
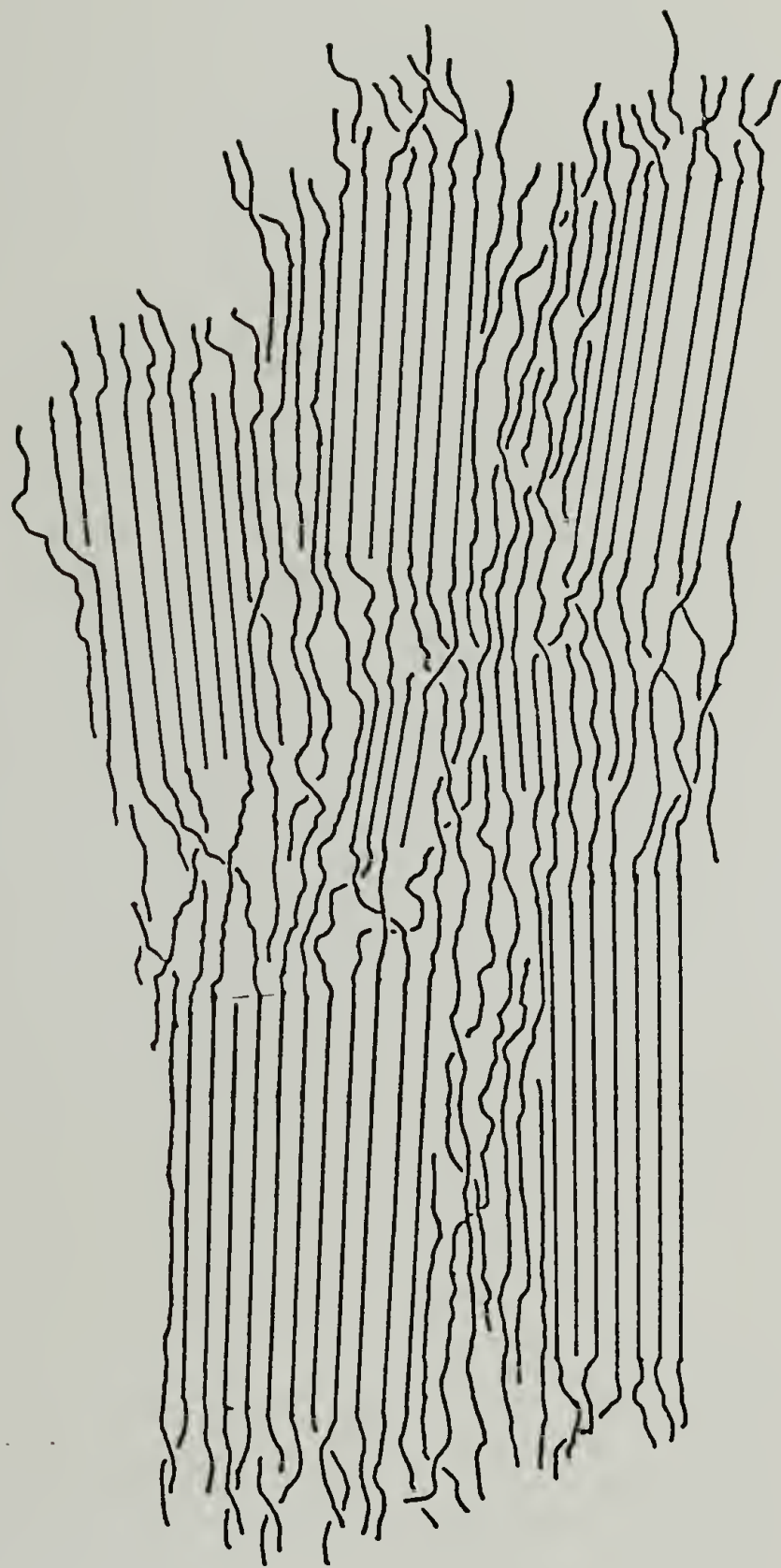
Figure 6.11   Schematic representation of the micellar crystal morphology of PPV. The crystallites are approximately 5.0 nm in width and length.
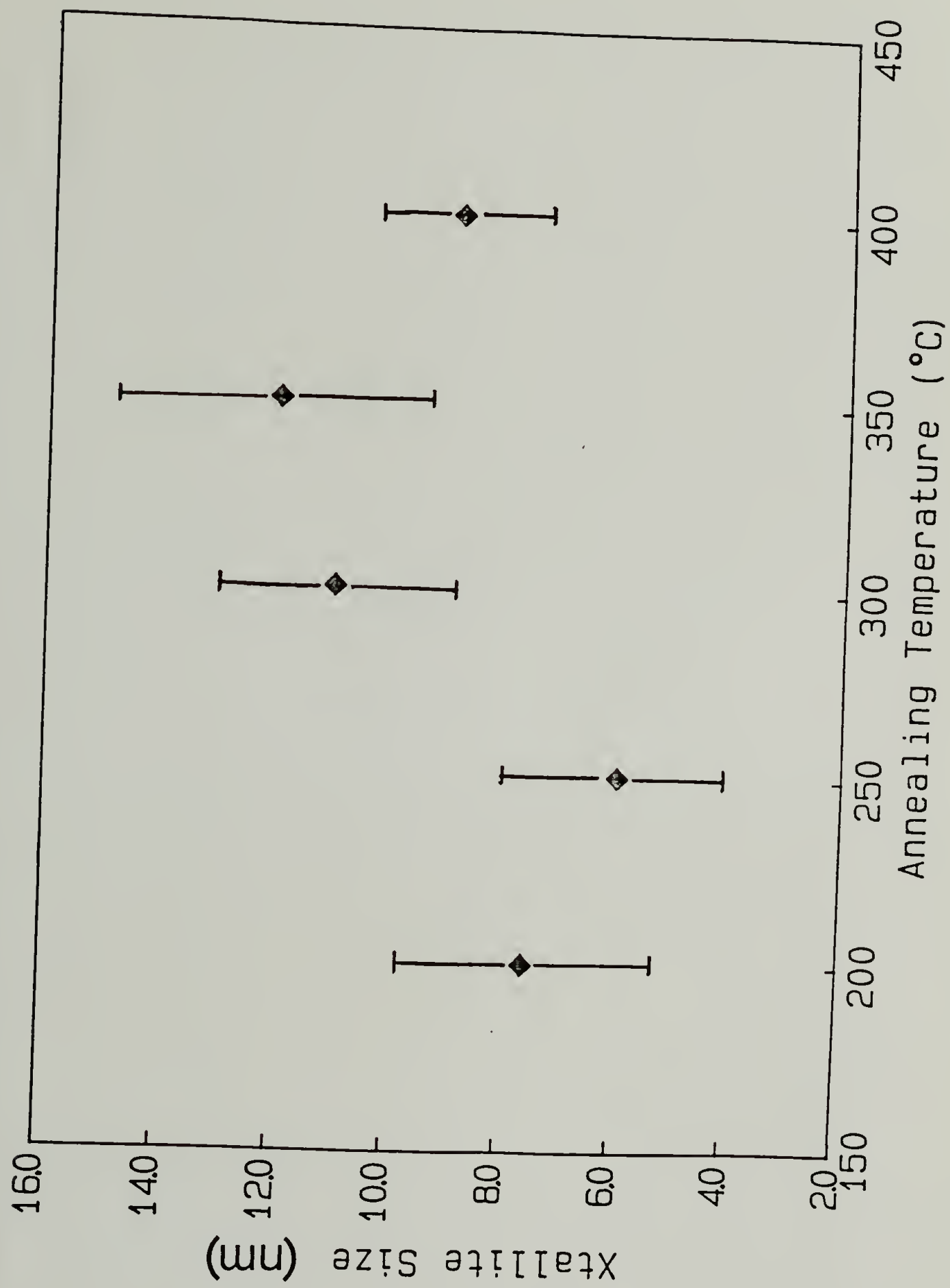
Figure 6.12   Effect of annealing temperature on PPV crystallite size.

Figure 6.14
Rotation series showing crystallites in misoriented
bands (draw ratio = 8). Image formed with aperture
rotated by approximately +20°.
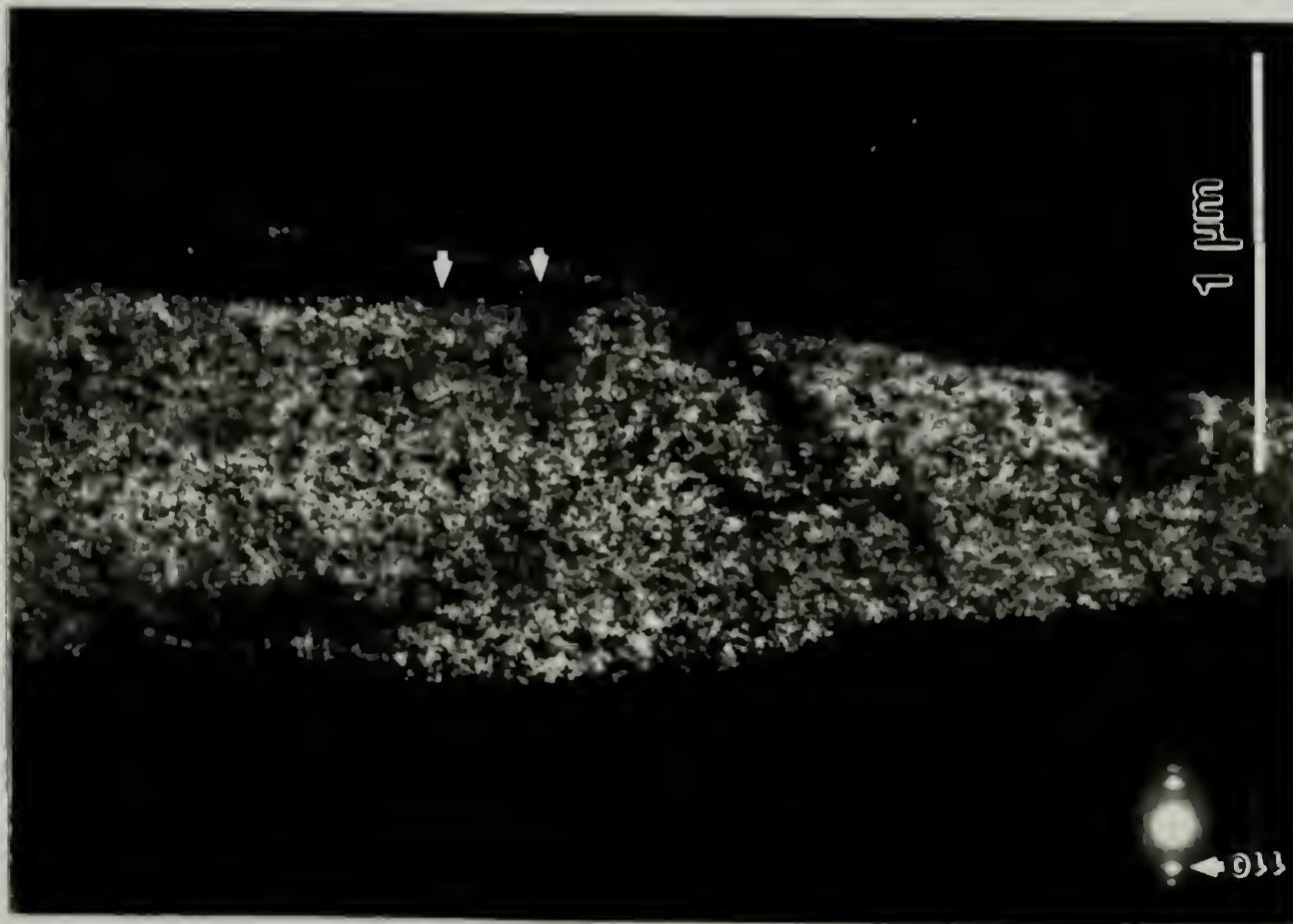
Figure 6.13
Rotation series showing crystallites in misoriented
bands (draw ratio = 8). Dark field image with aperture
centered on $g_{(110/200)}$.

147

Figure 6.16
Rotation series showing crystallites in misoriented
bands (draw ratio = 8). Schematic representation
of aperture placements.

Figure 6.15
Rotation series showing crystallites in misoriented
bands (draw ratio = 8). Image formed with aperture
rotated by approximately -20°.

148
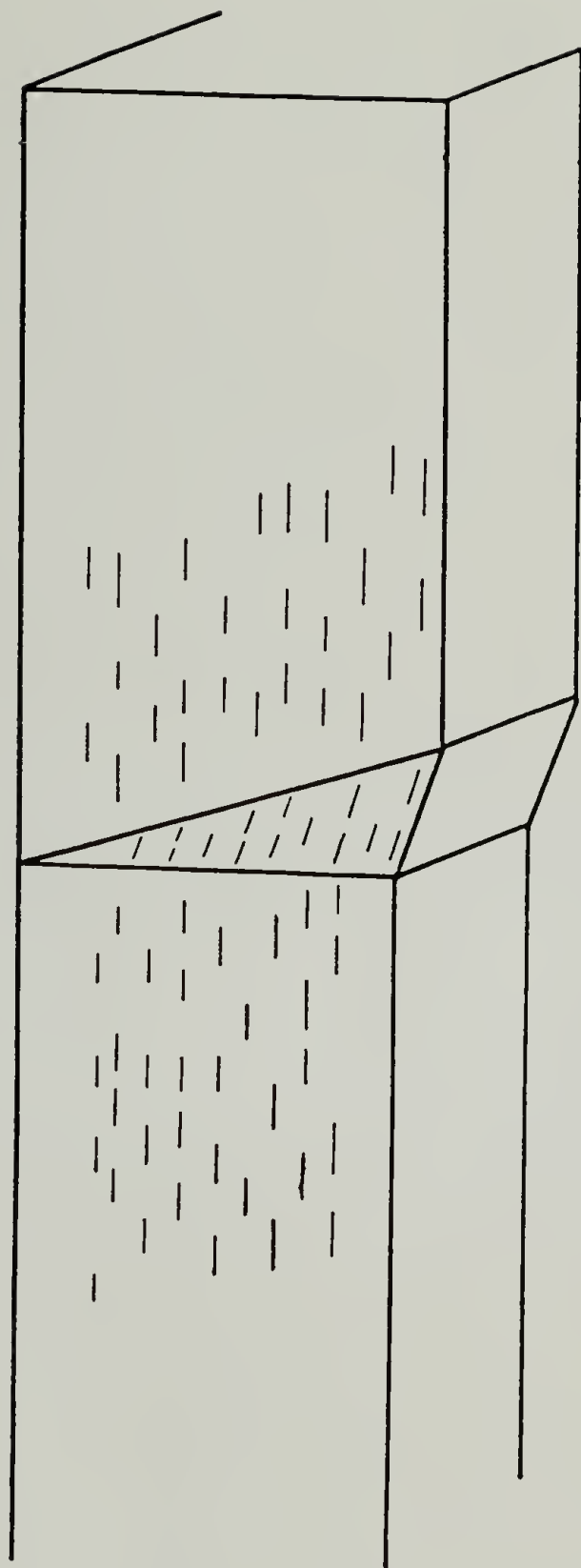
Figure 6.17   Schematic representation of crystallite orientation in and around misoriented bands.

Figure 6.19
Equatorial dark field image of AsF$_5$-doped PPV (draw ratio =8). Film doped for 160 minutes, the spherical electron dense regions are indicated.

Figure 6.18
Equatorial dark field image of AsF$_5$-doped PPV (draw ratio =8). Film doped for 75 minutes, the circular electron dense regions are indicated.

150
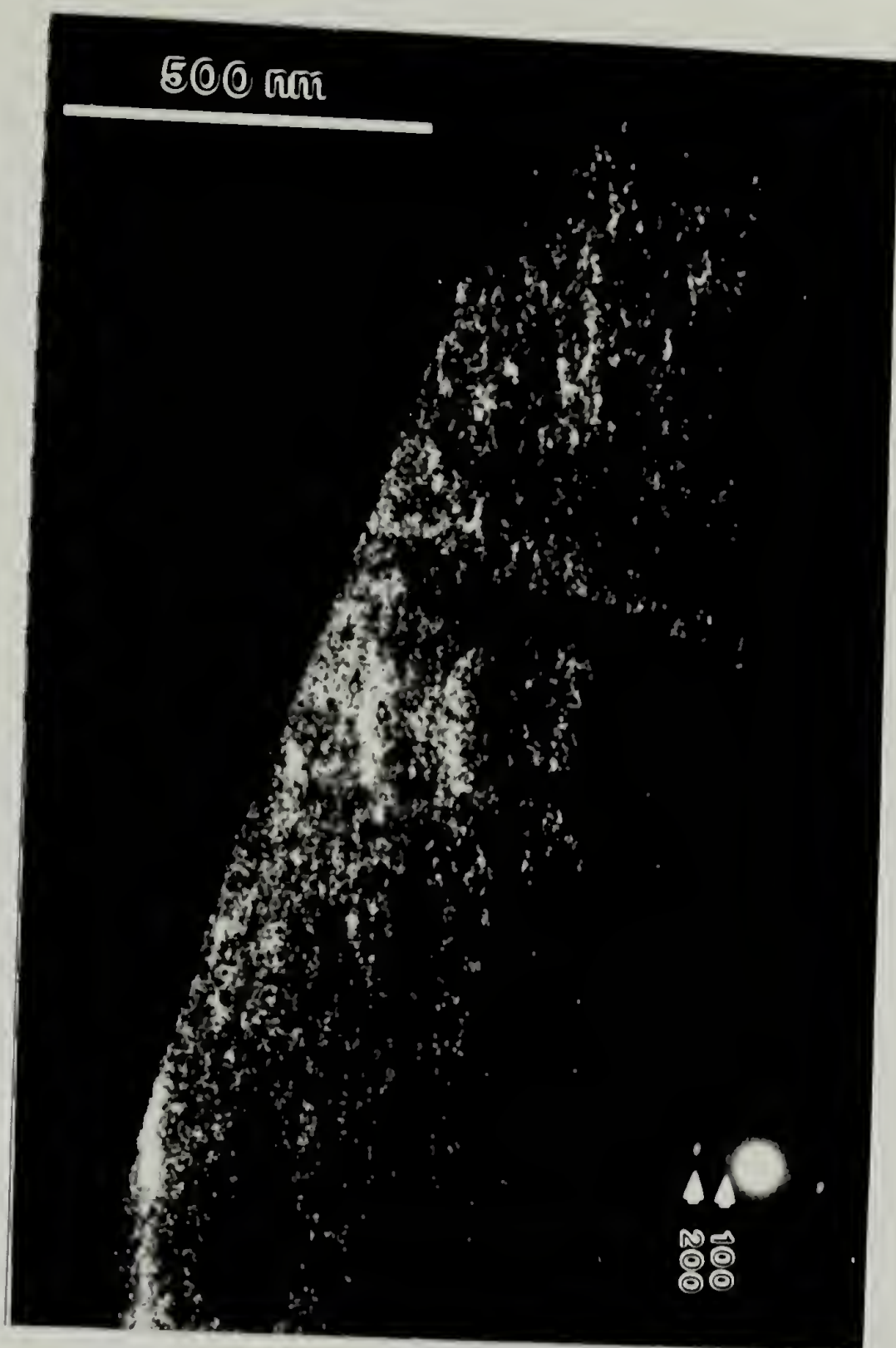
Figure 6.20   Dark field image ($g_{(200)}$) of H_2SO_4-doped PPV (draw ratio = 8).
The inset shows the electron diffraction pattern. The (200)
reflection is indicated.

CHAPTER 7

DOPANT PENETRATION IN BULK FILMS

152

The results of the previous chapter have shown that small equiaxed crystallites of the doped phase are formed in *thin* films by a nucleation and growth mechanism. However, in most circumstances it is the properties of *bulk* films that are of interest. This chapter describes experimental results concerning the penetration of the dopant in bulk films. Rutherford backscattering spectrometry has been employed as the experimental technique.

7.1 Backscattering Spectra

The backscattering spectrum for pristine (or undoped) PPV (C_8H_6) is shown in Figure 7.1. As expected carbon is the nucleus primarily observed. The slight background near 1.3 MeV may arise from residual S and Cl from the precursor polymer. Although bulk elemental analysis for S and Cl indicated trace amounts at most, the sensitivity of RBS allows observation at the impurity level. No oxygen is observed in the pristine films.

After doping As and F nuclei are observed in addition to carbon. Figure 7.2 shows the RBS spectrum for a PPV sample exposed to AsF_5 vapor for 5 days. Here, a significant oxygen peak is also observed even though samples were evacuated to 10^-4 mmHg before doping and all handling was done in an inert atmosphere. The backscattered particles for all nuclei are observed at their surface energies indicating the presence of all at or near the doped film surface. Further, for this particular doping condition the full width at half maximum of As and F peaks are greater than the instrumental resolution and show low energy tails. Thus, penetration of As and F

has occurred. The oxygen peak is narrow and within the instrumental resolution suggesting confinement to the film surface.

Figure 7.3 shows only the As region of the RBS spectra for PPV films exposed to AsF$_5$ vapor for 1 hour, 4 hours, 5 days, and 10 days. At one hour the As nuclei are confined within the first 60 nm of the film. After a 4 hour doping the yield of the As peak has increased but the peak displays only a slightly asymmetric tail on the low energy side. At this doping condition more As has been incorporated into the near surface layer, indicated by higher yields, without a significant penetration. As doping is continued to 5 days and 10 days the surface amounts of As increase again and dopant penetration is apparent. There is a high surface concentration of As at these long doping times. In fact, the surface concentration is highest for the 5 day doping. This is attributed to a high concentration of arsenic oxides at the film surface as will be discussed later. It is important to note that the As peak profile does not fall off smoothly on the low energy side. At depths below the surface the yields decrease to a nearly constant region and only then fall off smoothly to zero yields. The As penetration depth is given approximately by the scale included in Figure 7.3. This depth scale is calculated using the energy loss factor for pristine PPV. A more precise determination of the As penetration requires consideration of As, F, and O incorporation. This will be discussed in reference to the RUMP simulations. Regardless of the absolute depth scale it is clear that the As penetration depths for these doping conditions are shallow with respect to the total film thickness.

The As profiles at 5 and 10 day doping are not characteristic of Fickian diffusion and imply a more complex diffusion situation. If the diffusion were Fickian then the As concentration would decrease smoothly from its surface

153

concentration, C_o, according to the following error function profile as the distance from the surface, x, increased [150].

$$C = C_o erfc(x/2\sqrt{Dt}) \qquad (8)$$

Here, D is the effective diffusion coefficient and t is the doping time. Clearly, Fickian diffusion is not obeyed in this system. Another possibility is Case II diffusion commonly seen in amorphous polymers [150-154]. In this situation a front of constant concentration, C_o', would exist near the surface and this would be preceded by a Fickian precursor front. The As profiles observed in this system are also not characteristic of Case II diffusion. While some region of nearly constant concentration exists just below the surface a strong surface concentration is also evident in these doped films indicating a more complex diffusion situation.

In addition to the qualitative evaluation of diffusant profile shape the diffusion character can be evaluated by comparing the change in integrated amount of diffusant with time. For Fickian diffusion [150] the diffusant uptake increases as $t^{1/2}$ while Case II [154] uptake increases as t. As discussed in section 3.2.5.1 the total amount of As incorporated into the doped films is proportional to the integrated peak areas. The As peak area is plotted against doping time in Figure 7.4. After the initial doping period (1-4 hours) the As incorporation is linear with time to 10 days. Note that a simple As uptake measurement would indicate Case II diffusion. However, the profile shape has been directly observed and Case II behavior is discounted on this basis.

The carbon-oxygen-fluorine region of the RBS spectrum is shown in Figure 7.5 for pristine PPV and for PPV doped for 4 hours and 5 days. As doping proceeds both F and O yields increase. While the F and O yields are uncertain due to beam induced degradation the profile shapes are assumed to be unchanged. At 5 days the F peak exhibits a significant breadth while the O peak is relatively narrow. Thus, there is preferential penetration of F with O being mainly confined to the doped film

154

surface layer. The carbon edge appears at its surface energy at all doping levels. The carbon profile shape, however, does suffer a subtle change. The yield at the surface is slightly lessened. As will be apparent from the simulations the decreased carbon yield is entirely due to a dilution effect; the number of C nuclei per unit volume has been reduced at the surface by incorporation of As, F, and O nuclei.

7.2 RUMP Simulations and Depth Profiles

Computer simulations of the RBS spectra were performed by dividing the film thickness into many layers and requiring each layer to be chemically homogeneous. Because of the limited number of layers available in the RUMP program (ie., 25) a constant layer thickness could not be used to simultaneously fit profile depth and intensity. Thus, greater thicknesses were used for the deeper layers where the change in profile shape was more gradual. The same depth protocol was used for all simulations. The composition of each layer was referenced to the polymer repeat unit. Thus, each layer had the stoichiometry $C_8H_6As_xF_yO_z$ where x,y, and z were variable. The simulated spectrum was then fit to the data by iteratively modifying the composition of each layer. Typically, the depth scales in RBS are given in areal atomic densities (ie., atoms/cm^2). The calculated atomic density for pristine PPV is 1.008×10^{23} atoms/cm^3. This value has been used in the conversion from areal atomic density to depth. The simulated spectrum for the 5 day doped film is shown by the solid line in Figure 7.2. The entire spectrum is well fit using this approach. The layer thicknesses and compositions for the simulated 5 day doping spectrum are shown in Table 7.1. Here the depth is the distance below the surface at which the layer begins and is given in nanometers.

Using the simulated models as a reference to calculate the variation in atomic density with layer composition the atomic depth profiles were calculated from the RBS spectra. Figure 7.7 shows the As penetration for 4 hour, 5 day, and 10 day

155

dopings. At 4 hours the As profile decreases smoothly from ≈0.25 As atoms per PPV repeat to zero at 100 nm. For the 5 day doping the surface concentration of As is near 0.9. This falls steeply to a knee in the profile at 120 nm. The concentration at the knee is ≈0.15. At greater depths the As concentration decreases smoothly reaching the noise level at 250 nm. The profile for the 10 day doped sample is qualitatively similar to the 5 day profile. The surface concentration is 0.6 and falls to a nearly constant value of 0.22 between depths of 120 – 300 nm. Beyond this depth the concentration drops smoothly to zero at approximately 800 nm (not shown).

Atomic profiles for F and O were also calculated. Caution must be exercised in extracting quantitative information from the F and O profiles since they do suffer beam induced degradation. For the 5 day doping the F profile is nearly constant until it drops to the noise level near 300 nm. In the 5 day doped spectrum the depth profile of F may be correlated with the As profile in that both As and F are present to the same depths. The O, on the other hand, is confined to the first 60 nm for the 5 day doping. As such, oxygen can be correlated to As only at the doped film surface.

7.3 Physical Model of Depth Penetration

Using the elemental information gained from RBS an analysis of the sample stoichiometry can be attempted. For the AsF_5-PPV system some chemical binding information has been previously determined. Wide angle x-ray diffraction of AsF_5-doped PPV has suggested the presence of As_2O_5 and hydrates of this oxide to be formed during doping (see Chapter 4). Presumably, these compounds are formed through reaction of AsF_5 with residual O_2 or H_2O even though high vacuum and inert gas environments have been employed. Further, the presence of the AsF_6^- anion in AsF_5-doped PPV has been confirmed using FTIR and XPS. Also, mass spectrometry of the thermolysis products of doped films has not revealed fluorinated

hydrocarbons suggesting an absence of fluorinating side reactions in the AsF_5-doping process. One simple chemical model can thus be assumed:

$$(C_8H_6)_m \; [(C_8H_6^{\delta+})_x(AsF_6^-)]_n \; (As_2O_5)_p.$$
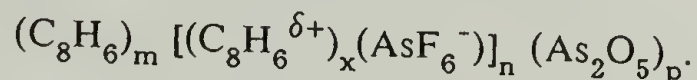
This model, however, cannot be satisfactorily fit using the RBS data. For instance, with the 5 day doped sample the elemental surface composition is $C_8H_6As_9F_3O_{15}$ (see Table 7.1). If all the F and O are assumed to be incorporated in the films as AsF_6^- and As_2O_5 respectively then an excess of 2.5 As atoms remains. Further, allowing the presence of arsenic oxide hydrates worsens the fit. The difficulty here in evaluating the doped film stoichiometry is partly attributable to beam induced degradation of F and O.

While the exact chemical composition of the doped films is uncertain the elemental profiles of O and F show that the arsenic oxides are confined to the film surface and the arsenic fluoride diffuses into the film. Further, Figure 7.8 shows the F/As atomic ratio as a function of depth for different doping conditions. This ratio is calculated from the simulated spectra. For all of the doping times shown the F/As ratio is less than 2 at the surface. At increasing depths this ratio tends toward 6, the expected ratio for AsF_6^-, even though beam induced degradation of F occurs. The presence of other arsenic fluoride species (ie., AsF_5 and AsF_3) would serve to lower the observed F/As. As expected, AsF_6^- is suggested as the dopant anion by the F/As ratio. Binding of As in the form of oxides is expected to be primarily responsible for the low F/As ratios at the film surface.

The dopant to polymer repeat ratio can be evaluated from the stable As profiles. As can be seen from the 10 day doping profile (Figure 7.6c) a region of nearly constant As concentration exists with 0.25 - 0.20 As atoms per polymer repeat. Thus, one AsF_6^- anion for every 4-5 polymer repeat units is suggested. This is consistent with results obtained from PPV electrochemically oxidized using AsF_6^- as the counterion. The electrochemical behavior is reversible up to an oxidation level of

157

25 mol% (ie., 4 PPV repeats per AsF_6^- counterion) [61]. Recall from Chapter 4 that a similar stoichiometry is also suggested from F/C ratios obtained from x-ray photoelectron spectroscopy of lightly doped PPV surfaces.

A physical model of AsF_5-doped PPV is schematically presented in Figure 7.9. This model is intended to represent only the qualitative features of the dopant concentration profiles for samples that have been subjected to heavy dopings. In the model an arsenic oxide surface layer exists. Below the surface layer resides a highly doped layer ($C_8H_6^{\delta+}/AsF_6^- = 4-5$) and at greater depths the dopant anion penetrates the undoped polymer as a precursor front. This profile bears some similarity to Case II diffusion fronts observed in the diffusion of small molecules in glassy polymers [154]. The polymer doping process, however, is compounded by the simultaneous diffusion and reaction of AsF_5 and therefore cannot be simply classified as either Fickian or Case II diffusion.

It is important to realize that the above results apply to specific doping conditions. Figure 7.9 shows the RBS spectrum obtained after a 1 hour AsF_5-doping in the presence of AsF_3. This was accomplished by holding the dopant at room temperature. In this way excess AsF_3 is not cold-trapped during doping. As can be seen from the figure, the dopant penetration in this case is essentially equivalent to the 10 day doping in the relative absence of AsF_3. The As surface concentration and the oxygen concentration suggest a much lower amount of arsenic oxides at these short times. Further, the profile shapes appear even more similar to those seen in Case II diffusion. The deeper dopant penetrations at these conditions are attributed to the plasticizing effect of AsF_3 in AsF_5 doped polymers. This effect has been previously noted in AsF_5-doped polyacetylene [102] and poly(p-phenylene sulfide) [155].

7.4 Normalized Electrical Conductivity Measurements

As previously stated, the conductivity of bulk films doped in the manner employed here is calculated using the entire film thickness. Clearly, such calculations are not representative of the true material properties since the doping is strongly heterogeneous, forming shallow doped layers. In this case, it is clear that the charge carriers created by doping will only reside in a relatively shallow conducting layer. Thus, a better calculation is one which takes into account the actual doped layer thickness. Table 7.2 shows the conductivities calculated using the entire film thickness, σ^{bulk}, and the measured doped layer thickness, σ^{norm}. For the purpose of these calculations the doped layer thickness has been taken as the maximum observable As penetration depth. With this calculation an intrinsic conductivity representative of the actual ability of PPV chains to support charge carrier transport is estimated. The normalized conductivity, σ^{norm}, is calculated as 3.5×10^4 $(\Omega \text{ cm})^{-1}$ for a 1 hour doping and 4.2×10^4 $(\Omega \text{ cm})^{-1}$ for a 5 day doping. Thus, the normalized conductivities are considerably higher than the bulk values. These values, while higher than previously reported PPV conductivities, are close to the highest conductivities ($\approx 10^5$ $(\Omega \text{ cm})^{-1}$) measured in I_2-doped polyacetylene [21]. If these normalized conductivities were indeed representative of an *intrinsic* PPV chain conductivity then the value should be invariant to doping time. As can be seen from Table II the normalized conductivity value fluctuates about 4.4×10^4 $(\Omega \text{ cm})^{-1}$ for all doping times. Even this calculation, however, underestimates the intrinsic conductivity since at early stages of doping the surface is not fully doped and at later stages the precursor front, which is also not a fully doped region, is included. On the basis of these results a lower limit to the intrinsic conductivity of 4×10^4 $(\Omega \text{ cm})^{-1}$ is suggested.

Table 7.1
Simulated composition of AsF_5-doped PPV (280 mmHg, 5 days). Each layer is chemically homogeneous with a stoichiometry $C_8H_6As_xF_yO_z$.

Depth (nm)	arsenic, x	fluorine, y	oxygen, z
0.0	9.000	3.00	15.00
20.0	7.000	3.00	13.00
40.0	3.000	3.00	10.00
70.0	1.250	3.00	3.00
100.0	0.900	3.00	1.50
130.0	0.700	3.00	1.00
160.0	0.550	3.00	0.80
190.0	0.450	2.00	0.70
220.0	0.350	1.30	0.60
270.0	0.150	0.80	0.50
320.0	0.100	0.60	0.00
370.0	0.070	0.50	0.00
420.0	0.050	0.40	0.00
470.0	0.045	0.04	0.00
520.0	0.040	0.30	0.00
570.0	0.035	0.25	0.00
620.0	0.030	0.20	0.00
670.0	0.025	0.15	0.00
720.0	0.020	0.10	0.00
1000.0	0.000	0.00	0.00

Table 7.2

PPV film conductivity normalized to doped layer thickness, d.

Doping Time	Resistance (Ω)	σ^{bulk} $(\Omega\ cm)^{-1}$ 10^4	d (cm) 10^{-7}	σ^{norm} $(\Omega\ cm)^{-1}$ 10^4
1.0 hr	2.23	0.206	60.0	3.5
2.0 hr	1.58	0.291	60.0	4.9
4.0 hr	1.13	0.407	100.0	4.1
*5.0 days	0.368	1.250	250.0	5.0

*This sample was doped for only 4 days. The σ^{norm} calculation was done using the penetration depth for the 5 day sample. Thus, σ^{norm} for this sample represents a lower limit to the intrinsic conductivity at 5 day doping.

$(L/A)^{bulk} = 4660\ cm^{-1}$
†$(L/A)^{norm} = (0.932)(1/2d)\ cm^{-1}$
See eqn(3.2).

†Twice the dopant penetration is used to calculate the conductivity since both sides of these films were exposed to AsF_5.

161
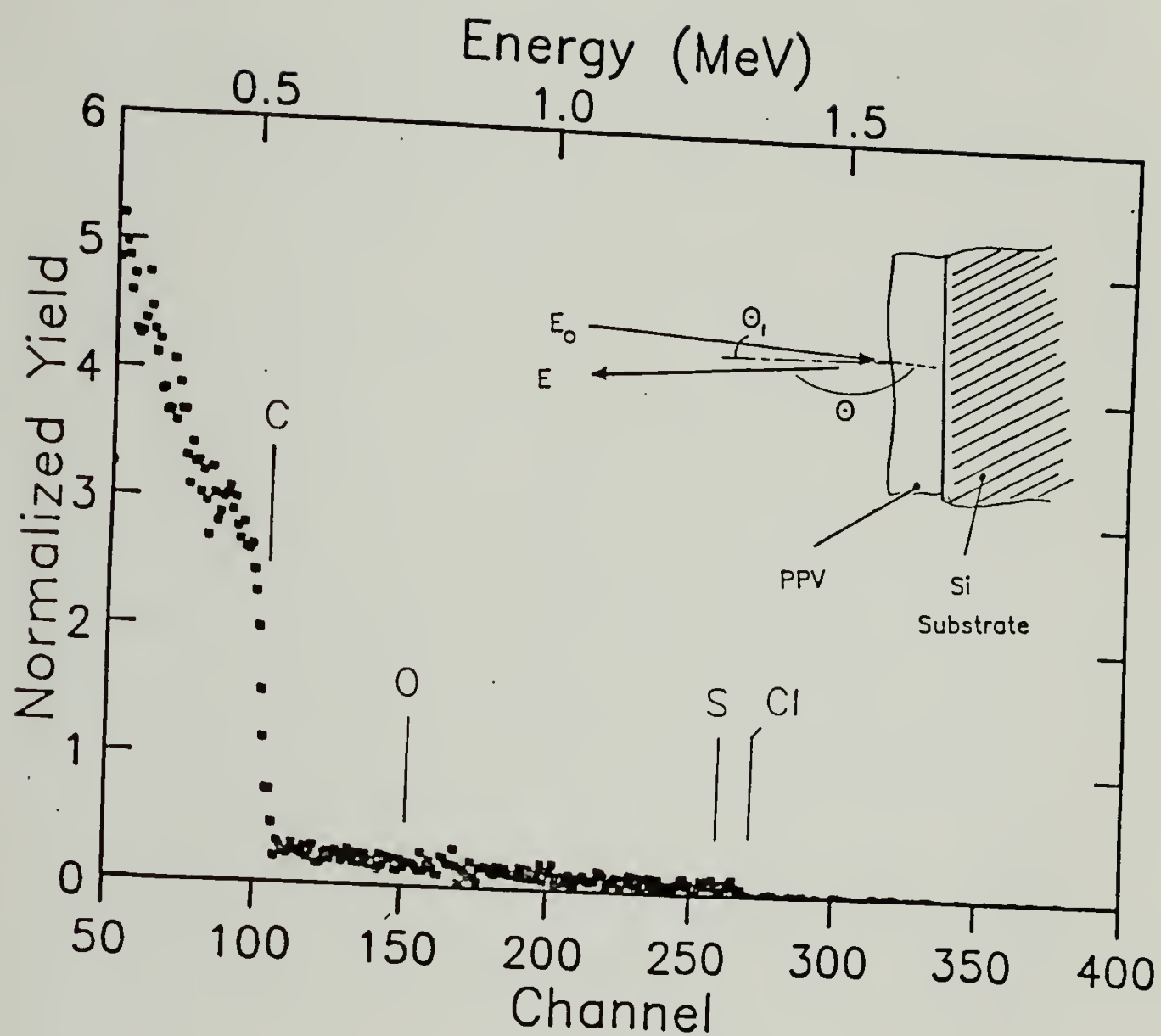
Figure 7.1   RBS spectrum of pristine PPV. The surface energies for C, O, S, and Cl are indicated. The inset schematically shows the sample configuration and experiment geometry.
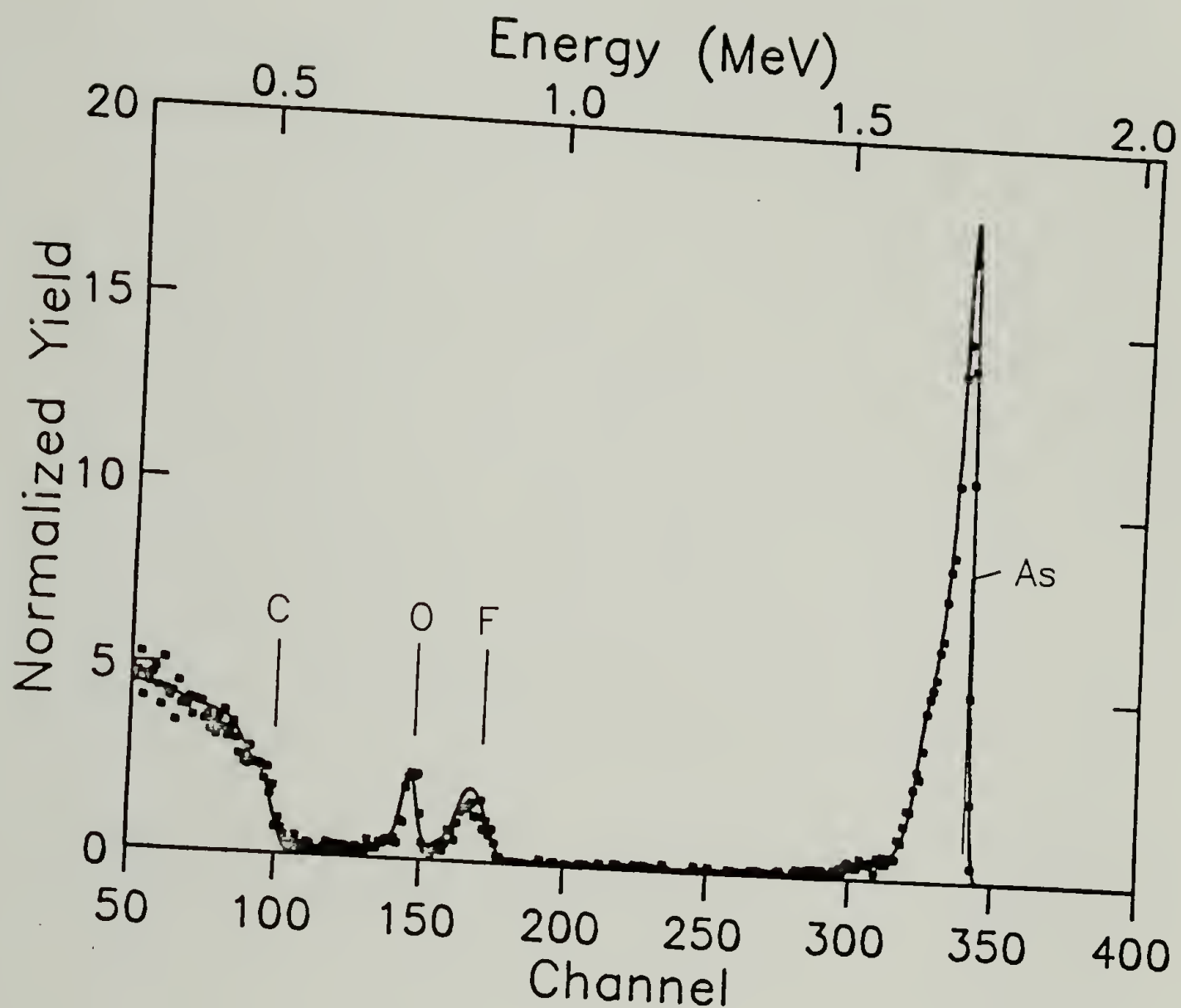
Figure 7.2   RBS spectrum of AsF$_5$-doped PPV (280 mmHg, 5 days). The surface energies for C, O, F, and As are indicated. The solid line represents the RUMP simulation (see text).
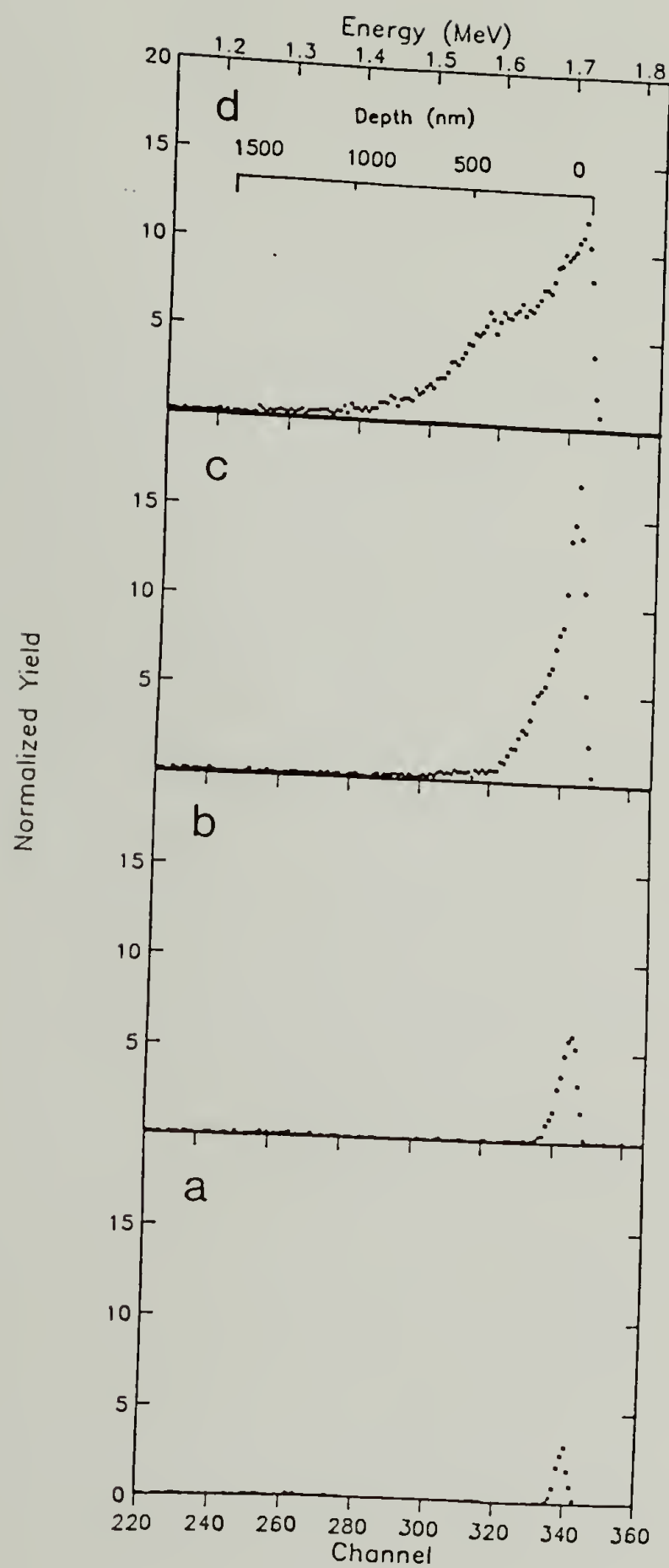
Figure 7.3   Arsenic region of the RBS spectra for various doping times: (a) 1 hour, (b) 4 hours, (c) 5 days, (d) 10 days. An estimated depth scale for the As nuclei is indicated (see text).
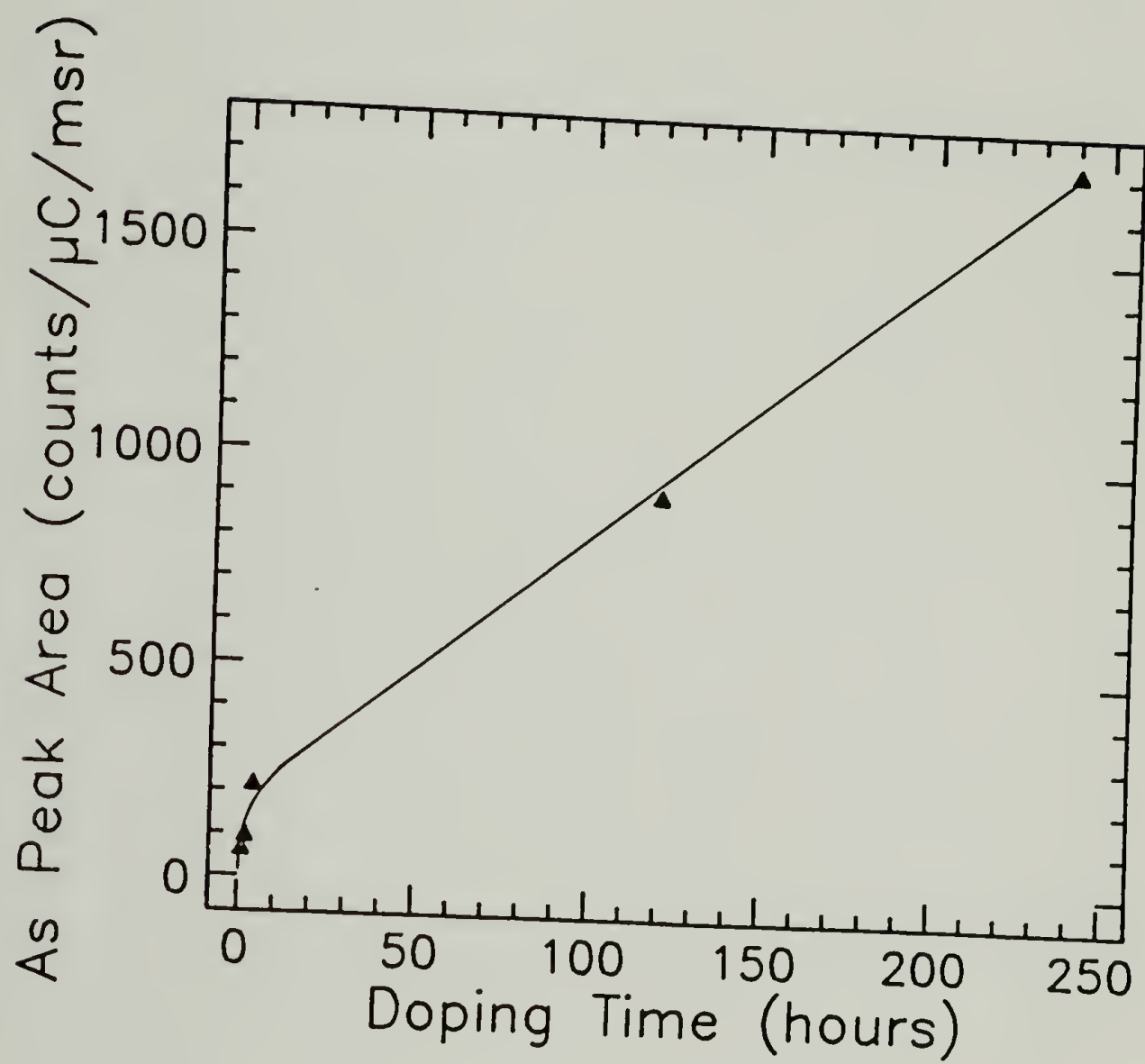
Figure 7.4   Integrated areas for As peak as a function of doping time.

165
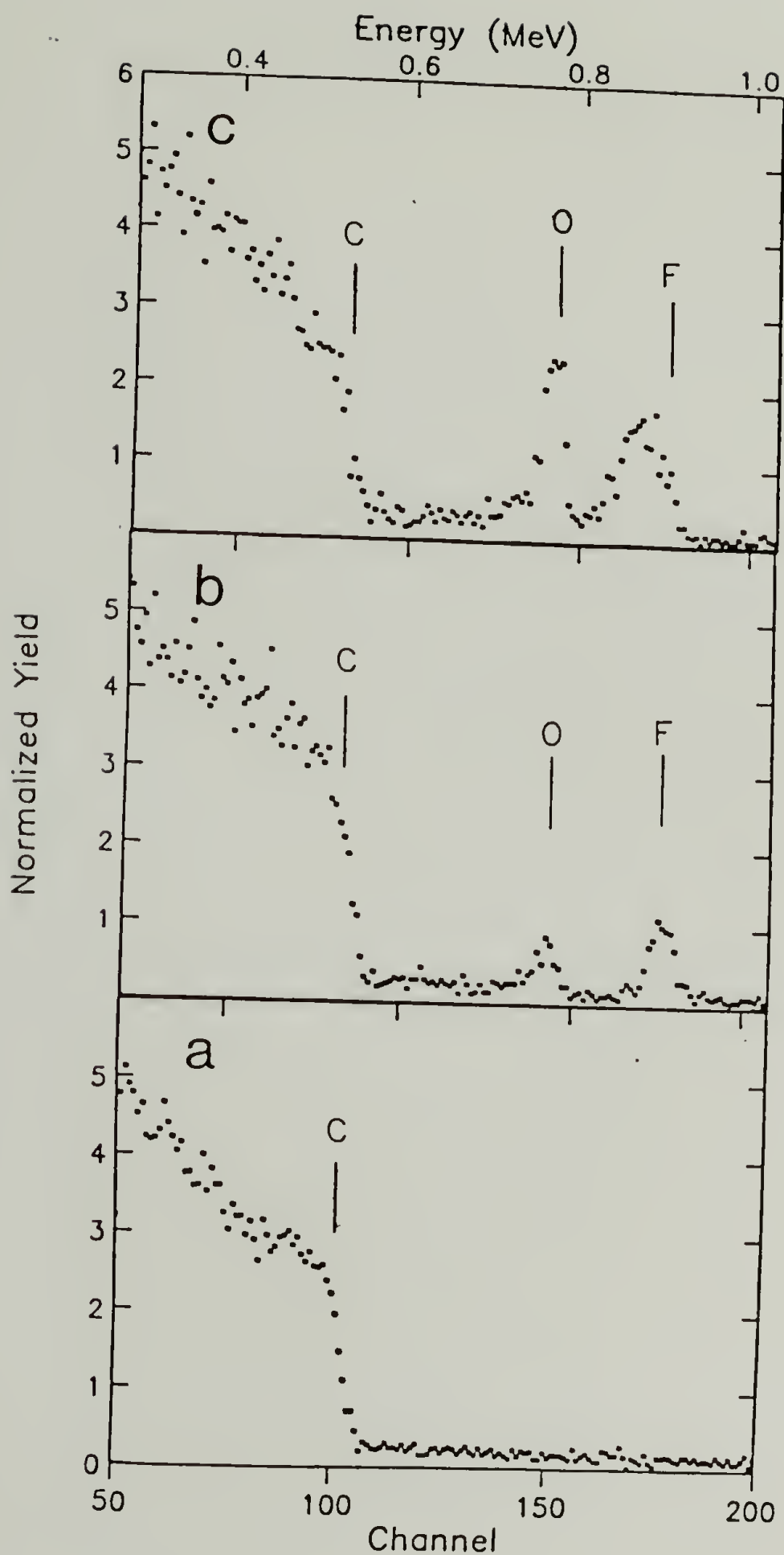
Figure 7.5   Carbon, Oxygen, Fluorine region of the RBS spectra for various
doping times: (a) pristine PPV, (b) 4 hours, (c) 5 days. The
surface energies of C, O, and F are indicated.
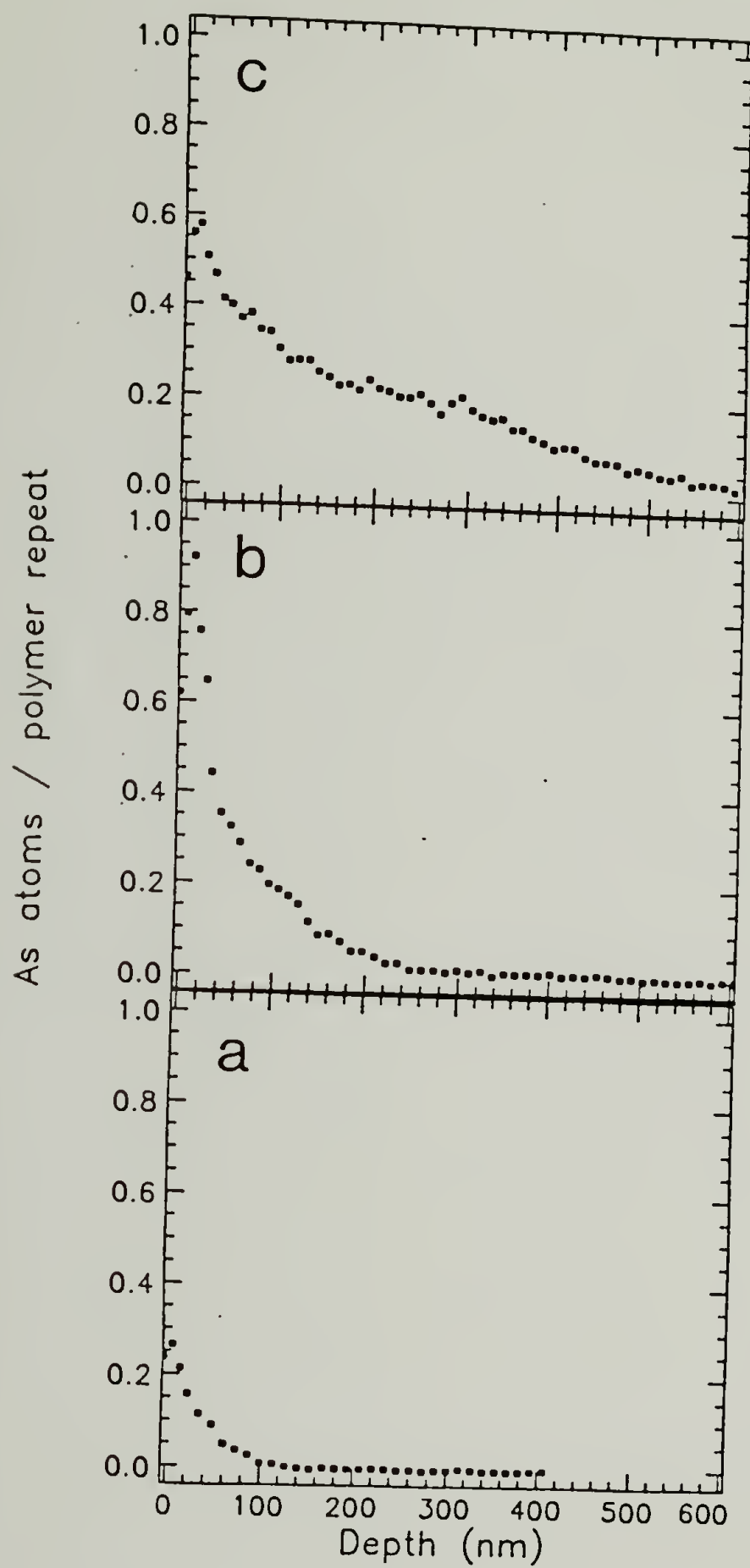
Figure 7.6   Depth profile of As in films doped for various times: (a) 4 hours,
(b) 5 days, (c) 10 days.
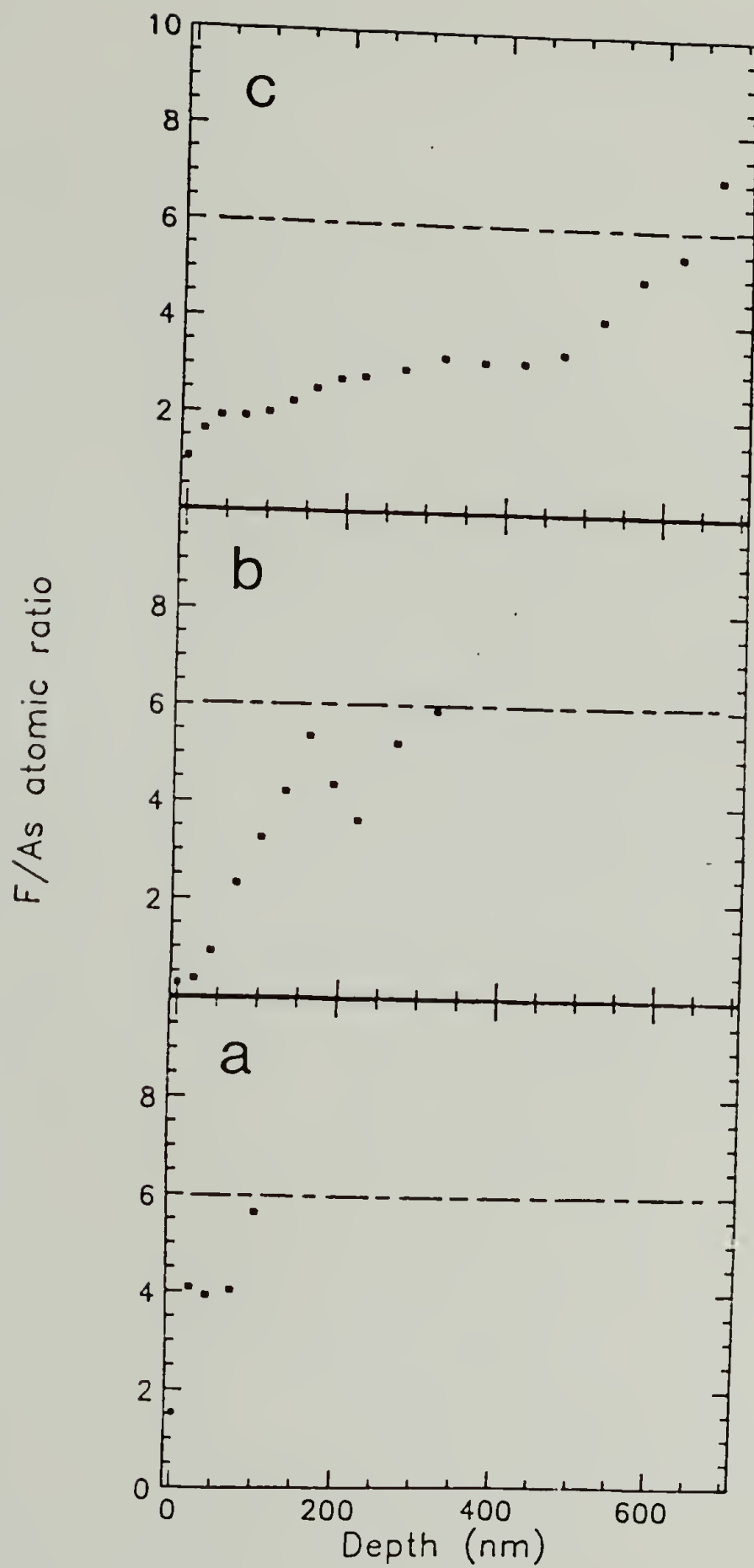
Figure 7.7   Fluorine to arsenic atomic ratio as a function of depth for various
doping times: (a) 4 hours, (b) 5 days, (c) 10 days.
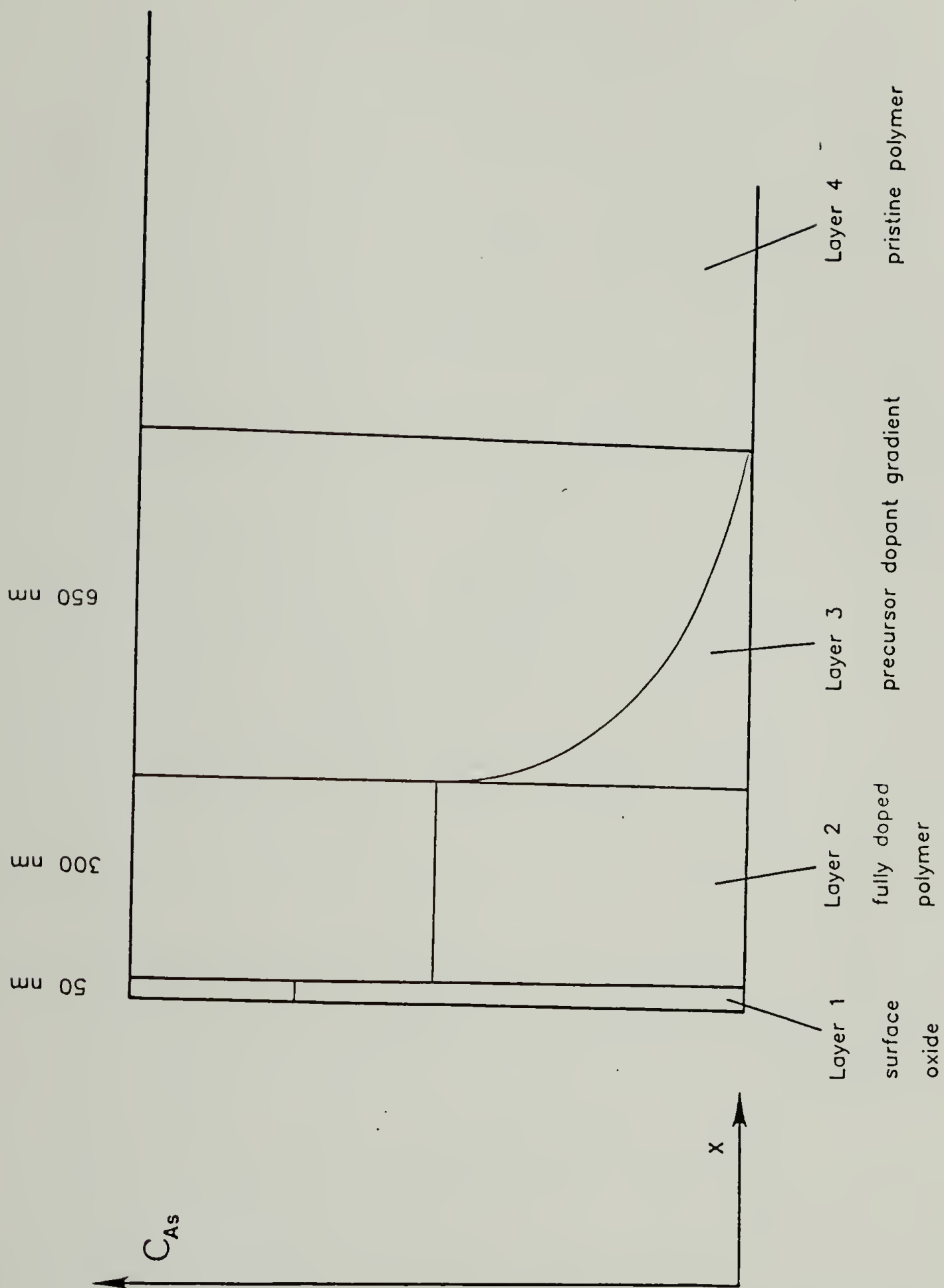
Figure 7.8   Physical model of "heavily doped" PPV.
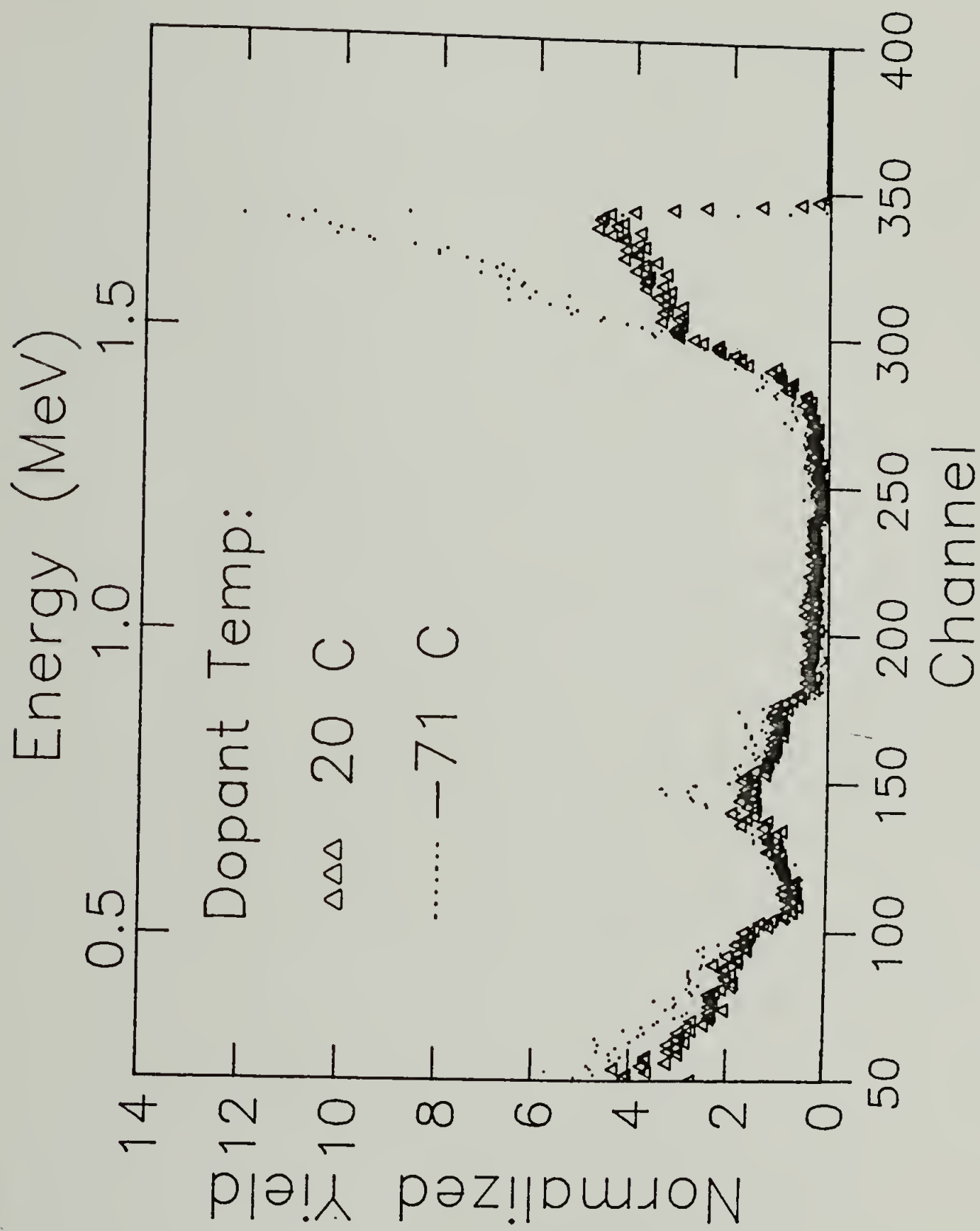
Figure 7.9   RBS spectra of AsF$_5$-doped PPV: .... doping performed while cryogenically trapping AsF$_3$ (T$_{dopant}$ = -71°C, 280 mmHg), △△△△△ doping performed at room temperature (total pressure 305 mmHg).

CHAPTER 8

CONCLUSIONS AND FUTURE DIRECTIONS

8.1 Summary of Results

The goal of this research has been to characterize the physical state of conductive PPV on levels ranging from the molecular crystalline state to bulk films.

The diffraction experiments have revealed a crystal-crystal transition to accompany the doping reactions. In the undoped state the PPV crystal has a monoclinic habit. Conductive PPV is found to have an expanded orthorhombic unit cell when the dopants are AsF_5, SbF_5, H_2SO_4 or ClO_4^-. With all these oxidizing dopants a 0.33 nm lateral spacing is observed which is characteristic of stacks of planar aromatic molecules. Thus, a crystal model is proposed in which the PPV chains stack one upon the other and these stacks are separated by a plane containing the dopant anion.

This physical arrangement of PPV chains has important implications for electron transport. Previous studies, both experimental and theoretical, have clearly demonstrated that conduction in organic polymers is related to the presence of an extensively π-conjugated backbone. This condition is satisfied in PPV and so electrical conduction within a single chain is easily envisioned. However, electrons or holes travelling under the influence of an applied electric field along a single PPV chain will encounter chain ends and other structural defects. Thus, interchain electron transport is crucial to the conduction of electricity in PPV. In the proposed structural model extensive overlap of π-orbitals exists between neighboring chains within a stack. In this way there is a pathway for transport transverse to the chain axis.

These conductive crystals are not large. The transmission electron microscopy presented in Chapter 6 has shown the undoped crystals to be on the order of 5.0 – 7.0 nm and equiaxed. As such only 8 – 10 repeat units along a single chain are incorporated into a single crystallite. The doped crystallites are also equiaxed and in the case of H_2SO_4 doping are somewhat smaller ranging around 4.0 nm. Therefore, even though electron transport is easily envisioned within the crystallite many grain boundaries must be traversed as charge carriers travel through the bulk film.

Within the first hour of AsF_5-doping the undoped crystals appear largely unchanged. However, high electrical conductivities are typically observed within minutes after commencement of the doping reaction. This implies that the disordered grain boundaries are preferentially doped at the early stages. This is reasonable since the grain boundaries are expected to present the least resistance to diffusion. At high doping levels undoped crystallites are not observed. Thus, the doped phase nucleates at the grain boundaries and subsequently grows at the expense of the undoped crystals in the thin layers observed by TEM.

The heterogeneous nature of the doping process has also been confirmed by x-ray diffraction in bulk films. At intermediate doping levels both undoped and doped phases are observed. Only at high doping levels does the undoped phase vanish.

The Rutherford backscattering results presented in Chapter 7 have followed the heterogeneous doping of bulk films. A strong surface effect is observed with only shallow dopant penetrations. Reaction with AsF_5 yielded a dopant penetration depth of approximately 1 μm after a 10 day exposure. The concentration profile is not characteristic of either Fickian or Case II diffusion. Rather, the profile is characteristic of diffusion accompanied by a rapid chemical reaction. These results indicate that the electrical conductivities typically measured on bulk films are only representative of charge carrier transport in a relatively shallow surface layer. In this

case the conductivity value can only represent a lower limit to the actual value since the entire sample thickness is used in the calculation. The spatial resolution (≈ 60 nm) of RBS in PPV allows an accurate measure of the actual conducting layer thickness. Using the RBS determined conducting layer thicknesses an intrinsic conductivity of 4×10^4 is estimated as a lower limit in AsF_5-doped PPV.

The stoichiometry of the doped complex is not certain. The x-ray diffraction analysis indicates a $AsF_6^-/C_8H_6^{\delta+}$ ratio of 1/2. However, analysis of the surface by XPS and the bulk by RBS suggest lower values in the range of 1/5 - 1/3. In addition, density measurements of highly doped bulk films indicate higher values between 1/2 - 1/1. The lower values may be attributable to imperfect complex formation in the significant volume of grain boundaries. The high density values may be due to chemical side reactions forming dense arsenic oxides. In any case, it is clear that the reactive nature of the dopants and the heterogeneous character of the doping process lead to serious complications in the determination of the doped phase stoichiometry. The x-ray diffraction results are judged to be the most reliable estimate of the stoichiometry since thay pertain to well formed regions possessing long range order.

8.2 Suggested Future Directions

Deeper understanding of the nature of conductive PPV could be gained in a number of areas. First, the physical arrangement and mobility of the AsF_6^- anions could be studied. ^{19}F NMR should be particulary suitable for this purpose. Second, the chemistry of H_2SO_4 doping in PPV needs to be addressed. This dopant is not as toxic or reactive as AsF_5 or SbF_5 and therefore is a more practical agent. Third, an extensive study could be initiated to investigate dopant penetration under a variety of doping conditions. Specifically, the plasticizing effect of AsF_3 in AsF_5-doped PPV is certainly a topic worth pursuing. Ultimately, this may lead to the fabrication of

electrical devices employing PPV as an active conducting component. In this regard it may also be important to investigate the ability to achieve preferred planar orientations by precursor polymer processing. With the doped crystal model proposed in this study a strong three-dimensional anisotropy should result if extensive preferred planar orientation could be attained.

The morphological study of this conducting polymer could also be furthered. Voltage contrast SEM studies would directly image the conductive pathways in a polymer under an applied electric field. Further, recent advances in SEM technology may allow imaging at a spatial resolution on the order of the crystallite size in uncoated conducting polymers. This type of study would be important for evaluating the effect of grain boundaries and kink bands on the electrical conduction process.

Aside from its electrical properties PPV also shows promising mechanical properties [57]. As thoroughly discussed elsewhere [49] precursor PPV is easily synthesized and processed. Because of its high modulus and strength PPV films and fibers could be effective reinforcing materials. Further, the undoped polymer possesses functional groups in the form of vinylene groups along the polymer backbone. Thus, chemical binding of a PPV reinforcing fiber could easily be made to a matrix material.

One further application in the area of PPV composites might be direct polymerization of a matrix compatible polymer from an SbF_5- or AsF_5-doped surface. As shown by the present study the dopant can be confined to a near-surface layer. In this way most of the fiber would possess the mechanical properties of undoped PPV. Lewis acids in general and organic SbF_6^- and PF_6^- salts in particular have been shown to be effective cationic polymerization initiators [156]. Contact of the doped surface with the appropriate monomer would result in the initiation of polymerization from the PPV surface. Composite materials containing PPV fibers

174

from whose surface another polymer has been synthesized may possess excellent matrix-fiber interfacial properties.

When considering the mechanical applications of PPV, however, it is important to note the low compressive strength implied by the ready formation of kink bands in PPV. Thus, as with high modulus fibers such as PBZT, PBZO, and Kevlar appropriate applications may be ones which primarily require improvements of tensile properties.

In summary, PPV is expected to be of practical importance based on its electrical, chemical, and mechanical properties.

STRUCTURE FACTOR CALCULATIONS FOR THE SIMULATION OF X-RAY DIFFRACTION PATTERNS

The x-ray intensities diffracted by PPV and doped PPV were calculated according to the following equations (see refs. [108] and [131] for a full description of scattering physics).

The total integrated intensity scattered by a crystallographic plane with Miller indices hkℓ is given by

$$I_{hk\ell} = F^2 PLTm \qquad \text{(A.1)}$$

where F is the structure factor for the periodic lattice, P is the polarization factor, L is the Lorentz factor, T is the temperature factor, and m is the multiplicity of the hkℓ plane.

The structure factor for the periodic crystalline lattice is calculated according to the following relation.

$$F_{hk\ell} = \sum_j f_j(2\Theta) \exp[2\pi i(hx_j + ky_j + \ell z_j)] \qquad \text{(A.2)}$$

In eqn(A.2) the summation is performed over all atoms, $f_j(2\Theta)$ is the angular dependent atomic scattering factor of the jth atom, and x_j, y_j, and z_j are the fractional atomic coordinates. Table A.1 lists the fractional atomic coordinates for the 16 carbon atoms residing in the undoped PPV unit cell. Scattering by hydrogen is neglected.

The polarization factor accounts for diffraction-induced x-ray polarization and is given by

$$P = (1 + \cos^2 2\Theta)/2 \qquad \text{(A.3)}$$

where 2Θ is the scattering angle.

The Lorentz factor is a weighting factor and describes the relative amount of the diffracted intensity sampled for each reflection. For equatorial reflections from fiber symmetric samples the Lorentz factor is given by the following equation.

$$L_{(hk0)} = 1/(\sin^2\Theta\cos\Theta) \tag{A.4}$$

The temperature factor is descriptive of the deviation of the atom from its equilibrium position due to thermal fluctuations and is given by

$$T = B(\sin^2\Theta/\lambda^2) \tag{A.5}$$

where B is the Debye-Waller factor. For these calculations the thermal fluctuations were assumed to be isotropic and a value of 0.2 nm^2 was used.

As calculated by the above equations the intensity can be plotted as delta functions at the appropriate scattering angle. However, for realistic graphical representations the total diffracted intensity was multiplied by the appropriate form factor. This factor accounts for the diffracting crystallite size and shape. Thus, the plotted intensity was calculated as

$$I_{hk\ell}(2\Theta) = I_{hk\ell} \, \Pi_{j=1,3} \, [\sin^2(\pi N_j r_j \, g)/\sin^2(\pi r_j \, g)] \tag{A.6}$$

where r_j is the vector representing the jth lattice parameter, g is the reciprocal lattice vector for the $hk\ell$ reflection, and N_j is the number of $hk\ell$ planes making up the crystal in the r_j direction.

Table A.1
Fractional atomic coordinates of the carbon atoms residing in a single undoped PPV unit cell.

Atom	x	y	z
Chain I			
C_1	0.130	0.358	0.075
C_2	0.150	0.319	0.273
C_3	0.029	0.101	0.238
C_4	0.186	0.563	0.497
C_5	0.014	0.001	0.429
C_6	0.171	0.463	0.688
C_7	0.085	0.245	0.653
C_8	0.070	0.206	0.851
Chain II			
C_9	0.630	0.706	0.000
C_{10}	0.615	0.745	0.236
C_{11}	0.529	0.963	0.421
C_{12}	0.686	0.564	0.279
C_{13}	0.514	1.000	0.649
C_{14}	0.671	0.601	0.507
C_{15}	0.585	0.819	0.692
C_{16}	0.570	0.858	0.928

```
C
C
C          Program:  SFACTOR.FOR
C
C          Author:  Mike Masse
C
C          Abstract:   This program calculates the integrated intensities
C                      expected in X-ray diffraction.  The intensities are
C                      corrected for polarization and the Lorentz factor
C                      for fiber symmetry is applied.  Reduction in intensity
C                      due to isotropic thermal vibrations is also performed.
C                      The atomic scattering factors are modelled using a
C                      fifth order polynomial.  The information required to
C                      run the program consists of the unit cell parameters
C                      and the fractional coordinates of all atoms in the
C                      unit cell.  This information must be held in an
C                      external data file.
C
C          Data file format:
C
C                      line 1:   material identification up to 64 characters
C                      line 2:   NC        the number of atoms in the UC
C                      line 3:   NA        the number of carbon atoms in the UC
C                      line 4:   NF        the number of fluorine atoms in the UC
C                      line 5:   AV(1-3)   the vector representation of a
C                      line 6:   BV(1-3)   the vector representation of b
C                      line 7:   CV(1-3)   the vector representation of c
C                      line 8:   alpha,beta,gamma
C              line 9 to 9+N:    X(I), Y(I), Z(I)  the atomic coordinates, these
C                                          should be arranged so that all carbons
C                                          are listed, then the arsenics, then the
C                                          fluorines.
C
C          Subroutines:
C
C                      BRAGG.FOR:   calculates the plane spacing given the
C                                   unit cell parameters and the Miller indices
C                      CROSS.FOR:   performs cross product of two vectors
C                      FCARBON.FOR:  holds the fifth order polynomial
C                                   modelling the atomic scattering factor
C                                   of carbon
C                      FARSENIC.FOR:  ditto for As
C                      FFLUORINE.FOR:  ditto for F
C
C          Written:  November 20, 1987
C
C**********************************************************************************
C
       DIMENSION X(100),Y(100),Z(100),AV(3),BV(3),CV(3),ASTAR(3),BSTAR(3)
      &,CSTAR(3),G(3)
       INTEGER H,K,L
       REAL LZ,LAMBDA,INT,P,FF,ILIM
       CHARACTER NAME*32,NAME2*32,POLYMER*64
       COMMON A,B,C,ALPHA,BETA,GAMMA
       DATA PI /3.14159/, LAMBDA /1.542/
C
       WRITE(6,*) 'Enter the name of the data file.'
       READ(5,1) NAME
       OPEN(UNIT=2,FILE=NAME,STATUS='OLD')
1      FORMAT(A32)
C
901    WRITE(6,*) 'Enter the name of the output file.'
       READ(5,1) NAME2
```

179

```fortran
C         OPEN(UNIT=3,FILE=NAME2,STATUS='NEW',ERR=901)

          WRITE(6,*) 'Enter dopant lattice multiplier.'
          READ(5,*) DM
C
          WRITE(6,*) 'Enter the minimum intensity limit.'
          READ(5,*) ILIM
C
          READ(2,99) POLYMER
99        FORMAT(A64)
C
          READ(2,*) NC
          READ(2,*) NA
          READ(2,*) NF
          READ(2,*)  (AV(I),  I=1,3)
          READ(2,*)  (BV(I),  I=1,3)
          READ(2,*)  (CV(I),  I=1,3)
          READ(2,*)  ALPHA,BETA,GAMMA
C
          N=NC+NA+NF
          DO 2 I=1,N
          READ(2,3)  X(I),Y(I),Z(I)
2         CONTINUE
3         FORMAT(3F8.3)
          CLOSE(UNIT=2)
C
          A=SQRT(AV(1)**2+AV(2)**2+AV(3)**2)
          B=SQRT(BV(1)**2+BV(2)**2+BV(3)**2)
          C=SQRT(CV(1)**2+CV(2)**2+CV(3)**2)
C
          ALPHA=2*PI*ALPHA/360.
          BETA=2*PI*BETA/360.
          GAMMA=2*PI*GAMMA/360.
C
C         PRINT HEADER
          WRITE(3,99) POLYMER
          WRITE(3,4)
4         FORMAT(2X,'h',3X,'k',3X,'l',4X,'d,A',9X,'Int',7x,'F**2',8x,'LZ',
         &10X,'T',8X,'P')
C
C         PICK CRYSTALLOGRAPHIC INDEX
C
          DO 30 L=0,3
          DO 20 K=0,4
          DO 10 H=0,4
C
          J=0
          IF(H.EQ.J.AND.K.EQ.J.AND.L.EQ.J) GO TO 10
C
C         COMPUTE BRAGG ANGLE
          CALL BRAGG(H,K,L,D)
          THETA=ASIN(LAMBDA/(2*D))
C
C         ATOMIC SCATTERING FACTOR
          W=1/(2*D)
          CALL FCARBON(W,FC)
          CALL FARSENIC(W,FA)
          CALL FFLUORINE(W,FFL)
          F1=0.
          F2=0.
C
```

```fortran
C         STRUCTURE FACTOP
          DO 40 I=1,N
          F=FC
          IF(I.GT.NC) F=FA*DM
          NT=NC+NA
          IF(I.GT.NT) F=FFL*DM
          F1=F1+COS(2*PI*(H*X(I)+K*Y(I)+L*Z(I)))*F
40        F2=F2+SIN(2*PI*(H*X(I)+K*Y(I)+L*Z(I)))*F
          FF=(F1**2+F2**2)
C
C         TEMPERATURE FACTOR SQUARED
          DW=2.0
          T=EXP(-2.0*DW*(SIN(2*THETA))**2/(LAMBDA**2))
C
C         POLARIZATION FACTOR
          P=(1+COS(2*THETA)**2)/2
C
C         LORENTZ FACTOR
C         Compute reciprocal lattice parameters
          VUC=A*B*C*SQRT(1-(COS(ALPHA))**2-(COS(BETA))**2-(COS(GAMMA))**2
         &-2*COS(ALPHA)*COS(BETA)*COS(GAMMA))
C
          CALL CROSS(BV,CV,ASTAR)
          DO 50 I=1,3
50        ASTAR(I)=ASTAR(I)/VUC
C
          CALL CROSS(CV,AV,BSTAR)
          DO 60 I=1,3
60        BSTAR(I)=BSTAR(I)/VUC
C
          CALL CROSS(AV,BV,CSTAR)
          DO 70 I=1,3
70        CSTAR(I)=CSTAR(I)/VUC
C
C         Reciprocal lattice vector
          DO 80 I=1,3
80        G(I)=H*ASTAR(I)+K*BSTAR(I)+L*CSTAR(I)
C
C         Modulus
          GABS=SQRT(G(1)**2+G(2)**2+G(3)**2)
C
C         Angle between G and z
          PHI=ACOS(G(3)/GABS)
C
          ITEST=ABS(H)+ABS(K)
          XLIM=0.035
          IF(ITEST.GT.-1.AND.ITEST.LT.1.AND.PHI.LT.XLIM) THEN
C         Half width at half height, radians( 2 degrees).
          HWHH=0.030
          CT=0.815*HWHH
C         Lorentz factor for meridional reflection (c and c* parallel)
          LZ=1/(CT*COS(THETA)*(SIN(THETA))**2)
C
          ELSE
C         Lorentz factor for general reflection
          LZ=1/(SIN(PHI)*COS(THETA)*(SIN(THETA))**2)
          ENDIF
C
C         COMPUTE INTEGRATED INTENSITY
          INT=FF*T*P*LZ
C
C         PRINT RESULTS
          IF(INT.GT.ILIM) WRITE(3,5) H,K,L,D,INT,FF,LZ,T,P
```

```
   5      FORMAT(I2,2X,I2,2X,I2,4X,F5.2,2X,F11.1,3X,F8.1,3X,F8.1
        &,3X,F8.3,3X,F6.4)
   C
  10      CONTINUE
  20      CONTINUE
  30      CONTINUE
          CLOSE(UNIT=3)
   C
          STOP
          END
```

```
C
      SUBROUTINE CROSS(A,B,C)
C
C     Abstract:  This subroutine calculates the cross-product
C                of two vectors A and B.  The result is returned
C                as vector C.
C
C     Author:  Mike Masse
C*****************************************************************
C
      DIMENSION A(3),B(3),C(3)
C
      C(1)=ABS(A(2)*B(3))-ABS(A(3)*B(2))
      C(2)=ABS(A(3)*B(1))-ABS(A(1)*B(3))
      C(3)=ABS(A(1)*B(2))-ABS(A(2)*B(1))
C
      RETURN
      END
```

```fortran
C*****************************************
C
      SUBROUTINE FCARBON(X,F)
C
C     Abstract:  This subroutine calculates the atomic
C                scattering factor carbon as a function
C                of sin(  theta)/lambda, here represented
C                by the variable X.  The equation is a fifth order
C                polynomial fit to the data listed in The International
C                Tables for X-Ray Diffraction.
C
C     Author:  Mike Masse
C*********************************************************************************
C
      FO=6.000
      A=-2.6035
      B=-93.440
      C=306.21
      D=-361.61
      E=147.36
C
      F=FO+A*X+B*X**2+C*X**3+D*X**4+E*X**5
C
      RETURN
      END
```

```fortran
C****************************************************
C
      SUBROUTINE FFLUORINE(X,F)
C
C     Abstract:   This subroutine calculates the atomic
C                 scattering factor fluorine as a function
C                 of sin(  theta)/lambda here represented
C                 by the variable X.  The equation is a fifth order
C                 polynomial fit to the data listed in The International
C                 Tables for X-Ray Diffraction.
C
C     Author:  Mike Masse
C**************************************************************************
C
      F0=10.000
      A=1.1608
      B=-136.01
      C=362.67
      D=-375.34
      E=139.06
C
      F=F0+A*X+B*X**2+C*X**3+D*X**4+E*X**5
C
      RETURN
      END
```

```fortran
C************************************************************************
C
      SUBROUTINE FARSENIC(X,F)
C
C     Abstract:   This subroutine calculates the atomic
C                 scattering factor arsenic as a function
C                 of sin(  theta)/lambda here represented
C                 by the variable X.  The equation is a fifth order
C                 polynomial fit to the data listed in The International
C                 Tables for X-Ray Diffraction.
C
C     Author:  Mike Masse
C************************************************************************
C
      FO=28.000
      A=1.1538
      B=-84.842
      C=82.316
      D=-1.8139
      E=-18.340
C
      F=FO+A*X+B*X**2+C*X**3+D*X**4+E*X**5
C
      RETURN
      END
```

```
C
C
C       Program:  EQINT.FOR
C
C       Author:  Mike Masse
C
C       Abstract:  This program calculates the intensity distribution
C                  along the equator for a crystal of finite size.
C                  The intensities are calculated as the product of the
C                  lattice structure factor and the lattice form factor.
C                  The intensities are corrected for polarization and the
C                  Lorentz factor for equatorial reflections is applied.
C                  Reduction in intensity due to isotropic thermal vibrations
C                  is also performed.  The atomic scattering factors are
C                  modelled using a fifth order polynomial.  The
C                  information required to run the program consists of the
C                  unit cell parameters and the fractional coordinates of all
C                  atoms in the unit cell.  This information must be
C                  held in an external data file.
C
C
C       Data file format:   (same as for SFACTOR.FOR)
C
C               line 1:   material identification up to 64 characters
C               line 2:   NC         the number of atoms in the UC
C               line 3:   NA         the number of carbon atoms in the UC
C               line 4:   NF         the number of fluorine atoms in the UC
C               line 5:   AV(1-3)    the vector representation of a
C               line 6:   BV(1-3)    the vector representation of b
C               line 7:   CV(1-3)    the vector representation of c
C               line 8:   alpha,beta,gamma
C          line 9 to 9+N:  X(I), Y(I), Z(I)  the fractional atomic
C                                 coordinates, these should be arranged
C                                 so that all carbons are listed, then
C                                 the arsenics, then the fluorines.
C
C       Subroutines:
C
C               BRAGG.FOR:  calculates the plane spacing given the
C                           unit cell parameters and the Miller indices
C               FCARBON.FOR:  holds the fifth order polynomial
C                             modelling the atomic scattering factor
C                             of carbon
C               FARSENIC.FOR:  ditto for As
C               FFLUORINE.FOR:  ditto for F
C               CROSS.FOR:  calculates the cross product of two vectors
C
C       Written:  March 3, 1988
C
C***************************************************************************
C
        DIMENSION X(100),Y(100),Z(100),AV(3),BV(3),CV(3),ASTAR(3),
       &BSTAR(3),CSTAR(3),G(3),PHI(3)
        INTEGER H,K,L,N1,N2,N3
        REAL LZ,LAMBDA,INT,P,FF,J1,J2,J3,JF,IMAX
        CHARACTER NAME*32,POLYMER*64
        COMMON A,B,C,ALPHA,BETA,GAMMA
        DATA PI /3.14159/, LAMBDA /1.542/
C
        WRITE(6,*) 'Enter the name of the data file.'
        READ(5,1) NAME
1       FORMAT(A32)
```

187

```fortran
      WRITE(6,*) 'Enter the dopant lattice multiplier.'
      READ(5,*) DM
C
      OPEN(UNIT=2,FILE=NAME,STATUS='OLD')
      OPEN(UNIT=3,FILE='EQINT.DAT')
C
      READ(2,99) POLYMER
99    FORMAT(A64)
C
      READ(2,*) NC
      READ(2,*) NA
      READ(2,*) NF
      READ(2,*) (AV(I), I=1,3)
      READ(2,*) (BV(I), I=1,3)
      READ(2,*) (CV(I), I=1,3)
      READ(2,*) ALPHA,BETA,GAMMA
C
      N=NC+NA+NF
      NT=NC+NA
      DO 2 I=1,N
      READ(2,3) X(I),Y(I),Z(I)
2     CONTINUE
3     FORMAT(3F8.3)
      CLOSE(UNIT=2)
C
      A=SQRT(AV(1)**2+AV(2)**2+AV(3)**2)
      B=SQRT(BV(1)**2+BV(2)**2+BV(3)**2)
      C=SQRT(CV(1)**2+CV(2)**2+CV(3)**2)
      ALPHA=2*PI*ALPHA/360.
      BETA=2*PI*BETA/360.
      GAMMA=2*PI*GAMMA/360.
C
      WRITE(6,*) 'Enter Miller indices, h and k:'
      READ(5,*) H,K
      L=0
C
      WRITE(6,*) 'Enter the number of planes N1 and N2:'
      READ(5,*) N1,N2
      N3=50
C
      WRITE(6,*) 'Enter multiplicity:'
      READ(5,*) MP
C
C     COMPUTE BRAGG ANGLE
      CALL BRAGG(H,K,L,D)
      THETA=ASIN(LAMBDA/(2*D))
C
C     ATOMIC SCATTERING FACTOR
      W=1/(2*D)
      CALL FCARBON(W,FC)
      CALL FARSENIC(W,FA)
      CALL FFLUORINE(W,FFL)
      F1=0.
      F2=0.
C
C     STRUCTURE FACTOR
      DO 40 I=1,N
      F=FC
      IF(I.GT.NC) F=FA*DM
      IF(I.GT.NT) F=FFL*DM
      F1=F1+COS(2*PI*(H*X(I)+K*Y(I)+L*Z(I)))*F
40    F2=F2+SIN(2*PI*(H*X(I)+K*Y(I)+L*Z(I)))*F
      FF=(F1**2+F2**2)
```

```fortran
C
C           TEMPERATURE FACTOR SQUARED
            DW=2.0
            T=EXP(-2.0*DW*(SIN(2*THETA))**2/(LAMBDA**2))
C
C           POLARIZATION FACTOR
            P=(1+COS(2*THETA)**2)/2
C
C           LORENTZ FACTOR, EQUATORIAL REFLECTIONS
            LZ=1.0/((SIN(THETA))**2*COS(THETA))
C
C           COMPUTE INTEGRATED INTENSITY
            IMAX=FF*T*P*LZ*MP
C           Compute reciprocal lattice parameters
            VUC=A*B*C*SQRT(1-(COS(ALPHA))**2-(COS(BETA))**2-(COS(GAMMA))**2
           &-2*COS(ALPHA)*COS(BETA)*COS(GAMMA))
C
            CALL CROSS(BV,CV,ASTAR)
            DO 150 I=1,3
150         ASTAR(I)=ASTAR(I)/VUC
C
            CALL CROSS(CV,AV,BSTAR)
            DO 160 I=1,3
160         BSTAR(I)=BSTAR(I)/VUC
C
            CALL CROSS(AV,BV,CSTAR)
            DO 170 I=1,3
170         CSTAR(I)=CSTAR(I)/VUC
C
C           Reciprocal lattice vector
            DO 180 I=1,3
180         G(I)=H*ASTAR(I)+K*BSTAR(I)
C
C           Modulus
            GABS=SQRT(G(1)**2+G(2)**2+G(3)**2)
C
C           Calculate angles between reciprocal lattice vector and
C           coordinate axes.
            DO 300 I=1,3
300         PHI(I)=ACOS(G(I)/GABS)
C
C           CALCULATE INTENSITY DISTRIBUTION USING FORM FACTOR
            DELT=0.020
            GMAX=(2.0/LAMBDA)*SIN(THETA+DELT)
            GMIN=(2.0/LAMBDA)*SIN(THETA-DELT)
            DELG=(GMAX-GMIN)/500.0
C
            GABS=GMIN
C
            DO 400 I=1,500
            THETA2=2*ASIN(LAMBDA*GABS/2.0)
            A1=1.0E-06
            B1=1.0E-06
            C1=1.0E-06
C
            DO 500 M=1,3
            G(M)=GABS*COS(PHI(M))
            A1=A1+(G(M)*AV(M))
            B1=B1+(G(M)*BV(M))
            C1=C1+(G(M)*CV(M))
500         CONTINUE
```

```fortran
      J1=(SIN(PI*A1*N1))**2/(SIN(PI*A1))**2
      J2=(SIN(PI*B1*N2))**2/(SIN(PI*B1))**2
      J3=(SIN(PI*C1*N2))**2/(SIN(PI*C1))**2
      JF=J1*J2*J3
      INT=IMAX*JF/(N1*N2*N3*1.0E+08)
      WRITE(3,600)  TAN(THETA2),INT
      GABS=GABS+DELG
400   CONTINUE
600   FORMAT(F14.7,1X,F14.7)
C
      CLOSE(UNIT=3)
C
      STOP
      END
```

```
C
C          Program:  COORD.FOR
C
C          Abstract:  This program calculates the coordinates of the
C                     atoms of a molecular structure after translation
C                     rotation operations.  The z-axis is defined to be
C                     initially colinear with the chain axis.
C                     The original structure must be supplied in a data
C                     file in the format acceptable by the Molecular
C                     Graphics Program.  The resulting molecule is written
C                     to file coord.dat.  The program is written to accept
C                     100 atoms in the original data.  If the number of atoms
C                     exceeds this limit the dimension statment only must be
C                     changed.
C
C          Written:  Mike Masse   August 7, 1987
C
C     ***************************************************************
C
           DIMENSION X(100),Y(100),Z(100),XN(100),YN(100),ZN(100),LABEL(100)
          +,T(2,2)
           CHARACTER LABEL*5,NAME*32,REPLY*1
C
           WRITE(6,*) 'Enter the name of the data file'
           READ(5,1) NAME
1          FORMAT(A32)
           OPEN(UNIT=2,FILE=NAME,STATUS='OLD')
           OPEN(UNIT=3,FILE='COORD.DAT')
C
           WRITE(6,*) 'Enter the number of atoms in molecule'
           READ(5,*) N
C
           DO 2 I=1,N
2          READ(2,3) X(I),Y(I),Z(I)
3          FORMAT(3F8.3)
C
C
           WRITE(6,*) 'Rotation? [y/n]'
           READ(5,201) REPLY
201        FORMAT(A1)
           IF(REPLY.EQ.'n') GO TO 8
           WRITE(6,*) 'Enter the angle of rotation about z (degrees)'
           READ(5,*) THETA
           CALL TRANSFORM(THETA,T)
C
           DO 7 I=1,N
           XN(I)=X(I)*T(1,1)+Y(I)*T(1,2)
7          YN(I)=X(I)*T(2,1)+Y(I)*T(2,2)
           DO 11 I=1,N
           X(I)=XN(I)
11         Y(I)=YN(I)
C
           WRITE(6,*) 'Enter the angle of rotation about x (degrees)'
           READ(5,*) THETA
           CALL TRANSFORM(THETA,T)
C
           DO 10 I=1,N
           YN(I)=Y(I)*T(1,1)+Z(I)*T(1,2)
10         ZN(I)=Y(I)*T(2,1)+Z(I)*T(2,2)
           DO 12 I=1,N
           Z(I)=ZN(I)
12         Y(I)=YN(I)
```

```fortran
C
      WRITE(6,*) 'Enter the angle of rotation about y (degrees)'
      READ(5,*) THETA
      CALL TRANSFORM(THETA,T)
C
      DO 13 I=1,N
      ZN(I)=Z(I)*T(1,1)+X(I)*T(1,2)
13    XN(I)=Z(I)*T(2,1)+X(I)*T(2,2)
      DO 14 I=1,N
      Z(I)=ZN(I)
14    X(I)=XN(I)
C
8     WRITE(6,*) 'Translation? [y/n]'
      READ(5,201) REPLY
C
      IF(REPLY.EQ.'n') GO TO 6
      WRITE(6,*) 'Enter the coordinates of the translation vector'
      WRITE(6,*) 'in Angstroms.'
      READ(5,*) A1,A2,A3
C
      DO 5 I=1,N
      X(I)=X(I)+A1
      Y(I)=Y(I)+A2
5     Z(I)=Z(I)+A3
C
6     DO 9 I=1,N
9     WRITE(3,3) X(I),Y(I),Z(I)
C
      CLOSE(UNIT=2)
      STOP
      END
C
      SUBROUTINE TRANSFORM(THETA,T)
      DIMENSION T(2,2)
      THETA=2*3.14159*THETA/360.
      T(1,1)=COS(THETA)
      T(1,2)=-SIN(THETA)
      T(2,1)=SIN(THETA)
      T(2,2)=COS(THETA)
      RETURN
      END
```

```
C
C       Program:  DIST.FOR
C
C       Abstract:  This program calculates the interatomic
C                  distances for a set of atoms represented
C                  by xyz atomic coordinates.  The data must be held
C                  in an external data file with the form:
C
C                  line 1: character string lable, 64 char. max.
C                  line 2: the total number of atoms
C                  line 3 to 3+NTOT:
C                          the atomic label and xyz coordinates in
C                          (a5,3f8.3) format.  The atomic label should
C                          be the atomic symbol and the atomic index.
C                          For instance, if the 13th carbon atom was at
C                          the origin then this line would appear as
C                          C13    0.000    0.000    0.000
C
C       Written: April 24, 1988   Mike Masse
C
C*******************************************************************
C
        CHARACTER NAME*32, LABEL*64, ATOM(100)*5
        REAL X(100), Y(100), Z(100)
C
        WRITE(6,*) 'Enter name of data file.'
        READ(5,100) NAME
100     FORMAT(A32)
C
        OPEN(UNIT=2, FILE=NAME, STATUS='OLD')
        READ(2,101) LABEL
101     FORMAT(A64)
C
C       Read data file
        READ(2,*) NTOT
C
        DO 20 I=1,NTOT
        READ(2,102) ATOM(I), X(I), Y(I), Z(I)
20      CONTINUE
102     FORMAT(A5,3F8.3)
        CLOSE(UNIT=2)
C
200     WRITE(6,*) 'Enter name of output file.'
        READ(5,100) NAME
        OPEN(UNIT=3, FILE=NAME, STATUS='NEW',ERR=201)
        GO TO 202
201     WRITE(6,*) 'File of that name already exists, pick another.'
        GO TO 200
202     WRITE(3,101) LABEL
        WRITE(3,*) NTOT
C
C       Calculate and distances and print to data file
        DO 40 I=1, NTOT-1
        DO 30 J=I+1, NTOT
        DIST=SQRT((X(I)-X(J))**2+(Y(I)-Y(J))**2+(Z(I)-Z(J))**2)
        WRITE(3,103)  ATOM(I), ATOM(J), DIST
30      CONTINUE
40      CONTINUE
103     FORMAT(A5,'-',A5,3X,F6.3)
C
        CLOSE(UNIT=3)

        STOP
        END
```

REFERENCES

1. Blythe, A.R. <u>Electrical Properties of Polymers</u> Cambridge University Press, Cambridge, 1979.

2. Seanor, D.A. "Electrical Conduction in Polymers" in <u>Electrical Properties of Polymers</u> (D.A. Seanor, ed.) Academic Press, NY, 1982.

3. Chiang, C.K., Fincher, C.R., Park, Y.W., Heeger, A.H., Shirakawa, H., Louis, E.J., Gau, S.C. and MacDiarmid, A.G. "Electrical Conductivity in Doped Polyacetylene" *Phys. Rev. Lett.* **39** 1098 (1977).

4. Omar, M.A. <u>Elementary Solid State Physics</u> Addison-Wesley, Reading, MA, 1975.

5. Bednorz, J.G. and Muller, K.A. "Possible High T_c Superconductivity in the Ba-La-Cu-O System" *Z. Phys. B* **64** 189 (1986).

6. Wu, M.K., Ashburn, J.R., Torng, C.J., Hor, P.H., Meng, R.L., Gao, L., Huang, Z.J., Wang, Y.Q. and Chu, C.W. "Superconductivity at 93K in a New Mixed-Phase Y-Ba-Cu-O Compound System at Ambient Pressure" *Phys. Rev. Lett.* **58** 908 (1987).

7. Gallagher, P.K., O'Bryan, H.M., Sunshine, S.A. and Murphy, D.W. "Oxygen Stoichiometry in $Ba_2YCu_3O_x$" *Mat. Res. Bull.* **22** 995 (1987).

8. Schuller, I.K. and Jorgensen, J.D. "Structure of High T_c Oxide Superconductors" *Mat. Res. Soc. Bull.* **14** 27 (1989).

9. Schrieffer, J.R. "Interview with Robert Schrieffer" *Supercurrents* March (1989).

10. Chaudhari, P. "Critical Currents in the YBaCuO Compound Superconducting Thin Films" *Jap. J. Appl. Phys. Suppl.* **26-3** 2023 (1987).

11. Deutscher, B. and Muller, K.A. "Origin of Superconductive Glassy State and Extrinsic Critical Currents in High-T_c Oxides" *Phys. Rev. Lett.* **59** 1745 (1987).

12. Heeger, A.J., Kivelson, S., Schrieffer, J.R. and Su, W.-P. "Solitons in Conducting Polymers" *Rev. Mod. Phys.* **60** 781 (1988).

13. Bredas, J.L. and Street, G.B. "Polarons, Bipolarons, and Solitons in Conducting Polymers" *Acc. Chem. Res.* **18** 309 (1985).

194

14. Lahti, P.M., Obrzut, J. and Karasz, F.E. "Use of the Pariser-Parr-Pople Approximation to Obtain Practically Useful Predictions for Electronic Spectral Properties of Conducting Polymers" *Macromolecules* 20 2023 (1987).

15. Gagnon, D.R., Capistran, J.D., Karasz, F.E. and Lenz, R.W. "Conductivity Anisotropy in Oriented Poly(*p*-Phenylene Vinylene)" *Polym. Bull.* 12 293 (1984).

16. Park, Y.W., Druy, M.A., Chiang, C.K., MacDiarmid, A.G., Heeger, A.J., Shirakawa, H. and Ikeda, S. "Anisotropic Electrical Conductivity of Partially Oriented Polyacetylene" *J. Polym. Sci. (Letters)* 17 195 (1979).

17. Shirakawa, H. and Ikeda, S. "Preparation and Morphology of As-Prepared and Highly Stretch-Aligned Polyacetylene" *Synth. Met.* 1 175 (1979).

18. Skotheim, T.A. (ed.) <u>Handbook of Conducting Polymers</u> Vol. 1 & 2, Marcel Dekker, NY, 1986.

19. Duke, C.B. and Paton, A. "Dependence of Polymer Electronic Structure on Molecular Architecture: Polyacetylenes, Polythiophenes, and Polythienylene" in <u>Conducting Polymers</u> Plenum Press, NY 1981.

20. Tanaka, K. and Yamabe, T. "Design of Synthetic Polymers with Metallic Properties" *Makrom. Chem. Supp.* 14 45 (1985).

21. Basescu, N., Liu, Z.-X., Moses, D., Heeger, A.J., Naarmann, H. and Theophilou, N. "High Electrical Conductivity in Doped Polyacetylene" *Nature* 327 403 (1987).

22. Thakur, M. "A Class of Conducting Polymers Having Nonconjugated Backbones" *Macromolecules* 21 661 (1988).

23. Wnek, G.E., Chien, J.C.W., Karasz, F.E. and Lillya, C.P. "Electrically Conducting Derivative of Poly(*p*-phenylene vinylene)" *Polymer Comm.* 20 1441 (1979).

24. Reynolds, J.R., Karasz, F.E., Chien, J.C.W., Gourley, K.D. and Lillya, C.P. "Electrically Conducting Aromatic Polymers: Poly(Phenylene Vinylene) and its Analogs" *J. Phys.* 44 C3-693 (1983).

25. Gourley, K.D., Lillya, C.P., Reynolds, J.R. and Chien, J.C.W. "Electrically Conducting Polymers: AsF$_5$-Doped Poly(phenylene vinylene) and Its Analogs" *Macromolecules* 17 1025 (1984).

26. Wessling, R.A. and Zimmerman, R.G. "Polyelectrolytes from Bis Sulfonium Salts" U.S. Patent 3,401,152 (1968).

27. Lahti, P.M., Modarelli, D.A., Denton III, F.R., Lenz, R.W., and Karasz, F.E. "Polymerization of α,α′-Bis(dialkyl-sulfonio)-*p*-xylene Dihalides via *p*-xylene Intermediates: Evidence for a Nonradical Mechanism" *J. Am. Chem. Soc.* **110** 7258 (1988).

28. Karasz, F.E., Capistran, J.D., Gagnon, D.R., and Lenz, R.W. "High Molecular Weight Polyphenylene Vinylene" *Mol. Cryst. Liq. Cryst.* **118** 327 (1985).

29. Gagnon, D.R., Capistran, J.D., Karasz, F.E., Lenz, R.W. and Antoun, S. "High Molecular Weight Polyphenylene Vinylene" *Mol. Cryst. Liq. Cryst.* **118** 327 (1985).

30. Murase, I., Ohnishi, T., Noguchi, T. and Hirooka, H. "Highly Conducting Poly(*p*-phenylene vinylene) Prepared from a Sulphonium Salt" *Polymer Comm.* **25** 327 (1984).

31. Murase, I., Ohnishi, T., Noguchi, T., Hirooka, M. and Murakami, S. "Highly Conducting Poly(*p*-phenylene vinylene) Prepared from Sulfonium Salt" *Mol. Cryst. Liq. Cryst.* **118** 333 (1985).

32. Gagnon, D.R. "Chemical, Structural, and Electrical Characterization of Poly(*p*-Phenylene Vinylene)" Ph.D. Dissertation, University of Massachusetts (1986).

33. Patil, A.O., Rughooputh, S.D.D.V. and Wudl, F. "Poly(*p*-phenylene vinylene): Incipient Doping in Conducting Polymers" *Synth. Met.* **29** E115 (1989).

34. Antoun, S., Gagnon, D.R., Karasz, F.E. and Lenz, R.W. "Synthesis and Electrical Conductivity of AsF$_5$-Doped Poly(Arylene Vinylenes)" *Polym. Bull.* **15** 181 (1986).

35. Antoun, S., Gagnon, D.R., Karasz, F.E. and Lenz, R.W. "Preparation and Electrical Conductivity of Poly(1,4-Naphthalene Vinylene)" *J. Polym. Sci. (Letters)* **24** 503 (1986).

36. Han, C.-C., Lenz, R.W. and Karasz, F.E. "Highly Conducting, Iodine-Doped Copoly(phenylene vinylene)s " *Polymer Comm.* **28** 261 (1987).

37. Murase, I., Ohinishi, T., Noguchi, T. and Hirooka, M. "Highly Conducting Poly(Phenylene Vinylene) Derivatives Via Soluble Precursor Process" *Synth. Met.* **17** 639 (1987).

38. Antoun, S., Karasz, F.E. and Lenz, R.W. "Synthesis and Electrical Conductivity of Poly(arylene vinylene). I. Poly(2,5-Dimethoxyphenylene vinylene) and Poly(2,5-Dimethylphenylene vinylene)" *J. Polym. Sci. (Chemistry)* **26** 1809 (1988).

39.   Askari, S.H., Rughooputh, S.D. and Wudl, F. "Substituted-PPV Conducting Polymers: Rigid Rod Polymers with Flexible Side Chains" *Poly. Mat. Sci. Eng.* **59** 1069 (1988).

40.   Momii, T., Tokito, S., Tsutsui, T. and Saito, S. "Synthesis of Poly(2,5-dimethoxy-*p*-phenylene vinylene) Film through a New Precursor Polymer" *Chem. Lett.* 1201 (1988).

41.   Machado, J.M., Karasz, F.E. and Lenz, R.W. "Electrically Conducting Polymer Blends" *Polymer* **29** 1413 (1988).

42.   Schlenoff, J.B., Machado, J.M., Glatkowski, P.J., and Karasz, F.E. "Chemical and Electrochemical Doping in Poly(Paraphenylene Vinylene) Blends" *J. Polym. Sci. (Physics)* **26** 2247 (1988).

43.   Machado, J.M. , Schlenoff, J.B., and Karasz, F.E. "Morphology, Doping and Electrical Properties of Poly(phenylene vinylene)/Poly(ethylene oxide) Blends" *Macromolecules* **4** 1964 (1989).

44.   Ohnishi, T., Murase, I., Noguchi, T. and Hirooka, M. "Highly Conductive Graphite Film Preparation from Pyrolysis of Poly(*p*-Phenylene Vinylene)" *Synth. Met.* **4** 207 (1986).

45.   Ueno, H. and Yoshino, K. "Properties of $FeCl_3$-Intercalated Graphite Film Prepared by Heat Treatment of Poly(*p*-phenylene vinylene) Film" *Phys. Rev. B* **36** 8138 (1987).

46.   Ueno, H., Nogami, T., and Yoshino, K. "Electrical Conductivity and Optical Reflectance of Potassium-Intercalated Graphitized Poly(*p*-phenylene vinylene) Films" *Phys. Rev. B* **36** 3142 (1987).

47.   Bradley, D.D.C., Friend, R.H., Lindenberger, H. and Roth, S. "Infra-red Characterization of Oriented Poly(phenylenevinylene)" *Polymer* **27** 1709 (1986).

48.   Kratky, O. "Zum Deformationsmechanismus der Faserstoffe. I." *Kolloid-Z.* **64** 213 (1933).

49.   Machado, J.M. "New Processes and Materials in Conducting Polymers" Ph.D. Dissertation, University of Massachusetts (1988).

50.   Gagnon, D.R., Karasz, F.E., Thomas, E.L. and Lenz, R.W. "Molecular Orientation and Conductivity in Highly Drawn Poly(*p*-phenylene vinylene)" *Synth. Met.* **20** 85 (1987).

51.   Moon, Y.B., Rughooputh, S.D.D.V., Heeger, A.J., Patil, A.O. and Wudl, F. "X-ray Scattering Study of the Conversion of Poly(*p*-phenylene vinylene) Precursor to the Conjugated Polymer" *Synth. Met.* **29** E79 (1989).

52. Bradley, D.D.C., Friend, R.H., Hartmann, T., Marseglia, E.A., Sokolowski, M.M. and Townsend, P.D. "Structural Studies of Oriented Precursor Route Conjugated Polymers" *Synth. Met.* **17** 473 (1987).

53. Granier, T., Thomas, E.L., Gagnon, D.R., Karasz, F.E., and Lenz, R.W. "Structure Investigation of Poly(p-Phenylene Vinylene)" *J. Polym. Sci. (Physics)* **24** 2793 (1986).

54. Granier, T., Thomas, E.L. and Karasz, F.E. "Paracrystalline Structure of Poly(paraphenylene vinylene)" *J. Polym. Sci. (Physics)* **27** 469 (1989).

55. Hosemann, R. and Bagchi, S.N. <u>Direct Analysis of Diffraction by Matter</u> North-Holland, Amsterdam, 1962.

56. Machado, J.M., Karasz, F.E., Kovar, R.F., Burnett, J.M., and Druy, M.A. "A Continuous Process for Preparing Highly Conducting, Uniaxially Oriented Poly(phenylene vinylene) Film" *New Polym. Mat.* (in press).

57. Machado, J.M., Masse, M.A. and Karasz, F.E. "Anisotropic Mechanical Properties of Uniaxially Oriented Electrically Conducting Poly(p-phenylene vinylene)" *Polymer* (in press).

58. Yoshino, K., Takiguchi, T., Hayashi, S., Park, D.H. and Sugimoto, R. "Electrical an Optical Properties of Poly(p-phenylene vinylene) and Effects of Electrochemical Doping" *Jap. J. Appl. Phys. Part 1* **25** 881 (1986).

59. Bradley, D.D.C., Evans, G.P. and Friend, R.H. "Characterisation of Poly(phenylenevinylene) by Infrared and Optical Absorption" *Synth. Met.* **17** 651 (1987).

60. Bradley, D.D.C., Friend, R.H. and Feast, W.J. "Photoexcitation in Poly(Arylenevinylenes)" *Synth. Met.* **17** 645 (1987).

61. Obrzut, J. and Karasz, F.E. "Defects in the Electronic Structure of Poly(p-phenylene vinylene): Electronic Spectra, Electrochemical Behavior, and Molecular Orbital Calculations" *J. Chem. Phys.* **87** 6178 (1987).

62. Meredith, G.R. "Organic Materials for Nonlinear Optics" *Mat. Res. Soc. Bull.* **13** 24 (1988).

63. Bloembergen, N. "Nonlinear Optics and Spectroscopy" *Science* **216** 1057 (1982).

64. Kaino, T., Kubodera, K., Tomaru, S., Kurihara, T., Saito, S., Tsutsui, T. and Tokito, S. "Optical Third-Harmonic Generation from Poly(p-phenylenevinylene) Thin Films" *Electron. Lett.* **23** 1095 (1987).

65. Singh, B.P., Prasad, P.N., and Karasz, F.E. "Third Order Non-Linear Optical Properties of Oriented Films of Poly(*p*-phenylene vinylene) Investigated by Femtosecond Degenerate Four wave Mixing" *Polymer* **29** 1941 (1988).

66. Prasad, P.N. and Karasz, F.E. (unpublished results).

67. Karasz, F.E., Chien, J.C.W., Galkiewicz, R., Wnek, G.E., Heeger, A.J. and MacDiarmid, A.G. "Nacent Morphology of Polyacetylene" *Nature* **282** 286 (1979).

68. Chien, J.C.W., Yamashita, Y., Hirsch, J.A., Fan, J.L., Schen, M.A. and Karasz, F.E. "Resolution of Controversy Concerning the Morphology of Polyacetylene" *Nature* **299** 608 (1982).

69. Chien, J.C.W. <u>Polyacetylene: Chemistry, Physics and Material Science</u> Academic Press, NY, 1984.

70. Epstein, A.J., Rommelmann, H., Fernquist, R., Gibson, H.W., Druy, M.A. and Woerner, T. "Morphology of Polyacetylene and Doped Polyacetylene" *Polymer* **23** 1211 (1982).

71. Edwards, J.H. and Feast, W.J. "A New Synthesis of Poly(acetylene)" *Polymer Comm.* **21** 595 (1980).

72. Edwards, J.H., Feast, W.J. and Bott, D.C. "New Routes to Conjugated Polymers: 1. A Two Step Route to Polyacetylene" *Polymer* **25** 395 (1984).

73. White, D. and Bott, D.C. "The Production of Oriented Crystalline Poly(acetylene) by the Durham Route" *Polymer. Comm.* **25** 98 (1984).

74. Pradere, P. and Boudet, A. "Influence of the Mode of Synthesis on the Morphology and Structure of Polyparaphenylene" *J. Mat. Sci.* **22** 4240 (1987).

75. Kovacic, P. and Kyriakis, A. "Polymerization of Benzene to *p*-Polyphenyl by Aluminum Chloride-Cupric Chloride" *J. Am. Chem. Soc.* **85** 453 (1963).

76. Yamamoto, T. and Yamamoto, A. "A Novel Type of Polycondensation of Polyhalogenated Organic Aromatic Compounds Producing Thermally Stable Polyphenylene Polymers Promoted by Nickel Complexes" *Chem. Lett.* 353 (1977).

77. Fauvarque, J.-F., Petit, M.A., Pfluger, F., Jutand, A., Hevrot, C. and Toupel, M. "Preparation of Poly(1,4-phenylene) by Nickel(0) Complex-Catalyzed Electropolymerization" *Makromol. Chem. Rapid Comm.* **4** 455 (1984).

78. Pradere, P. and Boudet, A. "Effect of Doping on the Crystalline Structure of Polyparaphenylene" *J. Mat. Sci. Lett.* **7** 10 (1988).

79. Shimamura, K., Karasz, F.E., Chien, J.C.W. and Hirsch, J.A. "Structure of Iodine Doped Polyacetylene" *Makromol. Chem. Rapid Comm.* **3** 269 (1982).

80. Chien, J.C.W., Karasz, F.E. and Shimamura, K. "Electron Diffraction Study of Pristine- and Iodine-Doped Poly(*cis*-Acetylene)" *J. Polym. Sci. (Letters)* **20** 97 (1982).

81. Chien, J.C.W., Karasz, F.E. and Shimamura, K. "Crystal Structure of Pristine and Iodine-Doped *cis*-Polyacetylene" *Macromolecules* **15** 1012 (1982).

82. Shimamura, K., Yamashita, Y., Kasahara, H. and Monobe, K. "Structure Change of Polyacetylene-I_x^- Complex by Iodine Doping" *Synth. Met.* **17** 485 (1987).

83. Baughman, R.H., Murthy, N.S., Miller, G.G. and Shacklette, L.W. "Staging in Polyacetylene-Iodine Conductors" *J. Chem. Phys.* **79** 1065 (1983).

84. Dresselhaus, M.S. and Dresselhaus, G. "Intercalation Compounds of Graphite" *Adv. Phys.* **30** 139 (1981).

85. Wieners, G., Weizenhofer, R., Monkenbusch, M., Stamm, M., Lieser, G., Enkelmann, V. and Wegner, G. "Packing and State of Order in Conducting Polymers. The Structure of $[(CH)(SbF_6)_{0.06}]_x$" *Makromol. Chem. Rapid Comm.* **6** 425 (1985).

86. Riekel, C., Hasslin, H.W., Menke, K. and Roth, S. "Crystalline Features in AsF_5-Doped Polyacetylene" *J. Chem. Phys.* **77** 4254 (1982).

87. Hasslin, H.W., Riekel, C., Menke, K. and Roth, S. "A Neutron Diffraction Study on the Doping of Polyacetylene by AsF_5" *Makromol. Chem.* **185** 397 (1984).

88. Blessings, R.H. and Coppens, P. "On the Crystallography of the TTF-TCNQ Salt at Reduced Temperatures" *Sol. State. Comm.* **15** 215 (1974).

89. Fritz, H.P., Gebauer, H., Friedrich, P., Ecker, P., Artes, R. and Schubert, U. "Electrochemische Synthesen, XIV[1]. Radikalkation-Salze des Naphthalins" *Z. Naturforsch.* **33b** 498 (1978).

90. Enkelmann, V., Morra, B.S., Krohnke, C., Wegner, G. and Heinze, J. "Structure and Properties of Cation-Radical Salts of Arenes. II. Crystal Structure, Phase Transitions and Analysis of the Electrochemical Crystallization Process of Fluoranthenyl Cation-Radical Salts" *Chem. Phys.* **66** 303 (1982).

91. Enkelmann, V., Gockelmann, K., Wieners, G. and Monkenbusch, M. "Radical Cation Salts of Arenes. Structure, Properties and Model Character for Conducting Polymers" *Mol. Cryst. Liq. Cryst.* **120** 195 (1985).

92. Baughman, R.H., Murhthy, N.S. and Miller, G.G. "The Structure of Metallic Complexes of Polyacetylene with Alkali Metals" *J. Chem. Phys.* **79** 515 (1983).

93. Winokur, M., Moon, Y.B., Heeger, A.J., Barker, J., Bott, D.C. and Shirakawa, H. "X-ray Scattering from Sodium-Doped Polyacetylene: Incommensurate-Commensurate and Order-Disorder Transformations" *Phys. Rev. Lett.* **58** 2329 (1987).

94. Hasslin, H.W. and Riekel, C. "A Real Time Neutron Diffraction Study on the Reaction of AsF$_5$ with Deuterated Polyparapheylene" *Synth. Met.* **5** 37 (1982).

95. Stamm, M. and Hocker, J. "Structural changes in Polyparaphenylene by the Doping with AsF$_5$ and Alkali Metals" *J. Phys. C3* **44** 667 (1983).

96. Pradere, P., Boudet, A., Goblot, J.Y., Froyer, G. and Maurice, F. "Crystalline Structure and Morphology of Undoped and AsF$_5$ Doped Polyparaphenylene" *Mol. Cryst. Liq. Cryst.* **118** 277 (1985).

97. Stamm, M. , Fink, J. and Tieke, B. "Crystal Structure of Undoped and Lithium-Doped Polyparaphenylene" *Mol. Cryst. Liq. Cryst.* **118** 218 (1985).

98. Janossy, A., Pogany, L., Pekker, S. and Swietlik, R. "Distribution of Iodine in Doped Polyacetylene Films" *Mol. Cryst. Liq. Cryst.* **77** 185 (1981).

99. Rolland, M., Cadene, M., Bresse, J.-F., Rossi, A., Riviere, D., Aldissi, M., Benoit, C. and Bernier, P. "S.E.M. and Castaing Microprobe Studies of Undoped and Doped Polyacetylene Films" *Mat. Res. Bull.* **16** 1045 (1981).

100. Beniot, C., Rolland, M., Aldissi, M., Rossi, A., Cadene, M., and Bernier, P. "Diffusion Study of Iodine and Antimony Pentafluoride in Polyacetylene" *Phys. Stat. Sol. (A)* **68** 209 (1981).

101. White, J.R. and Thomas, E.L. "Advances in SEM of Polymers" *Rubb. Chem. Tech.* **57** 457 (1984).

102. Foot, P.J.S., Mohammed, F., Calvert, P.D. and Billingham, N.C. "Diffusion in Conducting Polymers" *J. Phys. D: Appl. Phys.* **20** 1354 (1987).

103. Laskey, R.C., Kramer, E.J. and Hui, C.-Y. " The Initial Stages of Case II Diffusion at Low Penetrant Activities" *Polymer* **29** 673 (1988).

104. Lenz, R.W., Han, C.-C., Stenger-Smith, J., and Karasz, F.E. "Preparation of Poly(phenylene vinylene) from Cycloalkane Sulfonium Salt Monomers and Polymers" *J. Polym. Sci. (Chemistry)* **26** 3241 (1988).

105. Machado, J.M., Denton III, F.R., Schlenoff, J.B., Karasz, F.E., and Lahti, P.M. "Analytical Methods for Molecular Weight Determination of Poly(*p*-Xylyidene Dihalide Sulfonium Halide): Degree of Polymerization of Poly(*p*-Phenylene Vinylene) Precursors" *J. Polym. Sci. (Physics)* **27** 199 (1989).

106. Kemmitt, R.D.W. and Sharp, D.W.A. "Fluorides of the Main Group Elements" *Adv. Fluorine Chem.* 4 208 (1965).

107. ASTM procedure D-1505.

108. Buerger, M.J. <u>X-Ray Crystallography</u> J. Wiley & Sons, NY, 1942.

109. White, J.R. and Thomas, E.L. "Applications of Tilted Illumination in Transmission Electron Microscopy and Diffraction of Crystalline Materials" *J. Mat. Sci.* 20 2169 (1985).

110. Spence, J.C.H. <u>Experimental High Resolution Electron Microscopy</u> Clarendon Press, Oxford, 1981.

111. Chu, W.-K., Mayer, J.W., and Nicolet, M.-A. <u>Backscattering Spectrometry</u> Academic Press, NY, 1978.

112. Doolittle, L.R. "Algorithms for the Rapid Simulation of Rutherford Backscattering Spectra" *Nuc. Instr. Meth. Phys.* **B9** 344 (1985).

113. Muilenberg, G.E. (ed.) <u>Handbook of X-Ray Photoelectron Spectroscopy</u> Perkin-Elmer Corp., Eden Prairie, MN, 1979.

114. Powell, C.J. "Attenuation Lengths of Low-Energy Electrons in Solids" *Surface Sci.* **44** 29 (1974).

115. Harrick, N.J. <u>Internal Reflection Spectroscopy</u> Harrick Scientific Corp., Ossining, NY, 1979.

116. Cotton, F.A. and Wilkinson, G. <u>Advanced Inorgainc Chemistry</u> Interscience, NY. 1972.

117. Landauer, R. "The Electrical Resistance of Binary Metallic Mixtures" *J. Appl. Phys.* **23** 779 (1952).

118. Machado, J.M., Obrzut, J. and Karasz, F.E. (unpublished results).

119. Khidir-Aljibury, A.L. and Redington, R.L. "Infrared Spectra of Matrix-Isolated Antimony and Arsenic Pentafluorides" *J. Chem. Phys.* **52** 453 (1970).

120. Qureshi, A.M. and Aubke, F. "Vibrational Spectra of Some Perfluoro-arsenates and Antimonates with Nitrogen Heterocations" *Can. J. Chem.* **48** 3117 (1970).

121. Christie, K.O., Schack, C.J. and Wilson, R.D. "Novel Oxonuim Salts. Synthesis and Characterization of $OH_3^+SbF_6^-$ and $OH_3^+AsF_6^-$" *Inorg. Chem.* **14** 2224 (1975).

122. Clark, D.T. and Thomas, H.R. "Applications of ESCA to Polymer Chemistry. XVII. Systematic Investigation of the Core Levels of Simple Homopolymers" *J. Polym. Sci. (Chemistry)* **16** 791 (1978).

123. Obrzut, M.J. and Karasz, F.E. "X-ray Photoelectron Spectroscopy of Neutral and Electrochemically Doped Poly(*p*-phenylene vinylene)" *Macromolecules* **22** 458 (1989).

124. Clark, D.T., Feast, W.J., Kilcast, D. and Musgrave, W.K.R. "Applications of ESCA to Polymer Chemistry. III. Structures and Bonding in Homopolymers of Ethylene and the Fluoroethylenes and the Determination of the Composotions of Fluoro Copolymers" *J. Polym. Sci. (Chemistry)* **11** 389 (1973).

125. Brant, P., Moran, M.J. and Weber, D.C. "X-ray Photoelectron Spectra of Dopant Molecules for Conducting Polymers. Vapor Phase Core Level Binding Energies for Arsenic and Antimony Pentafluorides" *Chem. Phys. Lett.* **76** 529 (1980).

126. Martin, R.L., Mills, B.E. and Shirley, D.A. "Fluorine 1s Correlation States in the Photoionization of Hydrogen Fluoride: Experiment and Theory" *J. Chem. Phys.* **64** 3690 (1976).

127. D'Yvoire, F., Prades, F. and Guerin, H. "Diagramme de Phases du Systeme As_2O_3-As_2O_5-H_2O a 22°C et Etude des Composes $2As_2O_3$-As_2O_5-H_2O et As_2O_{4-x}" *C.R. Acad. Sci. Paris Ser. C* **268** 1514 (1969).

128. Jansen, M. "Die Kristallstruktur von As_2O_5 eine Neue Raumnetzstruktur" *Z. Anorg. Allg. Chem.* **441** 5 (1981).

130. Clarke, T.C., Geiss, R.H., Gill, W.D., Brant, P.M., Morawitz, H., Street, G.B. and Sayers, D.E. " The Mechanism of Arsenic Pentafluoride Doping of Polyacetylene" *Synth. Met* **1** 21 (1979/80).

131. Alexander, L.E. <u>X-Ray Difrraction Methods in Polymer Science</u> Wiley-Interscience, NY, 1969.

132. Chan, C.T., Kamitakihara, W.A., Ho, K.M., and Eklund, P.C. "Charge-Transfer Effects in Graphite Intercalates: Ab Initio Calculations and Neutron-Diffraction Experiment" *Phys. Rev. Lett.* **58** 1528 (1987).

133. Murthy, N.S., Shacklette, L.W. and Baughman, R.H. "Effect of Charge Transfer on Chain Dimension in *trans*-Polyacetylene" *J. Chem. Phys.* **87** 2346 (1987).

134. Ibers, J.A. "A Note on the Least-Squares Method: The Refinement of the Structure of $KAsF_6$" *Acta Cryst.* **9** 967 (1956).

135. Burns, J.H. "The Crystal Structure of Lithium Fluoroantimonate(V)" *Acta Cryst.* **15** 1098 (1962).

136. Bondi, A. <u>Physical Properties of Molecular Crystals, Liquids, and Glasses</u> Wiley, NY, 1968.

137. Bergland, B., Tellgren, R. and Thomas, J.O. "Hydrogen Bond Studies. CII. An X-ray Determination of the Crystal Structure of Sodium Perchlorate Monohydrate, $NaClO_4 \cdot H_2O$" *Acta Cryst.* B31 1842 (1975).

138. Klug, H.P. and Alexander, L.E. X-Ray Diffraction Procedures Wiley, NY, 1954.

139. MacDiarmid, A.G. and Heeger, A.J. "Organic Metals and Semiconductors: The Chemistry of Polyacetylene $(CH)_x$ and its Derivatives" *Synth. Met.* 1 101 (1979/80).

140. Han, C.-C. and Elsenbaumer, R.L. "Protonic Acids: Generally Applicable Dopants for Conducting Polymers" *Synth. Met.* 30 123 (1989).

141. Finder, C.J, Newton, M.G. and Allinger, N.L. "An Improved Structure of *trans*-Stilbene" *Acta Cryst.* B30 411 (1974).

142. Minter, J.R., Shimamura, K. and Thomas, E.L. "Microstuctural Study of As-Extruded and Heat-Treated Ribbons of Poly(*p*-phenylene benzobisthiazole)" *J. Mat. Sci.* 16 3303 (1981).

143. Krause, S.J., Haddock, T.B., Vezie, D.L., Lenhert, P.G., Hwang, W.-F., Price, G.E., Helminiak, T.E., O'Brien, J.F. and Adams, W.W. "Morphology and Properties of Rigid-Rod Poly(*p*-phenylene benzobisoxazole) (PBO) and Stiff-Chain Poly(2,5(6)-benzoxazole) (ABPBO) Fibres" *Polymer* 29 1354 (1988).

144. Simpson, J.H., Rice, D.M. and Karasz, F.E. (in preparation).

145. Mattoussi, H. and Karasz, F.E. (unpublished results).

146. DeTeresa, S.J., Allen, S.R., Farris, R.J. and Porter, R.S. "Compressive and Torsional Behaviour of Kevlar 49 Fibre" *J. Mater. Sci.* 19 57 (1984).

147. Roche, E.J., Takahashi, T. and Thomas, E.L. "Structure of High Modulus Fibres of Poly-*p*-Phenylene Benzbisthiazole" *ACS Sympos. Ser. No. 141* 303 (1980).

148. Dobb, M.G., Johnson, D.J. and Saville, B.P. "Compressional Behaviour of Kevlar Fibres" *Polymer* 22 960 (1981).

149. DeTeresa, S.J., Porter, R.S. and Farris, R.J. "Experimental Verification of a Microbuckling Model for the Axial Compressive Failure of High Performance Fibres" *J. Mater. Sci.* 23 1886 (1988).

150. Crank, J. The Mathematics of Diffusion 2nd ed., Oxford University Press, Oxford, 1975.

151. Crank, J. and Park, G.S. "Diffusion in High Polymers: Some Anomolies and their Significance" *Trans. Farad. Soc.* 82 1072 (1951).

152. Long, F.A. and Richmond, D. "Concentration Gradients for Diffusion of Vapors in Glassy Polymers and their Relation to Time Dependent Diffusion Phenomena" *J. Am. Chem. Soc.* **82** 513 (1960).

153. Thomas, N.L. and Windle, A.H. "Discontinuous Shape Changes Associated with Case II Transport of Methanol in Thin Sheets of PMMA" *Polymer* **18** 1195 (1977).

154. Mills, P.J., Palmstrom, C.J. and Kramer, E.J. "Concentration Profiles of non-Fickian Diffusants in Glassy Polymers by Rutherford Backscattering Spectrometry" *J. Mater. Sci.* **21** 1479 (1986).

155. Frommer, J.E., Elsenbaumer, R.L., Eckhardt, H. and Chance, R.R. "Arsenic Trifluoride-Arsenic Pentafluoride Synergism in the Formation of Electrically Conductive Poly(*p*-phenylene sulfide)" *J. Polym. Sci. (Letters)* **21** 39 (1983).

156. Odian, G. <u>Principles of Polymerization</u> Wiley-Interscience NY, 1980.